Quantum Dynamics of Strongly Interacting Many-Body Systems

A dissertation presented

by

Soonwon Choi

to

The Department of Physics

in partial fulfillment of the requirements

for the degree of

Doctor of Philosophy

in the subject of

Physics

Harvard University

Cambridge, Massachusetts

April 2018

Dissertation Advisor: Author

Professor Mikhail D. Lukin **Soonwon Choi**

Quantum Dynamics of Strongly Interacting Many-Body Systems

Abstract

Recent advances in coherent manipulation and control have led to new opportunities to study non-equilibrium dynamics in quantum many-body systems. Using a variety of experimental platforms ranging from cold atoms and ions to solid-state spin defects, small building blocks of fully controllable quantum systems can be assembled into a strongly interacting many-body system. With this approach, one can gain new insights into fundamental questions in basic science such as the mechanism of quantum thermalization or the existence of exotic phases of matter out of equilibrium. At the same time, a fully controllable large-scale quantum device has promising applications for high precision sensing, secure communication, and quantum information processing.

This thesis describes recent progress in engineering quantum dynamics that is robust against various imperfections such as environmental noise, disorder, or imprecise controls. We find that non-equilibrium quantum states of strongly interacting systems can be protected from imperfections upon appropriate external manipulations such as time-dependent periodic controls, engineered coherent or dissipative interactions, or an introduction of strong quenched disorder. Furthermore, under certain conditions, these imperfections can be utilized to stabilize non-trivial quantum states. Our results challenge conventional wisdom of statistical mechanics, shedding light on the microscopic mechanisms of thermal-

ization. We also discuss how engineered dynamics can be harnessed for applications such as quantum metrology, simulations, or information processing.

Contents

Citations to Previously Published Work

Most of the chapters in this thesis have previously appeared in print elsewhere. These are:

Chapter 2 and Appendix A:

Georg Kucsko*, Soonwon Choi*, Joonhee Choi*, Peter C. Maurer, Hengyun Zhou, Renate Landig, Hitoshi Sumiya, Shinobu Onoda, Junich Isoya, Fedor Jelezko, Eugene Demler, Norman Y. Yao, Mikhail D. Lukin, *Critical thermalization of a disordered dipolar spin system in diamond*, arXiv:1609.08216 (2016)

Chapter 3 and Appendix B:

Soonwon Choi*, Joonhee Choi*, Renate Landig*, Georg Kucsko, Hengyun Zhou, Junichi Isoya, Fedor Jelezko, Shinobu Onoda, Hitoshi Sumiya, Vedika Khemani, Curt von Keyserlingk, Norman Y. Yao, Eugene Demler, Mikhail D. Lukin, *Observation of discrete time-crystalline order in a disordered dipolar many-body system*, Nature **543**, 221-225 (2017) and Wen Wei Ho, Soonwon Choi, Mikhail D. Lukin, Dmitry A. Abanin, *Critical Time Crystals in Dipolar Systems*, Phys. Rev. Lett. **119**, 010602 (2017)

Chapter 4 and Appendix C:

Soonwon Choi, Norman Y. Yao, Mikhail D. Lukin, *Quantum metrology based on strongly correlated matter*, arXiv:1801.00042 (2018)

Chapter 5 and Appendix D:

Soonwon Choi, Norman Y. Yao, Mikhail D. Lukin, *Dynamical Engineering of Interactions in Qudit Ensembles*, Phys. Rev. Lett. **119**, 183603 (2017)

Chapter 6 and Appendix E:

Soonwon Choi, Norman Y. Yao, Sarang Gopalakrishnan, Mikhail D. Lukin, *Quantum control of many-body localized states*, arXiv:1508.06992 (2015)

Chapter 7 and Appendix F

Soonwon Choi, Dmitry A. Abanin, Mikhail D. Lukin, *Dynamically induced many-body localization*, Phys. Rev. B **97**, 100301(R) (2018)

Chapter 9 and Appendix G:

Leo Zhou*, Soonwon Choi*, Mikhail D. Lukin, *Symmetry-protected dissipative preparation of matrix product states*, arXiv:1706.01995 (2017)

Chapter 10 and Appendix H:

Jeff D. Thompson, Travis L. Nicholson, Qi-Yu Liang, Sergio H. Cantu, Aditya V. Venkatramani, Soonwon Choi, Ilya A. Fedorov, Daniel Viscor, Thomas Pohl, Mikhail D. Lukin, Vladan Vuletić *Symmetry-protected collisions between strongly interacting photons*, Nature **542**, 206-209 (2017) and Przemek Bienias*, Soonwon Choi*, Ofer Firstenberg, Mohammad F. Maghrebi, Michael Gullans, Mikhail D. Lukin, Alexey V. Gorshkov, Hans Peter Büchler, *Scattering resonances and bound states for strongly interacting Rydberg polaritons*, Phys. Rev. A **90**, 053804 (2014)

Chapter 11 and Appendix I:

Hannes Pichler*, Soonwon Choi*, Peter Zoller, Mikhail D. Lukin, *Universal photonic quantum computation via time-delayed feedback*, Proceedings of the National Academy of Sciences of the United States of America **114**, 11362-11367 (2017).

* These authors contributed equally to this work.

Acknowledgments

First and foremost, I would like to thank my advisor Professor Mikhail Lukin. As my academic advisor and personal mentor, Misha showed great patience in guiding and encouraging me to pursue an academic career over the past few years. I was first introduced to Misha during my senior year by my undergraduate mentor Professor John Preskill. At that time, I was very much intrigued by quantum information theory and research projects being done in the Preskill group. In particular, I was fascinated by how Alexey Gorshkov, Liang Jiang, and Darrick Chang – who were postdocs in the Preskill group – could explain a seemingly complicated theory concept using intuitive languages, come up with a new brilliant idea, and propose its potential realizations in laboratories. Highly influenced by these postdocs, I decided to proceed to a PhD program in physics. Only after consulting John about my academic career plan, did I learn that my postdoc heroes were actually trained by the same advisor, Misha at Harvard. I would like to acknowledge John and the postdocs, especially Alexey, for introducing a great mentor, Misha, and still providing advice in my academic career.

I was extremely blessed to have many other mentors during my PhD program. My thesis committee members, Professors Eugene Demler and Bertrand Halperin, were readily accessible, providing invaluable wisdom whenever it was needed. Also, most of my knowledge on condensed matter physics originates from courses taught by Eugene and Bert. I am also indebted to Professor Peter Zoller. Occasional conversations with him were not only academically interesting and inspirational, but they also provided opportunities to ponder about my own research direction and future vision. Professor Norman Yao is a special one. While my original mission to oversee his exercise routine became a complete failure, we have successfully gained many pounds from Chinese food and written multi-

ple research papers together. Talking about physics problems with Norm was more like having fun rather than doing work. As an international student, I have also benefited from the presence of Professors Hongkun Park and Philip Kim, who shared similar cultural and educational background with me and could provide unique advice.

One of the most important aspects of my graduate years is that, thanks to Misha's guidance, I had a lot of opportunities to interact with many different groups of people. It was my great pleasure to spend my graduate years together with Igor Lovchinsky, Elana Urbach, Tamara Sumarac, Helena Knowles, Javier Sanchez-Yamagishi, Alexei Bylinskii, Ziwei Qiu, Alex Sushkov, Kristine Rezai, Aditya Venkatramani, Sergio Hiram Cantu, Travis Nicholson, Jeff Thompson, Ofer Firstenberg, Qiyu Liang, Alexander Zibrov, Trond Andersen, Shimon Kolkowitz, Arthur Safira, Emma Rosenfeld, Aaron Kabcenell, Michael Gullans, Michael Goldman, Rivka Bekenstein, Ruffin Evans, Alp Sipahigil, Christian Nguyen, Bo Dwyer, Po Samutpraphoot, Mihir Bhaskar, David Levonian, Tamara Djordjevic, Paloma Ocola, Emil Khabiboulline, Paul Dieterle, Yiwen Chu, Brendan Shields, Joaquin Rodriguez-Nieva, Florentin Reiter, Ephraim Shahmoon, and Valentin Kasper.

In particular, I greatly enjoyed talking about physics and life with theorist friends, Hannes Pichler, Wen Wei Ho, Leo Zhou, Dominik Wild, Janos Perczel, Shengtao Wang, Vedika Khemani, Sarang Gopalakrishnan, Michael Knap, Martin Schütz, Rhine Samajdar, and Iris Cong. Finding unstable periodic orbits (Chapter 8) at 2am in the Lyman building together with Hannes, struggling to develop uniqueness proof (Chapter 9) with Leo, talking about seemingly ingenious ideas such as topological lasers over dinner (not published) with Dominik, and being welcomed every morning by Martin in our shared office were only a very small fraction of memories that I remember with fondness. Also, I would like

to express my special thanks to relatively junior group members Hengyun, Tamara, and Iris. Their unlimited curiosities and enthusiam towards science were strong motivational reminders for myself. I also appreciate Hengyun and Iris for their comments on my thesis chapters.

Starting from my third year, I have collaborated with the black diamond team, Peter Maurer, Georg Kucsko, Joonhee Choi, Hengyun Zhou (Harry), and Renate Landig. For more than two years, Georg, Joonhee and I met almost everyday to talk about new "crazy theory models" regarding our mysterious diamond samples, most of which were eventually disproven by experimental measurements. While this endless series of failures was one of the biggest challenges that I faced during my PhD program, it is also these experiences that taught me the pleasure of exploring unknown physics, followed by very rare, but still existent moments of discoveries. I am deeply grateful to Georg and Joonhee for teaching me how to look at experimental data from an experimentalist's perspective and for becoming my effective brothers in Cambridge over the last four years. I also thank Harry and Renate for their patience during our long, late evening writing sessions.

I was also very fortunate to work with the atom-array team, Alex Keesling, Harry Levine, Hannes Bernien, Ahmed Omran, Sylvain Schwartz, and Manuel Endres, over the last two years. It is my honor to be a friend and theory collaborator of the amazing experimentalists behind one of the world's best quantum simulator.

My six years of graduate studies might have not been bearable without the constant supports I have received from my friends. To this end, I would like to acknowledge my friends from G1 year, Alex Lukin, Shubhayu Chatterjee, and Lee Liu, and Korean friends in the department, Eun-Gook Moon, Eunmi Chae, Junhyun Lee, Junghyun Lee, Jong Yeon

Lee, Seung Hwan Lee, Minjae Cho, Monica Kang, and Jae Hyeon Lee. I would like to also express my special thanks to Lisa Cacciabaudo, Joan Hamilton, Karl Coleman, Clare Ploucha, and Samantha Dakoulas for their incredibly efficient administrative supports.

Finally, I would like to thank my mother, father, sister Seokyong, and my wife Aram for their endless love, support and cheers.

To my parents Minho Choi and Kwanghee Jun,
and my wife Aram Shin.

Chapter 1

Introduction

1.1 Quantum many-body dynamics

1.1.1 Quantum many-body systems and information processsing

Quantum mechanics is one of the most sophisticated and successful theories of the physical sciences. It is clearly distinguished from any classical theories starting from the way how the information about a physical state is described. A quantum state of a system is specified by a set of complex numbers called a wavefunction [1]. These numbers correspond to the quantum amplitudes for each possible configuration of the system. Any physically observable quantities can be computed from the wavefunction, hence it contains a complete information about the state of the system.

When a system consists of many particles, the amount of information contained in its wavefunction may become extremely large. This is because, unlike classical descriptions, a wavefunction allows a superposition of exponentially many different configurations of

particles. For example, the amount of memory required to describe a collection of a hundred spin-1/2 particles can already exceed the entire digital information human-kind has ever produced in history [2]. More than three decades ago, it was suggested that such richness may provide an opportunity to encode a large amount of information in a quantum many-body system and to utilize its coherent time evolution for applications such as sensing, simulations, and information processing [3]. However, current efforts are challenged by the extreme sensitivity of such systems to environmental noise, which completely destroys any encoded quantum information. Even when a system is well isolated from its environment, the natural dynamics of many particles generically exhibit complex chaotic behavior, which scrambles useful local information into non-local correlations that cannot be recovered.

1.1.2 Statistical mechanics and thermalization

The chaotic nature of many-body dynamics provides a good starting point to statistical mechanics, which forms another important pillar of modern physics. Statistical mechanics considers systems with a large number of degrees of freedom and relies on ergodic hypothesis: when any detailed information about initial conditions quickly becomes inaccessible, a many-body system after a sufficiently long time evolution should be characterized by only a few conserved quantities such as total energy or number of particles [4]. In this scenario, one may reasonably *assume* that the behavior of any typical observables in such system equals the behavior averaged over all possible configurations that have the same conserved quantities. The ensemble of such configurations is often called a thermal ensemble, or a thermal state, and the dynamical process from an out-of-equilibrium initial state to a ther-

mal state is called thermalization. This phenomenon seems ubiquitous, occurring in a wide range of systems from atomic gases to black holes.

The paradigm of thermalization and ergodic hypothesis has led to great success in describing complex systems in equilibrium. In particular, statistical mechanics allowed the quantitative explanation of transitions between different phases of matter and their applications to new technologies. However, the theoretical understanding behind its fundamental assumption still remains as an open question to this day. What are the necessary conditions for a system to thermalize? What are the microscopic mechanism of thermalization in a quantum many-body system? Is it possible to engineer an interacting many-body quantum system that evades rapid thermalization?

1.1.3 Experimental advances

Recent experimental progresses opened the opportunity to re-examine fundamental problems of quantum many-body physics from new perspectives. In a variety of systems ranging from trapped atoms and ions to superconducting circuits and solid-state defects, it is possible to prepare, manipulate, and read-out coherent quantum states of small systems. Exotic concepts that are unique in quantum mechanics such as the superposition principle and entanglement have been explicitly demonstrated in laboratories. Furthermore, using small quantum systems as building blocks, one can construct quantum many-body systems with designed Hamiltonian dynamics. Experimental developments have already reached the level where the engineered quantum dynamics cannot be simulated by any classical methods without making approximations.

These new technologies allowed exotic theory models to be directly implemented and

tested in laboratory. In turn, surprising observations that disobey conventional wisdom are often found, providing new insights towards unexplored physics. Therefore, the close interplay between theory and experiments are being emphasized in the study of non-equilibrium dynamics of quantum many-body systems.

1.2 Overview of thesis

This thesis presents recent progress on the study of quantum dynamics in strongly interacting many-body systems. In order to probe many-body physics at microscopic level, we perform both experiments and theoretical analysis aided by numerical calculations. Hence, this thesis consists of a mixture of theoretical and experimental results. The subjects of the studies are centered around controlling the dynamics of interacting quantum systems. In particular, we focus on many-body systems, which are either chaotic or non-interacting under their natural time evolutions. We aim to find applications of quantum dynamics in realistic settings that include the presence of noise, imperfect controls, and generic interactions. In this sense, these works attempt to bridge out-of-equilibrium quantum dynamics and quantum information science.

1.2.1 Critical thermalization and discrete time-crystalline order

Chapter 2 and 3 discuss novel experiments that utilize a high-density ensemble of nitrogen-vacancy color center defects in diamond in order to probe quantum dynamics in strongly disordered, dipolar interacting spins. We find that the speed of thermalization can be drastically reduced due to the presence of strong disorder. Then, we demonstrate that

such slowly thermalizing systems can host exotic temporal correlations, so-called discrete time-crystalline (DTC) order, that are forbidden in conventional matter in equilibrium. The mechanism behind DTC order can be utilized for high-precision sensing, which is discussed in Chapter 4.

1.2.2 Quantum control of interacting many-body systems

Chapter 5, 6, 7, and 9 present how time-periodic driving, strong disorder, or dissipative dynamics can be used as resources to control an interacting many-body system. More specifically, in Chapter 5, we show that interactions among particles can be modified, or even turned off, by means of rapid periodic manipulations. Such a method provides a way to transform an existing experimental system into a versatile quantum simulator. In Chapter 6, we study how to coherently manipulate quantum degrees of freedom that are present in many-body localized (MBL) phases. It has been recently realized that, unlike conventional beliefs, a closed system in the presence of sufficiently strong disorder may not thermalize, retaining the memory of its local initial conditions for an indefinitely long time. We present a protocol to prepare such a system into a low-entropy state and to make use of localized degrees of freedom for information processing. In realistic systems, disorder is often not strong enough to bring a quantum system into a MBL phase. In Chapter 7, we show that the technique elaborated in Chapter 5 can be harnessed to bring a system that is *a priori* thermalizing into an MBL phase if weak disorder is present. This result implies that the ergodicity assumption of statistical mechanics can be violated by appropriate external controls under certain conditions. In addition to the localization induced by strong disorder, there is another type of (weak) ergodicity-breaking called quantum scarring. It refers to a

phenomenon where certain energy eigenstates of a chaotic single-particle system reflect the presence of unstable periodic orbits of the particle in its classical description. In Chapter 8, we extend this phenomenology to quantum many-body chaotic systems.

Chapter 9 is dedicated to discuss how to utilize couplings between a quantum system and its environment – which are often regarded as noise – for the purpose of preparing a pure, strongly correlated quantum state. In particular, we present an explicit protocol to prepare the exact lowest energy eigenstate of the Affleck-Kennedy-Lieb-Tasaki (AKLT) model in one spatial dimension. The ground state of AKLT model has a wide range of applications from the study of symmetry-protected topological phases to quantum information transfer.

1.2.3 Interacting photons and quantum information processing

In Chapter 10 and 11, we explore the dynamics of interacting photons. In vacuum, photons do not interact with one another. In a tailored media, however, effective interactions between individual light quanta can be engineered by means of atom-mediated interactions. More specifically, in Chapter 10, we report recent experimental observations of such interactions enabled by the combination of electromagnetically induced transparency and strong dipole-dipole interactions between atoms in Rydberg states. We demonstrate a controlled and coherent exchange collision between two photons that is accompanied by a $\pi/2$ phase shift. Its theoretical analysis reveals that the value of the phase is determined by the interaction symmetry rather than the precise experimental parameters. The robustness of the phase value implies that this method provides a promising route to realize single-photon switches or all-optical quantum logic gates even in the presence of imperfections. We also

present a theoretical framework to evaluate scattering properties and bound-state structure of photons that interact via this mechanism in more general cases.

Chapter 11 introduces a novel way to construct a universal photonic quantum information processor. Here, our approach is to sequentially generate photons using a single quantum emitter that mediates quantum correlations between photons. We demonstrate that the use of delayed quantum feedback can dramatically increase the amount of the correlations. In particular, we show that in state-of-the-art experiments with single atom-like quantum emitters, the most basic form of delayed quantum feedback – as simple as the addition of a single mirror – already allows for creation of states that are universal resources for quantum computation. This opens new avenues for quantum information processing with photons using minimal experimental resources.

Chapter 2

Critical Thermalization of a Disordered Dipolar Spin System in Diamond

2.1 Introduction

Nearly six decades ago, Anderson predicted that the interplay between transport and disorder in long-range-interacting quantum systems can lead to a novel regime of slow, sub-diffusive thermalization [5]. This is in stark contrast to the case of short-range interactions, where he showed that disorder can arrest dynamics, resulting in the breakdown of ergodicity. Termed localization, this effect has been observed in systems ranging from acoustic waves to cold atomic gases [6, 7, 8, 9, 10]; more recently, it has been shown that localization can persist even in strongly-interacting, isolated quantum systems, a phenomenon dubbed many-body localization [11, 12, 13, 14, 15]. In addition to raising fundamental questions, such systems have also become a basis for the exploration of novel non-equilibrium phases of matter, including Floquet symmetry protected topological phases [16] and discrete time

crystals [17, 18]. The addition of long-range coupling tends to facilitate delocalization, leading to a regime where both localization and ergodicity compete [19, 20]. This so-called critical regime is precisely realized by dipolar spins in 3D, where a combination of power-law transport, dimensionality, and disorder govern the microscopic dynamics. Such systems have long been explored in the context of nuclear magnetic resonance spectroscopy, where a wide variety of techniques have been developed to effectively engineer and control spin dynamics [21, 22, 23, 24, 25]. Despite this, the direct observation of slow, critical dynamics in the presence of strong, controllable disorder remains an outstanding challenge, owing in particular to difficulties in preparing a low-entropy nuclear spin state.

2.2 Experimental approach

Our approach to the realization and study of critical dynamics makes use of disordered, strongly interacting electronic spin impurities associated with Nitrogen Vacancy (NV) centers in diamond. In particular, we study the thermalization dynamics of an initially polarized spin ensemble coupled to a bath of unpolarized spins (Fig. 1A). We directly probe the spin decay dynamics as a function of disorder and identify a regime of critically slow relaxation.

Our experimental system consists of a dense ensemble of NV centers under ambient conditions (Fig. 1B). Each NV center constitutes a $S = 1$ electronic spin with three internal states $|m_s = \pm 1\rangle$ and $|m_s = 0\rangle$, which can be initialized, manipulated and optically read out (Fig. 1C). The NV concentration in our sample is approximately 45 ppm (see Appendix A), yielding an average NV-to-NV separation of 5 nm and a corresponding typical dipolar interaction strength $J \sim (2\pi)\ 420$ kHz; crucially, this is significantly faster than

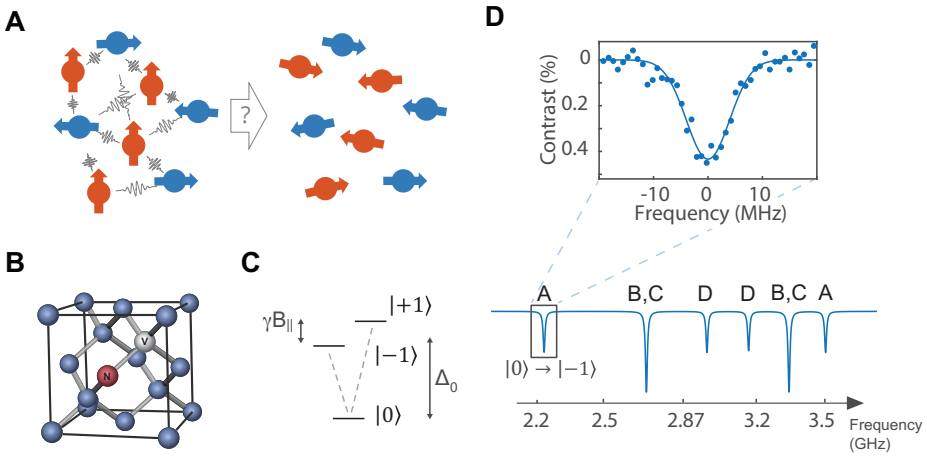

Figure 2.1: **Experimental System. (A)** Schematic depicting two groups of spin ensembles interacting via long-range dipolar interactions. An initially polarized system (red arrows) strongly coupled to a bath of unpolarized spins (blue arrows) will eventually thermalize to an unpolarized spin state. **(B)** The crystallographic structure of diamond contains four possible NV quantization axes, defined by the position of the nitrogen atom and the adjacent vacant lattice site. **(C)** Simplified NV level scheme showing the spin degrees of freedom in the optical ground state. A large zero-field splitting $\Delta_0 = (2\pi)\ 2.87$ GHz in combination with a magnetic field induced Zeeman shift $\gamma B_{\parallel}$ leads to individual addressability of the spin sub-levels. **(D)** The lower image shows a simulated ESR scan, revealing the spin transitions of all four NV groups $\{$A, B, C, D$\}$. For example, the orientation of the external magnetic field can be chosen in such a way that NV groups B and C experience the same magnetic field projection, leading to spectral degeneracy. The upper figure shows an ESR scan of a single transition of NV spins (blue points). Blue solid line represents a Gaussian fit with standard deviation W, corresponding to the average disorder in the sample.

the typical spin coherence times [26]. Owing to lattice strain and an abundance of other paramagnetic impurities (consisting mainly of P1 centers and ^{13}C nuclear spins), our system is also characterized by strong disorder; for each NV, this disorder arises from effective random fields generated by its local environment. The magnitude of the disorder W can be directly extracted from an electron spin resonance (ESR) measurement (Fig. 1D), yielding a Gaussian distribution with a standard deviation $W \approx (2\pi)\ 4.0$ MHz (see Appendix A). Such an environment can also undergo its own dynamics (e.g. due to spin diffusion among

the impurities), resulting in possible variation of the effective random fields over time.

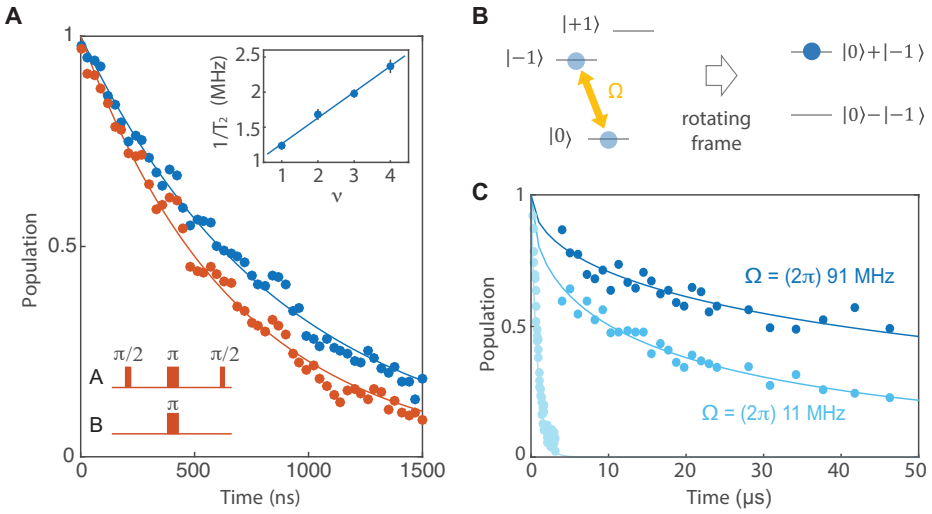

Figure 2.2: **Interacting Spin Ensemble. (A)** Spin echo on NV group A (blue points) and DEER scan on groups A and B (red points). The bottom left inset illustrates the DEER pulse sequence. Solid lines indicate exponential fits to the data. The inset shows the spin echo coherence time as a function of resonant NV groups (blue points). The blue solid line represents a linear fit to the data. **(B)** Schematic diagram depicting the NV level scheme during a spin-lock sequence with a driving strength Ω. In the rotating frame, the spin-locking creates a dressed spin basis with the two eigenstates $(|m_s = 0\rangle + |m_s = -1\rangle)/\sqrt{2}$ and $(|m_s = 0\rangle - |m_s = -1\rangle)/\sqrt{2}$. **(C)** Spin-lock coherence decay for low (light blue points) and high (dark blue points) CW driving power, showing significant extension beyond the spin echo decoherence (gray-blue points). The decay curves are fitted to a stretched exponential function $\exp\left[-\sqrt{t/T}\right]$ [27].

Each NV center in the ensemble can be oriented along any of the four crystallographic axes of the diamond lattice. Different projections of an external magnetic field naturally lead to distinct energy splittings and define four unique NV groups, {A, B, C, D}, which can be individually addressed and controlled in a finite B-field via resonant microwave radiation. By tuning the direction of the magnetic field, one can modify the number of spectrally overlapping groups (e.g. groups B, C in Fig. 1D) and hence the effective density of spins. To directly probe the interaction strength within our system, we perform a double

electron-electron resonance (DEER) measurement between two spectrally separated NV groups, A and B (Fig. 2A, bottom inset). In this measurement the spin echo protocol decouples group A from slowly varying magnetic noise. However, the additional π-pulse on group B after half of the total evolution ensures that the dephasing induced by interactions between the two groups is not decoupled. As depicted in Fig. 2A, by comparing the decay of group A with and without the π-pulse, this measurement allows us to extract the interaction strength $\sim (2\pi)\ 420$ kHz (see Appendix A). By tuning additional NV groups into spectral resonance, we can confirm that the spin dynamics are dominated by interactions. As a function of the number of resonant groups, ν, we find a total dephasing rate, $\gamma_T = \gamma_b + \nu\gamma_0$, with $\gamma_b \approx 0.9$ MHz and $\gamma_0 \approx 0.4$ MHz, consistent with 45 ppm NV center density (Fig. 2A inset) (see Appendix A). The linear dependence of γ_T on ν suggests that the dephasing is dominated by coherent interactions, whose strength is proportional to the density of resonant NV groups.

Central to our thermalization experiments is the ability to tune both the disorder strength and interactions. This is achieved by using spin-locking and Hartman-Hahn (HH) resonances, both of which rely upon continuous microwave driving resonant with the $|m_s = 0\rangle \rightarrow |m_s = -1\rangle$ transitions of the respective NV groups [28, 29]. For excitation with Rabi frequency Ω, this defines a "dressed-state" basis, $|\pm\rangle \approx (|m_s = 0\rangle \pm |m_s = -1\rangle)/\sqrt{2}$ (Fig. 2B). In the rotating frame, the energies of these two states are split by the effective on-site potential $\sqrt{\Omega^2 + \delta_i^2}$, where δ_i is the local disorder potential for spin i (of order W). In the limit of strong driving $\Omega \gg \delta_i$, we obtain an effective disorder potential $\tilde{\delta}_i$ with the reduced width $W_{\text{eff}} \sim W^2/\Omega$, allowing us to tune the disorder by simply adjusting the Rabi frequency. For spin-locking, we initialize NVs along the $\hat{x}$-axis via a $\pi/2$-pulse

around the $\hat{y}$-axis, thereby polarizing spins in the dressed-state basis. Following coherent driving around the $\hat{x}$-axis for time τ, an additional $\pi/2$-pulse allows the measurement of the polarization in this basis. Figure 2C shows a spin-lock experiment performed at two Rabi frequencies. In comparison to the spin coherence time obtained from a spin-echo measurement, we observe a dramatic enhancement of the lifetime. We find that the lifetime is limited by interactions with short-lived spins in our system, which is suppressed by increasing Ω [27]. Thus, spin-locking enables us to prepare a single group of polarized NVs with tunable disorder and long lifetime.

To control interactions, we utilize a HH resonance permitting cross-polarization transfer between the two spin ensembles [28, 29]. To identify the HH resonance condition, two groups of NVs are initialized along $+\hat{x}_A$ (group A) and $-\hat{x}_B$ (group B), and spin-locked along $+\hat{x}_A$ and $+\hat{x}_B$ with Rabi frequencies Ω_A and Ω_B, respectively (Fig. 3A). This prepares two oppositely polarized spin ensembles in the dressed-state basis with energy splittings Ω_A and Ω_B. The interaction between the groups results in spin exchange and leads to a resonant cross-relaxation when $\Omega_A = \Omega_B$ (HH condition). Figure 3B depicts the results of a spin-lock measurement on group A as a function of Ω_B, revealing a sharp resonance with a linewidth significantly narrower than the on-site disorder strength W. The linewidth of this resonance can be monitored as a function of the common Rabi frequency $\Omega = \Omega_A = \Omega_B$, showing a strong decrease for higher Ω caused by a reduction of the effective disorder W_{eff} (Fig. 3B inset).

This method allows us to probe the controlled thermalization dynamics with tunable disorder. To this end, we investigate the dynamics of an initially polarized spin sub-ensemble (group A) in HH resonance with another, unpolarized sub-ensemble (group B).

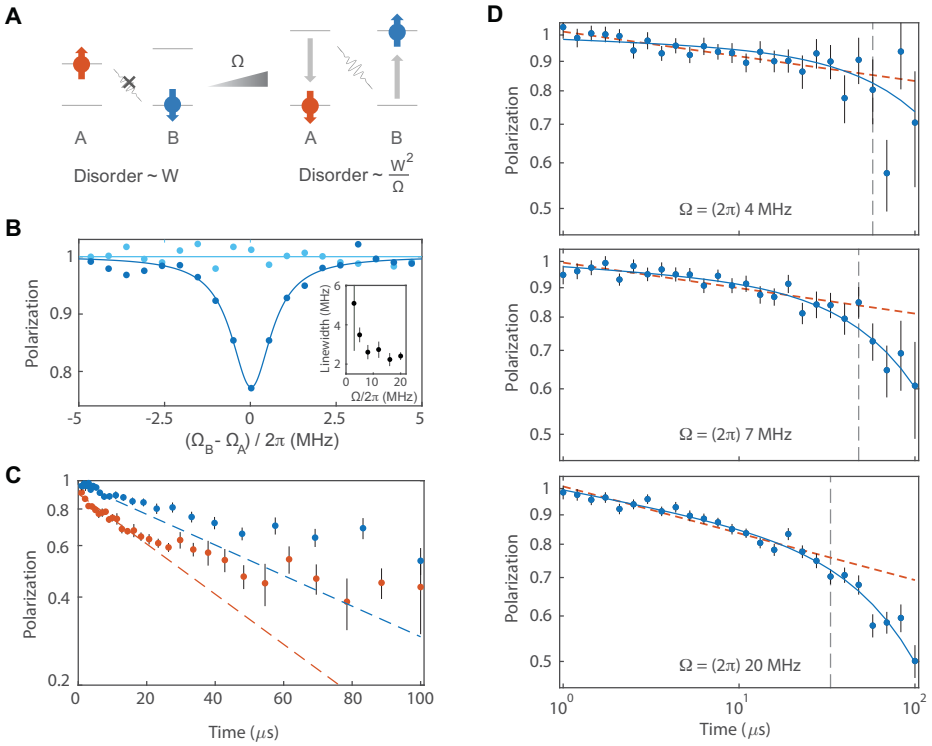

Figure 2.3: **Spin Cross-Relaxation.** **(A)** Schematic diagram depicting two oppositely polarized groups of spins (A and B) in the dressed state spin basis. Microwave fields with a common driving strength Ω are independently applied to the respective group parallel to their spin polarization directions. Under spin-locking, the effective disorder reduces from the natural disorder W with increasing Ω, thereby enhancing the rate of resonant spin exchange. **(B)** Population of group A as a function of driving power of group B, showing the HH resonance (dark blue points). Light blue data shows spin-lock coherence without driving of other groups. The corresponding solid curves represent a Lorentzian and constant fit to the data. Inset shows the HH resonance linewidth as a function of applied Rabi frequency. **(C)** Polarization dynamics of group A interacting with an oppositely polarized (red) and unpolarized (blue) spin bath, group B, at the HH condition with $\Omega = (2\pi)$ 9 MHz as a function of evolution time (on a semi-log scale). The polarized spin bath leads to faster polarization decay (see Appendix A). Dashed lines represent an exponential decay, illustrating significant deviation at long times. **(D)** Double-logarithmic plot of polarization decay of group A under HH conditions with unpolarized group B for different driving strengths. Dashed red lines are power-law fits to the data in the time window up to the vertical line. Curved solid lines are the fits to our theory model including time-dependent disorder. All errorbars correspond to 1 σ.

Physically, this situation corresponds to the thermalization of a polarized spin ensemble in contact with a spin bath held at infinite effective temperature. To extract the coherent thermalization dynamics, we normalize the polarization decay with a sufficiently detuned HH measurement (see Appendix A), wherein we observe a decay profile that fits neither a diffusive power law ($\sim t^{3/2}$) nor a simple exponential (Fig. 3C). By varying the driving strength Ω, we find that the polarization decays faster for larger Ω, consistent with a smaller effective disorder (Fig. 3D). Interestingly, the functional profile of the decays is consistent with power laws for over a decade, followed by accelerated relaxation at late times.

2.3 Theoretical description

To understand these observations, we turn to a theoretical description of our system. Spin dynamics are governed by the interplay between disorder and long-range dipolar interactions. Working in the dressed state basis with the quantization axis along $\hat{x}$, we find that the form of this interaction depends on whether spins reside in the same or in distinct groups. For spins in different groups (A and B), dipolar interactions naturally lead to spin exchange, $H_{AB} = \sum_{i\in A, j\in B} J_{ij}/r_{ij}^3 \; (\sigma_i^+\sigma_j^- + \sigma_i^-\sigma_j^+)$, where r_{ij} is the distance between spins, J_{ij} is the orientation dependent coefficient of the dipolar interaction with typical strength $J_0 = (2\pi)\ 52$ MHz·nm^3, and $\vec{\sigma}$ are spin-1/2 operators with $\sigma_i^{\pm} = \sigma_i^y \pm i\sigma_i^z$ (see Appendix A). However, for spins in the same group, the $S = 1$ nature of the NV centers and energy conservation in the rotating frame lead to an absence of spin exchange (see Appendix A); rather, the coupling between spins takes the form of an Ising interaction, $H_{A(B)} = \sum_{i,j\in A(B)} J_{ij}/r_{ij}^3 \; \sigma_i^x\sigma_j^x$. Thus, when initially polarized, a spin may depolarize only through exchange with spins of the other group. Specifically, in the limit of strong

disorder, one expects the dynamics to be dominated by rare resonant exchange processes between the two groups. To describe such dynamics, we consider a simplified model, where a single group A excitation is located at the center of an ensemble of group B spins (Fig 4A). The dynamics of this excitation are captured by an effective Hamiltonian,

$$H_{\text{eff}} = \sum_i \tilde{\delta}_i \sigma_i^x - \sum_{ij} \frac{J_{ij}}{r_{ij}^3} (\sigma_i^+ \sigma_j^- + h.c.). \tag{2.1}$$

where $\tilde{\delta}_i = \sqrt{\Omega^2 + \delta_i^2} - \Omega$ is the effective quenched disorder potential. While this single-particle model neglects the many-body nature of our experiments such as intra-group Ising interactions and complex dynamics of group B excitations, it captures the key features of slow relaxation in critical systems; however these additional features will be necessary to accurately describe the long time thermalization behavior.

To characterize the spin decay dynamics governed by H_{eff}, we calculate the survival probability, $P(t)$, of the excitation via a simple resonance counting analysis. For a given disorder realization, this resonance counting proceeds as follows. Two spins at sites i and j are on resonance at time t if: (1) their energy mismatch is smaller than their dipolar interaction strength, $|\tilde{\delta}_i - \tilde{\delta}_j| < \beta J_0 / r_{ij}^3$ (β is a dimensionless constant of order unity), and (2) the interaction occurs within the time-scale t, $J_{ij}/r_{ij}^3 > 1/t$. $P(t)$ is approximately given by the probability of having found no resonances up to time t or equivalently up to distance $R(t) \equiv (J_0 t)^{1/3}$ (see Appendix A). This probability can be computed as the product of probabilities of having no resonant spins at any r,

$$P(t) = \prod_r^{R(t)} \left(1 - 4\pi n r^2 dr \frac{\beta J_0 / r^3}{W_{\text{eff}}}\right) \propto t^{\frac{-4\pi n \beta J_0}{3W_{\text{eff}}}}. \tag{2.2}$$

$P(t)$ exhibits power-law decay with a disorder dependent exponent $\eta = 4\pi n \beta J_0 / (3W_{\text{eff}})$, where n is the density of spins that are oppositely polarized to the central excitation. This

sub-exponential relaxation is the essence of the slow critical dynamics predicted by Anderson [5]. Such single-particle power-law relaxation is also consistent with results obtained from random-banded matrix theory [30, 31] and is numerically verified for up to $N = 10^4$ spins (see Appendix A).

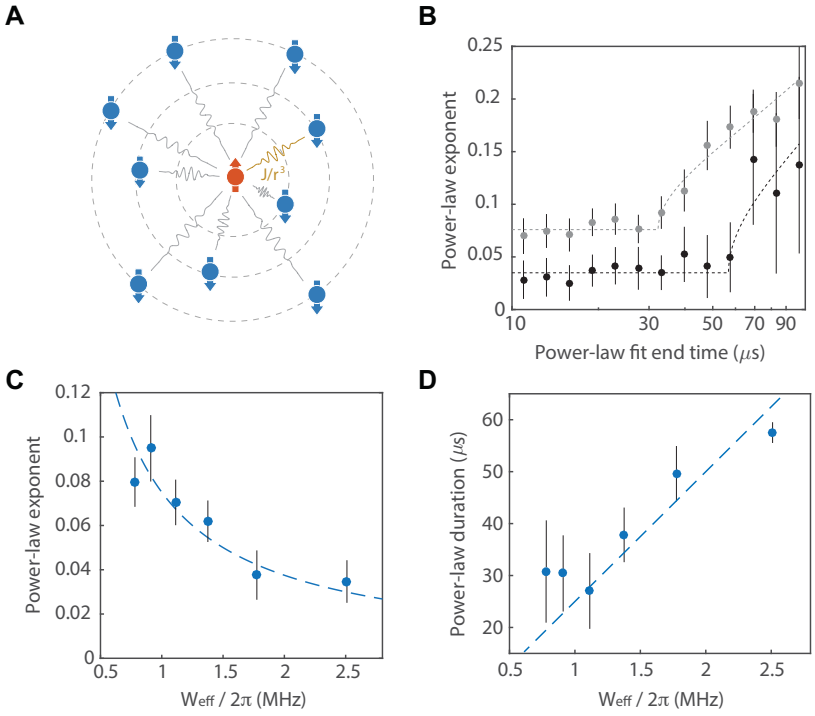

Figure 2.4: **Understanding Thermalization Dynamics. (A)** Schematic diagram of single particle resonance counting argument predicting a power-law decay profile. **(B)** Variation of power-law exponents extracted from a subset of data, consisting of seven subsequent points, swept from the beginning to the end of thermalization time traces. Black and gray data corresponds to the case of $\Omega = (2\pi)$ 4 and 9 MHz, respectively. Dotted lines corresponds to phenomenological fits, identifying the duration over which the power-law exponents remain constant. **(C)** Exponent of the power-law decay of group A polarization as a function of effective disorder W_{eff}. Dashed line corresponds to a theoretical prediction based on the single particle resonance counting. **(D)** Duration of power-law dynamics extracted for various strengths of effective disorder W_{eff}. Dashed line corresponds to a theoretical prediction based on a refined resonance counting including time-dependent disorder. All errorbars correspond to 1 σ.

A detailed comparison of our experimental observations with these theoretical predic-

tions is summarized in Fig. 4. In order to quantify the slow dynamics, we take subsets of our depolarization time trace over half-decade windows, fit the data to power laws, and extract the resulting exponents. Varying the starting time of the windows, we find that the extracted exponents remain constant up to a long time $T^* \gg 1/J$, beyond which they increase, indicating the deviation of the thermalization dynamics from a simple single particle prediction (Fig. 4B). Interestingly, the exponents scale linearly with the inverse effective disorder, as predicted by the counting argument (Fig. 4C). Furthermore, we find that their values are in excellent agreement with our theory based on numerical simulations of a single-particle Hamiltonian (see Appendix A).

At late times ($t > T^*$), the observed decay accelerates and deviates significantly from the power law. This is natural since the effects of multi-particle interactions cannot be neglected when a significant fraction of spins have already undergone depolarization. In particular, intra-group Ising interactions among randomly positioned spins $\delta_i^I \equiv \sum_j J_{ij}/r_{ij}^3$ $\langle \sigma_j^x \rangle$ may behave as an additional disorder that change in time with characteristic strength $J/4 \sim (2\pi)\, 105\,\text{kHz}$. Additionally, weak coupling to the bath may also give rise to corrections to our single particle model.

To understand this behavior, we modify our theoretical model by considering the time dependence of the on-site disorder potential. More specifically, we assume that the disorder potential consists of both static and dynamic parts with standard deviations W_s and W_d. The dynamic disorder is assumed to vary at a slow rate $1/\tau_d$. The survival probability $\tilde{P}(t)$ can then be computed using a modified resonance condition where two spins are considered resonant at time t, if at any prior time t', their energy mismatch is smaller than their dipolar interaction strength, $|\tilde{\delta}_i(t') - \tilde{\delta}_j(t')| < \beta J_0/r_{ij}^3$ (see Appendix A). Repeat-

ing our previous analysis, we find an analytical expression of $\tilde{P}(t)$ which, in the limit of strong quenched disorder ($1/\tau_d < W_d \ll W_s$), can be approximated by $\tilde{P}(t) \propto e^{-t/T^*} t^{-\eta}$ with $T^* \equiv 3W_s\tau_d/(4\pi n\beta J_0)$, predicting the deviation from the power law at time scale T^*. Intuitively, $1/T^*$ characterizes the rate at which a pair of initially off-resonant spins comes into resonance as the local potentials vary in time. Figure 3D shows that $\tilde{P}(t)$ provides an excellent fit to our observation over all time scales. Both extracted parameters $W_d \sim (2\pi)\, 0.5\,\text{MHz}$ and $\tau_d \sim 40\ \mu$s are comparable to the strength of Ising interactions and independently measured NV depolarization time, respectively [27]. This suggests that the dynamical disorder is dominated by intrinsic contributions from Ising interactions, which is related to the predicted thermalization enhancement due to multi-particle resonances and higher order processes [20, 19]. Moreover, the extracted power-law duration agrees well with the predicted linear dependence of T^* on effective disorder strengths (Fig. 4D). The quantitative agreement of the functional form $\tilde{P}(t)$, the disorder dependence of power-law exponents and durations, and the extracted values of W_d and τ_d corroborates our theoretical model describing the microscopic mechanism of thermalization dynamics in a critical system.

2.4 Conclusion and outlook

We have demonstrated that dense ensembles of NV centers constitute a powerful platform for exploring quantum dynamics of strongly correlated many-body systems. Complementary to recent studies of localization in cold atomic systems [14, 32], these spin systems exhibit slow, disorder-dependent relaxation associated with critical thermalization dynamics. The quantitative agreement between the observed spin relaxation and resonance

counting demonstrates that the dynamics are dominated by rare resonances. Moreover, the observed deviations from simple theory reveal the subtle role that many-body effects and coupling to the environment can play in such systems. These studies can be extended along several directions. A higher degree of spatial quantum control can be obtained via spin-based sub-wavelength imaging techniques [33]. Advanced dynamical decoupling can enable the engineering of a broader class of interaction Hamiltonians and the direct measurement of quantum entanglement dynamics [34, 35]. The use of strong magnetic field gradients or the fabrication of diamond nanostructures can allow for the exploration of spin dynamics in lower dimensional systems [36], where the existence of many-body localization is still in debate [19, 37]. In combination, these directions may enable the study of dynamical phase transitions from localization to thermalization [38, 39, 14] as well as exotic non-equilibrium phases of matter [17, 18, 16], and open up new opportunities for controlling such complex interacting systems [40, 41].

Chapter 3

Discrete Time-Crystalline Order in a Disordered Dipolar Many-body System

Understanding quantum dynamics away from equilibrium is an outstanding challenge in the modern physical sciences. Out-of-equilibrium systems can display a rich variety of phenomena, including self-organized synchronization and dynamical phase transitions [42, 43]. More recently, advances in the controlled manipulation of isolated many-body systems have enabled detailed studies of non-equilibrium phases in strongly interacting quantum matter [14, 38, 32, 44]; for example, the interplay between periodic driving, disorder, and strong interactions has been predicted to result in exotic "time-crystalline" phases [45], which spontaneously break the discrete time-translation symmetry of the underlying drive[46, 47, 48, 49]. Here we report the experimental observation of such discrete time-crystalline order in a driven, disordered ensemble of about one milion dipolar spin impurities in diamond at room temperature[50, 51, 52]. We observe long-lived temporal correlations at integer multiples of the fundamental driving period, experimentally iden-

tify the phase boundary and find that the temporal order is protected by strong interactions. This order is remarkably stable to perturbations, even in the presence of slow thermalization [5, 53]. Our work opens the door to exploring dynamical phases of matter and controlling interacting, disordered many-body systems[54, 55, 56].

3.1 Introduction

Conventional wisdom holds that the periodic driving of isolated, interacting systems inevitably leads to heating and the loss of quantum coherence. In certain cases, however, fine-tuned driving can actually decouple quantum degrees of freedom from both their local environment [51] and each other [57]. Recently, it has been shown that strong disorder, which leads to many-body localization [11, 58], allows a system to retain memory of its initial state for long times, enabling the observation of novel, out-of-equilibrium quantum phases [14, 32, 59]. One example is the discrete time crystal [46, 47, 48, 49] - a phase that is nominally forbidden in equilibrium [60, 61]. The essence of the discrete time-crystalline (DTC) phase is an emergent, collective, subharmonic temporal response. Although this phenomenon resembles the coherent revivals associated with dynamical decoupling [50], its nature is fundamentally different because it is induced and protected by interactions rather than by fine-tuned control fields. It is especially intriguing to investigate the possibility of DTC order in systems that are not obviously localized [62]. This is the case for dipolar spins in three dimensions, where the interplay between interactions and disorder can lead to critical subdiffusive dynamics [53, 27].

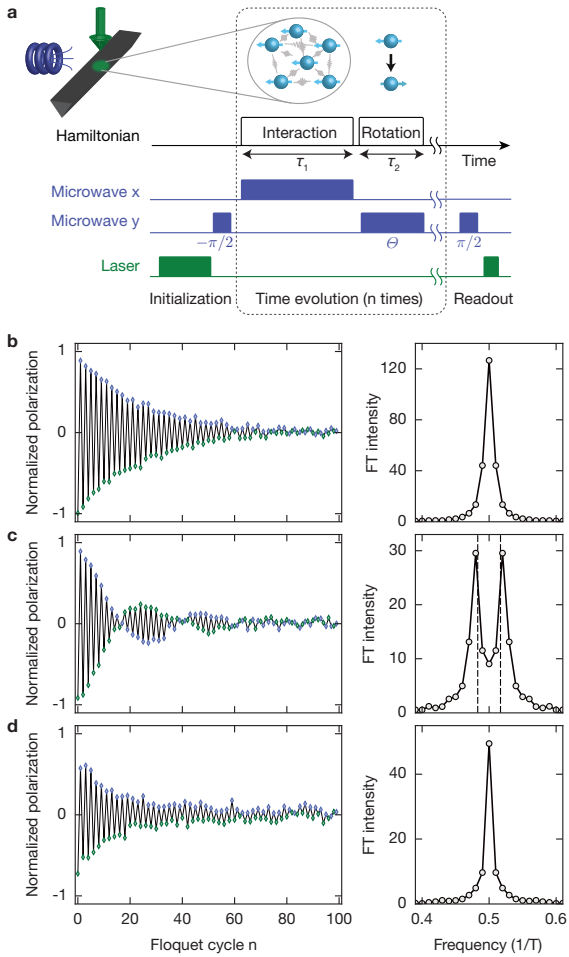

Figure 3.1: **Experimental setup and observation of time-crystalline order. a**, Nitrogen-vacancy centers (blue spheres) in a nanobeam fabricated from black diamond are illuminated by a focused green laser beam and irradiated by a microwave source. Spins are prepared in the $(|m_s = 0\rangle + |m_s = -1\rangle)/\sqrt{2}$ state using a microwave $(-\pi/2)$ pulse along the $\hat{y}$ axis. Subsequently, within one Floquet cycle, the spins evolve under a dipolar interaction and microwave field Ω_x aligned along the $\hat{x}$ axis for duration τ_1, immediately followed by a global microwave θ pulse along the $\hat{y}$ axis. After n repetitions of the Floquet cycle, the spin polarization the $\hat{x}$ axis is read out. We choose τ_1 to be an integer multiple of $2\pi/\Omega_x$ to minimize accidental dynamical decoupling [51]. **b-d**, Representative time traces of the normalized spin polarization $P(nT)$ measured at even (green) and odd (blue) integer multiples of T and respective Fourier spectra, $|S(\nu)|^2$, for different values of the interaction time τ_1 and θ: (**b**) $\tau_1 = 92$ ns, $\theta = \pi$, (**c**) $\tau_1 = 92$ ns, $\theta = 1.034\pi$, and (**d**) $\tau_1 = 989$ ns, $\theta = 1.034\pi$. Dashed lines in **c** indicate $\nu = 1/2 \pm (\theta - \pi)/2\pi$. Data are averaged over more than $2 \cdot 10^4$ measurements.

3.2 Experimental observations

We experimentally investigate the formation of discrete time-crystalline order in an ensemble of nitrogen-vacancy spin impurities in diamond. Each nitrogen-vacancy center has an electronic $S = 1$ spin, from which we isolate an effective two-level system by applying an external magnetic field. These isolated spin states can be optically initialized, detected and manipulated via microwave radiation[50, 52] (see Fig. 1a and Appendix B). Our sample has a high concentration (45 p.p.m.) of nitrogen-vacancy centers, giving rise to strong long-range magnetic dipolar interactions [53]. The spins are also subject to multiple sources of disorder, owing to lattice strain, paramagnetic impurities and the random positioning of nitrogen-vacancy centers. A strong, resonant microwave field is used to control spin orientations, resulting in an effective Hamiltonian (in the rotating frame),[53]

$$H(t) = \sum_i \Omega_x(t) S_i^x + \Omega_y(t) S_i^y + \Delta_i S_i^z + \sum_{ij} (J_{ij}/r_{ij}^3)(S_i^x S_j^x + S_i^y S_j^y - S_i^z S_j^z). \tag{3.1}$$

Here, S_i^μ ($\mu \in \{x, y, z\}$) are Pauli spin-$1/2$ operators acting on the effective two-level system spanned by the spin states $|m_s = 0\rangle$ and $|m_s = -1\rangle$, $\Omega_{x(y)}$ is the Rabi frequency of the microwave driving, Δ_i is a disordered on-site field with approximate standard deviation $W = 2\pi \times 4.0$ MHz, r_{ij} is the distance between spins i and j (average nearest-neighbor separation $r_0 \approx 8$ nm), and J_{ij} are the orientation-dependent coefficients of the dipolar interaction. The average interaction, $J_{ij}/r_0^3 \approx 2\pi \times 105$ kHz[53], is much faster than typical spin coherence times[52].

To probe the existence of time-crystalline order, we monitor the spin dynamics of an initial state that is polarized along the $+\hat{x}$ direction. We begin by applying continuous

microwave driving (spin locking) along $\hat{x}$ with Rabi frequency $\Omega_x = 2\pi \times 54.6$ MHz for a duration τ_1 (Fig. 1a). Next, we rotate the spin ensemble by an angle θ around the $\hat{y}$ axis using a strong microwave pulse with $\Omega_y = 2\pi \times 41.7$ MHz for duration $\tau_2 = \theta/\Omega_y \ll \tau_1$. This two-step sequence defines a Floquet unitary with a total period $T = \tau_1 + \tau_2$ and is repeated n times, before the polarization $P(nT)$ along the $\hat{x}$ axis is measured. The resulting polarization dynamics are analyzed in both the time and frequency domain (ν). Repeating these measurements with various values of τ_1 and θ allows us to independently explore the effect of interactions and global rotations.

Figure 1b-d depicts representative time traces and the corresponding Fourier spectra, $S(\nu) \equiv \sum_n P(nT)e^{i2\pi n\nu}$, for various values of τ_1 and θ. For relatively short interaction times ($\tau_1 = 92$ ns) and nearly perfect π pulses ($\theta \approx \pi$), we observe that the spin polarization $P(nT)$ alternates between positive and negative values, resulting in a sub-harmonic peak at $\nu = 1/2$ (Fig. 1b). In our experiment, the microwave pulses have an intrinsic uncertainty 0.9% stemming from a combination of spatial inhomogeneity in the microwave fields, on-site potential disorder, and the effect of dipolar interactions (see Appendix B). These effects eventually cause the oscillations to decay, after approximately 50 periods. Although such temporal oscillations nominally break discrete time-translation symmetry, their physical origin is trivial. To see this, we note that for sufficiently strong microwave driving, $\Omega_x \gg W, J_{ij}/r_0^3$, the dynamics during τ_1 are governed by an effective polarization-conserving Hamiltonian[53], $H_{\text{eff}} \approx \sum_i \Omega_x S_i^x + \sum_{ij}(J_{ij}/r_{ij}^3)S_i^x S_j^x$. During τ_2, the evolution can be approximated as a global spin rotation $R_y^\theta \approx e^{-i\theta\sum_i S_i^y}$. When $\theta = \pi$, this pulse simply flips the sign of the $\hat{x}$ polarization during each Floquet cycle, resulting in the $\nu = 1/2$ peak. However, this $2T$-periodic response originates from the fine tuning of θ and should

not be robust against perturbations. Indeed, a systematic change in the average rotation angle to $\theta = 1.034\pi$ causes the $2T$-periodicity to completely disappear, resulting in a modulated, decaying signal with two incommensurate Fourier peaks at $\nu = 1/2 \pm (\theta - \pi)/2\pi$(Fig. 1c). Remarkably, we find that a rigid $2T$-periodic response is restored when interactions are enhanced by increasing τ_1 to 989 ns, suggesting that the $\nu = 1/2$ peak is stabilized by interactions. In this case, we observe a sharp peak in the spectrum at $\nu = 1/2$ and the oscillations in $P(nT)$ continue beyond $n \approx 100$ (Fig. 1d), indicating a persistent subharmonic temporal response.

The robustness of this apparent periodic order is further explored in Fig. 2. With an interaction time $\tau_1 = 790$ ns and $\theta = 1.034\pi$, the polarization exhibits an initial decay followed by persistent oscillations over the entire time window of our experimental observations (Fig. 2a). We perform a Fourier transform on subsections of the time trace with a sweeping window of size $m = 20$ (Fig. 2a) and extract the intensity of the $\nu = 1/2$ peak as a function of the sweep position, n_{sweep} (Fig. 2b). The intensity of the $\nu = 1/2$ peak clearly exhibits two distinct decay timescales. At short times, we observe a rapid initial decay that corresponds to non-universal dephasing dynamics, whereas at late times we observe a slow decay. Only near the phase boundary ($\theta = 1.086\pi$) is the lifetime substantially decreased. We fit the slow decay to an exponential to extract a lifetime for the periodic order. As shown in Fig. 2c, for $\theta = 1.034\pi$, this lifetime increases with the interaction time (τ_1) and eventually approaches the independently measured spin depolarization time $T_1^{\rho} \approx 60\ \mu$s. This demonstrates that, for sufficiently long interaction times, the observed periodic order is limited by only coupling to the environment[27]. We associate this with DTC order [46, 47, 48, 49]. Remarkably, within the DTC phase, the lifetime is essentially

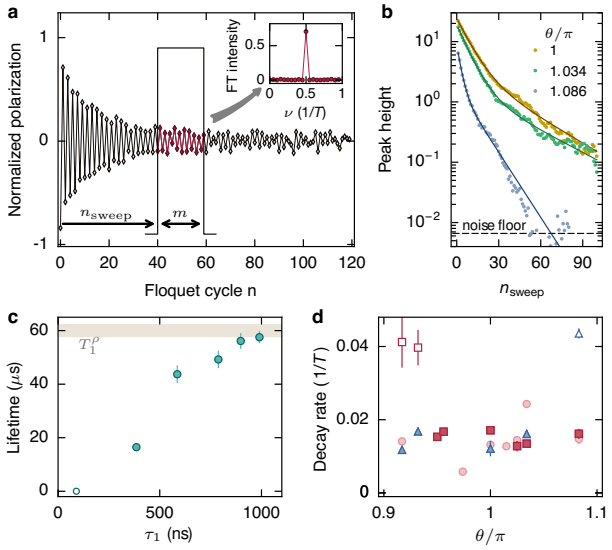

Figure 3.2: **Long-time behavior of discrete time-crystalline order.** **a** Representative time trace of the normalized spin polarization $P(nT)$ in the crystalline phase ($\tau_1 = 790\,\mathrm{ns}$ and $\theta = 1.034\pi$). The time-dependent intensity of the $\nu = 1/2$ peak (inset) is extracted from a short-time Fourier transformation with a time window of length $m = 20$ shifted from the origin by n_{sweep}. **b** Peak height at $\nu = 1/2$ as a function of n_{sweep} for different pulse imperfections at $\tau_1 = 790\,\mathrm{ns}$. Lines indicate fits to the data using a phenomenological double exponential function. The noise floor corresponds to 0.017, extracted from the mean value plus the standard deviation of $\sum_\nu |S(\nu)|^2$ excluding the ν = 1/2 peak. **c** Extracted lifetime of the time-crystalline order as a function of the interaction time τ_1, for $\theta = 1.034\pi$. Shaded region indicates the spin life-time $T_1^\rho = 60 \pm 2\ \mu s$ (extracted from a stretched exponential[27]) due to coupling with the external environment. **d** Extracted decay rate of the time-crystalline order as a function of θ for different interaction times, τ_1= 385 ns (circle), 586 ns (square) and 788 ns (triangle). Only very weak dependence on $\theta - \pi$ is observed within the DTC phase, contrary to a dephasing model (see Appendix B). In **c** and **d**, the vertical error bars display the statistical error (s.d.) from the fit and empty symbols mark data near the time-crystalline phase boundary.

independent of θ, indicating exceptional robustness (Fig. 2d).

We examined whether the observed periodic order could arise from an accidental XY sequence[51] or from inhomogeneous dephasing resulting from the effective single-particle disorder in the dressed state basis. To avoid the former, τ_1 is always choosen as an integer multiple of $2\pi/\Omega_x$. For the latter, although it has been shown that disorder alone is insuffi-

cient for stabilizing a DTC phase in the absence of interactions[46, 47, 48, 49], we verified this experimentally; implementing a rotary echo sequence that reduces such dephasing, we find no change in the lifetime of the DTC order and an enhancement in the subharmonic response at late times (see Appendix B). In principle, fast Markovian dephasing could also lead to apparent periodic order at extremely small values of $\theta - \pi$ by eliminating coherences along both $\hat{y}$ and $\hat{z}$, leaving only $\hat{x}$ polarization dynamics. In such a case, the decay rate of periodic order should increase quadratically with $\theta - \pi$. However, this explanation is inconsistent with the observed robustness of the lifetime of the DTC order for a range of $\theta - \pi$ (Fig. 2d) and the independently measured dephasing rate (see Appendix B).

To experimentally determine the DTC phase boundary, we focus on the long-time behavior of the polarization time traces ($50 < n \leq 100$) and compute the "crystalline fraction", which is defined as the ratio of the $\nu = 1/2$ peak intensity to the total spectral power, $f = |S(\nu = \frac{1}{2})|^2 / \sum_\nu |S(\nu)|^2$ (see Appendix B). Figure 3a shows f as a function of θ for two different interaction times. For weak interactions ($\tau_1 = 92$ ns), f has a maximum at $\theta = \pi$ and rapidly decreases as θ deviates by approximately 0.02π. However, for stronger interactions ($\tau_1 = 275$ ns), we observe a robust DTC phase which manifests as a large crystalline fraction over a wide range $0.86\pi < \theta < 1.13\pi$. We associate a phenomenological phase boundary with $f = 10\%$ and observe that the boundary enlarges with τ_1, eventually saturating at $\tau_1 \approx 400$ ns (Fig. 3b). The phase boundary can also be visualized as the vanishing of the $\nu = 1/2$ peak and the simultaneous emergence of two incommensurate peaks (Fig. 3c).

The rigidity of the $\nu = 1/2$ peak can be qualitatively understood by constructing effective eigenstates of $2T$ Floquet cycles, including spin-spin interaction. We approximate

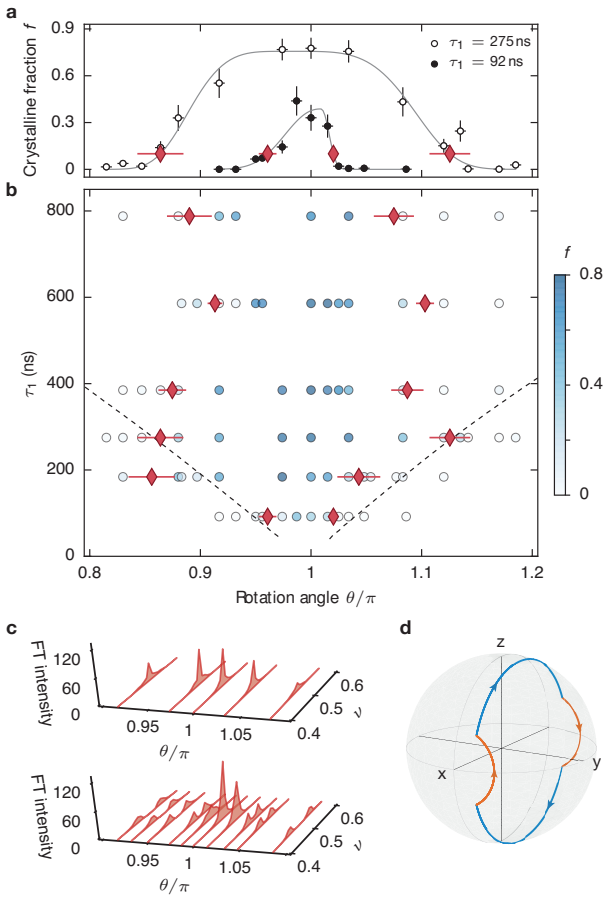

Figure 3.3: **Phase diagram and transition.** **a** Crystalline fraction f(**a**) and its associated phase diagram (**b**) as a function of θ and τ_1 obtained from a Fourier transform at late times ($50 < n \leq 100$). The red diamonds mark the phenomenological phase boundary, identified as a 10% crystalline fraction; horizontal error bars denote the statistical error (s.d.) from a super-Gaussian fit. In **a**, vertical error bars of data points (circles) are limited by the noise floor (see Appendix B) and horizontal error bars indicate the pulse uncertainty of 1%. Grey lines denote the fit to extract the phase boundary (see Appendix B). In **b**, the colors of the data points (circles) represent the extracted crystalline fraction at the associated parameter set. The dashed line corresponds to a disorder-averaged theoretical prediction for the phase boundary. Asymmetry in the boundary arises from an asymmetric distribution of rotation angles (see Appendix B). **c** Evolution of the Fourier spectra as a function of θ for two different interaction times, $\tau_1 = 385\,\text{ns}$ (top) and $\tau_1 = 92\,\text{ns}$ (bottom). **d** Bloch sphere indicating a single spin trajectory of the $2T$-periodic evolution under the long-range dipolar Hamiltonian (red) and global rotation (blue).

the unitary time evolution over a single period as $U_T = R_y^\theta e^{-iH_{\text{eff}}\tau_1}$ and solve for a self-consistent evolution using product states as a variational ansatz. To this end, we consider the situation in which a typical spin returns to its initial state after $2T$: $|\psi(0)\rangle \propto |\psi(2T)\rangle = e^{-i\theta S^y} e^{i\phi_i S^x} e^{-i\theta S^y} e^{-i\phi_i S^x} |\psi(0)\rangle$, and self-consistently determine the interaction-induced rotation angle $\phi_i \equiv \sum_j J_{ij}/r_{ij}^3 \langle S_j^x \rangle \tau_1 \approx \bar{J}_i \tau_1 \langle\psi(0)| S^x |\psi(0)\rangle$, where $|\psi(0)\rangle$ is the initial spin state and $\bar{J}_i = \sum_j J_{ij}/r_{ij}^3$ (see Appendix B). One expects ϕ_i to change sign after each Floquet cycle, because the average polarization $\langle\psi(0)| S^x |\psi(0)\rangle$ should be flipped. Intuitively, the self-consistent solution can be visualized as a closed path on the Bloch sphere (Fig. 3d), where each of the four arcs corresponds to one portion of the $2T$-periodic evolution. When $\theta = \pi$, such a solution always exists. More surprisingly, even when $\theta \neq \pi$, a closed path can still be found for sufficiently strong interactions, $|\bar{J}_i \tau_1| > 2|\theta_i - \pi|$; in such cases, the deviation in θ away from π is compensated by the dipolar interactions (Fig. 3d). We obtain a theoretical phase boundary by numerically averaging the self-consistent solution over both disordered spin positions and local fields. The resultant phase boundary is in reasonable agreement with the experimental observations for short to moderate interaction times τ_1, but overestimates the boundary at large τ_1 (dashed line, Fig. 3b, see Appendix B).

Finally, Fig. 4 demonstrates that the discrete time-translation symmetry can be further broken down to $\mathbb{Z}_3$ [63, 49, 47, 48], resulting in DTC order at $\nu = 1/3$. Here, we utilize all three spin states of the nitrogen-vacancy center. We begin with all spins polarized in the $|m_s = 0\rangle$ state and evolve under the bare dipolar Hamiltonian for a duration τ_1 (see Appendix B). Next, we apply two resonant microwave pulses, each of duration τ_2, first on the transition $|m_s = 0\rangle \rightarrow |m_s = -1\rangle$ and then on the transition $|m_s = 0\rangle \rightarrow |m_s = +1\rangle$. In combination, this sequence of operations defines a single Floquet cycle with period

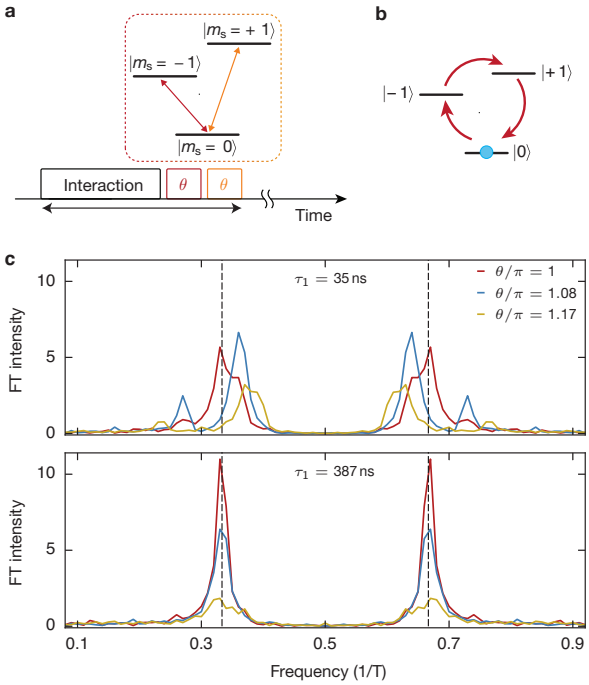

Figure 3.4: $\mathbb{Z}_3$ **discrete time-crystalline order. a** Experimental sequence to demonstrate a $3T$-periodic discrete time-crystalline order. A single Floquet cycle is composed of three operations: time evolution under long-range dipolar Hamiltonian and rapid microwave pulses for two different transitions. **b** Visualization of the $3T$-periodicity in the polarization dynamics for the case of $\theta = \pi$. **c** Fourier spectra of the polarization dynamics for two different interaction times and for three different rotation angles θ: 1.00π (red), 1.086π (blue) and 1.17π (yellow). Dashed lines indicate $\nu = 1/3, 2/3$.

$T = \tau_1 + 2\tau_2$. As before, we measure the polarization, $P(nT)$, which is defined as the population difference between the $|m_s = 0\rangle$ and $|m_s = -1\rangle$ states (Fig. 4a). When each of the applied microwaves corresponds to an ideal π pulse, this sequence realizes a cyclic transition with $\mathbb{Z}_3$ symmetry (Fig. 4b), which is explicitly broken by any change in the pulse duration. The Fourier spectra of $P(nT)$ for various pulse durations and two different values of τ_1 are shown in Fig. 4c. With weak interactions ($\tau_1 = 35$ ns), the position of the peaks is extremely sensitive to perturbations, but with sufficiently strong interactions ($\tau_1 = 387$ ns) the peaks are pinned to a value of $\nu = 1/3$ despite large perturbations,

indicating the observation of $\nu = 1/3$ DTC order. The lifetime of the observed $\nu = 1/3$ DTC order is shorter than that of the $\nu = 1/2$ DTC order, consistent with the presence of additional dynamics in the full dipolar Hamiltonian (see Appendix B). The ability for our system to exhibit stable period-tripling distinguishes it from *bifurcations* in driven, classical systems, in which period-tripling is typically accompanied by regions of chaos [64].

Our observation of DTC order cannot be simply explained within current theoretical frameworks based on either localization [46, 47, 48, 49] or pre-thermalization [59, 62]. In particular, our system with long-range dipolar interactions is not expected to be localized in either the static or the driven case. In the static case, it has previously been demonstrated that our system exhibits slow thermalization associated with critical dynamics [53]. In the driven case, the long-time evolution is governed by the average Hamiltonian $D \approx \sum_i (J_{ij}/r_{ij}^3) S_i^x S_j^x + (\theta - \pi)/T \sum_i S_i^y$, which likewise does not yield localized dynamics[5, 20]. We further note that the effective Hamiltonian of the $\mathbb{Z}_3$ DTC phase includes not only Ising-type interactions but also spin exchange interactions, providing additional channels for thermalization (see Appendix B).

In principle, even in the absence of localization, time-crystalline order can persist for a long, but finite, pre-thermal timescale [62, 59]. Within this timescale, the spin system relaxes to a pre-thermalized state, defined as the thermal ensemble of D with a temperature determined by the energy density of the initial state. Because our initially polarized state is effectively at infinite temperature with respect to D (owing to the anisotropy of the dipolar couplings), we do not expect to observe pre-thermal DTC order. This is in contrast to our actual observations, which show that the lifetime of the DTC order is limited by the depolarization time T_1^ρ due to coupling with the environment[27] (Fig. 2c). We have explicitly

verified that the DTC order is not greatly affected by varying the initial polarization (see Appendix B). One possible explanation is that, owing to slow critical thermalization [53], the spins in our system do not reach even a pre-thermal state. Finally, the interplay between coherent interactions and dephasing in open systems at long times could also have a role. Detailed understanding of such mechanisms requires further theoretical investigation.

3.3 Theory of critical time crystals

Here, we develop a theoretical treatment of DTC order in systems with long-range interactions. We utilize a perturbative approach to analyze the interplay of long-range interactions, periodic driving, and positional disorder of spins. Focusing on dipolar systems in 3D, we show that although DTC order is only transient, it can persist for asymptotically long times with strongly suppressed thermalization rate. This behavior is intrinsically connected to slow thermalization dynamics of disordered dipolar systems in 3D, which has been previously shown to be consistent with the so-called critical regime [5, 53] without periodic drive. As a function of experimental parameters, we find that the relaxation time shows a sharp crossover between a regime where DTC response is robust and a regime where it decays rapidly. This crossover is reminiscent of a phase transition, thereby allowing us to obtain the effective phase diagram of DTC which is in good agreement with experimental results. Thus, our work provides an explanation of the experimental observations introduced in the previous section, and also demonstrates the possibility of the DTC in systems with critical dynamics, a regime which we refer to as 'critical time crystals'. Furthermore, our perturbative approach can be used to study the non-equilibrium properties in other driven disordered systems with long-range interactions.

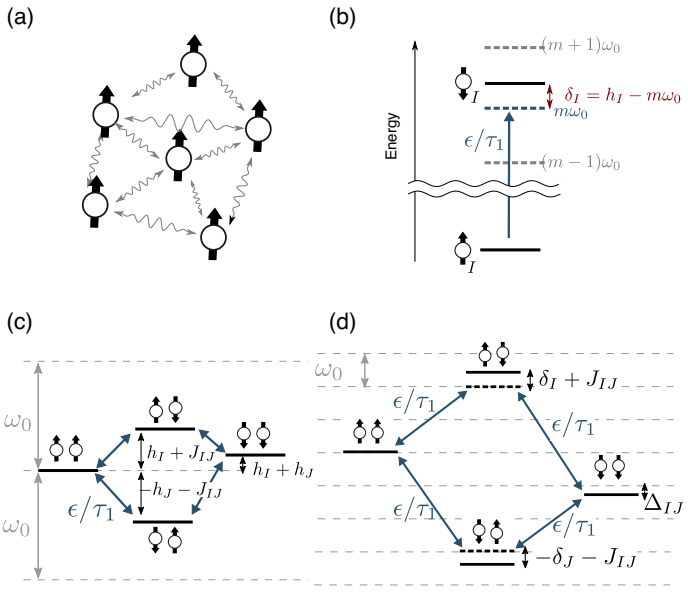

Figure 3.5: (a) Ensemble of randomly positioned spins in 3D interacting via dipolar interactions. (b) Illustration of single-spin-flip processes. (c, d) Energy level diagram for the second-order process of two spins flipping, in two regimes: (c) high frequencies ($\omega_0 \gg W$) and (d) low ($\omega_0 \ll W$) frequencies. The applied field flips a spin with magnitude ϵ/τ_1, which costs energy $\sim h_I - m^*\omega_0$.

Our key results can be understood by considering a simple spin model that describes an ensemble of dipolar interacting NV centers, used in the experiments of Ref. [18]. Using strong microwave excitations, the effective Ising interactions between spins were engineered, described by the following Hamiltonian:

$$H_0 = \sum_i \Omega S_i^x + \sum_{i,j} \frac{J_{ij}}{r_{ij}^3} S_i^x S_j^x, \tag{3.2}$$

where $\vec{S}_i = (S_i^x, S_i^y, S_i^z)$ are Pauli spin-1/2 operators, Ω the strong microwave driving along $\hat{x}$, J_{ij} the orientation dependent coefficient of dipolar interactions with typical strength J_0, and r_{ij} the distance between spins i and j. We assume that the spin-1/2 particles are randomly distributed in three dimensional space with density n_0 and neglect coupling to the environment [Fig. 3.5(a)]. DTC order was observed by interrupting the evolution under

Hamiltonian (3.2) with rapid, global pulses that rotate the spin ensemble along the $\hat{y}$-axis by an angle $\pi + \epsilon$. The corresponding Floquet unitary is given by

$$U_F = \exp\left[-i\sum_i (\pi+\epsilon) S_i^y\right] \exp\left[-iH_0\tau_1\right], \tag{3.3}$$

where τ_1 is the period for which the spins are allowed to interact for. In the experiment, the period is chosen such that $\Omega\tau_1 = 2\pi n$, and therefore Ω can effectively be taken to be 0 in Eq. (3.2). When the system is initialized in a state where all spins are polarized along the $+\hat{x}$ direction, a non-trivial temporal response may be revealed by measuring the average polarization $P(n\tau_1)$ of the ensemble along $\hat{x}$ after n Floquet cycles, or equivalently, $q(n) \equiv (-1)^n P(n\tau_1)$, which serves as an order parameter for the DTC phase. The stability of the DTC order can be ascertained by studying the decay rate of $q(n)$ for large number of cycles as a function of τ_1 and ϵ.

In order to describe the dynamics of $q(n)$, we move into a so-called toggling frame, which rotates by $P_\pi \equiv \prod_j \exp\left[-i\pi S_j^y\right]$ each time a global pulse is applied to the system. Since $P_\pi S_i^x (P_\pi)^{-1} = -S_i^x$, the $2\tau_1$-periodic oscillation in $P(n\tau_1)$ naturally appears as a time-indepdent spin polarization in this new frame. The dynamics of the system is then described by the Floquet unitary $\bar{U}_F = \exp\left[-i\sum_i \epsilon S_i^y\right] \exp\left[-iH_0\tau_1\right]$, or, equivalently, by an effective time-dependent Hamiltonian

$$H(t) = \sum_{ij} \frac{J_{ij}}{r_{ij}^3} S_i^x S_j^x + \epsilon \sum_i S_i^y \sum_n \delta(t - n^- \tau_1). \tag{3.4}$$

Thus, our problem reduces to studying the depolarization dynamics of an initialized polarized spin ensemble under the time evolution of $H(t)$.

Physical picture.—The essence of our analysis is to study resonant spin dynamics that lead to depolarization perturbatively in ϵ, while accounting for energy exchanges provided

by the external drive. In particular, since $\sum_n \delta(t - n^- \tau_1) = \frac{1}{\tau_1} \sum_m e^{im\omega_0 t}$, the pulsed periodic spin rotations can be viewed as spin excitation with harmonics of the fundamental frequency $\omega_0 \equiv 2\pi/\tau_1$ and fixed magnitude ϵ/τ_1. While this driving allows energy absorption and emission in integer multiples of ω_0, the interplay of strong interactions and positional disorder suppresses direct energy exchanges such that typical spins depolarize only via indirect higher order processes in ϵ.

Let us first consider the case without perturbations, i.e. $\epsilon = 0$. Then the polarization of each spin along $\hat{x}$ is conserved. When all spins are initially polarized, each spin therefore experiences a mean-field potential $h_i \equiv \sum_{j \neq i} (J_{ij}/r_{ij}^3) \langle S_j^x \rangle$. Due to the random positioning of spins, the strength of h_i is also random with zero mean and variance $W^2 = \langle \frac{1}{4} (\sum_{j \neq i} J_{ij}/r_{ij}^3)^2 \rangle$, where $\langle \cdot \rangle$ denotes averaging over different positions.

When $\epsilon \neq 0$, there is depolarization due to spins experiencing a time-varying on-site field along the $\hat{y}$-axis. Let us therefore consider the first order process where spins individually flip due to the action of this field. If a spin experiences a a strong mean-field potential h_i compared to the applied field, that is, if $h_i \tau_1 \gg \epsilon$, then it does not flip – it experiences an effective field that is approximately pointing along the $\hat{x}$-axis and therefore precesses around it without significant depolarization. On the other hand, if $h_i \tau_1$ is close to an integer multiple of 2π, then the spin rotates along the $\hat{y}$-axis and depolarizes. Physically, this corresponds to an effectively resonant excitation of (individual) spins that arises when one of the driving harmonics is tuned close to their energy: $|h_i - m^* \omega_0| < \epsilon/\tau_1$ for some optimal integer m^* [see Fig. 3.5(b)]. Such resonances occur with a small probability in the limit of $\epsilon \ll W\tau_1$, and amount to a reduction of the total polarization by a constant factor proportional to $\epsilon/(\min(W, \omega_0)\tau_1)$. However, if $\epsilon \sim W\tau_1$, a substantial fraction of spins rapidly

depolarize due to resonant processes shown in Fig. 3.5(b). Note that the phenomenological phase boundary extracted in Ref. [18], based on the existence of self-consistent closed spin trajectories, is consistent with the perturbative condition $\epsilon \ll W\tau_1$.

We next focus on the second order process illustrated in Fig. 3.5(c,d) in which a pair of spins I and J simultaneously flip their polarizations while exchanging their energies with each other *and* with the external drive. Such processes are resonant when

$$\Delta_{IJ} \approx |h_I + h_J - m^*\omega_0| < J_{IJ}^{\text{eff}}, \tag{3.5}$$

where h_I and h_J are effective on-site potential for spins I and J, m^* is the optimal harmonic number that minimizes the energy difference, and J_{IJ}^{eff} is the effective amplitude of the pair-flip process. The amplitude J_{IJ}^{eff}

$$J_{IJ}^{\text{eff}} \sim \left(\frac{\epsilon}{\tau_1}\right)^2 \frac{J_{IJ}}{r_{IJ}^3}\left(\frac{1}{\delta_I^2} + \frac{1}{\delta_J^2}\right), \tag{3.6}$$

can be estimated from the interference of two paths in second order perturbation theory, as illustrated in Fig.1(c,d). Here $\delta_{I(J)} \equiv \min_{\ell^*}(h_{I(J)} - \ell^*\omega_0)$ is the energy difference between initial/final states and intermediate virtual states, up to extra energy provided by a driving harmonic ℓ^*. We find that J_{IJ}^{eff} is an effective long-range interaction decaying as $\sim 1/r_{IJ}^3$ allowing the flipping of remote spin pairs.

The resonance condition (3.5) is sensitive to ω_0 and behaves qualitatively differently in two limiting cases: (i) $\omega_0 \gg W$ and (ii) $\omega_0 \ll W$ [see Fig. 3.5(c,d)]. In the former case, the optimal choice is $m^* = \ell^* = 0$ since spins cannot absorb or emit such a large energy ω_0. In the latter case, effective energy differences (both Δ_{IJ} and δ_I, δ_J) are bounded by ω_0 as the external drive can always compensate energy in units of ω_0. These considerations

yield the scaling $J^{\text{eff}}(r) \sim CJ_0/r^3$ with

$$C \approx \begin{cases} (\epsilon/\tau_1 W)^2 & \text{for } \omega_0 \gg W \\ \epsilon^2 & \text{for } \omega_0 \ll W \end{cases}, \tag{3.7}$$

and the effective range W^{eff} of the energy differences Δ_{IJ} becomes $W^{\text{eff}} \sim W$ for $\omega_0 \gg W$ and $W^{\text{eff}} \sim \omega_0$ for $\omega_0 \ll W$.

We now estimate the probability that a given spin finds a resonant partner within a ball of radius R. This is obtained by integrating the probability of finding such a partner in a shell R and $R + dR$

$$dP = \left(J^{\text{eff}}(R)/W^{\text{eff}}\right) n_0 4\pi R^2 dR, \tag{3.8}$$

from a short distance cut-off a_0 to R, which gives $P(R) \sim \log(R/a_0)$. Here the first factor in Eq. (3.8) is the probability of satisfying Eq. (3.5), and the second factor is the average number of spins within a shell of size R with the density n_0. As this probability diverges, it implies that pair-wise spin flips prevail, and the system thermalizes, with the DTC order slowly decaying over time. We can extract the timescale associated with these pair-spin flip processes using the typical distances R_* of resonant spin pairs. Solving $P(R_*) \sim 1$ gives $R_* \approx a \exp\left[W^{\text{eff}}/4\pi C J_0 n_0\right]$. Finally, the effective depolarization rate is estimated from the interaction strengths of typical pairs, i.e., $\tilde{\Gamma} \sim J^{\text{eff}}(R_*)$, leading to the decay rate per Floquet cycle $\Gamma \equiv \tilde{\Gamma}\tau_1$:

$$\Gamma \sim \begin{cases} \frac{J_0\epsilon^2}{a_0^3 \tau_1 W^2} \exp\left[-\frac{3W^3\tau_1^2}{4\pi J_0 n_0 \epsilon^2}\right] & \text{for } \omega_0 \gg W \\ \frac{J_0\epsilon^2\tau_1}{a_0^3} \exp\left[-\frac{3}{2J_0 n_0 \epsilon^2 \tau_1}\right] & \text{for } \omega_0 \ll W. \end{cases} \tag{3.9}$$

This exponentially slow in $1/\epsilon^2$ decay of the DTC order is a central result of the present Letter, and is a direct consequence of critically slow thermalization of dipolar systems in

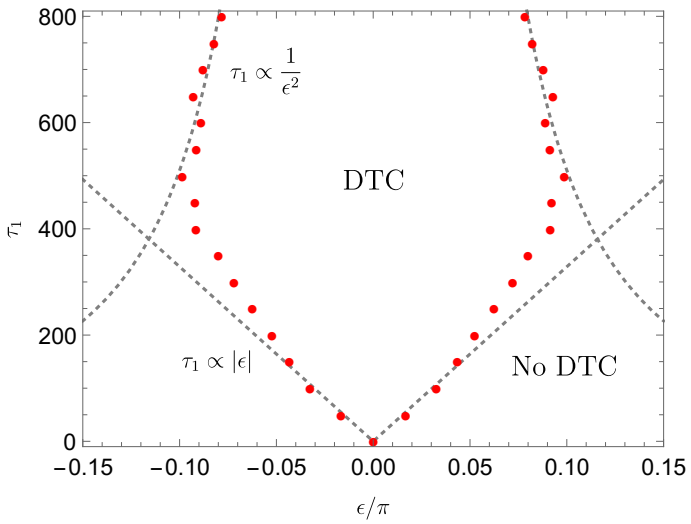

Figure 3.6: Phase diagram of the DTC obtained numerically (see Appendix B for details). Dotted lines indicate limiting behaviors of the phase boundary: at high driving frequencies, the phase boundary is linear, $\tau_1 \propto |\epsilon|$, while for low driving frequencies, it closes up as $\tau_1 \propto 1/\epsilon^2$, c.f. Eq. (3.9). This is in good agreement with the experimental observations of Ref. [18].

3D [5, 53]. Interestingly, the depolarization is exponentially sensitive to the parameters τ_1 and ϵ in two distinct ways: in regime (i) Γ is a function of τ_1^2/ϵ^2 while in regime (ii) it only depends on $1/\epsilon^2\tau_1$. These considerations allow us to identify an effective phase boundary using the criteria $\tau_1^2/\epsilon^2 = A$ or $1/\epsilon^2\tau_1 = B$ with some constants A and B. Remarkably, this boundary illustrated in Fig. 3.6 captures the key features observed in the experiment [18]: the linear growth of ϵ for short τ_1 and slow diminishing of ϵ at longer τ_1.

Technical procedure.—We now outline the technical procedure that formalizes the above discussion (see Appendix B for details). The key idea is to identify a time-dependent unitary transformation of the Hamiltonian $H(t)$ such that non-resonant single spin-flips are essentially "integrated out" and only residual two-spin-flip processes become dominant terms in the effective Hamiltonian $H'(t)$. More specifically, we start from the Hamiltonian (3.4) with H_0 representing the Ising interactions and V the applied field, and perform

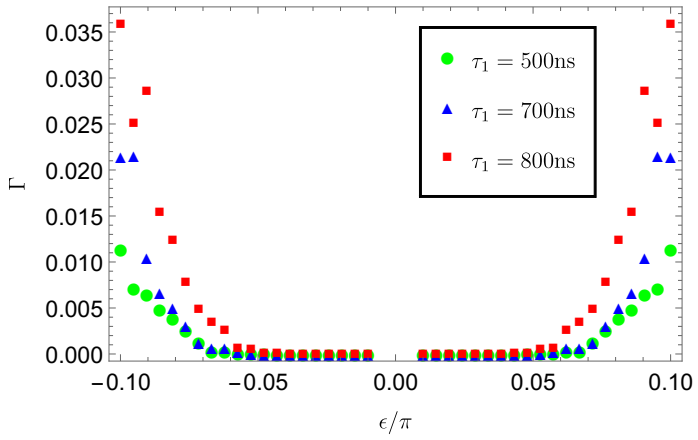

Figure 3.7: Decay rate versus perturbation ϵ for various τ_1s obtained numerically (see Appendix B). One sees a sharp rise of the decay rate as one crosses the DTC phase boundary (determined as the ϵ for which $\Gamma(\epsilon, \tau_1) = 1/100$), which is reminiscent of a phase transition.

a time-periodic unitary transformation $Q(t + \tau_1) = Q(t)$, which gives rise to:

$$H'(t) = Q(t)^\dagger (H_0 + \epsilon V \sum_n \delta(t - n^- \tau_1) - i\partial_t) Q(t). \tag{3.10}$$

Our goal is to eliminate terms that are linear in ϵ from $H'(t)$. Following Ref. [65], we look for $Q(t)$ of the form $Q(t) = e^{\epsilon\Omega(t)}$ with anti-Hermitian operator $\Omega(t) = \sum_n \Omega^{(n)} e^{in\omega_0 t}$. Expanding Eq. (3.10) in powers of ϵ, and requiring that the $O(\epsilon)$ term equals 0 gives an equation for the nth Fourier mode $\Omega^{(n)}$:

$$\frac{V}{\tau_1} - [\Omega^{(n)}, H_0] + n\omega_0 \Omega^{(n)} = 0. \tag{3.11}$$

The matrix elements of the operator $\hat{\Omega}^{(n)}$ can be computed in the eigenstate basis $|s\rangle$ of H_0 (which is a product state basis in S_i^x operators):

$$\langle s'|\Omega^{(n)}|s\rangle = \frac{\langle s'|V|s\rangle}{(E_s - E_{s'} - n\omega_0)\tau_1}. \tag{3.12}$$

Noting that $V = \sum_i S_i^y$, the operator $\Omega^{(n)}$ has non-zero matrix elements only between spin configurations s and s' that differ by one spin-flip. If $|s\rangle$ and $|s'\rangle$ differ by the value of spin

I, $E_s - E_{s'} = 2\sum_{j\neq I} \frac{J_{jI}}{r_{jI}^3} S_j^x(s) S_I^x(s) = 2h_I S_I^x$. We assume that the on-site field h_I is random (due to positional disorder and orientation dependence of J_{ij}) and sufficiently strong such that resonances are rare, i.e. the denominator in (3.12) typically does not diverge and the procedure controlled. Then, the rotated Hamiltonian to second order becomes

$$H'(t) = H_0 - \frac{\epsilon^2}{2}[\Omega(t), V] \sum_n \delta(t - n^- \tau_1) \tag{3.13}$$

A straightforward calculation using expression (3.12) gives an effective Hamiltonian of the following form:

$$H'(t) = H_0 + \sum_{IJ} \frac{A_{IJ} J_{IJ}}{r_{IJ}^3} \left(S_I^+ S_J^+ + h.c.\right) \sum_n \delta(t - n^- \tau_1), \tag{3.14}$$

where $S_I^+ \equiv (S_I^z + iS_I^y)/\sqrt{2}$ is the spin raising operator in S_I^x basis for the spin I, and A_{IJ} is the coefficient

$$A_{IJ} \approx -2S_I^x(s) S_J^x(s) \left(\frac{\epsilon}{\tau_1}\right)^2 \left(\frac{1}{\tilde{\delta}_I^2} + \frac{1}{\tilde{\delta}_J^2}\right), \tag{3.15}$$

where we introduced the notation $\frac{1}{\tilde{\delta}_J^2} = \sum_\ell \frac{1}{(h_J - \ell\omega_0)^2}$.

The effective Hamiltonian (3.14) contains the larger disordered part H_0, and long-range terms which can flip pairs of spins; the latter are suppressed proportional to ϵ^2, leading to slow relaxation. From Eq. (3.15) it is evident that the amplitudes for flipping a pair of spins depend on h_I, h_J, which in turn are determined by the positions of the spins. Assuming that h_I, h_J take typical values of the order W, and taking the contribution of the harmonic ℓ^* for which $h_J - \ell\omega_0$ is minimized (this gives the leading contribution to $\tilde{\delta}_J$), the expression (3.15) for the two-spin-flip amplitude reduces to the estimate (3.6) above.

We emphasize that the above unitary transformation is distinct from the rotating frame transformations employed to derive effective Hamiltonians in the high-frequency limit [66,

67]. Rather, it utilizes the randomness of our Hamiltonian in order to effectively integrate out non-resonant single spin flip processes.

Phase diagram.—Using the effective Hamiltonian approach described above, we obtain the phase diagram of the critical DTC. To improve upon the estimates for $\Gamma(\epsilon, \tau_1)$, we take into account the fact that the distribution of the potential h_i stems from positional randomness of spins, and numerically sample h_i from a distribution of 2000 spins in a 3D region with density 9.26×10^{-3} nm^{-3} with a short distance cut-off of 3 nm [53].

While Eq. (3.9) already provides analytical predictions for the decay rate Γ by estimating the typical distance R_* of resonant spin pairs, in numerics we find it more amenable to estimate Γ from an explicit depolarization in time profile; the counting arguments in Eq. (3.8) predicts a power-law decay of polarization $q(n)$, from which the decay timescale $1/\Gamma$ is extracted by equating $q(n)$ to a small threshold (see Appendix B). The phase boundary is then identified from a criteria $\Gamma(\epsilon, \tau_1) = \Gamma_* = 1/100$.

This approach yields the phase diagram illustrated in Fig. 3.6, which is in very good agreement with the experimental observations [18]. Note that this phase boundary is consistent with the perturbative condition $\epsilon \ll W\tau_1$. At high driving frequency, the boundary approximately follows a relation $\tau_1 \propto |\epsilon|$ (also obtainable using a semi-classical argument), while at low frequency $\tau_1 \propto 1/\epsilon^2$, which indicates that DTC order becomes less stable as τ_1 is increased, due to the fact that multi-photon processes lead to faster depolarization. The DTC phase is most robust in the crossover regime, where $\omega_0 \sim W$.

We also note that strictly speaking DTC order has finite relaxation rate at any $\epsilon \neq 0, \tau_1 \neq 0$. However, we find that the relaxation rate Γ increases very sharply at a certain value of ϵ, as illustrated in Fig. 3.7, which matches the experimental observations and is

reminiscent of a phase transition. Note, however, that unlike for a true phase transition, this increase does not become infinitely sharp even in the thermodynamic limit.

3.4 Conclusion and outlook

A number of remarkable phenomena in quantum dynamics have recently been observed in engineered many-body systems consisting of ten to a few hundred particles [38, 14, 32, 44]. The observations that we have presented here indicate that robust DTC order can occur in large systems without fine-tuned interactions and disorder, even in the regime in which localization is nominally not expected to occur. Our work raises important questions about the role of localization, long-range interactions and coupling to the environment in driven systems and opens up several new avenues for fundamental studies and potential applications. In particular, it should be possible to extend these studies to realize novel dynamical phases in more complex driven Hamiltonians, and to explore if such phases can be used to create and stabilize coherent quantum superposition states for applications such as quantum metrology [54, 55, 56].

We described a new approach to analyze dynamics of periodically driven spin systems with long-ranged interactions and applied it to explain the recently observed surprising stability of DTC in dipolar spin system. The results of our analysis are in very good agreement with experimental observations. They demonstrate that these observations correspond to a novel, critical regime of the DTC order.

Furthermore, our general approach can be applied to analyze the interplay of long-range interactions, randomness, and periodic driving in a broad class of experimental systems. The present analysis focused on the experimentally relevant case of critical interactions,

decaying as $1/r^{\alpha}$, where α coincides with the dimensionality of the system, $\alpha = d = 3$. This leads to direct relaxation processes of spin pairs. It is interesting to extend the analysis to the case $\alpha > d$ (e.g. $\alpha = 3, d = 2$), where resonant spin-pair-flip processes are rare and presumably do not provide the main relaxation channel. Experimentally, such a situation can be realized by reducing the dimensionality of the dipolar spins systems. In the static case, relaxation is expected to occur via multi-spin processes: in essence, a sparse resonant network may form, which can act as a heat bath that mediates relaxation of other spins [19, 68]. We expect that future experiments on DTC in reduced dimensions will allow one to probe such delicate interplay of various relaxation mechanisms in driven systems with long-range interactions. Our theoretical approach is well suited for analyzing such systems. Finally, apart from these specific realizations, our analysis demonstrates that the DTC response to periodic perturbations can be used as a sensitive probe of non-equilibrium quantum states and phases of matter.

Chapter 4

Quantum Metrology based on Strongly Correlated Matter

We propose and analyze a new method for quantum metrology based on stable non-equilibrium states of quantum matter. Our approach utilizes quantum correlations stabilized by strong interactions and periodic driving. As an example, we present an explicit protocol to perform Floquet enhanced measurements of an oscillating magnetic field in Ising-interacting spin systems. Our protocol allows one to circumvent the interaction-induced decoherence associated with high density spin ensembles and is robust to the presence of noise and imperfections. Applications to nanoscale magnetic sensing and precision measurements are discussed.

4.1 Introduction

The ability to interrogate a physical system and precisely measure its observables forms the basis of both fundamental and applied sciences [69]. While certain techniques are based on specially controlled individual particles [70, 71, 72], in general, large ensembles can be used to enhance measurement sensitivity. For example, in the context of spectroscopy, collections of *non-interacting* particles such as atoms, molecules, and electronic or nuclear spins are often used to maximize precision [73, 74, 75, 76, 77]. For an ensemble of N uncorrelated two-level systems, the standard quantum limit (SQL) for measuring a small energy shift, scales as $\delta\omega \propto 1/\sqrt{NT_2T}$, where T_2 is the relevant coherence time and T is the total measurement duration [69]. While this scaling suggests that increasing the number of particles always improves the signal to noise ratio, crucially, this argument does not capture the effect of inter-particle interactions. Above a certain density, these interactions fundamentally limit T_2 and thus the maximum achievable sensitivity. At its core, this limit arises from the fact that interactions typically drive thermalization, wherein the system loses both its local coherences and any accumulated spectroscopic signal.

Recent theoretical and experimental work has demonstrated that, under certain conditions, a many-body quantum system may evade rapid thermalization [78, 58, 14, 32, 53]. Such intrinsically out-of-equilibrium systems can exhibit remarkably robust dynamical features that are forbidden in equilibrium [79, 80, 65, 59, 81, 46, 47, 48, 49]. One such example is the discrete time crystal (DTC) [46, 47, 48, 49, 17, 18, 82], which is protected by an interplay between strong interactions and rapid periodic pulses [62]. The spatio-temporal ordering of the DTC phase is robust to arbitrary static perturbations and has been experimentally observed in both a trapped-ion quantum simulator [17] and a dipolar spin

ensemble [18].

Here, we demonstrate that strongly interacting, non-equilibrium states of matter can be used to enhance quantum metrology. In particular, we propose and analyze a class of protocols that allows one to circumvent limitations on the effective coherence time imposed by many-body interactions; rather, our protocols explicitly leverage interactions to develop additional quantum correlations leading to improved performances in both measurement sensitivity and bandwidth. In the case of sensitivity, the enhancement partially arises from an ability to utilize a higher density of sensors, similar to prior studies [83, 84], which utilize strong spin-exchange interactions to improve the spin lifetime [1]; on the other hand, our approach offers additional improvements in sensitivity and bandwidth, arising from an ability to prepare and utilize quantum correlated states.

The key idea is to engineer a Floquet system, where large quasi-energy gaps protect strongly-entangled states from static perturbations, while still ensuring their sensitivity to an oscillating signal [Fig 4.1(a)]. To this end, our approach can be understood as a generalization of spin-echo spectroscopy, where the states composing our effective two level system are in fact, entangled many-body states. More specifically, we employ periodic driving and strong interactions to stabilize Schrödinger's-cat-like states, which are typically extremely fragile against local perturbations in an equilibrium setting [85, 86, 87, 88]; thus, the essence of our approach is similar to the physics behind discrete time crystals [46, 47, 48, 49, 62, 82, 17, 18]. As specific examples, we analyze two techniques that allow for the precise measurement of AC magnetic fields in Floquet spin ensembles.

[1] We note that our approach does not change the SQL sensitivity scaling. However, if the external noise which limits T_2 exhibits spatial correlations, it is well known that one can achieve an enhanced scaling with N [69].

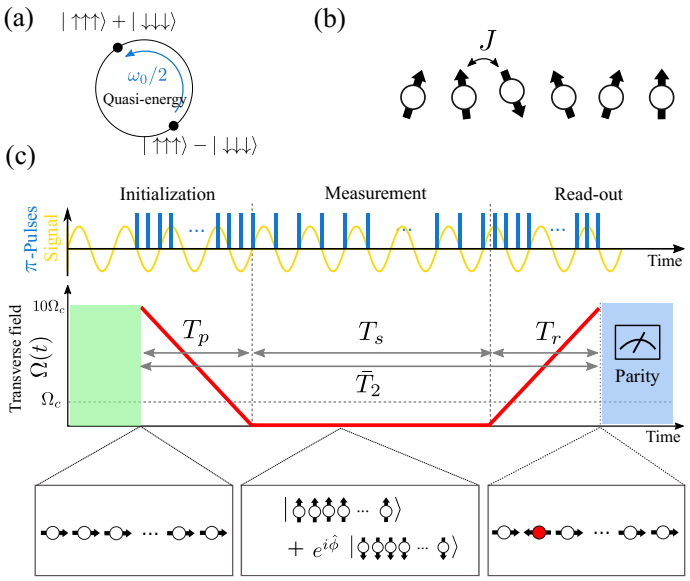

Figure 4.1: (a) Quasi-energy separation between two many-body entangled states. (b) Schematic for a spin chain with ferromagnetic interactions. (c) Sensing protocol. The protocol consists of three steps: initialization, measurement, and read-out. In each step, the transverse field Ω and the frequency of π-pulses are tuned. The signal strength is extracted from parity measurements.

We demonstrate that these protocols are robust to imperfections in the external control parameters such as the strength and duration of the pulses. This robustness distinguishes our approach from prior studies that utilize either strongly correlated states or advanced dynamical decoupling techniques [85, 86, 87, 88, 89, 90, 91, 92, 93, 94, 95, 96, 35, 97, 98, 99].

4.2 Sensing protocols

The central idea of our scheme can be understood by considering an ensemble of N spin-1/2 particles in a d-dimensional array with ferromagnetic Ising interactions and a tunable transverse field Ω [Fig. 4.1(b)]. The spins are also coupled to a weak magnetic field signal, B, in the $\hat{z}$-direction oscillating at frequency ω_s. The total Hamiltonian for the

system is given by $\hat{H} = \hat{H}_0 + \hat{H}_{\text{signal}}$ with $\hat{H}_{\text{signal}} = B\sin(\omega_s t)\sum_i \hat{S}_i^z$ and

$$\hat{H}_0 = -\sum_{i,j} J_{ij}\hat{S}_i^z\hat{S}_j^z - \Omega\sum_i \hat{S}_i^x, \tag{4.1}$$

where $\hat{S}_i^\mu$ ($\mu \in \{x, y, z\}$) are spin-1/2 operators, and $J_{ij} > 0$ is the interaction strength between spins at site-i and j with characteristic strength $J \sim \sum_j J_{ij}$. We envision that the spins are also subject to fast, global, periodic π-pulses, $\hat{P} \equiv \exp\left[-i\pi\sum_i \hat{S}_i^x\right]$, that rotate each spin around the $\hat{x}$ axis. For $B = 0$, the dynamics are driven by a Floquet unitary $\hat{U}_F = \hat{P}e^{-2\pi i\hat{H}_0\tau}$, where τ is the time-duration between π-pulses, setting the Floquet frequency, $\omega_0 = 2\pi/\tau$. Our goal is to measure the strength of the small magnetic field signal, B.

Our sensing protocol consists of three steps: (i) initialization, (ii) measurement, and (iii) read-out. In each step, the transverse field Ω and the Floquet frequency ω_0 are dynamically ramped to different values as indicated in Fig. 1(c). In the initialization step, the spins are first polarized along the strong transverse field ($\Omega \gg J$), which is subsequently decreased to zero over time duration T_p. During this process, ω_0 is sufficiently detuned from $2\omega_s$ such that the effect of $\hat{H}_{\text{signal}}$ on the spin dynamics is negligible [2]. In the measurement step, the Floquet frequency is adjusted to be resonant with the signal, $\omega_0 = 2\omega_s$, and the system evolves for a time duration T_s. Finally, the initialization step is reversed over a time T_r and each spin's polarization is then measured along the $\hat{x}$ axis. These three steps must be completed within the relevant coherence time of the system, $\bar{T}_2 \geq T_p + T_s + T_r$ and will be repeated over a total integration time T. As we will show, the magnetic field signal can be extracted from the average parity, $\langle\hat{P}\rangle \propto \langle\prod_i(2\hat{S}_i^x)\rangle$ [3].

[2] More specifically we require $|\omega_0 - 2\omega_s| \gg \Omega, J$.

[3] Note that the parity operator P conicides with the unitary that globally rotates the spin ensemble by π up to an unimportant complex phase.

In order to understand how sensitive the parity changes as a function of signal strength, we now analyze the Floquet dynamics in each of the three steps in detail. During the initialization step, we utilize interactions to prepare a quantum state with strong spin-spin correlations. To understand the dynamics during state preparation, we move into the so-called toggling frame, which rotates with every π-pulse, $\hat{P}$, by applying the unitary transformation $\hat{H} \mapsto \hat{P}^{-1}\hat{H}\hat{P}$ [21]. In this frame, $\hat{H}_0$ remains invariant while $\hat{H}_{\text{signal}}$ changes sign during every Floquet period, modifying the time-dependence of the original signal to $B_{\text{eff}}(t) = B\sin(\omega_s t)\Theta(\omega_0 t/4\pi)$, where $\Theta(x)$ is a square function with unit period. The dynamics of such a system are well approximated by an effective, quasi-static Hamiltonian [100, 66]

$$\hat{D} = \hat{H}_0 + \bar{B}_{\text{eff}} \sum_i \hat{S}_i^z \tag{4.2}$$

where $\bar{B}_{\text{eff}}$ is the time-averaged signal strength and we have neglected a small correction of order $\sim \mathcal{O}(B\Omega/\omega_s)$ [4]. When ω_0 is far-detuned from $2\omega_s$, $B_{\text{eff}}(t)$ rapidly oscillates with vanishing mean. Our polarized initial state corresponds to the ground state of $\hat{D}$ for large Ω. As Ω is slowly decreased to zero, the system undergoes a phase transition from a paramagnet to a ferromagnet with two degenerate ground states $|G_\pm\rangle = (|\uparrow\uparrow\cdots\uparrow\rangle \pm |\downarrow\downarrow\cdots\downarrow\rangle)/\sqrt{2}$. Crucially, during this process the effective Hamiltonian conserves parity and hence, for a sufficiently slow ramp, our initialization deterministically prepares the even parity Greenberger-Horne-Zeilinger (GHZ) state, $|G_+\rangle$, a well-known resource for quantum-enhanced metrology.

During the measurement step, tuning the Floquet frequency to $\omega_0 = 2\omega_s$ gives rise to

[4]This description is valid up to an exponentially long time $\sim \exp[\omega_0/\max(\Omega, J)]$, beyond which the system absorbs energy from the periodic driving and heats up to infinite temperature [59, 81, 100, 66].

a non-zero time-averaged signal strength $\bar{B}_{\text{eff}} = (2/\pi)B$, which resonantly couples the two degenerate ground states ($|G_{\pm}\rangle$), inducing coherent oscillations between them. After time evolving for T_s, the system is in a superposition $|G_{\phi}\rangle = \cos(\phi)\,|G_{+}\rangle - i\sin(\phi)\,|G_{-}\rangle$, where $\phi = 2NBT_s$ is the collective phase accumulated by the spin ensemble during the measurement sequence. This phase can be extracted from by measuring the parity $\langle\hat{P}\rangle = \cos(2\phi)$ in the paramagnetic phase, since $|G_{-}\rangle$ is adiabatically mapped to a single spin excitation, while $|G_{+}\rangle$ maps to zero excitations [see Fig. 1(c)].

Let us begin by analyzing the measurement sensitivity in the ideal case without external noise. When our protocol is repeated $k = T/\bar{T}_2$ times, the uncertainty in the phase is reduced to $\delta\phi \sim 1/\sqrt{k}$. Assuming a long measurement duration, $\bar{T}_2 \approx T_s \gg T_p, T_r$, the sensitivity scales as:

$$\delta B^{-1} \sim \delta\phi^{-1} N T_s \sim N\sqrt{\bar{T}_2 T}, \tag{4.3}$$

saturating the Heisenberg limit [69]. Note that the relevant coherence time here is determined by external noise at the probing frequency ω_s (and is not limited by interactions between the spins).

A natural constraint for our protocol is the adiabatic preparation fidelity of the GHZ state. The energy gap at the phase transition decreases with system size, which in turn requires a longer preparation step, and hence, a longer coherence time. By crossing a phase transition in limited time, one necessarily creates a finite density of excitations. However, even in this case, owing to ferromagnetic spin-spin correlations, our protocol can still achieve a sensitivity better than that of the SQL. These correlations can be characterized by a length scale ξ, where $\langle\hat{S}_i^z\hat{S}_j^z\rangle \sim e^{-|i-j|/\xi}$ and can be estimated from Kibble-Zurek scaling as $\xi \sim (JT_p)^{\nu/(1+z\nu)}$ [101]. Here, z and ν are the correlation-length and dynamical critical

exponents of the transition [102, 103, 104, 105, 106, 107, 108, 109].

In this scenario, the initialization step prepares an even parity state of the form $|\xi_+\rangle = (|\xi\rangle + P|\xi\rangle)/\sqrt{2}$, where $|\xi\rangle$ is ferromagnetically ordered with correlation length ξ. [hat them] The state accumulates a collective phase $\hat{\phi} = 4BT_s \sum_i \hat{S}_i^z$ during the measurement stage, leading to a parity expectation value $\langle \hat{P} \rangle = \langle \xi | \cos(2\hat{\phi}) | \xi \rangle$. For a weak signal, $\langle \hat{P} \rangle$ varies quadratically as: $1 - \langle \hat{P} \rangle \approx 2 \langle \xi | \hat{\phi}\hat{\phi} | \xi \rangle \sim \xi^d N (BT_s)^2$, which results in a sensitivity scaling

$$\delta B^{-1} \sim \sqrt{T/(T_p + T_s + T_r)} \sqrt{\xi^d N}\, T_s. \tag{4.4}$$

Intuitively, this scaling be understood as follows. The state $|\xi_+\rangle$ can be viewed as multiple copies of a GHZ state with size $\sim \xi^d$. While each GHZ state allows Heisenberg limited sensitivity $\sim \xi^d \sqrt{T\bar{T}_2}$, simultaneous measurements with all N/ξ^d copies can further improve the signal to noise by a factor $\sqrt{N/\xi^d}$, leading to the observed scaling [Eq. (4.4)]. When the correlation length approaches the system size, this scaling reaches the limit in Eq. (4.3).

A few remarks are in order. First, given a limited coherence time, one should optimize the relative duration of each step. This optimum is achieved when $\beta \equiv T_p/\bar{T}_2 \simeq 1 - T_s/\bar{T}_2 = (1 + 2(\nu z + 1)/d\nu)^{-1} \gg T_r/\bar{T}_2$. For example, in one dimension with nearest neighbor interactions, the phase transition is characterized by exponents $\nu, z = 1$, and the optimized sensitivity scales as

$$\delta B^{-1} \sim \sqrt{NT\bar{T}_2} (J\bar{T}_2)^{1/4}. \tag{4.5}$$

We note that this scaling improves upon the SQL by a factor $\sim (J\bar{T}_2)^{1/4}$. Second, we emphasize that periodic π-pulses are essential to our protocol, since they suppress low

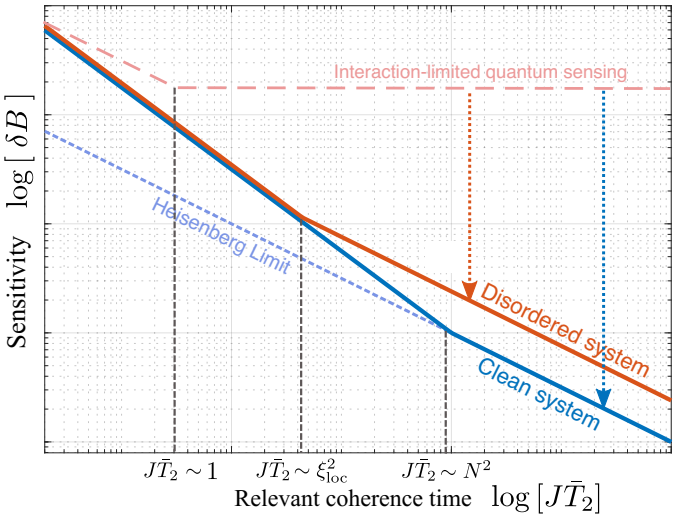

Figure 4.2: Sensitivity scaling δB as a function of $\bar{T}_2$ for a given system size N and total integration time T. As an example, we assumed a system of a spin chain with short-range interactions. Ideally, the sensitivity approaches Heisenberg limit when $\bar{T}_2$ is sufficiently long to prepare a GHZ state, e.g. $J\bar{T}_2 > N^2$. For a disordered system, this scaling is limited by the Anderson localization of quasi-particles with the localization length ξ_{loc}. In both cases, the protocol outperforms standard quantum limit, where the coherence time is limited by inter-particle interactions.

frequency noise and prevent changes to the parity of the spin ensemble. This protection originates from the quasi-energy gap between pairs of Floquet eigenstates with opposite parity [Fig. 4.1(a)].

Robustness.— We now turn to an analysis of our protocol in the presence of both imperfections and noise. First, we consider quasi-static local perturbations $\epsilon \sum_i \delta\hat{H}_i$, which we decompose into parity-preserving and parity-changing terms: $\delta\hat{H}_i = \delta\hat{H}_i^+ + \delta\hat{H}_i^-$ with $\delta\hat{H}_i^\pm \equiv (\delta\hat{H}_i \pm \hat{P}\delta\hat{H}_i\hat{P})/2$. The parity-preserving term, $\delta\hat{H}_i^+$, does not affect the nature of the phase transition nor the sensitivity scaling of our protocol. The parity-changing term, $\delta\hat{H}_i^-$, hinders both the state preparation and the measurement fidelity of the magnetic field signal. However, this effect is parametrically suppressed by the presence of our periodic π-pulses, which effectively "echoes" out this contribution to leading order. More specifically, higher order corrections to the effective Hamiltonian appear only as $\sim \epsilon J/\omega_0$ [100, 66] and can be safely neglected assuming $\epsilon J/\omega_0 \ll (\xi^d T_p)^{-1}$ (initialization) and $\epsilon J/\omega_0 \ll B$ (measurement).

Second, we consider the presence of inhomogeneities in $\delta\Omega_i$, δJ_i, and $\delta\theta_i$. Such inhomogeneities can lead to localization, which limits the maximum correlation length of the system. In general, the localization length at the critical point scales as $\xi_{\text{loc}} \sim (W/J)^{-\mu}$, where W is the disorder bandwidth of the coupling parameters and μ is the corresponding critical exponent. When the localization length ξ_{loc} is shorter than the original correlation length $\xi \sim \sqrt{JT_p}$, one must reduce the state preparation time to $T_p^* = (W/J)^{-2\mu}/J$ (so that more time can be allocated for the measurement step). This leads to a modified sensitivity scaling as summarized in Fig. 4.2. Interestingly, the effect of disorder can be favorable during the measurement stage; while domain wall excitations can be mobile in the absence

of disorder (in 1D), relatively weak disorder in J may localize the excitations, allowing stable accumulation of phase information over long times. This effect is particularly relevant when the localization lengths during the measurement step is much shorter than that at the critical point, which is often satisfied in realistic systems, where the dominant source of disorder arises from random positioning of spins (disorder in J) (see Appendix C).

Finally, we now consider the effect of external noise from the environment, which limits the coherence time, $\bar{T}_2$. Given a noise spectral density $S(\omega) \sim A_0^{1+\alpha}/\omega^\alpha$, the periodic π-pulses decouple the system from low frequency noise $\omega < \omega_s$, implying that the decoherence rate is determined by the noise density at the probe frequency, $S(\omega_s)$. If the noise on each spin is independent, then the relevant coherence time of the entangled spin state is shortened to $\bar{T}_2 \sim T_2^0/\xi^d$, where T_2^0 is the lifetime of a single spin. In this case, the reduction of the coherence time off-sets any potential gain in the sensitivity in Eq. (4.4). This reduction is well-known and is in fact, fundamental for all methods that utilize entangled states for spectroscopy [69].

We note, however, that our protocol still benefits from a shorter measurement duration T_s (since the phase is accumulated N times faster in $|G_\phi\rangle$), which provides a broader sensing bandwidth without compromising the sensitivity (see Appendix C). Finally, for solid-state spins, external noise often arises from nearby fluctuating dipole moments, which generates a spatially correlated $S(\omega)$. In this case, $\bar{T}_2$ can be significantly longer than T_2^0/ξ^d owing to spatial averaging of the noise field in the collective phase $\hat{\phi} = 4BT_s \sum_i \hat{S}_i^z$, leading to an enhanced sensitivity (see Appendix C).

Sensing protocol without parity measurements.— Parity measurements become challenging in an ensemble experiment where one lacks the ability to resolve individual spin

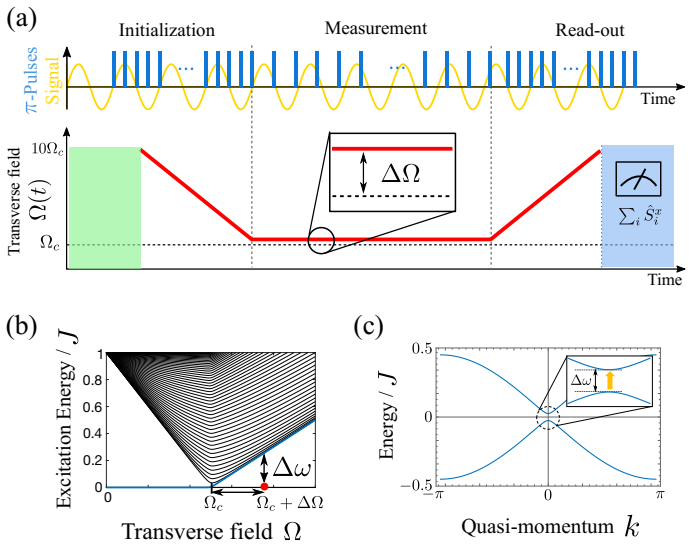

Figure 4.3: Sensing protocol without parity measurement. (a) Modified protocol. During the initialization, Ω does not cross the critical point. During the spectroscopy, π-pulse frequency is detuned from the signal frequency by $\Delta\omega$ (see main text). For read-out, the totally magnetization $\sum_i \hat{S}_i^x$ is measured. (b) Exemplary excitation spectrum of $\hat{H}_0$ (for a short-range interacting spin chain). In the vicinity of the critical point, the effective signal resonantly excites the system. (c) The dispersion relation of Bogoliubov quasi-particle excitations (for a short-range interacting spin chain). Low momentum modes are resonantly excited by the signal.

projections. To this end, we provide an alternative approach based upon measuring an extensively scaling observable. Our modified protocol is shown in Fig. 4.3(a). During the initialization step, Ω is adiabatically decreased close to the critical point $\Omega = \Omega_c + \Delta\Omega$ without crossing the phase transition. Meanwhile, in the measurement step, rather than setting the Floquet frequency equal to $2\omega_s$, we now detune it by $\Delta\omega \equiv \omega_s - \omega_0/2$, such that the magnetic field signal resonantly excites the system [Fig. 4.3(b-c)]; in an experiment, this resonance condition would need to be calibrated. Finally, Ω is slowly brought back to its original value, and the number of spin-flip excitations, N_e, now encodes the signal strength B [5].

The resonant magnetic field signal creates, on average, a single collective excitation within the correlation volume, ξ^d. The probability of creating such an excitation, $p \sim (\chi\xi^{d/2}BT_s)^2$, depends on the proximity to the critical point, which leads to the factor, $\chi \equiv (\Delta\Omega/\Omega)^{-\eta}$, where η is the scaling dimension of the operator $\hat{S}_i^z$ [110, 34]. Since there are N/ξ^d correlated spin segments in the system, the average number of excitations $N_\mathrm{e} \sim pN/\xi^d$, while its fluctuations $\delta N_\mathrm{e} \sim \sqrt{p(1-p)N/\xi^d}$. This results in a signal-to-noise ratio: $\partial_B N_\mathrm{e}/\delta N_\mathrm{e} \sim \sqrt{N}T_s(JT_p)^{\eta/(z\nu+1)}$. As before, when this procedure is repeated over a total duration T with optimal T_p, the sensitivity scales as,

$$\delta B^{-1} \sim \sqrt{NT\bar{T}_2}(J\bar{T}_2)^{\eta/(z\nu+1)}. \tag{4.6}$$

For nearest neighbor interactions in 1D (Ising universality class), the scaling dimension is $\eta = 3/8$ and $\delta B^{-1} \sim \sqrt{NT\bar{T}_2}(J\bar{T}_2)^{3/16}$. [111, 112, 113]

[5] For this protocol, excitations should not be created during the initialization or read-out steps. This condition can be estimated from the Kibble-Zurek "freezing point" $\Delta\Omega \geq \Omega(JT_p)^{-1/(z\nu+1)}$ [101].

4.3 Experimental implementations and outlook

We describe two potential platforms for realizing our protocol. First, we consider an AC magnetic field sensor using a 2D array of shallow implanted nitrogen-vacancy (NV) color centers in diamond [73, 76, 77]. The maximum sensitivity per unit area in this approach is limited by the dipolar interactions between the $S = 1$ NV centers [53], which cannot be easily decoupled using conventional NMR techniques [57, 21, 35]. Our protocol provides a way to circumvent this interaction-induced limitation and enable significant improvements to the sensitivity (see Appendix C). A second platform for realizing our protocol is provided by nuclear spin ensembles in layered materials such as hexagonal boron-nitride or ^{13}C enriched graphene. A particularly intriguing application of such systems includes the detection of time-varying signals resulting from weakly interacting massive particles such as axions [75].

Our scheme can also be extended along several directions. While we have focused on probing magnetic field signals, similar methods can enable the detection of phase fluctuations in the external driving [70, 74, 114]. Moreover, at present, our scheme enables the suppression of symmetry breaking perturbations at leading order via periodic π-pulses. An intriguing possibility is to extend such suppression to higher order corrections in the effective Hamiltonian. Indeed, in the limit of fast driving, it has been shown that the system can exhibit an emergent symmetry up to exponentially long times [62].

Chapter 5

Dynamical Engineering of Interactions in Qudit ensembles

We propose and analyze a method to engineer effective interactions in an ensemble of d-level systems (qudits) driven by global control fields. In particular, we present (i) a necessary and sufficient condition under which a given interaction can be decoupled, (ii) the existence of a universal sequence that decouples any (cancellable) interaction, and (iii) an efficient algorithm to engineer a target Hamiltonian from an initial Hamiltonian (if possible). We illustrate the potential of this method with two examples. Specifically, we present a 6-pulse sequence that decouples effective spin-1 dipolar interactions and demonstrate that a spin-1 Ising chain can be engineered to study transitions among three distinct symmetry protected topological phases. Our work enables new approaches for the realization of both many-body quantum memories and programmable analog quantum simulators using existing experimental platforms.

5.1 Introduction

The controlled manipulation of quantum systems with pulsed coherent fields is important in nearly all branches of quantum science. The techniques associated with dynamical coherent control have a long and storied history, originating in nuclear magnetic resonance (NMR), where periodic sequences of instantaneous control pulses enable the isolation of nuclear spins from unwanted external noise sources [93]. Over the past few decades, advanced techniques have been developed with goals ranging from frequency-selective decoupling to higher-order error suppression, and applications ranging from metrology to information processing [115, 94, 95, 96, 116, 97, 117, 118, 98, 99, 119, 120].

Periodic control pulses can also be used to engineer many-body interactions. In particular, they can enable the realization of driven (Floquet) systems that exhibit phenomena richer than the original system without dynamical control [121, 122, 123, 46, 47, 48, 49]. This approach falls under the moniker of average Hamiltonian theory [124], a term prevalent in the context of solid-state NMR, where sequences of spin-rotations are used to modify the intrinsic interactions between magnetic dipoles [57, 124]. A particularly powerful example is the celebrated WAHUHA pulse sequence [57] which cancels the dipole-dipole interaction between spin-1/2 particles and has been extensively utilized in systems ranging from solid-state spin defects to ultracold polar molecules [97, 125]. More generally, pulsed periodic driving has enabled the experimental exploration of a variety of exotic many-body quantum phenomena including: dynamical phase transitions, quantum chaos, glassy dynamics in disordered systems, and discrete time-crystalline order [126, 127, 128, 17, 18]. While the majority of existing pulse sequences are designed to engineer Hamiltonians constructed from spin-1/2 or qubit-like systems [129, 130, 131, 132], recent experimental

progress has opened the door to the manipulation of many-body *qudit* systems, whose basic degrees of freedom possess d internal states. Indeed, in platforms ranging from trapped ions and Rydberg atoms to superconducting qubits and solid-state spin defects, coherent interactions among multiple qudits have already been observed [125, 133, 18]. This enables the study of quantum many-body qudit systems that can exhibit phenomena qualitatively distinct from their spin-1/2 counterparts, such as generalized Potts model and parafermionic topological phases [134, 135, 136, 137]. Generalizing Hamiltonian engineering methods to qudit systems may enable exploration of such unique phenomena with important potential applications in areas such as quantum simulations.

Here, we report two advances toward this goal. First, we present a complete generalization of the WAHUHA pulse sequence for an arbitrary qudit system. We derive a necessary and sufficient condition that diagnoses when generic interactions can be cancelled. Moreover, we prove the existence of a universal pulse sequence that decouples any cancelable interaction. This result implies that locally encoded quantum information can be protected even in a strongly interacting qudit ensemble. As a specific example, we present a novel pulse sequence that decouples spin-1 dipolar interactions. Second, we present an algorithm that uniquely determines when a given initial Hamiltonian H_0 can be mapped to a desired final Hamiltonian H_f, using a predetermined set of global pulses. Such a technique provides a recipe to transform an interacting many-body system into a programmable analog quantum simulator [132]. In this context, we demonstrate that a spin-1 classical Ising chain can be directly mapped to a family of Hamiltonians whose ground states include a variety of symmetry protected topological (SPT) phases. In both cases, we consider an ensemble of d-level systems with generic pairwise inter-

actions and assume that only *global* $SU(d)$ manipulations are available. This setting is ubiquitous and particularly relevant to recent experimental developments in a variety of platforms [125, 126, 127, 128, 17, 18, 53, 138, 139, 140]. We note that in the case where qudits can be *independently* addressed and controlled, arbitrary modifications of the underlying interactions are possible [141, 142, 143, 131, 132]; however, such precise individual controls are typically challenging to implement in strongly interacting many-body systems.

5.2 Hamiltonian engineering protocol

We consider an N qudit system with Hamiltonian,

$$H = \sum_{ij} J_{ij} h_{ij}, \tag{5.1}$$

where h_{ij} represents a homogeneous two-qudit interaction between i and j, and the scalars J_{ij} fully characterize the geometry, range and strength of the interactions. Hamiltonian evolution is interspersed with a rapid and repeated sequence of k pulses, denoted P_i. More specifically, each pulse is followed by free evolution under H for a duration τ_i. Assuming that the manipulations are sufficiently fast, one can rewrite the unitary evolution (Floquet unitary) over one such k-cycle as,

$$U(T) = e^{-iH\tau_k} P_k \dots e^{-iH\tau_2} P_2 e^{-iH\tau_1} P_1, \tag{5.2}$$

where $T = \sum_{i=1}^{k} \tau_i$ is the total time duration of the cycle [1]. At integer multiples of the driving period T, the time evolution is captured by an effective Hamiltonian H_{eff}, defined by $U(T) = \exp(-iH_{\text{eff}}T)$.

[1] More specifically, we consider a sequence $\{P_i\}$ such that $P_k \dots P_2 P_1 = \mathbb{I}$ by appropriately setting either P_1 or P_k.

In the case of both dynamical decoupling and Hamiltonian engineering, the key idea underlying our approach is to design a finite pulse sequence such that H_{eff} approximates a desired target Hamiltonian. Defining $U_i \equiv P_i P_{i-1} \dots P_2 P_1$ and $U_0 \equiv \mathbb{I}$, one can rewrite Eq. (5.2) as

$$U(T) = e^{-i\bar{H}_k \tau_k} \dots e^{-i\bar{H}_2 \tau_2} e^{-i\bar{H}_1 \tau_1}, \tag{5.3}$$

where $\bar{H}_i = U_i^\dagger H U_i$. By moving into this so-called toggling frame [124], the pulsed unitary dynamics [Eq. (2)] can be captured by continuous evolution under a time-dependent Hamiltonian. Recently, it has been shown that H_{eff} can be approximated by a controlled Magnus expansion in the high frequency limit, leading to an effective Hamiltonian description valid up to exponentially long times [144, 66, 81, 100]. In particular, for a driving frequency, $\omega = 2\pi/T$, that is large compared to local energy scales $\sim J$, $H_{\text{eff}} \simeq \sum_{q=0}^{q*} (J/\omega)^q H_{\text{eff}}^{(q)}$, where $H_{\text{eff}}^{(q)}$ denotes the q-th order term while $q*$ is the maximum order beyond which heating effects become non-negligible. Here, we assume a rapid pulse sequence satisfying $\omega \gg J$ and focus on the leading order effective Hamiltonian,

$$H_{\text{eff}} \approx H_{\text{eff}}^{(0)} = \sum_i \frac{\tau_i}{T} \bar{H}_i. \tag{5.4}$$

Once a desired pulse sequence is found, one can always symmetrize it such that the next order correction $H_{\text{eff}}^{(1)}$ also vanishes, leaving only a strongly suppressed second order ($q \geq 2$) contribution (see Appendix D). From the linearity of Eq. (5.4), we only need to consider a single term h_{ij} and hence omit the qudit indices below.

Consistent with the control available in many-body qudit systems, we focus on the case where one can only apply global single-qudit rotations, i.e., $P_i = p_i^{\otimes N}$ for some $p_i \in SU(d)$. To represent the interactions, we use a trace orthonormal operator basis $\{\lambda_\mu\}$ with

$\mathrm{tr}\,(\lambda_\mu\lambda_\nu) = 2\delta_{\mu\nu}$. In this basis, the most general two-qudit interaction can be written as

$$h = \sum_{\mu\nu} C_{\mu\nu}\lambda_\mu \otimes \lambda_\nu. \tag{5.5}$$

Hermiticity and the exchange symmetry imply that C is a real symmetric $m \times m$ matrix with $m = d^2 - 1$. For a given h, the matrix C can be explicitly obtained using $C_{\mu\nu} = \mathrm{tr}\,(h\lambda_\mu \otimes \lambda_\nu)\,/4$.

Interaction Decoupling.—We now derive a necessary and sufficient condition for the full decoupling of an interacting qudit Hamiltonian.

Theorem 1. *For a given two-qudit interaction h, there exists a finite sequence $\{p_i\} \subset SU(d)$, or equivalently $\{u_i\} \subset SU(d)$, and $\{\tau_i\} \subset \mathbb{R}^+$, such that $h_{\mathit{eff}} = \sum_i \frac{\tau_i}{T}(u_i^\dagger \otimes u_i^\dagger)h(u_i \otimes u_i) = 0$ if and only if the C matrix of h is traceless, i.e. $\mathit{tr}\,(C) = \sum_\mu \mathit{tr}\,(h\lambda_\mu \otimes \lambda_\mu)\,/4 = 0$.*

Proof. For convenience we work with interactions represented as C matrices, whose transformation under a unitary rotation $u_i \otimes u_i$ is given by,

$$\sum_{\mu\nu} C_{\mu\nu}\lambda_\mu \otimes \lambda_\nu \mapsto \sum_{\mu\nu} C_{\mu\nu}\left(u_i^\dagger\lambda_\mu u_i\right) \otimes \left(u_i^\dagger\lambda_\nu u_i\right) \tag{5.6}$$

$$\equiv \sum_{\mu\nu} C^{(i)}_{\mu\nu}\lambda_\mu \otimes \lambda_\nu, \tag{5.7}$$

where the coefficients $C^{(i)}_{\mu\nu}$ are defined by the equality above. More specifically, two matrices $C^{(i)}$ and C are related by the transformation $C^{(i)} = (O^i)^T CO^i$, where $O^i_{\nu'\nu} \equiv \frac{1}{2}\mathrm{tr}\left(\lambda_\nu u_i^\dagger \lambda_{\nu'} u_i\right)$. Taking into account the full sequence of unitary pulses yields the C matrix for the effective Hamiltonian as,

$$C_{\text{eff}} = \sum_i \alpha_i \left(O^i\right)^T CO^i. \tag{5.8}$$

where $\alpha_i = \tau_i/T$ characterizes the relative timescale of the various intermediary free evolutions. Intuitively, Eq. (5.8) demonstrates that the effective interaction is simply given by a weighted average of "rotated" versions of the original interaction. Indeed, it can be easily shown that O^i is a real orthogonal matrix.

First, one immediately sees that the trace of C is preserved. Thus, it is necessary for the original C matrix to be traceless in order for the effective Hamiltonian to be fully decoupled. Second, this also naturally suggests a decomposition of a general interaction into two components: an isotropic part with non-zero trace and a traceless anisotropic part. Since C is a real-symmetric matrix, there exists only one linearly independent isotropic component, which is proportional to the identity matrix. The corresponding two-qudit interaction is $h_{\text{iso}} \propto \sum_\mu \lambda_\mu \otimes \lambda_\mu$. Eq. (5.8) shows that any isotropic interaction cannot be modified by global pulses as it is invariant under $SU(d)$ rotations.

To prove sufficiency, we construct a pulse sequence that explicitly cancels any interaction ($C_{\text{eff}} = 0$) given that the interaction is purely anisotropic. The design principle of this "universal decoupling" sequence is simple: find a finite set of $\{u_i\}$, where the corresponding $\{O^i\}$ are distributed among all possible rotations such that their weighted average vanishes; this strategy is reminiscent of unitary $2-$designs, but here, we have one additional control knob, corresponding to the choices of α_i. Interestingly, a very related problem has been already studied in quantum information science. In Ref. [145], Dür *et al* introduce a depolarization superoperator $\mathcal{D}$ that acts on a density matrix ρ of a two-qudit system

$$\mathcal{D}(\rho) = A_d \frac{\text{tr}\,(A_d\rho)}{\text{tr}\,(A_d)} + S_d \frac{\text{tr}\,(S_d\rho)}{\text{tr}\,(S_d)}, \tag{5.9}$$

where $S_d(A_d)$ is the projector onto even(odd) eigenspace of the exchange operator $\Pi_d = \sum_{i,j=1}^{d} |ij\rangle\langle ji|$, i.e., $A_d = (\mathbb{I} - \Pi_d)/2$ and $S_d = 1 - A_d = (\mathbb{I} + \Pi_d)/2$. It is shown, by explicit

construction, that $\mathcal{D}(\cdot)$ can be implemented by a finite sequence of probabilistic bilocal operations, $\sum_{i=1}^{k} p_i \left(v_i^\dagger \otimes v_i^\dagger\right) \rho \left(v_i \otimes v_i\right) = \mathcal{D}(\rho)$, where $\{p_i\}$ is a probability distribution and $\{v_i\} \subset SU(d)$. Here, we re-interpret the super-operator as dynamical decoupling sequence via the mapping: $p_i \to \alpha_i$ and $v_i \to u_i$. To show that this is a universal decoupling sequence, we demonstrate that for an arbitrary interaction h, $\text{tr}\left(S_d h\right) = -\text{tr}\left(A_d h\right) = \text{tr}\left(C\right)$; thus, $\text{tr}\left(C\right) = 0$ implies $\mathcal{D}(h) = 0$. The proof is simple: for h acting on qudits A and B,

$$\text{tr}\left(h\Pi_d\right) = \sum_{\mu\nu ij} C_{\mu\nu} \text{tr}\left(\lambda_\mu^A \otimes \lambda_\nu^B \left|ij\right\rangle \left\langle ji\right|\right) \tag{5.10}$$

$$= \sum_{\mu\nu ij} C_{\mu\nu} \left\langle j_A\right| \lambda_\mu^A \left|i_A\right\rangle \left\langle i_B\right| \lambda_\nu^B \left|j_B\right\rangle \tag{5.11}$$

$$= \sum_{\mu\nu} C_{\mu\nu} \text{tr}\left(\lambda_\mu \lambda_\nu\right) = 2\text{tr}\left(C\right), \tag{5.12}$$

where we have explicitly dropped the qudit indices and the tensor product [Eq. (5.12)] to emphasize that $\lambda_{\mu(\nu)}$ are matrices. Finally, noting that $\text{tr}\left(h\right) = \sum_{\mu\nu} \text{tr}\left(\lambda_\mu^A \otimes \lambda_\nu^B\right) = 0$, we obtain $\text{tr}\left(S_d h\right) = -\text{tr}\left(A_d h\right) = \text{tr}\left(h\Pi_d\right)/2 = \text{tr}\left(C\right)$, which completes the proof of Theorem 1. □

Hamiltonian Engineering.—The previous case of interaction decoupling can be viewed as a specific example of a more general question: given an initial set of interactions h_0, a target Hamiltonian h_f and a finite set of available unitaries $\mathcal{U}$, is there a pulse sequence such that, $\sum_i \frac{\tau_i}{T}(u_i^\dagger \otimes u_i^\dagger) h_0 (u_i \otimes u_i) = \beta h_f$ for a constant $\beta > 0$? If so, does there exist an efficient algorithm to construct the desired pulse sequence? In what follows we describe such an algorithm.

Let us begin by rewriting h_0 and h_f in their corresponding C matrices C_0 and C_f. We denote the strengths of their isotropic components as $s_0 = \text{tr}\left(C_0\right)$ and $s_f = \text{tr}\left(C_f\right)$. As previously discussed, if only one of their C is traceless, h_0 cannot be mapped to h_f since

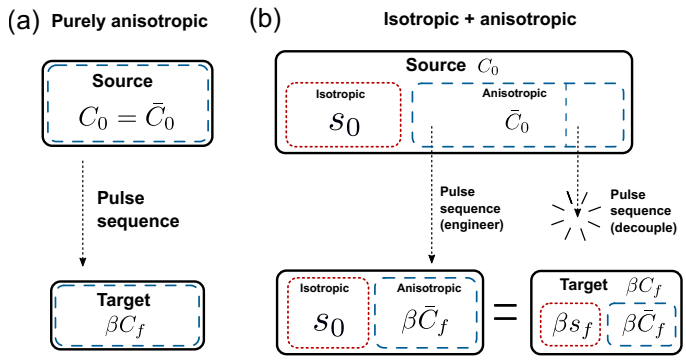

Figure 5.1: Schematic diagram of interaction engineering. Black solid, red dotted, and blue dashed lines indicate full interactions, isotropic components and anisotropic components, respectively. Dotted arrows represent applications of dynamical decoupling sequence. (a) When both source and target interactions are purely anisotropic ($s_0 = s_f = 0$), one directly maps interactions. (b) For interactions with both isotropic and anisotropic components, one engineers only the anisotropic component and matches the relative strength by canceling some fraction.

the isotropic components can never be decoupled by any pulse sequence. We will now divide our analysis into two cases: (i) $s_0 = s_f = 0$ and (ii) $s_0, s_f \neq 0$ (Fig. 5.1).

Case (i) [Fig. 5.1(a)]: Our strategy is to cancel the portion of the interaction that is *orthogonal* to C_f while maximizing the strength of the remaining piece. To illustrate this idea more clearly, we introduce a vector representation of interactions

$$(\vec{w})_a \equiv \mathrm{tr}\left(C\eta_a\right)/2, \tag{5.13}$$

using a matrix basis $\{\eta_a\}$ of dimension $m = d^2 - 1$. In this representation, Eq. (5.8) becomes $\vec{w}_{\text{eff}} = \sum_i \alpha_i M^i \vec{w}$ with $M^i_{ab} \equiv \frac{1}{2}\mathrm{tr}\left(\eta_a \left(O^i\right)^T \eta_b O^i\right)$. Our objective is to maximize $\vec{w}_{\text{eff}} \cdot \vec{w}_f$ while satisfying $\vec{w}_{\text{eff}} \cdot P_\perp = 0$, where $\vec{w}_q$ ($q \in \{0, f\}$) is the vector representation of C_q and $P_\perp$ is the projector on to a space that is orthogonal to $\vec{w}_f$, i.e., $(P_\perp)_{ab} = \delta_{ab} - (\vec{w}_f)_a(\vec{w}_f)_b/|\vec{w}_f|^2$. Interestingly, this task can naturally be cast into the canonical form of Linear Programming, i.e. maximize $\sum_i \alpha_i \vec{w}_f \cdot M^i \vec{w}_0$ with respect to $\{\alpha_i\}$ under constraints

$\sum \alpha_i P_\perp M^i \vec{w}_0 = 0$, $\sum \alpha_i = 1$, and $\alpha_i \geq 0$ [146].

Case (ii) [Fig. 5.1(b)]: In this case, the contributions from the isotropic components cannot be ignored, and they fix the rescaling parameter, $\beta = s_0/s_f$. Thus, one has to not only engineer the "shape" of the anisotropic interaction but also adjust its strength to match with the fixed β. Now our strategy is to decompose the given interaction into three pieces: an isotropic part, a fraction of the anisotropic part to be modified, and the remaining portion to be cancelled. To this end, one is searching for two pulse sequences, $\mathcal{P}_1 = (\{\tau_i^1\}, \{u_i^1\})$, which maps $\bar{C}_0 \mapsto \beta^* \bar{C}_f$ and $\mathcal{P}_2 = (\{\tau_i^2\}, \{u_i^2\})$, which cancels $\bar{C}_0 \mapsto 0$. Here, $\bar{C}_q$ ($q \in \{0, f\}$) is the anisotropic component of C_q and β^* is the maximum possible strength. As before, one can use linear programming to efficiently find these sequences. If both maps are possible and the engineered interaction strength is sufficiently strong $\beta^* \geq \beta$, one can concatenate two sequences to form $\mathcal{P}_3 = (\{(\beta/\beta^*)\tau_i^1, (1-\beta/\beta^*)\tau_i^2\}, \{u_i^1, u_i^2\})$, which maps $C_0 \mapsto \beta C_f$.

Decoupling spin-1 dipolar interactions.—We now turn to two examples. First, we present a 6-pulse sequence that decouples effective dipole-dipole interactions $H_d = \sum J_{ij} h_{ij}^d$ in an ensemble of spin-1 particles (states $\{|\pm 1\rangle, |0\rangle\}$) with anharmonic level spacings [53],

$$h^d = \sum_{a=1}^{2} (X_a \otimes X_a + Y_a \otimes Y_a) - (Z_1 + Z_2) \otimes (Z_1 + Z_2), \tag{5.14}$$

where X_a, Y_a, and Z_a are Pauli matrices associated with two different transitions, $|0\rangle \leftrightarrow |+1\rangle$ $(a = 1)$ and $|0\rangle \leftrightarrow |-1\rangle$ $(a = 2)$, of a single spin-1 particle [see Fig. 5.2(a)]. This interaction can be readily decomposed in an orthonormal basis (see Appendix D). Such a Hamiltonian is ubiquitous in quantum optical systems and arises in the context of ultracold polar molecules, NV centers, and quadrupolar nuclear spins [125, 99, 18]. While the solution for the analogous question in dipolar spin-1/2 systems has been known for a

half-century (e.g. WAHUHA), the spin-1 problem remains an open question.

Motivated by typical experimental constraints, we assume that the available manipulations are limited to a set of composite pulses constructed from up to four $\pm\pi$ or $\pm\frac{\pi}{2}$-pulses between any of the three transitions with two different phases [Fig. 5.2(a)]. Using a simple linear programming algorithm, we find an explicit decoupling sequence using only 6 pulses $\{P_1, \dots P_6\}$ with equal time durations $\tau_i = T/6$ as depicted in Fig. 5.2(b). More detailed explicit expressions for these pulses are provided in Appendix D. In order to test our sequence, we simulate the dynamics of $N = 6$ spin-1 particles with random interaction strengths $J_{ij} \in [-J, J]$ between every pair. We compute the Floquet unitary $U_T \equiv P_6 e^{-iH_d T/6} P_5 \dots P_1 e^{-iH_d T/6}$ and generate stroboscopic time evolution via $(U_T)^n$ with $n \in \mathbb{Z}$. To benchmark the performance of our decoupling sequence, we introduce the fidelity $\mathcal{F}(nT) \equiv |\mathrm{tr}\left((U_T)^n\right)/D|^2$, where $D = 3^N$ is the dimension of the Hilbert space. Since $\mathcal{F}(t) = 1$ if and only if the evolution corresponds to the identity, the decay of $\mathcal{F}$ serves as a conservative measure of the performance of our interaction decoupling sequence.

Figure 5.2(c) depicts $\mathcal{F}(t)$ for various values of T, demonstrating that the evolution remains trivial up to $\sim 10/J$ for $JT < 1$. Once a given decoupling sequence is found, one can always symmetrize it to further suppress the leading order correction in Magnus expansion (see Appendix D). In our case, such a sequence involves 10 pulses within the period $2T$. As shown in Fig. 5.2(c), the symmetrized sequence significantly suppresses the interaction for timescales up to $\sim 100/J$.

Engineering SPT Hamiltonians.—As a second example, we show that a spin-1 chain with nearest neighbor Ising interactions can be directly mapped to a family of SPT Hamiltonians (see Appendix D). More specifically, given a basic Ising interaction $H_I = \sum_i S_i^z S_{i+1}^z$,

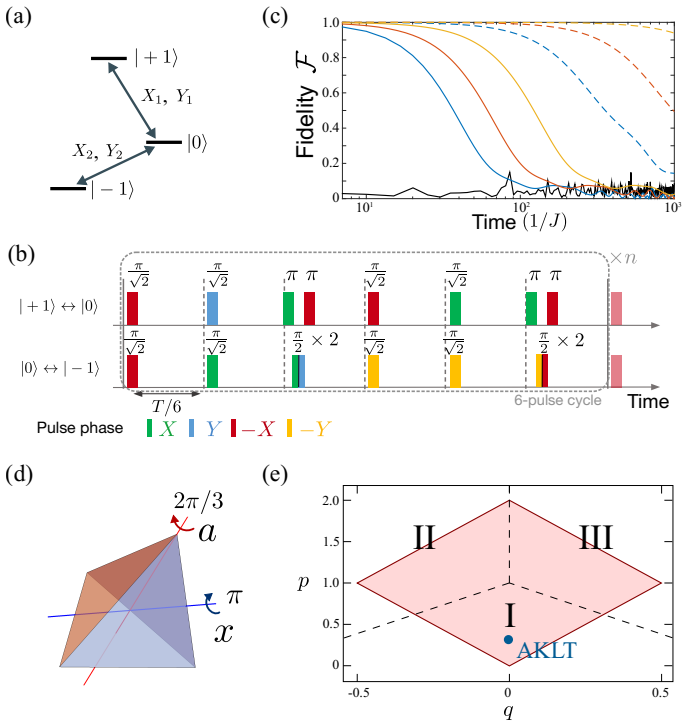

Figure 5.2: **(a)** Level diagram for an anharmonic three level system. **(b)** Decoupling sequence for spin-1 dipolar interactions. Pulse durations are indicated by rotation angles, and phase choices are color-coded. **(c)** Numerical simulations of decoupling dipolar interactions among $N = 6$ spin-1 particles. Black solid line indicates $\mathcal{F}(t)$ in the absence of pulse sequence. Blue, red, and yellow solid lines correspond to $\mathcal{F}(t)$ under a decoupling sequence with $1/JT = 3, 5, 10$, respectively. Dashed lines are for symmetrized sequences. **(d)** Two generators $\{a, x\}$ of the symmetry group A_4. **(e)** Phase diagram. Three SPT phases (I, II, and III) are distinguished by the transformation of ground state wavefunctions under the action of $a \in A_4$. The colored area indicates the domain of (p, q) that can be engineered from Ising interactions. Blue dot indicates the AKLT point $(p, q) = (1/3, 0)$.

one can engineer a two-parameter family of Hamiltonians $H(p, q) = H_1 + pH_2 + qH_3$ with

$$H_1 = \sum_i \vec{S}_i \cdot \vec{S}_{i+1}, \quad H_2 = \sum_i (\vec{S}_i \cdot \vec{S}_{i+1})^2,$$

$$H_3 = \sum_i \sum_{(a,b,c)\in S_3} (S_i^a S_i^b S_{i+1}^c + S_i^a S_{i+1}^b S_{i+1}^c),$$

where $p, q \in \mathbb{R}$, $\vec{S}_i = (S_i^x, S_i^y, S_i^z)$ is the spin-1 vector operator, and $\sum_{(a,b,c)\in S_3}$ indicates the

summation over all permutations of (x, y, z). The symmetries of the Hamiltonian include lattice translation, the bond-centered inversion, and a global internal symmetry A_4, which is the symmetry group of a tetrahedron [see Fig. 5.2(d)]. All possible SPT phases protected by these symmetries are explicitly enumerated in Ref. [147].

When $p = 1/3$ and $q = 0$, the Hamiltonian reduces to celebrated Affleck-Kennedy-Lieb-Tasaki (AKLT) model, whose ground state is exactly solvable and exhibits non-trivial topological edge degrees of freedom [148]. As (p, q) deviates from this solvable point, phase transitions arise among three distinct regions, I, II, and III, as indicated in the numerically obtained phase diagram in Fig. 5.2(e) (see Appendix D). The ground states in the three phases respect all the symmetries while they are distinguished by the complex $U(1)$ phase that the state picks upon a 120° rotation $a \in A_4$ of underlying spins (see Appendix D). Using our algorithm, we find that $H(p, q)$ with $2|q| \leq p \leq 2-2|q|$ can be engineered from H_I [Fig. 5.2(e)]. The strength of $H(p, q)$ is set to $1/(3 + p)$ by isotropic components, and the range of (p, q) is limited by the maximum possible strength of the engineered anisotropic components (see Appendix D).

5.3 Discussions and outlook

We now consider the dominant operational imperfections which may arise during our protocol. First, our periodic driving pulses may cause heating in the many-body system, eventually leading to a featureless infinite temperature state [149, 150, 151]. As discussed earlier, it has been shown that such energy absorption is irrelevant until exponentially long times $t^* \sim \exp[O(1/\bar{J}T)]$, where $\bar{J} \equiv \max_{i,j} J_{ij}||h_{ij}||$. A second natural concern is that our method is based upon engineering the low order Magnus Hamiltonian $H_{\text{eff}}^{(0)}$, which

provides only an approximate description of the full many-body dynamics. However, for gapped Hamiltonians, higher order terms are strongly suppressed so long as $\bar{J}T \ll 1$, and the phase should remain stable. Third, in the presence of weak coupling to a bath, our protocol can enhance qudit sensitivity to external noise at harmonics of $1/T$ [116, 98, 120]. However, this extra sensitivity can be mitigated if the control pulses are significantly faster than the bandwidth of noise spectrum. In a similar vein, the limited strength of control pulses also imposes additional practical constraints for any experimental implementation; in certain cases, further numerical optimization may help to solve these practical issues [115, 117, 119].

Interestingly, the decoupling of interactions may result in dynamical quantum phase transitions for isolated, weakly disordered systems [152]. In such cases, the interplay of weak disorder, suppressed interactions, and an exponentially slow heating rate can lead to many-body localization, where initial state memories survive for extremely long times. Harnessing these effects may enable the coherent manipulation and storage of quantum information in an interacting many-body system [40, 41].

Chapter 6

Quantum Control of Many-body Localized States

We propose and analyze a new approach to the coherent control and manipulation of quantum degrees of freedom in disordered, interacting systems in the many-body localized phase. Our approach leverages a number of unique features of many-body localization: a lack of thermalization, a locally gapped spectrum, and slow dephasing. Using the technique of quantum phase estimation, we demonstrate a protocol that enables the local preparation of the many body system into an effective eigenstate. This leads to the ability to encode information and control interactions without full microscopic knowledge of the underlying Hamiltonian. Finally, we analyze the effects of weak coupling to an external bath and provide an estimate for the fidelity of our protocol.

6.1 Introduction

The coherent control and manipulation of a complex quantum system is one of the central challenges of modern physics. The majority of ongoing research focuses on building up this complexity starting from individual, isolated qubits [153, 154, 155, 156, 157, 158, 159]. In contrast, the opposite approach, where one seeks the coherent manipulation of a strongly interacting system, especially subject to disorder, is generally thought to be intractable. The main difficulty is the exponentially growing Hilbert space with a typical many-body eigenstate strongly coupled to a dense set of other states. Even when the structure of relevant eigenstates is known, their many-body character generally makes them difficult to manipulate using most experimental controls.

Here, we explore an alternate approach toward the coherent control of many-body systems. Our approach follows a new paradigm introduced by recent studies of many-body localization (MBL) [5, 78, 12, 160, 13, 161, 162, 163, 164, 165, 166, 167, 168, 169, 170, 171, 172, 173, 174, 175, 176, 19, 177, 178, 179]. In the presence of strong disorder, the many-body eigenstates of an isolated, interacting system can be localized in Fock space [161]. These MBL eigenstates exhibit a discrete local spectral response, suggesting that one can coherently manipulate and store quantum information (using external controls with both finite spatial and spectral resolution) [169, 172, 170]. This is remarkable because it implies that, in the presence of sufficiently strong disorder, local quantum bits naturally emerge from a strongly interacting many-body system [173, 170].

Further, in the MBL phase, these emergent qubits interact with one another via diagonal (i.e., dephasing) interactions; for two qubits separated by a distance d, this interaction time scales as $\sim \tau \exp(d/\xi)$, where τ is a characteristic timescale and ξ is the localization

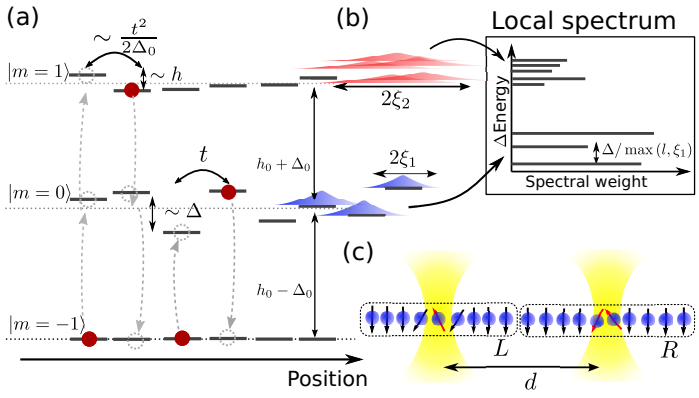

Figure 6.1: (a) Schematic energy spectrum of the disordered spin-1 model. (b) A discrete local spectrum with excitations exhibiting different localization lengths. (c) External electromagnetic driving (yellow beam) defines the location of an MBL qubit.

length [168, 164]. In this respect, the MBL phase differs crucially from, e.g., a conventional Anderson insulator, in which such interactions are absent [5, 162, 180]. This weak interaction brings about two implications for quantum control: (i) the coherence time of a single MBL qubit can be extremely long and (ii) dephasing can be leveraged as a way to coherently couple spatially separated MBL qubits [164]. Unfortunately, in general, the parametric dependence of both the coherence and dephasing times are identical. To make use of many-body localization as a platform for quantum control, one must devise a method to implement interactions (e.g. two-qubit quantum gates) on much shorter timescales than the decoherence.

6.2 Quantum control protocol

Our approach relies upon three key ingredients. First, the local spectral gap of the MBL phase enables one to encode and manipulate quantum information using controls of both finite spatial and spectral resolution. Second, we demonstrate the ability to enhance inter-

actions between MBL qubits by exploiting variations in the localization length of different eigenstates. Finally, we utilize quantum phase estimation and projective measurements to locally prepare the system in a many-body eigenstate ensuring that the interactions between spatially separated MBL qubits is coherent. In contrast to previous work [176], our approach uses the intrinsic dephasing interactions of the MBL phase as a resource to purify the system. The combination of these ingredients can in principle, form the basis for a many-body localized quantum information processor. We find that such an approach can achieve a fidelity that asymptotically approaches the conventional method using isolated qubits. Perhaps more significantly, the local encoding of information provides new routes for studying and quantifying dynamics in the MBL phase. For example, one can imagine directly probing the decay of both the classical and quantum information, extracting the characteristic decay length for each, thereby gaining new insights into the nature of MBL systems.

Spin-1 model—To illustrate the key idea of our approach, we start with a simple model Hamiltonian that clearly exhibits two separate localization lengths. We will utilize excitations with a short localization length ("qubit" excitation) to encode information; meanwhile, to implement gates, we envision off-resonantly coupling such qubit excitations to a more delocalized excitation ("bus" excitation), thereby enhancing interactions on demand [156]. This idea is analogous to the quantum information processing using trapped ions, where the interaction between ions (qubits) are mediated by phonon (bus) modes.

Consider a chain of spin-1 particles with Hamiltonian,

$$H = \sum_{i=1}^{N} h_i S_i^z + \Delta_i \left(S_i^z\right)^2 + 2t\vec{S}_i \cdot \vec{S}_{i+1} \tag{6.1}$$

where N is the total number of sites (Fig. 1a). Disorder exists in both the magnetic field

strength h_i and the single spin anisotropy Δ_i, which are randomly drawn from uniform distributions $[h_0 - h, h_0 + h]$ and $[\Delta_0 - \Delta, \Delta_0 + \Delta]$, respectively. As the Hamiltonian conserves total z-magnetization, $\sum_i S_{\mathrm{i}}^z$, we can define a logical ground state $|G\rangle$ as the eigenstate with all spins in $|S_i^z = -1\rangle$. We focus on the regime in which the field disorder is much weaker than the anisotropy disorder, with a hierarchy,

$$t \ll h\Delta_0/\Delta \ll \Delta \ll \Delta_0 \lesssim h_0. \tag{6.2}$$

In this limit, there are two types of well-defined single-particle excitations. The first (qubit-type) consists of a single spin flipped into the $|S_i^z = 0\rangle$ state. This excitation moves in a disorder potential of strength Δ, analogous to Anderson localization [5]. As such, all single-particle states are localized and in the limit $t \ll \Delta$, the typical localization length of an excitation is given by $\xi_1^{-1} \sim \log \Delta/t$. The second single-particle excitation (bus-type) consists of a single spin flipped into the $|S_i^z = +1\rangle$ state; it can be regarded as a bound state of two qubit-type excitations, with binding energy $\sim \Delta_0$ (Fig. 1a). A bus excitation propagates via a second-order hopping process of amplitude $\sim t^2/(2\Delta_0)$. It, too, can be regarded as a localized single-particle excitation, with localization length, $\xi_2^{-1} \sim \log(h\Delta_0/t^2) = \xi_1^{-1} - \log[t\Delta/(h\Delta_0)]$. Under the hierarchy of equation (6.2), $\xi_2 \gg \xi_1$ (Fig. 1b).

We now turn to the case of multiple excitations. For sufficiently small t or sufficiently low energy densities, the many-body eigenstates of this system are expected to exhibit many-body localization. The effective interaction between two excitations in the MBL phase falls off exponentially with distance; in the limit of low energy density, it is simply given by the overlap of their wavefunctions. Thus, for two qubit-type excitations a distance

d from one another, the interaction strength is

$$\delta_I \sim t \exp(-d/\xi_1), \tag{6.3}$$

while for two bus-type excitations, the interactions scale as $\sim t \exp(-d/\xi_2)$.

Single qubit encoding and manipulation—In order to encode N_q qubits, we partition a given disordered system of size L into $N_q = L/d$ smaller segments of length $d > \xi_2 \gg \xi_1$. We select a single qubit-type excitation centered near the middle of each segment, and use it to encode the state of the MBL qubit (Fig. 1c). An arbitrary superposition of qubit states will dephase on a time scale $1/\delta_I$, and all gate operations must be fast compared to this timescale [168, 164].

The coherent manipulation of a single qubit state is feasible with local external control of finite spatial ℓ and spectral $\delta\omega$ resolution [172]. After initializing the system to the logical ground state $|G\rangle$, one applies a time-dependent electromagnetic field of frequency ω (Fig. 6.1c); to within exponentially small corrections, this transverse field couples $|G\rangle$ with only a finite number $\sim \max(\ell, \xi_1)$ of localized eigenstates, as depicted in Fig. 6.1b.

Thus, one can induce a high-fidelity transition between $|G\rangle$ and a specific eigenstate by weakly driving the system with ω tuned to the particular many-body transition ω_L. The requirements for the spatial and spectral resolution are: (i) $\ell < d$ and (ii) $\delta\omega < \Delta/\max(\ell, \xi_1)$. In this encoding scheme, information readout is performed by directly measuring the local spin polarization. In the limit $\xi_1 \to a$, this corresponds to the measurement of a single spin. When $\xi_1 > a$, the total polarization in the region determines the qubit state.

Two-qubit gates—To perform universal quantum control, we only need to demonstrate a controlled phase gate. As previously mentioned, such a gate can in principle, be achieved via the dephasing interactions of Eq. (6.3). However, since decoherence occurs at the same

rate, one must effectively enhance this interaction strength. Since the dephasing between bus excitations occurs at a much faster rate te^{-d/ξ_2}, the effective interaction strength can be enhanced by several orders of magnitude upon dressing [181] a qubit-type excitation with a bus-type excitation. This enhancement ratio is given by,

$$\frac{\delta_I^{\text{driven}}}{\delta_I} \sim \frac{|\Omega|^2}{|\delta|^2} e^{d\left(\frac{1}{\xi_1}-\frac{1}{\xi_2}\right)} \tag{6.4}$$

where Ω is the Rabi frequency and δ is the detuning of the external driving field. A numerical demonstration of this enhancement in the simplified spin-1 model is provided in Appendix E.

Generic MBL system—We now generalize our protocol from the spin-1 model to any MBL system with a fully localized spectrum [5, 78, 12, 160, 13, 161, 162, 163, 164, 165, 166, 167, 168, 169, 170, 171, 172, 173, 174, 175]. Such systems can be represented in terms of conserved local spin-1/2 degrees of freedom termed "l-bits" [168, 164]:

$$H_{\text{mbl}} = \sum_i \bar{h}_i \tau_i^z + \sum_{i,j} \bar{J}_{ij} \tau_i^z \tau_j^z + \sum_{i,j,k} \bar{K}_{ijk} \tau_i^z \tau_j^z \tau_k^z \cdots \tag{6.5}$$

where the τ_i are spin-1/2 operators describing localized excitations of size $\tilde{\xi}$, $\bar{h}_i$ is the energy of each excitation, $\bar{J}_{ij}$ is the two-body interaction shift, etc. An l-bit overlaps with $\sim \tilde{\xi}$ microscopic degrees of freedom, and can therefore be individually addressed (up to exponentially small infidelities) using a drive with spectral resolution greater than $t/2^{\tilde{\xi}}$. In addition, the l-bits have effective diagonal interactions that also fall off exponentially, with a localization length ξ that varies from site to site and (unlike the l-bit size $\tilde{\xi}$) from eigenstate to eigenstate [168]. All of the qualitative arguments from the spin-1 model extend to the generic case, provided (a) there are excitations that overlap spatially but have

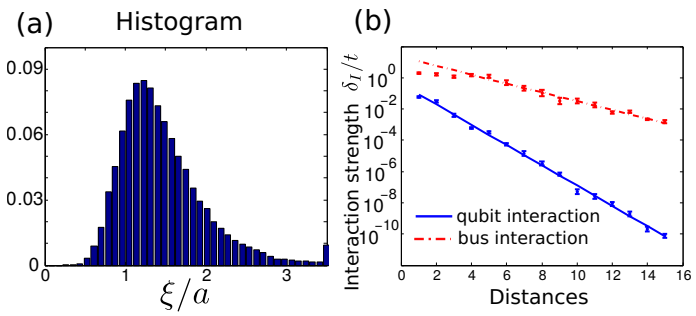

Figure 6.2: Numerical study of localization lengths in the low spin density, weakly localized regime of Eq. (6.6). (a) Histogram of localization lengths in units of lattice spacing. Since the model conserves total S^z, one can choose to work in manifolds with a fixed density of excitations. Here, we consider two spin-flips. (b) Decay of the interaction strength as a function of distance for both qubit and bus excitations.

different localization lengths ξ, and (b) one can initially prepare the system in a particular eigenstate.

To understand the first of these issues, we numerically study the variation of localization lengths for the Hamiltonian,

$$H = \sum_i 2t\vec{S}_i \cdot \vec{S}_{i+1} + h_i S_i^z \tag{6.6}$$

where h_i is randomly drawn from a uniform distribution $[-\Delta, \Delta]$. This model is "generic" in that we have not engineered its localization lengths to have any particular features. In Fig. 6.2a, the histogram of localization lengths ξ is shown for low excitation density (up to two spin-flips) with weak disorder $\Delta/t = 3$ (see Appendix E). The distribution exhibits heavy tails, evincing the fact that there is significant probability to find ξ longer than its average value. It turns out that variations always exist (even at high excitation densities) and are largest near the localization transition (see Appendix E for a quantitative analysis).

We note that our protocol does not require a parametric separation between long and short localization lengths; rather, one can optimize d to achieve as large an interaction en-

hancement as desired. To quantify the enhancement of the interaction strength, we numerically extract the localization length of typical qubit and bus excitations. We diagonalize systems up to length $L = 50$ with at most two excitations and perform 100 disorder averages. For each disorder realization, we apriori choose approximate positions for the left and right MBL qubits (at L and R). Starting from the polarized state $|G\rangle$, we identify computational qubits with significant local support around L, R. These basis states are chosen as energy eigenstates that have significant overlap with local excitation operators $\Sigma^{L(R)} = S^x_{L(R)-1} + S^x_{L(R)} + S^x_{L(R)+1}$. In particular, we select states $(\phi^L, \phi^R, \phi^{LR})$, such that $|\langle\phi^L|\Sigma^L|G\rangle|^2, |\langle\phi^R|\Sigma^R|G\rangle|^2, |\langle\phi^{LR}|\Sigma^L\Sigma^R|G\rangle| > 10^{-2}$; moreover, to ensure that the MBL qubits are self-consistently defined, we require $|\langle\phi^{LR}|\Sigma^L|\phi^R\rangle|, |\langle\phi^{LR}|\Sigma^R|\phi^L\rangle| > 10^{-2}$.

This enables us to directly estimate the effective interaction between the MBL qubits from energy eigenvalues, with $\delta_I \equiv E_{LR} - E_L - E_R + E_G$. As the qubit(bus)-type excitation, we select basis states, $(\phi^L, \phi^R, \phi^{LR})$ that exhibit the smallest(largest) interaction strength (see Appendix E). As depicted in Fig. 6.2b, bus-type excitations interact significantly more strongly than qubit-type excitations, enabling multiple quantum gates to be performed within a decoherence window. While this simplified simulation does not account for the dynamical "dressing" of the qubits, the nature of the qualitative enhancement is the same: it comes from intrinsic variations of the many-body localization length (see Appendix E for full numerical simulations).

Initial state preparation—To enable fully coherent evolution, the interactions between MBL qubits must be coherent. This is indeed the case when the system is prepared in a fiducial many-body eigenstate; however, such a preparation is very difficult for a generic (high temperature) system. Since the MBL phase has a simple description in terms of local

conserved quantities, each many-body eigenstate can be labeled by specifying the values (± 1) of all τ spins. The question is then: how can one efficiently prepare the system into a desired τ-spin superposition, starting from an arbitrary many-body state, with only local control over small sub-regions A and B. Let us label the two excitations L and R (in each region) to be our MBL qubits. The effective interaction between these qubits takes the form $\delta_I = J_{LR} + \sum_{k \notin \{A,B\}} K_{LkR}\tau_k + \ldots$ for each τ-spin configuration [168]. Thus, starting from a generic many-body state, the effective interaction varies from eigenstate to eigenstate and cannot enable a coherent quantum gate.

Interestingly, the interaction itself can be used as a resource to purify the entire system of τ-spins; in particular, by observing the interaction strength between the MBL qubits, one can effectively perform a quantum non-demolition measurement of the τ-spin configuration. Such an observation can be done via a modified spin-echo protocol [180], which projects the τ spins onto a set of configurations that have the same δ_I, up to the precision of the measurement.

Specifically, using an adaptive phase estimation algorithm [154, 176, 182], one can repetitively measure the interaction strength, $\delta_I = 2\pi t \sum_{\alpha=1}^{M} s_\alpha 2^{-\alpha}$ (in binary), to a precision set by its smallest significant digit s_M. To measure each digit, s_k, requires a time, $T_k = \frac{2^k}{t}$, yielding a total measurement time,

$$T_{tot} = \sum_{k=1}^{M} T_k = 2\tau_M(1 - 2^{-M}). \tag{6.7}$$

A few observations are in order: (1) this procedure is extremely efficient since the number of measurements M scales logarithmically with the desired precision and (2) the total measurement time T_{tot} is also the time-scale over which the MBL qubits can now be expected to interact coherently. This result implies that one can perform coherent quantum

manipulations in the infinite temperature MBL phase with a preparation overhead scaling only linearly in time.

Imperfections—In what follows, we analyze a variety of realistic imperfections and provide a quantitive estimate for achievable fidelities in a number of experimental systems. In particular, we will consider the effect of finite spatial(ℓ) and spectral($\delta\omega$) resolution, leading to: (1) imperfect initialization, (2) off-resonant excitation, and (3) population loss into nearby modes.

For single qubit gates, the fidelity is given by,

$$\mathcal{F}_1 \simeq 1 - \frac{\ell}{\xi_1}\left(\frac{1}{T_2\mathcal{E}}\right)^2, \tag{6.8}$$

where T_2 characterizes the extrinsic decoherence time and $\mathcal{E}$ represents the local spectral gap. The lack of individual addressability manifests as a ratio of the spatial extent to the qubit localization length ℓ/ξ_1, while off-resonant excitations induce an error $\sim 1/(T_2\mathcal{E})^2$.

Turning to the fidelity for two qubit gates, we note that finite resolutions (spatial and spectral) bring about two consequences, namely, an optimal choice of qubit separation d_{opt} and a renormalized bus localization length $\xi_2 \rightarrow \xi'$ (see Appendix E). The former arises when the decoherence rate begins to dominate the bare interaction strength, while the latter occurs for line-widths larger than the local spectral gap. The physics of this latter case is analogous to coupling a single bound state (qubit excitation) with a multi-particle continuum (bus excitation) of effective mass $m^* \simeq 1/ta^2$, and leads to a renormalized excitation size $\xi' \approx a\sqrt{tT_2}$ [183, 184, 185]. Combining these two effects gives an overall fidelity,

$$\mathcal{F}_2 \sim 1 - (t/\Gamma)^{-1+\xi_1/\xi_2^{eff}}, \tag{6.9}$$

where $\Gamma \simeq \ell^2/tT_2^2a^2 + 1/T_2$ is an effective decoherence rate estimated from Fermi's Golden rule and $\xi_2^{eff} = \xi_2(\xi')$ for spectrally (un)-resolved bus excitations.

Interestingly, these bounds are consistent with traditional quantum information processing schemes based upon isolated qubits. In particular, for $\xi_1, \ell \to a$ and $\xi_2 \to \infty$, one discovers $\mathcal{F}_2^{opt} \simeq 1 - (tT_2)^{-1+\frac{1}{\sqrt{tT_2}}}$. This corresponds to two tightly localized qubits (e.g. atoms or bound states) interacting via a band of delocalized states (e.g. phonons or photons).

Fidelity Estimates—Our protocol applies most readily to quantum optical systems with local addressing. A number of such platforms are promising candidates for realizing many-body localization, including ultracold atoms, dipolar molecules, superconducting qubits, and solid-state spins [20, 186, 125, 187]. In the case of ultracold atoms, a direct implementation of a spin system is feasible via multi-component Fermi- or Bose-Hubbard models. From recent experiments [188, 189, 190], the spatial resolution $\ell \sim a$, the typical superexchange interaction strength $t \sim 10$Hz, and the coherence limited by particle loss $T_2 \sim 3$s are feasible, yielding an overall fidelity $\mathcal{F}_2 \approx 0.92$. Recent progress towards the engineering of large superconducting flux-qubit arrays is particularly intriguing [191, 192]; disorder naturally arises from the fabrication process and full tomography of the couplings within the system is daunting. Thus, the ability to define MBL qubits in a modular fashion is particularly applicable. With recent coherence times [193] $> 10\mu$s, typical interaction strengths ~ 1GHz, and individual flux-qubit control, one finds a fidelity $\mathcal{F}_2 \approx 0.99$. In the case of molecules and solid-state spin impurities, the interactions are long-range and the dominant disorder arises from random bonds. For effectively short-range power-laws, many-body localization persists and the main idea of this work is still

applicable [19, 177, 174, 20].

6.3 Conclusion and outlook

In summary, we have introduced a scheme for the coherent control of local degrees of freedom in the many-body localized phase. Our approach enables encoding quantum information as well as to perform quantum logic between separated MBL qubits. This suggests that in certain cases, strongly disordered, interacting systems may be a resource for quantum information applications. The ability to efficiently prepare (high temperature) many-body eigenstates via local spectroscopy also opens the door to studying coherent dynamics in the MBL phase. By probing the decay of both classical and quantum information, it may be possible to characterize many-body localized states and their dynamics.

Chapter 7

Dynamically Induced Many-body Localization

We show that a quantum phase transition from ergodic to many-body localized (MBL) phases can be induced via periodic pulsed manipulation of spin systems. Such a transition is enabled by the interplay between weak disorder and slow heating rates. Specifically, we demonstrate that the Hamiltonian of a weakly disordered ergodic spin system can be effectively engineered, by using sufficiently fast coherent controls, to yield a stable MBL phase, which in turn completely suppresses the energy absorption from external control field. Our results imply that a broad class of existing many-body systems can be used to probe non-equilibrium phases of matter for a long time, limited only by coupling to external environment.

7.1 Introduction

Pulsed coherent manipulation is an indispensable tool in almost every branch of quantum science and technology. First introduced as spin echo in nuclear magnetic resonance (NMR) experiments [93], a sequence of pulsed controls has proven highly successful in isolating quantum systems from unwanted noise sources. Since then a variety of specialized dynamical decoupling techniques have been developed, ranging from frequency selective decouplings for quantum metrology to complex composite pulses for high fidelity quantum gate operations [94, 98, 99, 194].

Periodic manipulation of a many-body system has been utilized in order to effectively engineer interaction and to probe exotic quantum phases of strongly interacting systems [57, 121, 195, 123, 80, 65, 79, 46, 47, 48, 49]. Indeed, in a number of systems ranging from ultracold atoms, molecules, and, ions to solid-state spin defects, coherent interactions among many particles and time-dependent controls are already being used for quantum simulations of strongly correlated dynamics [125, 133, 17, 18, 53, 128, 196]. Despite its apparent success, this pulsed Hamiltonian engineering approach is generally prone to heating and imprefections. In particular, it has been commonly believed that periodic external controls generically heat up an ergodic many-body system, eventually leading it to infinite temperature, featureless states [150, 149, 151]. Likewise, any imperfections in pulsed manipulations may accumulate over a long time, resulting in uncontrolled dynamics. Therefore, it may seem that the ultimate fate of any driven ergodic system corresponds to featureless, incoherent states.

7.2 Engineered driving and MBL phase transition

Here, we demonstrate that a periodic control field can *induce* a phase transition of an isolated, ergodic system with weak disorder into a stable many-body localized (MBL) phase with completely suppressed energy absorption [58]. In such a case, the system retains the memory of its initial state for asymptotically long time. This is in contrast to previously studied situations where systems under periodic driving ultimately thermalize [150, 149, 151] unless the original system is localized by strong disorder [80, 65, 79]. Our result challenges the ergodicity assumption of statistical physics in a wide range of driven systems, where the presence of weak disorder is often inevitable. It also implies that dynamical decoupling with a finite repetition rate is sufficient for simulating MBL phases in existing experimental platforms for very long times limited only by coupling to external environment.

This seemingly counter-intuitive phase transition can be understood as a consequence of the interplay between weak disorder and parametrically suppressed heating [59, 81, 144, 100]. The key idea is to utilize external driving in order to suppress transport of a system, similar to dynamical localization [197, 198, 199, 200]. The addition of weak disorder can completely suppress the transport and energy absorption, leading to many-body localization. More specifically, we focus on a situation where dynamical decoupling is employed to engineer an effective MBL hamiltonian that is valid for a long but *a priori* finite lifetime t^* without substantial heating. We show that the resulting spectral properties of such a system further suppress energy absorptions, effectively extending t^*. Then, the evolution features completely suppressed heating, ultimately leading to the exact localization. Furthermore, since localization is robust against local perturbation, we find that the dynamically induced

MBL phase remains stable even in the presence of certain systematic experimental imperfections.

In what follows we first focus on a specific many-body spin model Hamiltonian, initially in the ergodic phase, and show that carefully chosen sequences of pulses can localize the system. We prove the existence of MBL transition by using a time-dependent local unitary transformation which maps the dynamics of our model into that of previously studied systems [65]. We also present intuitive analytical arguments illustrating the mechanism of this transition as well as exact numerical simulations with finite size scaling supporting this conclusion. Finally, we generalize our analysis to a broad class of qudit (d-level systems) ensembles with global manipulations.

Model.— We consider a chain of spin-1/2 particles with Heisenberg interactions between nearest neighboring pairs, described by the following Hamiltonian:

$$H_0 = \sum_i h_i S_i^z + \sum_i J \left(S_i^x S_{i+1}^x + S_i^y S_{i+1}^y + S_i^z S_{i+1}^z \right),$$

where S_i^μ ($\mu \in \{x, y, z\}$) is the Pauli spin-1/2 operator for a particle at site i, h_i is a random on-site field uniformly and independently distributed among $[-W, W]$, and J is the interaction strength between nearest neighboring spins. Dynamics governed by Hamiltonian H_0 has been explored in detail [13, 201]. For a fixed value of J the system is ergodic if the disorder strength W is smaller than a critical value W_c. For $W > W_c$, the system exhibits MBL dynamics. Extensive numerical simulations in Ref. [13, 201] suggest that $W_c/J \approx 3.5 \pm 1.0$.

In what follows we focus on $W = J$, which resides deeply in the ergodic phase. However, the dynamics can be many-body localized by periodically applying pulses $P(\theta) = \exp\left[-i \sum_j \theta S_{2j}^z\right]$, which rotate every spin on even sites by an angle θ along the $\hat{z}$ axis. This

conceptually simple sequence resembles a spin echo technique, which isolates the static magnetic field of a single spin from unwanted coupling to the environment. In our case, it is used to suppress spin exchange interactions while preserving on-site potential disorder. Such a suppressed transport by periodic driving is also known as dynamical localization and has been previously studied in both theory and experiments [197, 198, 199, 200]. When this pulse is repeated with period τ, the system undergoes dynamics governed by Floquet unitary [1]:

$$U_F(\theta, \tau) = P(\theta) \exp\left[-iH_0\tau\right]. \tag{7.1}$$

In order to understand the dynamics under Eq. (7.1), we move into the so-called toggling frame [57], where a time-dependent local unitary transformation eliminates $P(\theta)$. As an example, for $\theta = \pi$ we work in the frame that rotates by $P(\pi)$ after each pulse, where the effective Hamiltonian becomes periodic in 2τ [2]. More specifically, the unitary evolution over two cycles can be written as

$$(U_F)^2 = P(\pi)e^{-iH_0\tau}P(\pi)e^{-iH_0\tau} \tag{7.2}$$

$$= \mathcal{T}e^{-i\int_0^{2\tau} H(t)dt}, \tag{7.3}$$

where we introduced a time-*dependent* Hamiltonian $H(t) = H_z + H_\perp(t)$ with

$$H_z = \sum_i h_i S_i^z + \sum_i J S_i^z S_{i+1}^z \tag{7.4}$$

$$H_\perp(t) = \Theta(t) J \sum_i (S_i^x S_{i+1}^x + S_i^y S_{i+1}^y). \tag{7.5}$$

[1] We note that U_F commutes with total magnetization along $\hat{z}$-axis $S^z_{\text{total}} \equiv \sum_i S_i^z$, making it easier to numerically simulate for a relatively large system sizes (up to $N = 16$). Below, we always work in the zero magnetization subspace.

[2] Similarly one can define a toggling frame for any angle $\theta = 2\pi(p/q)$ with integer $p, q \in \mathbb{Z}$ such that $H(t)$ is periodic in $q\tau$.

Here H_z corresponds to the time averaged component of $H(t)$, and $H_\perp$ is the remaining time-dependent component with rectangular envelope function $\Theta(t)$ that is periodic in 2τ: $\Theta(t) = \text{sgn}[\sin(\pi t/\tau)]$.

Since H_z describes a trivially localized phase, our task is reduced to performing the stability analysis of this phase upon the time-dependent driving $H_\perp(t)$. Such a problem has been rigorously analyzed in Ref. [79, 80, 65, 202], where it has been shown that a MBL system remains localized as long as the fundamental frequency ω_0 of the time-dependent perturbation is large compared to perturbation strength J and on-site disorder energy scale h. In our case, $h \sim J$, and the required condition corresponds to a rapid repetition of the pulse sequence with $\omega_0 \equiv \pi/\tau \gg J$. Since moving into the toggling frame only involves a strictly local unitary transformation $P(\theta)$, the localization in this frame also implies the localization in the original basis, which completes the proof that the dynamics under U_F belongs to a MBL phase [58].

In order to clarify the mechanism of the localization, we next present an intuitive picture of dynamically induced localization based on the combination of slow heating rates and spectral response of a typical MBL system. Underlying principles of the analysis are closely related to frameworks introduced in Ref. [151, 59, 81, 65]. We rewrite the envelope function as

$$\Theta(t) = \sum_m \frac{1-(-1)^m}{i\pi m} e^{im\omega_0 t}, \tag{7.6}$$

where m enumerates harmonics of the fundamental frequency. The components of this time-dependent perturbation become relevant only when they resonantly couple two many-body states with energy separation $\Delta E \approx m\omega_0$ for some $m \in \mathbb{Z}$. When $\omega_0 \gg J$ and the perturbations are local, such resonant processes are absent since a rearrangement of a

single spin alone cannot accommodate the absorption of a large energy quantum. Instead, $H_\perp(t)$ affects the dynamics of the system via higher order processes, which renormalize the effective Hamiltonian. These corrections can be perturbatively analyzed with a small parameter J/ω_0, and it has been shown that, for a *generic* quantum many-body system, such perturbation theory is asymptotic with optimal order $k^* \equiv \omega_0/J$ [59, 81, 65]. The physical meaning of k^* is the minimal number of particles that need to cooperatively rearrange in order to absorb or emit one unit of energy quantum from external driving. The perturbative procedure integrates out the processes that affect $k < k^*$ spins, producing an effective Hamiltonian [59, 81, 65]:

$$H_{\text{eff}}(t) = H^*_{\text{eff}} + V^*(t),\ H^*_{\text{eff}} = H_z + \sum_{k=2}^{k^*-1} H^{(k)} \tag{7.7}$$

where H^*_{eff} denotes the static part of the effective Hamiltonian, which includes corrections $H^{(k)}$ up to order $k^* - 1$, and V^* contains all remaining time-dependent AC perturbations that can potentially heat up the system. While V^* now contains $k \geq k^*$ spin processes, the quantum amplitude for rearranging $O(k)$ nearby spins becomes exponentially small in k: $A_k \sim J(J/\omega_0)^{k-1}$. Hence, the dynamics of the system can be approximated by H^*_{eff} for a long but finite time $t^* \sim 1/A_{k^*}$ (see Appendix F).

In our case, the static part of the effective Hamiltonian H^*_{eff} is perturbatively close to H_z, and therefore it remains in the MBL phase for $J \ll \omega_0$. Moreover, owing to this localization of H^*_{eff} the remaining AC corrections given by $V^*(t)$ do not typically lead to resonant energy absorption, indicating that the system fails to heat up. This is in strong contrast to the case where the static part of the effective Hamiltonian describes an ergodic phase – then the AC corrections do lead to resonant processes, and the system eventually heats up to infinite temperature (though at a rate exponentially slow in ω_0) [59, 81, 65].

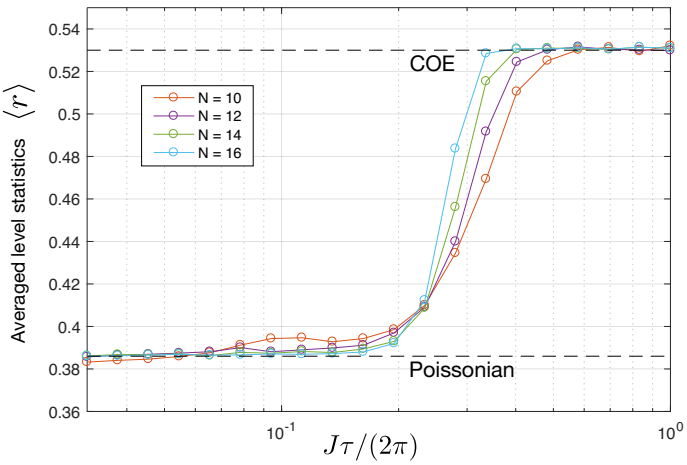

Figure 7.1: Averaged level statistics $\langle r \rangle$ as a function of τ for various system sizes $N = 10$, 12, 14, and 16. Black dotted lines indicate the expected values of $\langle r \rangle$ in two limits: the distribution from circular orthogonal ensemble (top) and Poissonian distributions (bottom). For sufficiently fast pulses $\tau < \tau_c$, the level statistics approaches to the value corresponding to Poissonian distribution, indicating that the system belongs to a MBL phase. The transition becomes sharper as system size increases. Each data point has been averaged over at least 100 disorder realizations

To show that AC corrections are non-resonant, we consider $k > k^*$-th order perturbative process in $V^*(t)$. Due to the locality of H^*_{eff} and $H_\perp(t)$, such a process may rearrange only up to $k + 2\xi$ spins, where ξ is the localization length of H^*_{eff}. Since typical many-body level spacing of k-spin rearrangement scales as $\delta_k \sim \sqrt{k}J/2^k$, the probability of having a resonant k-body process becomes

$$P_k(\text{heating}) \sim \frac{A_k}{\delta_{k+2\xi}} \sim \frac{2^{2\xi+1}}{\sqrt{k+2\xi}} \left(\frac{2J}{\omega_0}\right)^{k-1}, \tag{7.8}$$

which is exponentially small in increasing k for $\omega_0 \gg J$. This indicates that the system fails to heat up and remains in the MBL phase.

Numerical simulations.—In order to corroborate our analytical arguments and check their self-consistency, we performed numerical simulations based on exact diagonalization of unitary evolution U_F for system sizes up to $N = 16$. We extract quasi energy $\epsilon_i \in$

$[-\pi, \pi]$ from eigenvalues of U_F by taking the imaginary parts of their logarithms. We identify the MBL phase transition using a parameter $\langle r \rangle$ which characterizes level statistics of ϵ_i:

$$\langle r \rangle = \left\langle \frac{\min\left(\Delta\epsilon_i, \Delta\epsilon_{i+1}\right)}{\max\left(\Delta\epsilon_i, \Delta\epsilon_{i+1}\right)} \right\rangle, \tag{7.9}$$

where $\Delta\epsilon_i \equiv \epsilon_{i+1} - \epsilon_i$ and the averaging $\langle\cdot\rangle$ is taken over both the entire spectrum and disorder realizations of U_F. If the system belongs to an ergodic phase $\langle r \rangle \approx 0.53$, corresponding to the value for a circular orthogonal ensemble (COE), while if it is in the MBL phase $\langle r \rangle \approx 0.386$, corresponding to the value for the Poisson statistics that lacks level repulsion. We compute $\langle r \rangle$ as a function of τ and θ for varying system sizes $N = 10, \ldots, 16$ as summarized in Fig. 7.1. The value of $\langle r \rangle$ changes between two expected values as a function of τ (in units of $2\pi/J$). As the system size is increased, the transition of $\langle r \rangle$ values becomes sharper, suggesting a quantum phase transition in a thermodynamic limit. We extract a critical point $2\pi/\tau_c \sim 4J$. We note that, at this extracted critical point, the fundamental driving frequency ω_0 is still smaller than the many-body band width $\sim 7J$ of the finite size system ($N = 16$), confirming that our numerics cannot be explained by a trivial finite-size effect.

In order to demonstrate the interacting nature of the MBL phase, we numerically probe the logarithmic growth of entanglement entropy [162, 164]. For a system of size N, we prepare an initial state $|\psi_0\rangle$ with total $N/2$ spin up excitations such that every pair of nearby sites are oppositely polarized:

$$|\psi_0\rangle = \prod_{i=1}^{N/2} \left[\sqrt{2}(S^x_{2i-1} + S^x_{2i})\right] |\downarrow\rangle^{\otimes N}. \tag{7.10}$$

After Floquet time evolution for n cycles, we compute the entanglement entropy $S(n)$

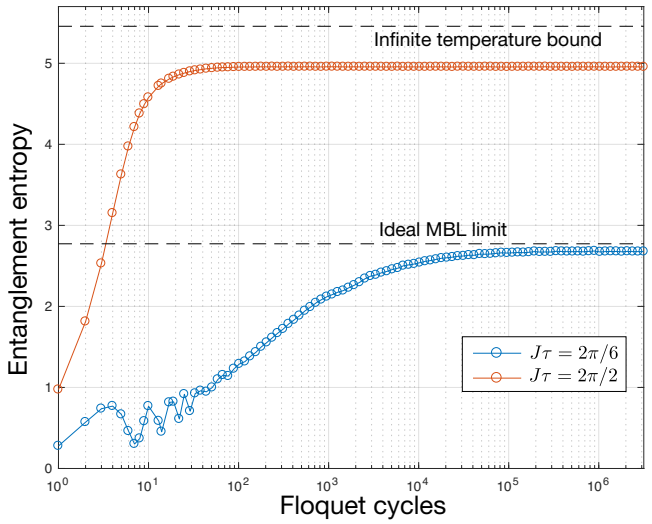

Figure 7.2: Slow growth of entanglement entropy in a system of $N = 16$ particles. For a sufficiently fast pulse sequence with $J\tau = 2\pi/6$ (blue), the entanglement entropy grows only logarithmically in time, while, for a slow pulse sequence with $J\tau = 2\pi/2$ (red), it grows rapidly and saturates. The saturation values are different in two cases since spin excitations cannot propagate in a localized phase. Data has been averaged up to 100 disorder realizations. Two dotted lines indicate theoretical bounds for infinite temperature ensemble (top), in which all microscopic configurations are equally populated, and for an ideal MBL limit (bottom), in which spin excitations are completely localized while they still get entangled via Ising-type interactions.

along the cut at the middle of the system. As illustrated in Fig. 7.2, we find qualitatively distinct behaviors in two cases: a long pulse period ($J\tau = 2\pi/2$) and a short pulse period ($J\tau = 2\pi/6$). In the former case, $S(n)$ quickly saturates to a value that is close to the theoretical bound S_∞ of an infinite temperature ensemble. In the latter case, however, $S(n)$ grows logarithmically over multiple decades and saturates to a value $S_{\rm MBL}$ that is much smaller than S_∞. The difference between the two saturation values originates from the absence of transport in a localized phase, in which case entanglement entropy can only increase via phase correlations [164]. Indeed, $S_{\rm MBL}$ is close to the theoretical prediction corresponding to maximal entanglement entropy achievable from $|\psi_0\rangle$ for completely lo-

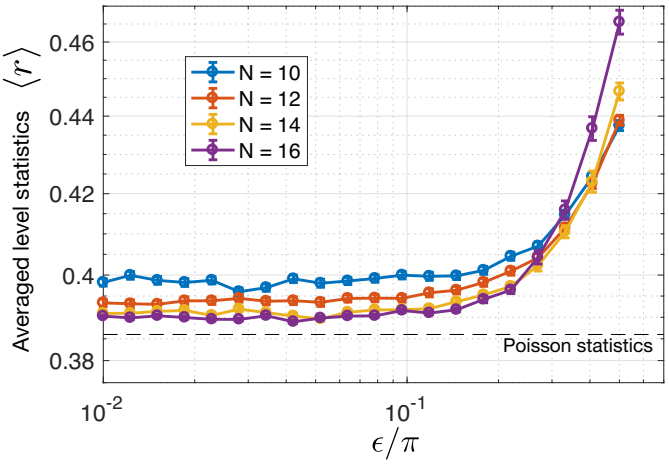

Figure 7.3: Averaged level statistics $\langle r \rangle$ as a function of $\epsilon = \theta - \pi$ for a fixed value $J\tau = 2\pi/5.5$. The finite size scaling suggest that the observed MBL transition is valid for a finite range of θ close to π. Each data point has been averaged over at least 100 disorder realizations.

calized spin excitations but with phase correlations [3]. Once saturated, the entanglement entropy does not grow further even for multiple decades, indicating the absence of slow heating. We also check the robustness of our MBL phase with respect to finite deviation ϵ of the rotation angle θ from π. As demonstrated in Fig. 7.3, we find that the MBL phase is stable over a range of ϵ, in which a dynamical phase transition can be induced by a fast enough pulse sequence.

7.3 Generalization and discussions

Our analysis can be generalized to a variety of quantum systems where global manipulations of spin ensembles are available for dynamical decoupling techniques. Consider,

[3]The theoretical bound in this case can be derived by treating each half of the chain as $N/4$ qubits made out of pairs of spins. The corresponding maximum entropy is given by $N/4 \log(2)$

for example, a WAHUHA sequence that consists of four global spin rotations that are separated by uneven time durations [57]. When the sequence is applied to a chain of dipolar interacting spin-1/2 particles with disordered on-site magnetic field, the time averaged Hamiltonian displays exactly vanishing interactions while the disorder is only reduced by a constant factor, e.g. $h_i S_i^z \mapsto h_i(S_i^x - S_i^y + S_i^z)/3$. Therefore, as long as the total duration of the pulses is sufficiently short, the chain of spin-1/2 particles can be turned to a strict MBL system [37, 19, 20], whose lifetime is only limited by coupling to the environment. Indeed a closely related experiment has been already performed in Ref. [128], where slow development of correlations is observed in an effective one dimensional spin system. More generally, we envision exploiting an ensemble of d-level systems with pair-wise short-range interactions and strong disorder. Such experimental settings are ubiquitous ranging from ultracold atoms, ions, molecules to solid state spin defects or superconducting qubits [125, 133, 17, 18, 53]. One can design a finite k-pulse sequence with time separations τ_k; if the sequence cancels the transport terms of the interactions and preserves weak disorder, one expects that a system can be dynamically induced to a MBL phase. For an ensemble of d-level systems, the conditions for cancellation of interactions have been recently identified in Ref. [35].

7.4 Conclusion and outlook

One intriguing future possibility is to dynamically engineer Hamiltonians of long-range interacting systems [35]. On one hand, such a technique has already been used for observation of stable non-equilibrium states [18] in the so-called critical regime [53, 82], where the ergodicity is only marginally retained via rare long-range resonances. On the other hand,

recent work [203] theoretically showed that the range of interactions can be effectively reduced via time modulated controls. While the scheme presented in Ref. [203] is relevant for short time evolution, the generalization of the scheme for asymptotically long time presents an intriguing avenue for future studies. In combination with the present results, this may open the possibility of studying the interplay between long-range interactions and dimensionality of a system for a MBL phase transition, which still remains as an open question [37, 19, 20].

We have demonstrated that an ergodic interacting system with weak disorder can be transformed into a MBL phase via dynamical decoupling techniques. Our analytical arguments illustrate how the combination of slow heating and weak disorder leads to complete suppression of energy absorption. From a practical perspective, our results provide a theoretical support for using driven systems for studying quantum phase transitions among MBL phases such as paramagnetic MBL to time-crystalline MBL. Our results demonstrate that the non-equilibrium phases created in our approach can be stable against experimental imperfections and that their lifetimes are only limited by coupling to environment. In addition, by tuning the pulse repetition rates, one can study the interplay between disorder and heating of a system.

Chapter 8

Quantum Many-body Scars

Quantum scarring refers to a phenomenon where certain energy eigenstates of a chaotic single-particle system reflect the presence of unstable periodic orbits of the particle in its classical description. Such phenomenon raises important questions regarding our understanding of quantum chaos, since scarred eigenstates constitute counter examples to conventional beliefs in the theory of single-particle quantum chaos such as Berry's conjecture [204]. Here, we extend this phenomenology to quantum many-body chaotic systems. We find that similar unstable periodic trajectories can occur in the semiclassical description of a many-body system. The presence of these orbits affects exact quantum dynamics, leading to atypical behavior such as slow thermalization. As exemplary systems, we focus on constrained spin models, and construct their Feynman path integrals over weakly entangled matrix product states. We show that the associated saddle point trajectories indeed host such special orbits, around which quantum fluctuations are small. Quantum many-body scarring represents a new form of weak ergodicity breaking in a many-body chaotic system.

8.1 Introduction

Quantum chaos is reflected in the ergodic nature of dynamics and energy eigenstates. In single-particle chaotic systems, this is captured by Berry's conjecture [204], which states that every high energy eigenstate locally resembles a random superposition of plane waves sharing the same energy and hence that its probability density is uniformly distributed in position space. A striking departure from this generic behavior is the phenomenon of quantum scarring [205]. An important work of Heller [206] showed that scarring is rooted in the presence of classical unstable periodic orbits — the probability densities of certain eigenstates are enhanced along such trajectories (see Fig. 8.1), which gives rise to observable consequences such as slow relaxation and also dynamical localization. Experimentally, scarring has been observed in microwave cavities, graphene sheets and quantum wells [207, 208, 209, 210].

In many-body systems, quantum chaos plays a fundamental role in our understanding of modern physics as it underpins the foundations of quantum statistical mechanics, and provides an explanation behind the mechanism of thermalization in isolated systems. Exceptions to this paradigm are highly interesting, as they represent deviations from such a universality class of dynamics. Along this front, much progress has been made in recent years: the complete breakdown of ergodicity was shown to occur in strongly disordered systems via many-body localization, which generalizes Anderson localization of single particles to strongly interacting many-body systems. A natural question is therefore whether an ergodicity-breaking mechanism like quantum scarring also exists in the many-body context.

In this chapter, we show that quantum many-body chaotic systems can indeed host a

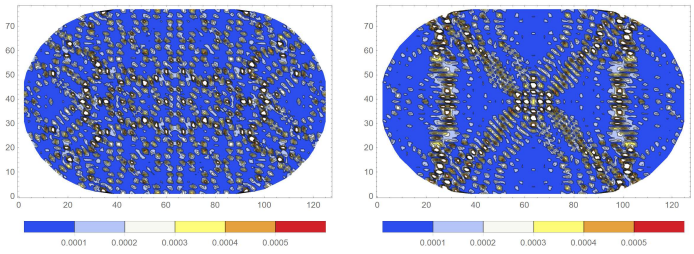

Figure 8.1: Probability densities of certain high energy eigenstates of the chaotic Bunimovich stadium billiard. (Left) A typical, ergodic eigenstate. (Right) A quantum scar. In this case, the eigenstate is clearly concentrated in certain regions of configuration space.

phenomenology similar to single-particle quantum scarring. Concretely, we demonstrate that unstable periodic classical orbits can similarly arise in a Feynman path integral formalism of many-body dynamics and can lead to atypical, nonergodic behavior. As exemplary systems, we focus on constrained, interacting spin models, inspired by a recent experiment on arrays of interacting Rydberg atoms [140]. We construct Feynman path integrals for these systems over matrix product states, and obtain semiclassical, non-linear, chaotic equations of motion from a saddle-point approximation. Remarkably, we find that there exists an isolated, periodic orbit satisfying these chaotic equations of motion. Furthermore, quantum fluctuations about the orbit are small, so that its presence is directly reflected in the exact quantum many-body unitary dynamics. We find that when the system is initialized close to this special trajectory, it undergoes atypically slow thermalization, in which local observables do not relax to their thermal equilibrium values for a long time compared to dynamics resulting from generic initial states. Thus, this strongly motivates the concept of 'quantum many-body scarring', a weak form of ergodicity breaking in an otherwise chaotic, thermalizing system. We note that a connection of the aforementioned experimental system to quantum scarring has already been put forth (and some features explored) by

Turner *et al*. [211]; one of the purposes of this chapter is to put this connection on a firmer footing by providing analysis that is directly analogous to Heller's theory of quantum scars.

8.2 Theory of quantum scars

Before presenting our results on quantum many-body systems, we first briefly review Heller's theory of quantum scars in single-particle chaotic systems [206, 212, 213]. Heller pointed out that the assumption of ergodicity in every high energy eigenstates (c.f. Berry's conjecture [204]) is inconsistent with the dynamical behavior of certain test wavefunctions. More specifically, he considered a test wavefunction of a particle that is initially placed on a classical, unstable periodic trajectory. When the wavefunction is tightly localized in the position-momentum phase space, the time evolution of the particle is well approximated by semiclassical equations of motions, and, after a certain time period T, the wavefunction should return close to its original configuration. In particular, if the Lyapunov exponent λ associated with the orbit is sufficiently small, $\lambda T \ll 1$, the wavepacket of the particle is expected to revive multiple times before eventually being delocalized. Heller showed that the presence of these recurrences imply that the initially localized wavefunction decomposes into energy eigenstates with approximately harmonic energy spacing. In other words, some eigenstates at harmonic energies have atypically large overlap with the localized wavefunction, contrary to Berry's conjecture. For example, Figure 8.1 shows an eigenstate of the Bunimovich stadium, which is concentrated on a 'bouncing ball' orbit and is clearly not uniformly distributed over the entire stadium.

8.3 Theory of quantum many-body scars

As seen from Heller's theory, the presence of weakly unstable ($\lambda T \ll 1$) periodic orbits is central to the phenomenon of quantum scarring. It is, however, not a priori obvious how to extend this concept to the many-body context. One of the challenges is that a quantum many-body system often lacks a straightforward classical limit; many quantum systems, such as interacting spins, often arise as effective descriptions of other models and do not come from direct quantization of a classical system.

8.3.1 Path integral formalism

One of our observations is that, despite this difficulty, a semiclassical description of a many-body system can nevertheless be achieved within the Feynman path integral formalism. More specifically, given a manifold $\mathcal{M}$ of many-body wavefunctions $|\psi(\mathbf{z})\rangle \in \mathcal{M}$ parametrized by a generalized coordinate $\mathbf{z}$, one can compute the quantum transition amplitudes between two states $|\psi(\mathbf{z})\rangle$ and $|\psi(\mathbf{z}')\rangle$ under unitary time evolution from a weighted sum of all possible trajectories:

$$\langle\psi(\mathbf{z}')|e^{-i\hat{H}t}|\psi(\mathbf{z})\rangle = \int \mathcal{D}\mathbf{z} e^{i\int_0^t dt' L(\mathbf{z},\dot{\mathbf{z}})}, \tag{8.1}$$

where $\hat{H}$ is the quantum Hamiltonian, $\mathcal{D}\mathbf{z}$ are path integral measures, and

$$\mathcal{L}(\mathbf{z},\dot{\mathbf{z}}) = i\langle\psi(\mathbf{z})|\partial_{\mathbf{z}}\psi(\mathbf{z})\rangle\dot{\mathbf{z}} - \langle\psi(\mathbf{z})|\hat{H}|\psi(\mathbf{z})\rangle \tag{8.2}$$

is the classical Lagrangian associated with the manifold. Conventionally, the parametrization of wavefunctions is chosen in a way that $|\psi(\mathbf{z})\rangle$ resembles most "classical" states such as product states or coherent states. Importantly, however, a path integral can be constructed

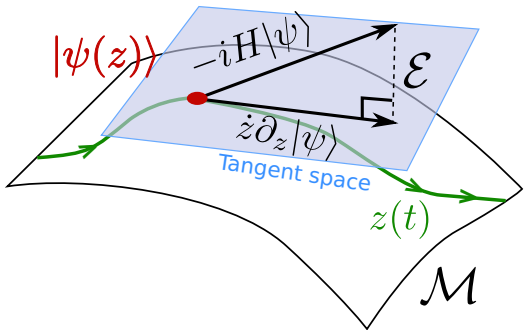

Figure 8.2: Geometric interpretation of the semiclassical equations of motion in the manifold $\mathcal{M}$. The Hamiltonian flow of the phase space coordinate $z(t)$ can be obtained by minimizing the length of the error $\mathcal{E}$.

over any family of states as long as they are dense in the entire Hilbert space and support a well-defined measure for a resolution of the identity. For example, as we will use below, this includes entangled states such as matrix product states, which may yield more insights into physics not captured by a product state manifold.

The saddle point evaluation of a path integral yields semiclassical equations of motion (EOM), which describes a Hamiltonian flow in the phase space $\mathbf{z}$. If the quantum many-body system is chaotic, the resulting semiclassical EOM are generally also chaotic. We note that the same EOM can be derived from the time-dependent variational principle (TDVP), which allows a useful geometric interpretation and provides a method to quantify the deviation of semiclassical solutions from exact many-body quantum evolution [see Fig. (8.2)]. In particular, the instantaneous error $\mathcal{E}$ of the saddle-point trajectory is captured by the component of the vector, $-iH\,|\psi(\mathbf{z})\rangle$, that is perpendicular to the tangent space of the manifold at $\psi(\mathbf{z})$. Unlike in single-particle cases, $\mathcal{E}$ scales with the system size and diverges in the thermodynamic limit. Therefore, we introduce an intensive quantity ϵ by normalizing the error with the size of the system V (either volume or the number of parti-

cles):

$$\epsilon(z) \equiv \frac{1}{\sqrt{V}} \left|\left|\dot{\mathbf{z}}\partial_{\mathbf{z}} \left|\psi(\mathbf{z})\right\rangle + iH \left|\psi(\mathbf{z})\right\rangle\right|\right|, \tag{8.3}$$

where $\mathbf{z}(t)$ has to be evaluated at the solution of the semiclassical EOM. This analysis suggests a natural generalization of Heller's theory of scars to many-body chaotic systems: we identify a quantum many-body scar by the presence of an unstable, periodic solution $\mathbf{z}(t)$ with a small integrated error $\oint \epsilon(\mathbf{z}(t))dt \ll 1$, and its effects on exact quantum many-body dynamics.

8.3.2 Constrained spin model

We turn to explicit examples, where the semiclassical EOM can be analytically evaluated and support unstable, periodic orbits. Our models are inspired by recent experiments on an array of strongly interacting Rydberg atoms, where it has been already demonstrated that the system in a certain initial state undergoes atypically slow thermalization dynamics [140].

We consider a chain of L spin-s particles with $2s + 1$ internal degrees of freedom. The quantum states of each spin are enumerated by $|n\rangle$ with $n \in 0, 1, \ldots, 2s$. The spins are subject to an external magnetic field Ω along the x-direction, which can potentially induce coherent Rabi rotation of spins. In our model, however, nearest neighboring spins strongly interact with one another via so-called blockade constraints which do not allow any neighboring spins to be simultaneously away from $|0\rangle$, i.e. if a spin at site-i is in $|n_i\rangle$ with $n_i \neq 0$, the spins at site-$(i \pm 1)$ have to be in $|0\rangle$. More precisely, our model describes

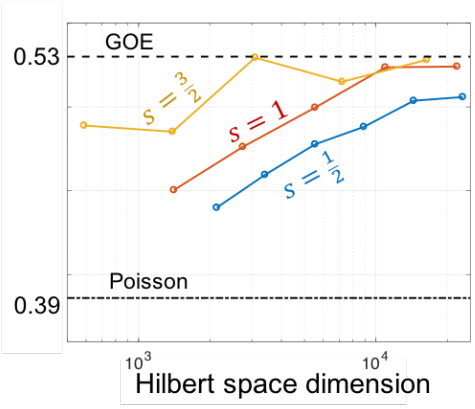

Figure 8.3: Scaling of level spacing statistics $\langle r \rangle$ of the model (8.4). The parameter $\langle r \rangle \equiv \min(\Delta\epsilon_i, \Delta\epsilon_{i+1}) / \max(\Delta\epsilon_i, \Delta\epsilon_{i+1})$ characterizes the degree of level repulsion, where $\Delta\epsilon_i$ is the difference between two consecutive eigenvalues, and the averaging $\langle \cdot \rangle$ is taken over the entire spectrum. In increasing Hilbert space dimension, the statistics $\langle r \rangle$ approaches toward $r_{\text{GOE}} \approx 0.53$, corresponding to that of a random matrix drawn from the gaussian orthogonal ensemble (GOE).

spins under a transverse field in a constrained Hilbert space:

$$\hat{H}_s = \Omega \sum_i \mathcal{P} S_i^x \mathcal{P}, \tag{8.4}$$

where $\mathcal{P} = \prod_i \left(\mathbb{I} - \mathbb{P}_i^{(1)} \mathbb{P}_{i+1}^{(1)} \right)$ is the product of local projectors $\mathbb{P}^{(1)} = 1 - |0\rangle\langle 0|$, describing the constraints, and S_i^x is the conventional spin operator at site-i. The dimension of constrained Hilbert space grows exponentially $\sim d_{\text{eff}}^L$ with a reduced effective local dimension $d_{\text{eff}} = \frac{1+\sqrt{8s+1}}{2}$. The presence of the constraints also renders the system non-integrable and hence quantum chaotic, as seen from level repulsion in the energy eigenvalues in Fig. (8.3). In what follows, we focus on the spin $s = 1/2$ case for concreteness, while similar results can also be obtained for higher spin models, to be reported elsewhere.

Our model exhibits atypical thermalization dynamics when the system is prepared in a special initial state $|\mathbb{Z}_2\rangle \equiv |0101\cdots\rangle$; instead of rapidly relaxing to its thermal equilibrium, the system displays multiple oscillations of spins, toggling between $|\mathbb{Z}_2\rangle$ and its

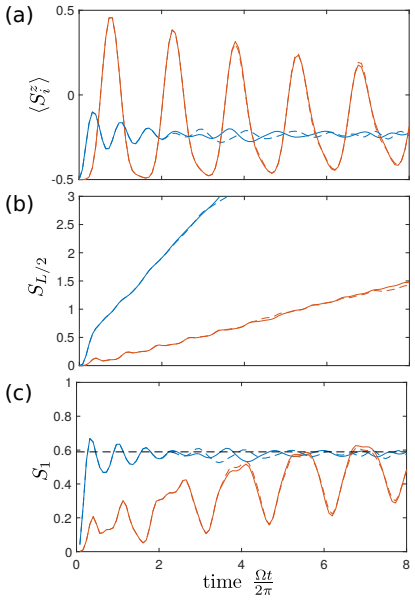

Figure 8.4: Numerical simulations. Blue and red solid lines correspond to simulations results for initial states $|\mathbf{0}\rangle$ and $|\mathbb{Z}_2\rangle$ for $L = 20$, respectively. We also present simulation results for $L = 18$ using dashed lines in order to illustrate finite size effects. (a) The spin polarization $\langle S_i^z(t)\rangle$ oscillates multiple times for the initial state $|\mathbb{Z}_2\rangle$ while it rapidly approaches to a steady state value for $|\mathbf{0}\rangle$. (b) Entanglement entropy grows linearly in both cases, but the growth rate is substantially smaller for the initial state $|\mathbb{Z}_2\rangle$. (c) Entropy of a single spin (at the center of the chain) also displays contrasting behavior. For the special initial state $|\mathbb{Z}_2\rangle$, the spin repeatedly entangles and disentangles with the rest of the system. Black dashed line indicates the saturation value corresponding to the case of an infinite temperature ensemble.

conjugate configuration $|\mathbb{Z}_2'\rangle = |1010\cdots\rangle$. This is in strong contrast to the dynamics of a different initial state $|\mathbf{0}\rangle = |0000\cdots\rangle$ with the same energy density; in this case, local observables indeed quickly approach a steady state value predicted by the eigenstate thermalization hypothesis. Figure 8.4(a) compares the dynamics in these two cases by showing the polarizations $\langle S_i^z\rangle$ as a function of time, obtained from exact numerical simulations of our model up to $L = 20$ spins. The dynamics of entanglement entropy between two half-chains [Fig. 8.4(b)] also demonstrates that two different initial states thermalize at very

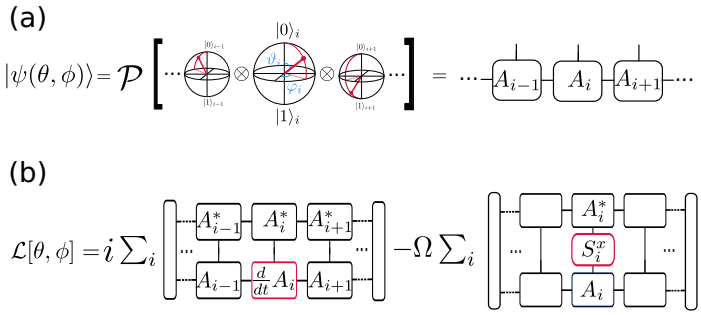

Figure 8.5: (a) MPS representation of states $|\psi(\theta,\phi\rangle$. (b) Construction of the semiclassical Lagrangian in pictorial representations.

different rates. Furthermore, the entropy of a single spin (at the middle of the chain) shows a striking difference: for initial state $|\mathbf{0}\rangle$, the single-spin entropy quickly saturates to the maximum value possible, while in the case of the $|\mathbb{Z}_2\rangle$ state it oscillates, indicating that a single spin repeatedly entangles and then disentangles with the rest of the spins.

In order to explicitly demonstrate the connection between quantum many-body scarring and atypical dynamics associated with the initial state $|\mathbb{Z}_2\rangle$, we construct a Feynman path integral. Crucially, we parametrize the many-body wavefunction in such a way that it always satisfies the blockade constraints:

$$|\psi(\boldsymbol{\vartheta},\boldsymbol{\varphi})\rangle \propto \mathcal{P}\bigotimes_{i=1}^{L}|(\vartheta_i,\varphi_i)\rangle, \tag{8.5}$$

where ϑ_i and φ_i denote two angles in the Bloch sphere for each spin at site-i, and the projection $\mathcal{P}$ ensures that $|\psi\rangle$ satisfies the blockade constraints. Interestingly, the wavefunction in Eq. (8.5) can be conveniently represented in terms of matrix product states (MPS) with bond dimension $D = 2$:

$$|\psi(\boldsymbol{\theta},\boldsymbol{\phi})\rangle = \sum_{\{n_i\}} \mathrm{Tr}\left(A_1^{[n_1]}A_2^{[n_2]}\cdots A_L^{[n_L]}\right)|n_1 n_2,\cdots,n_L\rangle\,, \tag{8.6}$$

where

$$A_i^{[0]} = \begin{pmatrix} \cos(\theta_i/2) & 0 \\ 1 & 0 \end{pmatrix} \quad \& \quad A_i^{[1]} = \begin{pmatrix} 0 & e^{i\phi_i}\sin(\theta_i/2) \\ 0 & 0 \end{pmatrix}, \tag{8.7}$$

and $\boldsymbol{\theta}$ and $\boldsymbol{\phi}$ are (nonlinear) reparametrization of $\boldsymbol{\vartheta}$ and $\boldsymbol{\varphi}$, that originates from the gauge choice of our MPS representation [see Fig. 8.5(a)]. We further note that an appropriate resolution of the identity in the constrained space, $\mathcal{P} = \int d\boldsymbol{\theta} d\boldsymbol{\phi}\, \mu(\boldsymbol{\theta}, \boldsymbol{\phi}) |\psi(\boldsymbol{\theta}, \boldsymbol{\phi})\rangle\langle\psi(\boldsymbol{\theta}, \boldsymbol{\phi})|$ can be written down in these new set of variables, which is essential for the construction of the path integral. The corresponding Lagrangian $\mathcal{L}(\boldsymbol{\theta}, \boldsymbol{\phi}, \dot{\boldsymbol{\theta}}, \dot{\boldsymbol{\phi}})$ [cf. Eq. (8.2)] can be analytically obtained by evaluating diagrams in Fig. 8.5(b). In the thermodynamic limit, one finds

$$\mathcal{L} = \sum_i K_i(\boldsymbol{\theta}) \left(\sin^2(\theta_i/2)\dot{\phi}_i + \Omega \cos(\theta_{i+1}/2)\sin(\theta_i)\cos(\phi_i/2) \right)$$

$$K_i(\boldsymbol{\theta}) = g(\theta_i) + \sum_{j \neq i} (g(\theta_j) - g(\theta_{j+1})) \prod_{n=j+1}^{i-1} (-\sin^2(\theta_n/2))$$

where $g(\theta) = 1/(\sin^2(\theta/2) + 1)$. From $\mathcal{L}$, one can also derive $2L$ coupled, non-linear Euler-Lagrange equations describing the semiclassical dynamics of this system.

Here, one crucial point is that these EOM support isolated, unstable, periodic orbits. To see this, we first note that the variables ϕ_i do not evolve for initial states with $\phi_i = \pi/2$. Second, for initial states exhibiting a two-site translational symmetry $\theta_i = \theta_{i+2}$ (as in the case of our special initial state $|\mathbb{Z}_2\rangle$), the equations of motion become significantly simplified to coupled equations for two variables θ_e and θ_o at even and odd sites. They are given by $\dot{\theta}_\mathrm{e} = f(\theta_\mathrm{e}, \theta_\mathrm{o})$ and $\dot{\theta}_\mathrm{o} = f(\theta_\mathrm{o}, \theta_\mathrm{e})$, with

$$f(x, y) = \Omega \left(\sin(x/2)\cos^2(x/2)\tan(y/2) + \cos(y/2) \right). \tag{8.8}$$

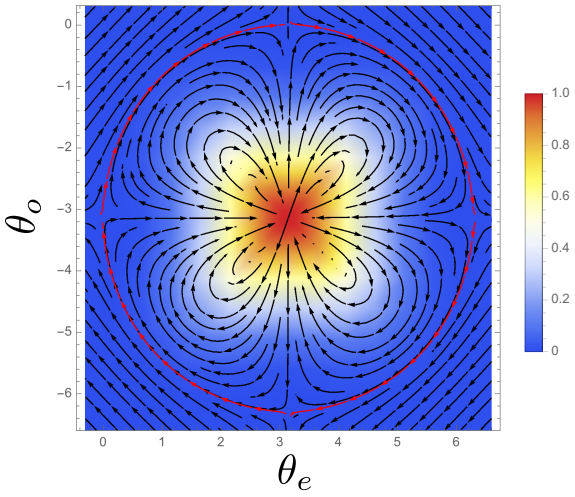

Figure 8.6: Flow diagram of Eq. (8.8). We find an isolated unstable, periodic orbit (red arrows), along which the $|\mathbb{Z}_2\rangle$ state $(\pi, 0)$ and its conjugate configuration $|\mathbb{Z}_2'\rangle$ state $(0, -\pi)$ reside. Additionally, fluctuations about the orbit, as measured by ϵ, are relatively small, indicating that exact quantum unitary evolution also approximately follows this trajectory.

Figure 8.6 shows the flow diagram of Eq. (8.8), clearly demonstrating the presence of an isolated periodic trajectory. In particular, we note that the orbit includes the points $(\theta_e, \theta_o) = (\pi, 0)$, and $(\theta_e, \theta_o) = (0, -\pi)$ corresponding to the state $|\mathbb{Z}_2\rangle$ and its conjugate configuration $|\mathbb{Z}_2'\rangle$ [1]. Thus, in essence, within the semiclassical equations of motion, the system is following a trajectory in $\mathcal{M}$ along which the state oscillates between $|\mathbb{Z}_2\rangle$ and $|\mathbb{Z}_2'\rangle$. Numerical integration of the Euler-Lagrange equations above gives the period of these oscillations, $\Omega T \approx 1.51$, matching the one observed in exact quantum simulations of finite size systems, which is a strong indicator that the dominant contribution to the exact quantum dynamics is indeed due to the semi-classical path. To quantify this, we calculate the local error ϵ as defined above and indicate it as a color scale in Fig. 8.6.

[1] Note that due to the parametrization, $(\theta_e, \theta_o) = (\pi, 0)$ corresponds to the same state as $(\theta_e, \theta_o) = (\pi, -2\pi)$. The singularity at these points is irrelevant and arises simply because the tangent space there does not have the full dimensionality.

Indeed one can see that ϵ remains small along the entire periodic trajectory. In contrast, the initial state $|\mathbf{0}\rangle$, corresponding to $(\theta_e, \theta_o) = (0, 0)$, lies on a trajectory that terminates in a saddle point (Fig. 8.6). There, $\epsilon/\Omega \to 1$ indicates that dynamics on $\mathcal{M}$ cannot approximate the exact quantum dynamics well. This is indeed the generically expected behavior for a thermalizing system, since the associated entanglement growth cannot be captured within the low bond dimension MPS manifold $\mathcal{M}$ considered here.

8.4 Discussion

In this section, we demonstrated that quantum scarring can also occur in chaotic quantum many-body systems. We utilized Feynman path integral formalism in order to derive semiclassical equations of motion and showed that an unstable periodic orbit may arise in such description. The presence of the special trajectory affects the exact quantum many-body dynamics, leading to unusually slow thermalization dynamics as demonstrated in our exemplary model.

While the analysis in this chapter clearly draws parallels between Heller's theory of quantum scars and our generalization using Feynman path integral, it also raises a few important questions. In single particle cases, the Lyapunov exponent λ for a periodic orbit can be well defined and needs to be small $\lambda T \ll 1$ for strong quantum scarring. While analogous exponents can be in principle obtained for many-body systems using semiclassical EOM, such quantities scale extensively and diverge in the thermodynamic limit. Here, we introduced an intensive measure ϵ in order to quantify the deviation of the semiclassical solution from exact quantum evolution. This difference implies a conceptual distinction between single particle and many-body scarring: while the former can be manifested in

energy eigenstates disobeying Berry's conjecture, the latter is characterized by dynamics of local observables rather than the global eigenstate structure. It remains as future studies to investigate how quantum many-body scarring affects matrix elements of local observables in the energy eigenbasis in comparison to the prediction of eigenstate thermalization hypothesis.

Another intriguing possibility is the connection between quantum many-body scarring and exotic nonequilibrium phases of matter in strongly disordered systems such as many-body localization and discrete time crystals introduced in Chapters 2, 3, 6, and 7. In particular, we have seen that the physics behind the stable, persistent sub-harmonic oscillation in discrete time-crystalline (DTC) phase can be understood as the existence of closed trajectories in a semiclassical description of the system [see Fig. 3.3(d)]. The application of the formalism developed in this chapter to systems exhibiting DTC order may provide new insight towards the unconventional out-of-equilibrium dynamics.

Chapter 9

Symmetry-Protected Dissipative Preparation of Matrix Product States

We propose and analyze a method for efficient dissipative preparation of matrix product states that exploits their symmetry properties. Specifically, we construct an explicit protocol that makes use of driven-dissipative dynamics to prepare a many-body quantum state that features symmetry-protected topological order and non-trivial edge excitations. The preparation protocol is protected from errors that respect the symmetry, allowing for robust experimental implementation without fine-tuned control. Numerical simulations show that the preparation time scales polynomially in system size n. Furthermore, we demonstrate that this scaling can be improved to $\mathcal{O}(\log^2 n)$ by using parallel preparation of individual segments and fusing them via quantum feedback. A concrete scheme using excitation of trapped neutral atoms into Rydberg state via Electromagnetically Induced Transparency is proposed, and generalizations to a broader class of matrix product states are discussed.

9.1 Introduction

Entangled many-body states play a central role in understanding strongly correlated quantum matter and constitute the key resource for quantum information science. Matrix product states (MPS) [214] form an important class of many-body entangled states that can describe a variety of one dimensional quantum systems, including those featuring symmetry-protected topological (SPT) order [215]. Such states can be prepared either through a sequence of unitary quantum gate operations, or by first engineering the parent Hamiltonian and subsequently preparing its ground state via adiabatic evolution or cooling [91, 216, 217, 218, 219, 125, 220]. However, generating entanglement among many particles using these approaches is challenging, as it typically requires high-fidelity control of individual interactions while maintaining low entropy for intrinsically out-of-equilibrium systems. In particular, unavoidable coupling to environment limits the lifetime of these states and hinders their potential applications.

9.2 Dissipative state preparation

Here we propose and analyze an alternative method involving efficient dissipative preparation of matrix product states by coupling to environment so that the desired state is obtained as the unique steady state of time evolution. While such approaches to prepare entangled states have been described previously [221, 222, 223, 224, 225, 226, 227, 228, 229, 230] and can potentially outperform corresponding unitary schemes [231], their implementations in many-body systems are challenging as they require engineering of complex interactions with environment. Here, we show how symmetries can be used to design a

simple, translation-invariant dissipative process that only requires a single decay channel and global manipulations to create a desired MPS. Similar to symmetry-protected equilibrium phases, this dissipative dynamics can be protected from imperfections that respect the symmetry, allowing for experimental realizations in large systems with current technologies.

As a specific example, we describe a scheme to deterministically prepare a chain of spin-1 particles into the ground states of a gapped, frustration-free Hamiltonian

$$H_{\text{AKLT}} = \sum_i [\vec{S}_i \cdot \vec{S}_{i+1} + \frac{1}{3}(\vec{S}_i \cdot \vec{S}_{i+1})^2], \tag{9.1}$$

where $\vec{S}_i$ is the spin-1 vector operator acting on a particle at site i. First studied by Affleck, Kennedy, Lieb, and Tasaki (AKLT), the ground states of H_{AKLT} are examples of MPS and model states for the Haldane phase [148, 232, 233]. While under periodic boundary condition, H_{AKLT} has a unique ground state; under open boundary condition, the ground states are 4-fold degenerate due to two fractionalized degrees of freedom on the edges. These constitute a signature of topological order, which can be experimentally verified by measuring a non-local string order parameter [234, 235].

Our approach makes use of $\mathrm{SO}(3)$ symmetry of the parent Hamiltonian H_{AKLT} for preparation of an exact AKLT ground state. By converting energy penalties imposed by H_{AKLT} into dissipative penalties in the form of decay channels, we can engineer a process that effectively cools to the ground states. More specifically, we start with a dissipative dynamics that eliminates one type of excitations in H_{AKLT}. Then, all other types of excitations can be eliminated using global spin-rotations. Since spin-rotations are symmetries of H_{AKLT}, their implementations are robust against imperfections in control parameters such as durations, phases, or strengths of electromagnetic driving. Using numerical simulations,

we find the state-preparation time scales polynomially with system size n. We further show how this scaling can be improved to $\mathcal{O}(\log^2 n)$ by first preparing multiple spin chains in parallel and then connecting them via repeated measurements with feedback. This corresponds to an exponential improvement over previously known scaling $\mathcal{O}(n^{\log n})$ for injective MPS [222]. We also describe an example implementation of our protocol in a system of trapped neutral atoms [236, 237, 140, 138, 140, 238] using Rydberg-EIT mechanism [239]. Our strategy generalizes to a broader class of MPS, including the ground states of all one-dimensional SPT phases.

Dissipative dynamics.— We consider a Markovian driven-dissipative dynamics described by a quantum master equation: $\dot{\rho} = \mathcal{L}\rho \equiv -i[H,\rho] + \sum_\mu \Gamma_\mu \mathcal{D}[c_\mu]\rho$, where ρ is density operator of a system, H is a Hamiltonian governing coherent dynamics, and $\mathcal{D}[c_\mu]\rho \equiv c_\mu \rho c_\mu^\dagger - \{c_\mu^\dagger c_\mu, \rho\}/2$ characterizes incoherent dynamics by jump operators c_μ at rate Γ_μ. We can interpret the dynamics of $\mathcal{L}$ as the system evolving with a non-Hermitian Hamiltonian $H_{\text{eff}} = H - i\sum_\mu \Gamma_\mu c_\mu^\dagger c_\mu/2$, while stochastically undergoing quantum jumps $\rho \mapsto c_\mu \rho c_\mu^\dagger$ at rates $\text{tr}\,([]\,\Gamma_\mu c_\mu^\dagger c_\mu \rho]$ for each jump operator [240].

Our construction of $\mathcal{L}$ exploits the $\mathrm{SO}(3)$ symmetry that conserves total angular momentum. In particular, each term in H_{AKLT} can be written as $2P_i - 2/3$, where P_i is the projection operator onto the subspace of total angular momentum $J_i = S_i + S_{i+1} = 2$ for the pair of particles $(i, i+1)$. Hence, a state $|G\rangle$ minimizes the energy if it has no population in the $J_i = 2$ manifold, i.e. $P_i |G\rangle = 0$ for every nearest-neighboring pair. Under open boundary condition, there are four such states $|G_{ab}\rangle$, labelled by two spin-1/2 edge degrees of freedom $a, b \in \{\uparrow, \downarrow\}$. Under periodic boundary condition, only a unique state $|G_\circ\rangle \propto |G_{\uparrow\uparrow}\rangle + |G_{\downarrow\downarrow}\rangle$ satisfies the constraints (see Appendix G). Below, we use $|G\rangle$ to

denote the ground state(s) when boundary conditions are not specified.

To prepare $|G\rangle$, we use jump operators to depopulate $J_i = 2$ manifold of every neighboring pair. For example, we can set $H = 0$ and use five types of jump operators, $c_m^{(i)} = |\phi_m\rangle\langle J = 2, J^z = m|_{i,i+1}$, where $\{|J = 2, J^z = m\rangle_{i,i+1} : m = -2, \ldots, 2\}$ is an orthonormal basis spanning the $J_i = 2$ manifold for the pair $(i, i+1)$, and $|\phi_m\rangle$ is any other quantum state with non-zero population in $J_i = 0, 1$ manifolds ($\langle\phi_m| P_i |\phi_m\rangle < 1$). With these jump operators, quantum jumps occur at rate $\Gamma_{\text{total}} = \Gamma \sum_{i,m} \text{tr}\left(\rho c_m^{(i)\dagger} c_m^{(i)}\right) = \Gamma \sum_i \text{tr}\,(\rho P_i)$, which vanishes only for ground state $|G\rangle$. This implies $|G\rangle$ is a steady state of $\mathcal{L}$, and any other quantum state will undergo a series of quantum jumps.

Using $\mathrm{SO}(3)$ symmetry, this construction can be effectively realized with only one type of jump operator via global coherent manipulations H. More specifically, let us consider a dynamics with only one jump operator, $c_2 = |00\rangle\langle J{=}2, J^z{=}2| = |00\rangle\langle{+}{+}|$, written in the S^z basis $\{|+\rangle, |0\rangle, |-\rangle\}$. After time evolution over duration $\tau/5$, we apply a fast global pulse $V = \exp[i(2\pi/5)\sum_i S_i^y]$, rotating the entire spin ensemble by an angle $2\pi/5$ about the y-axis. In a rotating frame, this operation implements the jump operator $V^\dagger c_2 V$. Repeated multiple times, we obtain five distinct jump operators $\bar{c}_\alpha \equiv (V^\dagger)^\alpha c_2 (V)^\alpha$ for $\alpha \in \{0, \ldots, 4\}$ after the α-th (modulo 5) pulses. For sufficiently short $\tau \ll 1/\Gamma$, the effective Liouvillian of the 5-pulse cycle can be well-approximated using leading order Magnus expansion by $\mathcal{L}_{\text{MP}} = (\Gamma/5)\sum_i \sum_{\alpha=0}^4 \mathcal{D}[\bar{c}_\alpha^{(i)}]$. Note the purpose of global rotations is to use a single jump operator for depopulating different states; different choices of angles and axes are equally possible as long as states rotated from $|{+}{+}\rangle$ span the entire $J = 2$ manifold. We may also employ a time-independent Hamiltonian $H_{\text{CW}} = \omega \sum_i S_i^y$ to continuously rotate the ensemble, leading to an effective Liouvillian $\mathcal{L}_{\text{CW}} = \frac{\omega}{2\pi}\int_0^{2\pi/\omega} dt\, \Gamma \sum_i \mathcal{D}[e^{iH_{\text{CW}}t} c_2^{(i)} e^{-iH_{\text{CW}}t}]$. In both

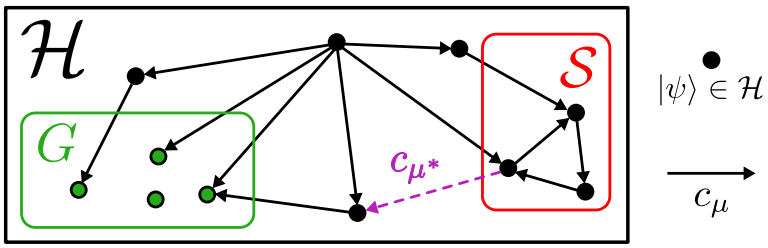

Figure 9.1: Visualizing incoherent quantum jumps as random walks on a directed graph in Hilbert space $\mathcal{H}$. G is the subspace of steady states that do not undergo quantum jumps. In the absence of the dashed arrow c_{μ^*}, the subspace of three states $\mathcal{S}$ is closed under quantum jump, allowing a mixed steady state to form. The presence of c_{μ^*} eliminates this possibility.

cases, the corresponding quantum jump rates vanish if and only if the system is in $|G\rangle$.

Uniqueness.— While our construction of $\mathcal{L}_{\text{MP}}$ and $\mathcal{L}_{\text{CW}}$ ensures that $|G\rangle$ is a steady state, one can imagine an undesired mixed steady state that forms in dynamical equilibrium from the combination of coherent evolution and incoherent quantum jumps (Fig. 9.1). Such mixed steady states may arise only if there exists a subspace $\mathcal{S}$ orthogonal to $|G\rangle$ and closed under jump operators, $c_\mu \mathcal{S} \subseteq \mathcal{S}$ [221]. Physically, it means that states in $\mathcal{S}$ cannot reach $|G\rangle$ even with arbitrarily many applications of jump operators, allowing an equilibrium to form by their mixtures. In our scheme, the uniqueness is guaranteed by the following Lemma:

Lemma. *For any finite system with size $n \geq 2$ under open boundary condition, and $n \geq 4$ under periodic boundary condition, all states can reach $|G\rangle$ with some application of jump operators in $\mathcal{L}_{\text{MP}}$ or $\mathcal{L}_{\text{CW}}$, implying $|G\rangle$ is the unique steady state.*

We now prove this Lemma for open boundary condition, where the four $|G_{ab}\rangle$ states are unique steady states; the proof for periodic boundary condition can be found in Appendix G. We use induction on system size n. For $n = 2$, the uniqueness can be trivially checked by exact calculations. For the sake of contradiction, let us assume a subspace $\mathcal{S}$ exists in a system of size $n+1$ supporting a mixed steady state $\rho_{\mathcal{S}}$. We will show $\rho_{\mathcal{S}}$

can reach at least one of the four $|G_{ab}\rangle$ by jump operators in $\mathcal{L}_{\text{MP}}$, leading to a contradiction. (The same argument holds for $\mathcal{L}_{\text{CW}}$.) First, consider the infinite-time evolution $\rho_\infty \equiv \lim_{t\to\infty} \exp\left(t\mathcal{L}_{\text{MP}}^{[n]}\right)\rho_{\mathcal{S}}$, where $\mathcal{L}_{\text{MP}}^{[n]}$ is the Liouvillian acting only on the first n particles. On one hand, from the inductive assumption, the first n particles must reach an AKLT ground state. This implies ρ_∞ is a mixture of states in the form $|\psi\rangle = \sum_{abs} \psi_{abs} |G_{ab}^n\rangle |s\rangle$, where $|G_{ab}^n\rangle$ are AKLT states for n particles, and index s enumerates the $(n+1)$-th particle's basis states. On the other hand, since $\mathcal{S}$ is by assumption closed under jump operators, $|\psi\rangle$ must also be in $\mathcal{S}$ and hence orthogonal to $\left|G_{cd}^{n+1}\right\rangle$. Hence, we have the following set of linear equations for ψ_{abs}:

$$\sum_{abs} \psi_{abs} \left\langle G_{cd}^{n+1}\right| f_\mu^{(n)} \left(|G_{ab}^n\rangle |s\rangle\right) = 0, \quad \forall c, d, \mu, \tag{9.2}$$

where $f_\mu = \bar{c}_\mu$ for $\mu \in \{0, \ldots, 4\}$, and $f_5 = \mathbb{1}$. Since $|G_{ab}^n\rangle$ and $\left|G_{cd}^{n+1}\right\rangle$ are known, one can analytically compute these expressions and find only the trivial solution $\psi_{abs} = 0$ (see Appendix G). This yields a contradiction, implying $\mathcal{S}$ cannot exist and all states can reach the ground states.

Numerical simulations.— We numerically study the efficiency of our protocol via stochastic wavefunction method for systems of up to $n = 25$ particles, using both exact diagonalization ($n \leq 8$) and time-evolving block decimation (TEBD) algorithm [241] in MPS representations ($n \leq 25$). We initialize the system in a random product state (representing maximally mixed state), and evolve under $\mathcal{L}_{\text{MP}}$ with open boundary condition. We then monitor energy density with respect to H_{AKLT}, as well as fidelity of state preparation $\mathcal{F} = \langle P_G \rangle$, where P_G is the projector onto the ground states. The results in Fig. 9.2(a)(b) demonstrate both observables exponentially converge to their corresponding values for AKLT states in all system sizes. We extract the state-preparation time T by first fitting $1-\mathcal{F}$ to an exponen-

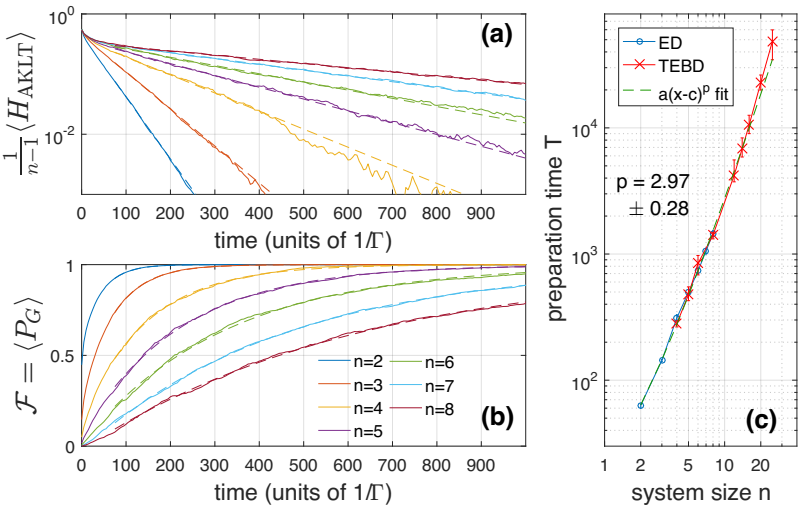

Figure 9.2: (a)(b) Numerical simulation of $\mathcal{L}_{\text{MP}}$ for $\Gamma = 1$ with maximally mixed initial state, using exact diagonalization (ED) for system size up to $n = 8$. The data in the long-time regime are fitted to an exponential function (dashed lines). (c) Fitted preparation time to achieve $\mathcal{F} = 0.9$ from simulations using ED and TEBD algorithms, as a function of system size, up to $n = 25$. Error bars are 90% confidence intervals.

tial in the long-time regime and extrapolating $\mathcal{F}(T) = 0.9$. We find T generally increases with system size n. Plotted as a function of n [Fig. 9.2(c)], we find a polynomial scaling $T \sim \mathcal{O}(n^{2.97})$, which is consistent with previous predictions [222].

9.3 Parallel preparation and quantum feedback

We now show that the scaling can be improved to $\mathcal{O}(\log^2 n)$. Similar to approaches used in quantum repeaters [242], this exponential speedup is possible by preparing multiple chains in parallel, which are subsequently connected into a single long chain [Fig. 9.3(a)].

The key ingredient is the ability to efficiently connect or fuse two AKLT chains into a single entangled state [Fig. 9.3(b)]. First, we independently prepare two length-m chains in AKLT states, $|\psi_0\rangle = |G^m_{ab}\rangle\,|G^m_{cd}\rangle$. Then we turn on only the jump operators $\{\bar{c}^{(m)}_\alpha\}$ acting on

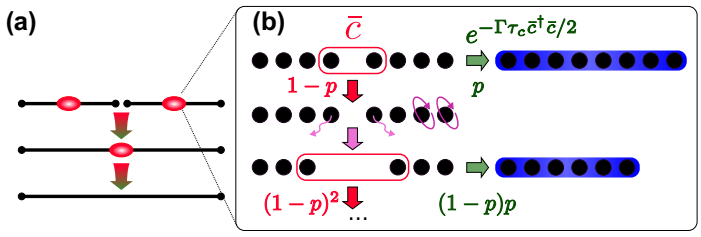

Figure 9.3: (a) Scheme for preparing AKLT states in parallel to achieve logarithmic scaling. (b) Illustration of connection algorithm, where success occurs with probability p, while failure can be corrected with constant overhead.

particles $(m, m+1)$ at the interface, evolving for some time τ_c. Lastly, we monitor quantum jump events to determine if we have succeeded in creating an AKLT state $|\psi_f\rangle = |G_{ad}^{2m}\rangle$ with doubled length; a successful connection is heralded by absence of quantum jumps, in which case evolution under the non-Hermitian Hamiltonian guides the system into an AKLT state of the combined chain. For sufficiently long τ_c, the success probability is given by overlap between initial and target states $p \simeq |\langle\psi_f|\psi_0\rangle|^2$, which is on average $1/4$ for random edge states, and maximally $1/2$ when the two chains share the same edge states at the interface ($b = c$) (see Appendix G). The resultant state has an exponentially small error $\epsilon \leq e^{-\mathcal{O}(\tau_c)}$. The failure of the connection is signaled by detection of a quantum jump, after which the state of particle pair at the interface is affected through $|\psi_0\rangle \mapsto \bar{c}_\alpha^{(m)} |\psi_0\rangle$. In this case, one discards the pair of edge spins and attempts the connection procedure with chains of length $m-1$. Interestingly, in such instances we can ensure the next attempt succeeds with the maximum probability by performing a global rotation $U = (e^{i\pi S^y})^{\otimes m-1}$ on one of the chains (see Appendix G). This quantum feedback makes the procedure very efficient, since multiple repeated failures are exponentially unlikely, leading to an average loss of $2(1-p)/p$ particles per connection.

The analysis of the scaling shows an exponential improvement. To prepare a length-n

chain, we nest the above connection algorithm in a binary tree of $\mathcal{O}(\log_2 n)$ levels; at the ℓ-th level, the average chain-length is approximately doubled $n_\ell \simeq 2n_{\ell-1} - 2(1-p)/p$. On average, the cumulative time to reach the ℓ-th level is $T_\ell \simeq T_{\ell-1} + \tau_c/p + \tau_r(1-p)/p$, where τ_r is the time necessary to reset edge states after each failed connection. Provided that at the initial level $\ell = 0$, the lengths of chains $n_0 > n_c = 2(1-p)/p$, then the average time to prepare a length-n chain is $T(n) = T_0 + [(\tau_c + \tau_r(1-p))/p] \log_2[(n-n_c)/(n_0-n_c)]$, where T_0 is the preparation time of the length-n_0 chains. The approximately n/n_0 connections yield a final error of $\mathcal{E} \leq n\epsilon/n_0 \leq (n/n_0)e^{-\mathcal{O}(\tau_c)}$, which mean we should choose $\tau_c = \mathcal{O}(\ln(n/n_0\mathcal{E}))$ to achieve a final error of $\mathcal{E}$. Hence, the average time necessary to prepare an AKLT state of length n with bounded error in this parallelized protocol is $T(n) \sim \mathcal{O}(\log^2 n)$. Imperfect detections of quantum jumps do not significantly affect the scaling, and can be largely accounted by modifying the effective success probability p (see Appendix G).

9.4 Experimental realization

The key task in implementing our protocol is to engineer the nearest-neighbor jump operators. Such engineering has been previously demonstrated in systems of trapped ions [227]. Here, we provide an explicit method to realize our scheme in systems of trapped atoms [236, 237, 140, 138, 140, 238] based on the Rydberg-EIT mechanism [239]. We consider a five-level system consisting of a meta-stable Rydberg state $|r\rangle$, a short-lived excited state $|e\rangle$, and three long-lived hyperfine ground states $|+\rangle, |0\rangle, |-\rangle$ as shown in Fig. 9.4(a). Using lasers, we coherently couple the ground state $|+\rangle$ to the excited state with a time-dependent Rabi frequency $g(t)$. The excited state is further coupled to the Rydberg state with Rabi fre-

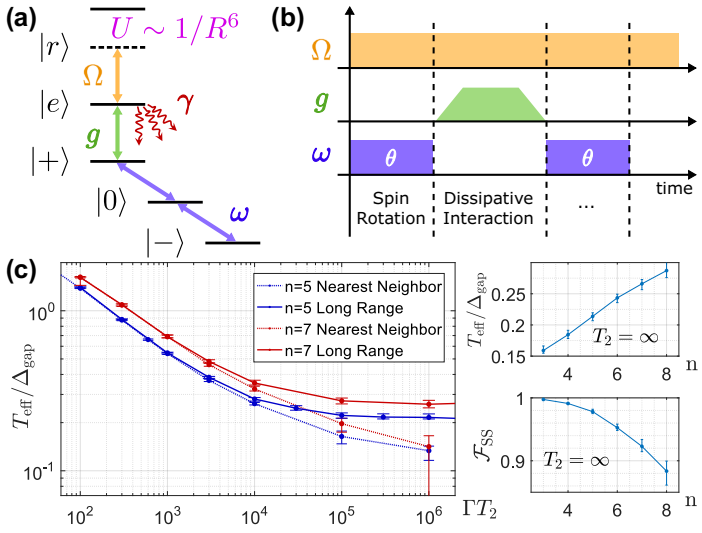

Figure 9.4: (a) Atomic level diagrams for Rydberg-EIT implementation of our jump operators, where $|r\rangle$ is a Rydberg level with strong interaction, and $|e\rangle$ is an excited level with short lifetime $1/\gamma$. The lower three levels encode the spin-1. (b) Pulse sequence to engineer $\mathcal{L}_{\rm MP}$. (c) Effects of finite dephasing time (T_2) of spin-1 levels and long-range interaction. We use steady state fidelity $\mathcal{F}_{\rm SS}$ from numerical simulations to calculate effective temperature $T_{\rm eff}$ in units of $\Delta_{\rm gap}$, the energy gap of $H_{\rm AKLT}$.

quency Ω. Owing to large dipole moments, simultaneous excitations of two Rydberg states within distance R are suppressed by interaction energy shift that decays as $1/R^6$ [243].

In the absence of interactions, our coherent driving ensures every atom supports three stable states $|-\rangle, |0\rangle$, and $|D(t)\rangle \propto \Omega\,|+\rangle - g(t)\,|r\rangle$ for arbitrary choices of g and Ω. We use these three states to encode the spin-1 degree of freedom. When $g(t)$ slowly increases starting from zero, $|+\rangle = |D(t{=}0)\rangle$ adiabatically follows $|D(t)\rangle$ without populating any excited states. In the presence of strong interactions, however, population in Rydberg state of one atom prevents another Rydberg excitation in its vicinity. Thus, as one gradually turns on $g(t)$, any neighboring atoms initially in $|{+}{+}\rangle$ necessarily populate the excited states, followed by their decay into one of the three ground states. When $0 < g \ll \Omega$, this dissipative dynamics produces effective jump operators of the form $c_\phi = |\phi\rangle\langle DD|$ with a total rate $\Gamma_{DD} \approx -2(g/\Omega)^4 \mathrm{Im}\,[U/(1+i\chi U)]$, where $\chi \approx 1/\gamma + \gamma/(4\Omega^2)$ and ϕ is one of

9 different combinations of two-particle ground states [244]. To engineer the full Liouvillian, we apply microwave pulses to the three ground states and globally rotate the spin-1 particles by $\theta \approx 2\pi/5$ [Fig. 9.4(b)]. When dissipative interactions and global rotations are alternated, this protocol effectively realizes a dynamics similar to $\mathcal{L}_{\text{MP}}$ and deterministically prepares AKLT states. The experimental platform with rearrangeable atom array in Ref. [236, 237, 140, 138, 140, 238] is particularly well-suited to parallelize the implementation and exponentially shorten preparation times for large systems.

In practice, unwanted dissipations or interactions can affect the fidelity of our protocol by perturbing the steady state of dissipative dynamics. There are two main imperfections in our proposed implementation: i) atomic states have finite dephasing time T_2, and ii) long-range Rydberg interaction can lead to dissipative coupling with particles beyond nearest neighbors. For the latter, we find pairs of particles separated by distance R with interaction $U \sim 1/R^6$ acquire decay rates $\Gamma_{DD}(R) \sim 1/R^{12}$. We study effects of these imperfections by numerical simulations of long-range effective Hamiltonian and stochastic quantum jumps that now include dephasing operators $|s\rangle\langle s|$ for $s = +, 0, -$. We introduce an effective temperature T_{eff} defined by $\text{tr}[P_G \rho(T_{\text{eff}})] = \mathcal{F}_{\text{SS}}$, where $\mathcal{F}_{\text{SS}}$ is the steady state fidelity and $\rho(T_{\text{eff}}) = \exp(-H_{\text{AKLT}}/T_{\text{eff}})/Z$ with $Z = \text{tr}[\exp(-H_{\text{AKLT}}/T_{\text{eff}})]$ [245, 246]. When the steady state is near the gapped ground state, T_{eff} characterizes the quality of prepared state in the thermodynamic limit. The results in Fig. 9.4(c) show the temperature decreases with increasing dephasing time T_2 and eventually saturates due to long-range interactions. While T_{eff} also depends on system size n, we find it stays below the gap of H_{AKLT} for all n studied in present work (up to 8). We note the effect of long-range interaction is mitigated in our parallelized protocol, where jump operators are turned on only for a few spin pairs well-

separated by the length of connected chains. Also, throughout the parallelized protocol, the effective temperature does not increase because our connection procedure ensures that $1-\mathcal{F}$ scales linearly in system sizes while the density of excited states grows at least as fast (see Appendix G).

9.5 Generalization and outlook

Our approach can be generalized to a broader class of matrix product states. Let us consider a translation-invariant MPS with internal symmetry $\mathcal{G}$, which includes ground states of SPT phases [247, 215]. Our goal is to find a minimal number $k_{\min}$ of jump operators $\{c_1, c_2, \ldots, c_{k_{\min}}\}$ acting on pairs of neighboring particles that deterministically prepare ground state(s) of the MPS parent Hamiltonian, assuming global symmetry operations are available. In Appendix G, we derive a lower bound for $k_{\min}$ based on irreducible representations of the symmetry group $\mathcal{G}$, and provide an explicit construction of a minimal set of jump operators saturating the bound. Given such a set $\{c_\mu\}$, uniqueness of the steady states can be checked via inductive proof using Eq. (9.2), which is exactly computable by diagonalizing the transfer matrix of the MPS. For the purpose of preparing ground states of SPT phases, the symmetry $\mathcal{G}$ of a parent Hamiltonian may be larger than the symmetry $\mathcal{G}' \subset \mathcal{G}$ that protects the topological order, e.g. $\mathcal{G} = \mathrm{SO}(3)$ while $\mathcal{G}' = \mathrm{D}_2$ in the case of AKLT states [233]. Also, our parallelized protocol can be extended to this broader class. For injective [214] MPS, the success probability of connection is roughly $p \simeq 1/D^2$ or $1/D$ for random or aligned edge configurations, where D is the bond dimension of the MPS (e.g. $D=2$ for AKLT states) (see Appendix G). The scaling of preparation time remains $\mathcal{O}(\log^2 n)$, exponentially outperforming existing dissipative protocols that do not involve

parallelization and feedback [222].

Finally, we note it may be possible to generalize our symmetry-based dissipative preparation scheme to higher dimensional many-body entangled states. Many such states are described by Projected Entangled Pair States (PEPS), a natural generalization of MPS for arbitrary lattices, which also allow construction of frustration-free parent Hamiltonians [248] to be converted into jump operators [222, 221, 223]. However, our inductive uniqueness proof does not extend straightforwardly, since exact computation of expectation values of a generic PEPS is intractable [249]. Further investigations are thus necessary to extend our strategy to higher dimensions, which can support even more interesting, long-range entangled states.

Chapter 10

Strongly Interacting Photons

Strong interactions between individual photons can be realized by coupling light to individual atoms [250, 251] or to strongly interacting collective excitations in atomic ensembles [243]. In the latter approach, photons are coherently coupled to highly excited Rydberg states in an atomic gas by means of electromagnetically induced transparency (EIT) [252, 253, 239]. The resulting hybrid excitations of light and matter—Rydberg polaritons—inherit strong interactions from their Rydberg components, and can, in principle, propagate with very low loss. Recently, these interactions have enabled the observation of photon blockade [254, 255, 256] and bound states of attractive photons [257], as well as the implementation of single-photon transistors [258, 259, 260]. Despite these advances, the realization of controlled, coherent interactions between single photons under conditions of low loss, as required for efficient, deterministic, all-optical quantum logic [261, 262], remains an outstanding experimental challenge.

10.1 Symmetry-protected collisions between strongly interacting photons

10.1.1 Introduction

Realizing robust quantum phenomena in strongly interacting systems is one of the central challenges in modern physical science. Approaches ranging from topological protection to quantum error correction are currently being explored across many different experimental platforms, including electrons in condensed-matter systems [263], trapped atoms [264], and photons [265]. Although photon-photon interactions are typically negligible in conventional optical media, strong interactions between individual photons have recently been engineered in several systems [266, 250, 254, 255, 256, 261, 262]. Here, using coherent coupling between light and Rydberg excitations in an ultracold atomic gas, we demonstrate a controlled and coherent exchange collision between two photons that is accompanied by a $\pi/2$ phase shift. The effect is robust in that the value of the phase shift is determined by the interaction symmetry rather than the precise experimental parameters [258, 259, 260, 261, 262], and that it occurs under conditions where photon absorption is minimal. The measured phase shift of $0.48(3)\pi$ is in excellent agreement with a theoretical model. These observations open a route to realizing robust single-photon switches and all-optical quantum logic gates, and exploring novel quantum many-body phenomena with strongly interacting photons.

10.1.2 Experimental observations

Our approach to realize robust, low-loss photon interactions makes use of a collision between stationary and propagating polaritons in a dense atomic gas (Fig. 1A), with the polaritons composed of distinct Rydberg states with opposite parity. This choice of atomic states results in a long-range dipole-dipole interaction [181, 267, 268] between the polaritons. As the polaritons approach each other in the cloud, they coherently switch places under the dipole-dipole interaction, acquiring a phase shift of exactly $\pi/2$ in the process (Fig. 1C). This phase is analogous to that acquired by a spin-1/2 particle undergoing resonant spin rotation. As discussed below, the half-integer value of the phase shift in units of π is protected by the symmetry of the effective Hamiltonian against variations in the experimental parameters, in contrast to recent demonstrations of Rydberg-mediated optical nonlinearities [257, 258, 259, 260].

Experimentally, we engineer collisions between polaritons coupled to two Rydberg levels $|S\rangle$ and $|P\rangle$ (Fig. 1B) using a combination of EIT and microwave manipulation between Rydberg states [267], in a sequence depicted in Figure 2A,B. Initially, a single photon from a weak optical "gate" pulse enters the atomic cloud and is slowed and stored in the $|S\rangle \equiv \left|100S_{1/2}\right\rangle$ state by switching off the control field in the EIT configuration. A microwave pulse coherently converts the stored, collective $|S\rangle$ excitation to the Rydberg level $|P\rangle \equiv \left|99P_{3/2}\right\rangle$. Then, a second "signal" pulse coupled to the $|S\rangle$ state enters the medium. Since the control laser only addresses $|S\rangle$ (Fig. 1B), the polariton in $|P\rangle$ does not propagate, leading to a collision between the propagating S-state polariton and the stationary excitation in $|P\rangle$. The S-polariton ultimately leaves the cloud and is detected as a photon. Finally, the excitation stored in the $|P\rangle$ state is converted back to a propagating S-polariton

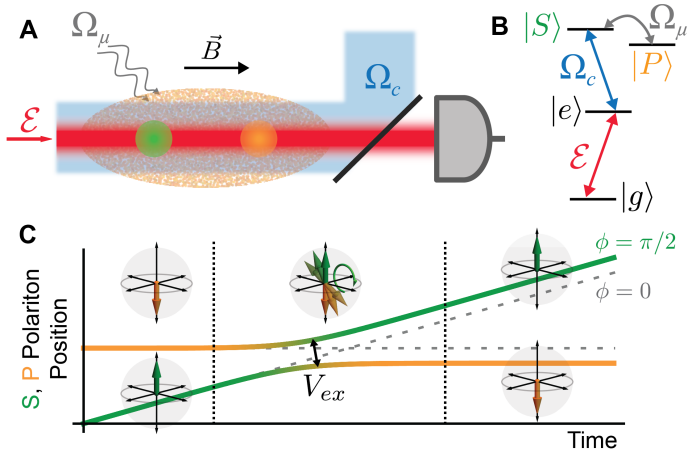

Figure 10.1: **Photon collisions mediated by long-range exchange interactions** (A) Interactions between photons are realized in a gas of laser-cooled ^{87}Rb atoms [256, 257]. Single photons from a weak probe beam ($\mathcal{E}$, red) are focused to a waist $w_p = 4.5$ μm, smaller than the transverse cloud dimensions, and coherently coupled to the Rydberg state $|S\rangle \equiv \left|100S_{1/2}, m_J = 1/2\right\rangle$ by an intense, counter-propagating control beam with Rabi frequency $\Omega_c/(2\pi) = 16$ MHz (blue) (here 100 is the principal quantum number of the Rydberg state). Both beams are circularly polarized, and propagate along the direction of the magnetic field ($B = 0.3$ mT). (B) The probe field at 780 nm is resonant with the $|g\rangle \equiv \left|5S_{1/2}, F = 2, m_F = 2\right\rangle$ to $|e\rangle \equiv \left|5P_{3/2}, F = 3, m_F = 3\right\rangle$ transition, where F and m_F indicate the hyperfine and magnetic quantum numbers, respectively. The control field at 479 nm couples $|e\rangle$ to $|S\rangle$. Microwave radiation at 3.7 GHz (Rabi frequency $\Omega_\mu/(2\pi) = 3$ MHz) is used to transfer population between Rydberg states, from $|S\rangle$ to $|P\rangle \equiv \left|99P_{3/2}, m_J = 3/2\right\rangle$. (C) A collision is realized between a single, stationary Rydberg excitation in $|P\rangle$ (orange line), and a single, propagating polariton coupled to $|S\rangle$ (green line). As they approach in the cloud, the dipole-dipole interaction V_{ex} causes them to switch places and acquire a phase shift of $\pi/2$. Without interactions, the polaritons pass through each other with no phase acquired (gray dashed lines). The Bloch spheres denote the state of each polariton during the interaction (upward arrows denote $|S\rangle$; downward, $|P\rangle$).

(with another microwave pulse) and retrieved. The influence of polariton interactions is observed via the correlations of the transmitted signal and gate photons.

The measured transmitted intensity through the atomic cloud (Fig. 2C) shows the portion of the incident gate pulse that is not stored (which henceforth is neglected), the transmitted signal pulse, and the retrieved gate pulse. The incoming signal and gate pulses have mean photon numbers less than one ($\langle n_s^{in} \rangle = 0.25$, $\langle n_g^{in} \rangle = 0.15$ for signal and gate, respectively). Therefore, the transmitted intensity averaged over many repetitions of the experiment (Fig. 2C, dashed lines) consists mainly of events with only one of the signal or gate photons present, in which interactions play no role. By examining the retrieved gate conditioned on the detection of a signal photon in the same experimental cycle, we directly observe the polariton interactions, as the gate photons in this case are delayed by an average of ~ 40 ns (corresponding to 13 μm propagation distance without interactions; Fig. 2C, solid line). We attribute this to the S and P polaritons switching places in the cloud, as shown schematically in Fig. 2A. At the same time, the probability to retrieve the gate photon remains high in the presence of interactions ($0.82(7)$ relative to the non-interacting case). The gate retrieval probability decays exponentially with the number of input signal photons (Fig. 2E), and from the decay constant we extract that the probability for a single signal photon to destroy the stored gate excitation is $0.26(5)$. This loss is significantly lower than in similar experiments using blockade-type interactions on EIT resonance [269, 270].

To observe the phase shift resulting from the interaction, we analyze the transmitted signal pulse conditioned on the detection of a retrieved gate photon. The conditioned phase of the transmitted signal (measured by interference with a co-propagating, far-detuned local oscillator) is $\phi_c = 0.48(3)\pi$ (Fig. 2D). Without conditioning, the signal phase $\phi = 0.03\pi$;

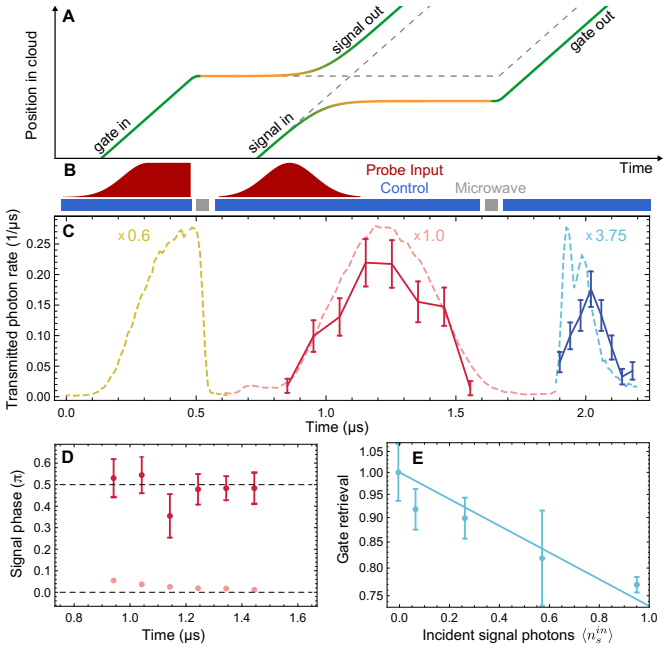

Figure 10.2: **Observation of photon collisions** (A, B) Illustration of experimental procedure (see text). (C) Average transmitted intensity through the atomic cloud (dashed lines), showing the leaked gate pulse (yellow, scaled by a factor of 0.6 for display), the signal pulse (red), and the retrieved gate pulse (blue, scaled by a factor of 3.75). Because of the low incident photon number, the average transmitted intensity is approximately equal to the intensity in the absence of interactions. We measure the transmission probability for an incident signal (gate) photon to be 0.56 (0.06) in this case. The dark blue points show the retrieved gate intensity conditioned on the detection of a signal photon in the same experimental cycle, while the dark red points show the transmitted signal intensity conditioned on the detection of a retrieved gate photon. The conditional signal transmission and gate retrieval are 77% and 82% (respectively) relative to their values without interactions. All of the features in the data are quantitatively described by a numerical simulation with independently measured parameters (see Appendix H). (D) Phase of the transmitted signal field with (dark points) and without (light points) conditioning on the detection of a retrieved gate photon. The uniform phase of $\phi_c = 0.48(3)\pi$ in the conditioned case results from the collision with a gate excitation inside the cloud. The phase shift is nearly absent without conditioning ($\phi = 0.03\pi$). (E) Normalized retrieval efficiency of the stored gate excitation as a function of average signal photon number $\langle n_s^{in} \rangle$. The data are fit to an exponential decay of the form $\exp(-\langle n_s^{in} \rangle / n_d)$, where $n_d^{-1} = 0.26(5)$ is the gate polariton destruction probability per incident signal photon. All displayed error bars are ± 1 standard deviation.

this difference confirms that the phase arises from interaction with a single gate excitation ($\phi = 0$ is defined by a control experiment with $n_g^{in} = 0$). At the same time, the signal transmission is only reduced by a factor of $0.77(6)$ compared to its value without interactions (Fig. 2C). The high transmission together with the uniformity of the $\pi/2$ phase shift across the pulse establishes that polariton collisions under dipolar interactions are highly coherent.

To demonstrate the robustness of the phase shift, we have repeated the measurements in Fig. 2C,D for a range of atomic densities, as summarized in Fig. 3. For each density, we measure the conditioned phase shift ϕ_c of the transmitted signal field, as well as the joint probability T_c for both signal and gate photons to be transmitted, relative to their independent transmission probabilities. The phase shift saturates at $\phi_c = \pi/2$ at high densities, indicating that it is a robust property of the photon collision. The transmission probability has a minimum at intermediate densities and it improves in the high-density limit, in stark contrast to conventional resonant dipole blockade, where transmission is exponentially suppressed at high densities [256].

The emergence of the phase shift can be understood from a simple model incorporating propagation and interactions. Letting $\psi(r, r')$ denote the two-body spatial wavefunction for polaritons at positions r and r' coupled to states $|S\rangle$ and $|P\rangle$, respectively, we show in the next section that the evolution of the system (in the limit of large atomic density) is governed by the effective Schrödinger equation:

$$i\frac{\partial}{\partial t}\psi(r, r') = -iv_g\frac{\partial}{\partial r}\psi(r, r') + \hbar^{-1}V_{ex}\left(r - r'\right)\psi(r', r), \tag{10.1}$$

where v_g denotes the S-polariton group velocity (see Appendix H), and $V_{ex}\left(r - r'\right) = C_3/|r - r'|^3$ is the dipolar interaction between the states $|S\rangle$ and $|P\rangle$, whose action on the

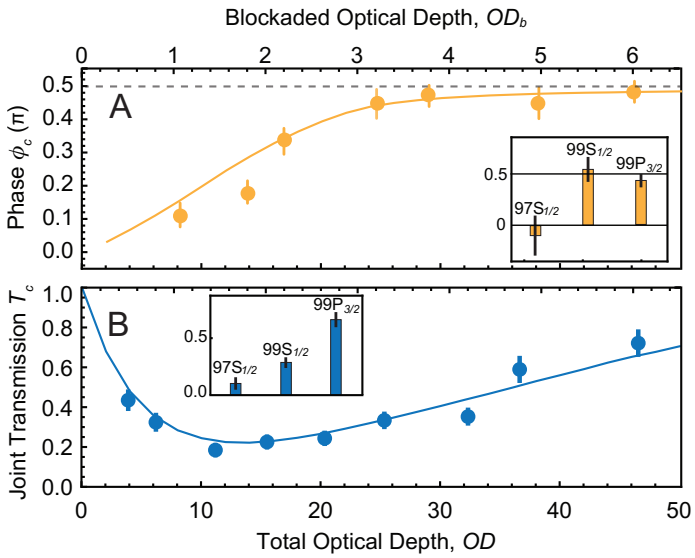

Figure 10.3: **Density dependence and robustness of the scattering phase** (A) Conditioned phase shift ϕ_c over a range of atomic densities, quantified by the total optical depth, OD. Also shown on the top axis is the estimated optical depth over one blockade radius r_b, for a Rydberg excitation at the center of the cloud (OD_b, see text). (B) Joint probability for the signal and gate photons to be transmitted, relative to their independent transmission without interactions: $T_c = \frac{\langle n_s n_g \rangle}{\langle \tilde{n}_s \rangle \langle \tilde{n}_g \rangle}$. Here, $\tilde{n}_s$ ($\tilde{n}_g$) denotes the number of detected signal (gate) photons in a control measurement with $n_g^{in} = 0$ ($n_s^{in} = 0$), while n_s, n_g are the number of detected photons for average input photon numbers, $\langle n_s^{in} \rangle = 0.25$ and $\langle n_g^{in} \rangle = 0.15$. The lines show the result of a numerical simulation of the storage, interaction and retrieval stages of the experiment, including experimental non-idealities such as dephasing from Rydberg-ground state collisions (see Appendix H). The insets show the results of similar experiments at high optical depths ($OD = 55$), with the state $|P\rangle$ replaced by $|97S_{1/2}\rangle$ or $|99S_{1/2}\rangle$. These have weaker or absent dipole-dipole interaction with $|S\rangle$ (see text).

polaritons at r and r' is to swap their positions, coupling the state $\psi(r, r')$ to $\psi(r', r)$. Eq. (10.1) has a simple time-independent solution in the continuous-wave limit: $\psi(r, r') = e^{-r_s^2/2(r-r')^2} e^{-i\,\mathrm{sign}[(r-r')C_3]\pi/4}$. Here $r_s = \sqrt{C_3/(v_g \hbar)}$ is the "hopping radius," which is the distance at which the approaching polaritons exchange their positions and start propagating away from each other. Correspondingly, there is very little probability to find the polaritons at distances $|r - r'| < r_s$. The complex transmission coefficient $t_c =$

$\lim_{(r-r')\to\infty}\psi(r,r')/\lim_{(r-r')\to-\infty}\psi(r,r')$ takes the value $e^{\pm i\pi/2}$, depending on the sign of C_3.

Remarkably, the robust phase shift can be understood by considering the symmetry $\mathbb{P}$ of the effective Hamiltonian H_{eff} governing Eq. (1). In the center of mass frame, $\mathbb{P}H_{\text{eff}} = -H_{\text{eff}}\mathbb{P}$, under the transformation $\mathbb{P}:\psi(r,r')\mapsto \text{sgn}(r'-r)\psi^*(r,r')$. In analogy to the particle-hole symmetry encountered in fermionic condensed matter systems [271, 272], this symmetry constrains the structure of the eigenstates of H_{eff} such that t_c must be purely imaginary for low-energy scattering processes, ensuring a phase shift of $\pm\pi/2$ regardless of the precise parameters in Eq. (10.1) (see Appendix H for a detailed discussion).

The model in Eq. (10.1) does not include absorption from interaction-induced level shifts, which may occur when $V_{ex}(r-r')$ exceeds the linewidth of the EIT transparency window γ_{EIT} [253]. Absorption will occur when polaritons are within the so-called blockade radius, $r_b = (2C_3/\gamma_{EIT})^{1/3}$. The blockade radius is related to the hopping radius by $r_s = \sqrt{OD_b/2}\,r_b$. Here, OD_b is the optical depth over a distance r_b, which is proportional to the atomic density. Importantly, if $OD_b > 2$, then $r_s > r_b$, which allows the exchange interaction to take place before the polaritons are sufficiently close to experience absorption. Experimentally, the minimum transmission measured in Fig. 3B occurs at $OD_b \approx 2$, beyond which the transmission indeed steadily increases. This analysis validates the use of Eq. (10.1) in the high-density limit $OD_b \gg 1$. A more detailed calculation in Appendix H shows that the photon loss decreases asymptotically as $OD_b^{-3/2}$ while the phase difference from $\pi/2$ decreases as e^{-OD_b}. This scaling is more favorable than that corresponding to off-resonant Rydberg blockade, where the loss under optimized conditions decreases as OD_b^{-1} [253, 260].

To further verify the interaction mechanism, we repeated the experiment with other pairs of Rydberg states (Fig. 3, insets) that exhibit different interactions. In contrast to the interaction between $|P\rangle = \left|99P_{3/2}\right\rangle$ and $|S\rangle$, which is almost purely dipolar (resulting in a much stronger exchange interaction compared to the blockade), $\left|97S_{1/2}\right\rangle$ interacts with $|S\rangle$ almost entirely through a level-shifting van der Waals process (see Appendix H). This results in very low transmission, in agreement with recent photon transistor experiments [259, 258]. The state $\left|99S_{1/2}\right\rangle$ has comparable van der Waals and (second-order) dipolar interactions with $|S\rangle$, and shows moderately high transmission and a large phase shift. Since the van der Waals interaction breaks the symmetry protecting the $\pi/2$ phase shift, its value is not robustly $\pi/2$, and will depend on a variety of experimental parameters, including the atomic density and Ω_c.

Finally, in Figure 4, we demonstrate that the long-range nature of the interaction allows photons to hop between separated transverse optical modes. We repeat the experimental sequence in Figure 2A, but with the gate and signal fields incident in distinct transverse spatial modes (Fig. 4A). Intensity cross-correlation measurements between the transmitted light in the two modes (Fig. 4B) reveal anti-correlations between signal and gate photons exiting in their incident modes ($g^{(2)}_{inc} = 0.18$) and positive correlations between signal and gate photons exiting in swapped modes ($g^{(2)}_{sw} = 5.8$). Together, these show that the interaction causes pairs of photons to hop between modes in the atomic cloud, such that the signal exits in the mode in which the gate was incident, and vice versa. By comparison to a control measurement without interactions, we estimate an 8% probability for photons to swap modes due to the exchange process (see Appendix H). As compared to the analogous quantity $T_c = 0.77$ measured for single-mode interactions in Figure 3, this value is lower

because of the increased distance between the photons, lower atomic density in the wings of the cloud, and nonlinear effects resulting from higher input power.

The overall efficiency is mostly determined by the finite signal transmission (0.56, limited by laser linewidth) and finite retrieval probability for the gate photon (0.06, limited by imperfect storage and dephasing of the spin wave) in the absence of interactions. These probabilities can be increased to greater than 0.9 with realistic technical improvements: improved laser stability, larger optical depth, better cooling and an optimal choice of Rydberg states (see Appendix H). The losses associated with the interaction (resulting in an additional 20% reduction of the two-photon transmission) can be suppressed by increasing OD_b, as in Figure 3B. Since the phase shift is protected against these imperfections by symmetry, higher-fidelity quantum logic may be achieved probabilistically by heralding on the detection of the final transmitted photons.

10.1.3 Conclusion and outlook

Our results open up new possibilities for realizing robust quantum gates and many-body phenomena with strongly interacting photons. A modest extension of this work should allow for a controlled-π phase shift quantum gate between two photons [261], by using microwave control to pass the polaritons through each other a second time before they exit the cloud. The demonstrated interaction between polaritons is also a powerful tool for studying quantum many-body dynamics of photons. In particular, the symmetries that result in the robust phase shifts observed in this work are identical to those that result in Majorana fermions in one dimensional wires [273, 274], which are expected to feature similarly robust $\pi/2$ phase shifts under braiding operations [263]. While the present two-

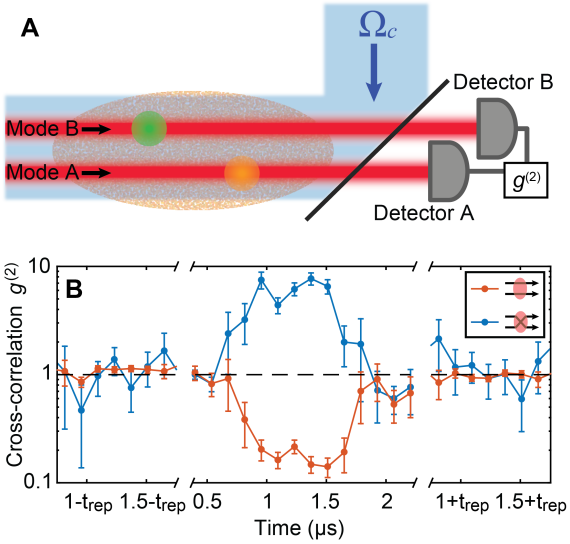

Figure 10.4: **Polariton exchange between separated transverse modes** (A) The gate and signal pulses are now incident in distinct transverse spatial modes, A and B, respectively, separated by $1.2w_p = 5.4\,\mu$m. The control beam addresses both modes. (B) The intensity cross-correlation between signal and gate photons exiting in their incident modes (red points, $g^{(2)}_{inc}$) and in swapped modes (blue points, $g^{(2)}_{sw}$) shows that polaritons switch modes in the cloud. $g^{(2)}_{inc}(t) = \langle n^B_s(t) n^A_g \rangle / \langle n^B_s(t) \rangle \langle n^A_g \rangle$ where $n^B_s(t)$, denotes the number of signal photons detected at time t in mode B, and n^A_g is the total number of gate photons detected in mode A. The definition for $g^{(2)}_{sw}(t)$ is the same, with the modes A and B reversed.

particle scattering process has important distinctions, in that the low energy mode is not protected by an energy gap, the latter could potentially be engineered (*e.g.* via polariton interactions). Likewise, extensions along the lines of recent proposals [275, 276] could be explored to realize topological photonic systems.

10.2 Theory of symmetry-protected collisions

In this section, we provide more detailed theory of symmetry-protected photon exchange process. We will focus on the derivation of the effective Schrödinger equation (Eq. 10.1) provided in the previous section and its analytical solution. We shall see that such model is asymptotically valid in the limit of large atomic density. A more rigorous theoretical treatment of the problem, including the effects of inhomogeneous density of the atomic cloud and the finite lifetime of Rydberg states, is provided in Appendix H.2.

10.2.1 Effective Schrödinger equation

The dynamics in our system are described by a Hamiltonian $\hat{H} = \hat{H}_{\text{EIT}} + \hat{V}_{\text{ex}}$, where $\hat{H}_{\text{EIT}}$ and $\hat{V}_{\text{ex}}$ characterize the propagation and the interaction of photons, respectively. In the rotating frame, this Hamiltonian can be efficiently written in terms of bosonic field operators $\hat{\mathcal{E}}^\dagger(z)$, $\hat{\mathcal{P}}^\dagger(z)$, $\hat{\mathcal{S}}^\dagger(z)$, and $\hat{\mathcal{C}}^\dagger(z)$ for a signal photon, an atomic excitation in the $5P_{3/2}$ state, an excitation in the nS state, and an excitation in the $n'P$ state (the gate photon)

[277]:

$$\hat{H}_{\text{EIT}} = \int dz \left(\hat{\mathcal{E}}^\dagger(z), \hat{\mathcal{P}}^\dagger(z), \hat{\mathcal{S}}^\dagger(z)\right) \begin{pmatrix} -ic\partial_z & \bar{g} & 0 \\ \bar{g} & -i\gamma & \Omega \\ 0 & \Omega & 0 \end{pmatrix} \begin{pmatrix} \hat{\mathcal{E}}(z) \\ \hat{\mathcal{P}}(z) \\ \hat{\mathcal{S}}(z) \end{pmatrix} \tag{10.2}$$

and

$$\hat{V}_{\text{ex}} = \int dx dy V(x-y)\hat{\mathcal{C}}^\dagger(y)\hat{\mathcal{S}}^\dagger(x)\hat{\mathcal{S}}(y)\hat{\mathcal{C}}(x), \tag{10.3}$$

where c is the speed of light, $\bar{g}$ is the collectively enhanced coupling of a signal photon to the ensemble of atoms, Ω is the Rabi frequency of the control field laser, γ is the decay rate of the $5P_{3/2}$ state, and $V(r) = C_\alpha/r^\alpha$ is the strength of the long-range interaction. $\hat{V}_{\text{ex}}$ can arise from a dipolar ($\alpha = 3$) or van der Waals interaction ($\alpha = 6$), but we concentrate on the $\alpha = 3$ case here. We use units such that $\hbar = 1$. Note that the relationship to the experimental units in the main text is $\Omega = \Omega_c/2$ and $\gamma = \Gamma/2$, where $\Gamma/(2\pi) = 6.1$ MHz for Rb. The EIT linewidth used in the main text is defined as $\gamma_{EIT} = \Omega_c^2/\Gamma$.

Owing to EIT, photons propagate as dark state polaritons in the atomic cloud, so we introduce the dark and bright polariton basis $\hat{\mathcal{D}}(z) = \cos\theta\hat{\mathcal{S}}(z) - \sin\theta\hat{\mathcal{E}}(z)$ and $\hat{\mathcal{B}}(z) = \sin\theta\hat{\mathcal{S}}(z) + \cos\theta\hat{\mathcal{E}}(z)$. Here the mixing angle is given by $\sin\theta \equiv \Omega/\sqrt{\bar{g}^2 + \Omega^2}$ [278], and in our system, $\theta \ll 1$ by several orders of magnitude. The propagation of the dark state polariton is well described by a Hamiltonian

$$\hat{H}_{\text{D}} = -i \int dz\ v_g \hat{\mathcal{D}}^\dagger(z)\partial_z\hat{\mathcal{D}}(z) \tag{10.4}$$

with the slow light group velocity $v_g = c\ \Omega^2/(\bar{g}^2 + \Omega^2)$. The reduced group velocity arises from the fact that the polariton is composed of atomic and photonic components,

and a larger atomic component will result in slower light [278]. Also, in this basis, the interaction becomes

$$\hat{V}_{\text{ex}} = \int dxdy \cos^2\theta V(x-y)\ \hat{\mathcal{C}}^\dagger(y)\hat{\mathcal{D}}^\dagger(x)\hat{\mathcal{D}}(y)\hat{\mathcal{C}}(x) + \mathcal{O}(\sin\theta), \tag{10.5}$$

where we may only keep the leading order term with an approximation $\cos\theta \approx 1$. These approximations are valid as long as bright state polaritons or $5P_{3/2}$ states are not populated, which we will confirm for self-consistency. In order to describe the photon collision dynamics, we define a two-photon wavefunction $\psi(r, r')$ as the probability amplitude of finding a dark state polariton (signal photon) at r and a $n'P$ excitation (gate photon) at r', namely $\psi(r, r') = \langle 0|\, \hat{\mathcal{D}}(r)\hat{\mathcal{C}}(r')\, |\psi\rangle$. Then, the time evolution of the wavefunction can be obtained from the Schrödinger equation

$$\frac{\partial}{\partial t}\psi(r,r') = \langle 0|\, \hat{\mathcal{D}}(r)\hat{\mathcal{C}}(r')\frac{\partial}{\partial t}\, |\psi\rangle = -i\, \langle 0|\, \hat{\mathcal{D}}(r)\hat{\mathcal{C}}(r')(\hat{H}_D + \hat{V}_{\text{ex}})\, |\psi\rangle \tag{10.6}$$

$$= -v_g\frac{\partial}{\partial r}\psi(r,r') - iV(r-r')\psi(r',r), \tag{10.7}$$

where we recover Eq. (1) from the main text. To obtain the second line, we have used the commutation relations of bosonic field operators, e.g.,

$$\langle 0|\, \hat{\mathcal{D}}(r)\hat{\mathcal{C}}(r')\hat{H}_D\, |\psi\rangle = -i\int dz\ v_g\, \langle 0|\, \hat{\mathcal{D}}(r)\hat{\mathcal{D}}^\dagger(z)\partial_z\hat{\mathcal{D}}(z)\hat{\mathcal{C}}(r')\, |\psi\rangle \tag{10.8}$$

$$= -i\int dz\ v_g\, \langle 0|\, \left(\hat{\mathcal{D}}^\dagger(z)\hat{\mathcal{D}}(r) + \delta(z-r)\right)\partial_z\hat{\mathcal{D}}(z)\hat{\mathcal{C}}(r')\, |\psi\rangle \tag{10.9}$$

$$= -iv_g\partial_r\, \langle 0|\, \hat{\mathcal{D}}(r)\hat{\mathcal{C}}(r')\, |\psi\rangle = -iv_g\partial_r\psi(r,r'), \tag{10.10}$$

and similarly for $\langle 0|\, \hat{\mathcal{D}}(r)\hat{\mathcal{C}}(r')\hat{V}_{\text{ex}}\, |\psi\rangle$.

Now, we solve the Schrödinger equation in Eq. (10.7). Note that the exchange interaction is not in the conventional form since it couples two wavefunction amplitudes at re-

versed positions $r \leftrightarrow r'$. In order to convert this into a local interaction, we divide the wavefunction into two components $\psi(r,r') = \psi_{SP}(r,r')$ for $r < r'$ and $\psi(r,r') = \psi_{PS}(r',r)$ for $r > r'$, where our Schrödinger's equation becomes

$$i\frac{\partial}{\partial t}\begin{pmatrix}\psi_{SP}\\ \\ \psi_{PS}\end{pmatrix} = \begin{pmatrix} -iv_g\partial_r & V_{ex}(r-r') \\ \\ V_{ex}(r-r') & -iv_g\partial_{r'}\end{pmatrix}\begin{pmatrix}\psi_{SP}\\ \\ \psi_{PS}\end{pmatrix}. \tag{10.11}$$

Then, we move into the center of mass frame by introducing $R = (r+r')/2$ and $z = r'-r$, where the propagation is described by $\partial_r \mapsto \frac{1}{2}\partial_R - \partial_z$ and $\partial_{r'} \mapsto \frac{1}{2}\partial_R + \partial_z$. Finally, introducing a new effective time variable $\partial_\tau \equiv \partial_t + \frac{v_g}{2}\partial_R$ in this frame, we obtain

$$i\frac{\partial}{\partial \tau}\begin{pmatrix}\psi_{SP}\\ \\ \psi_{PS}\end{pmatrix} = \begin{pmatrix} iv_g\partial_z & V_{ex}(z) \\ \\ V_{ex}(z) & -iv_g\partial_z\end{pmatrix}\begin{pmatrix}\psi_{SP}\\ \\ \psi_{PS}\end{pmatrix} = [i\sigma^z v_g\partial_z + V(z)\sigma^x]\begin{pmatrix}\psi_{SP}\\ \\ \psi_{PS}\end{pmatrix}, \tag{10.12}$$

where σ^μ are the Pauli operators.

In the continuous-wave limit (where the R dependence vanishes), we are interested in the properties of the zero-energy eigenstates of this equation, which describe the interaction between photons with vanishing relative momentum. By setting the left hand side of Eq. (10.12) to zero and multiplying by σ^z, we obtain $-iv_g\partial_z\Psi = iV_{ex}(z)\sigma^y\Psi$ with $\Psi = (\psi_{SP}, \psi_{PS})^T$. We integrate from $z = \infty$ to $z = z'$ to get

$$\Psi(z') = e^{-\frac{1}{v_g}\int_\infty^{z'} V_{ex}(z)dz\sigma^y}\Psi(\infty) = \begin{pmatrix} \cosh\phi(z') & -i\sinh\phi(z') \\ \\ i\sinh\phi(z') & \cosh\phi(z')\end{pmatrix}\Psi(\infty), \tag{10.13}$$

with $\phi(z') \equiv \frac{1}{v_g}\int_{z'}^{\infty} V_{ex}(z)dz$. For a normalizable solution, we require that $|\Psi(z')| < \infty$ as $z' \to 0$. Since $\phi(z')$ diverges for decreasing z', such a solution is possible only when $\Psi(\infty) \propto (1,-i)$ for positive C_α and $\Psi(\infty) \propto (1,i)$ for negative C_α. Therefore, the zero

energy eigenstate is given by

$$\begin{pmatrix} \psi_{SP} \\ \psi_{PS} \end{pmatrix} \propto \begin{pmatrix} e^{-|\phi(z')|} \\ -\text{sign}(C_\alpha) i e^{-|\phi(z')|} \end{pmatrix}. \tag{10.14}$$

For a dipolar interaction, this solution reduces to

$$\psi(r, r') = e^{-\frac{1}{2v_g}\frac{|C_3|}{(r-r')^2}} e^{-i\,\text{sign}[(r-r')C_3]\pi/4}. \tag{10.15}$$

By defining the hopping length scale $r_s \equiv \sqrt{|C_3|/v_g}$, we recover the solution following Eq. (1) in the main text. This can also be expressed in terms of the blockade radius as $r_s = \sqrt{OD_b/2} r_b$, where $r_b = (|C_3|\gamma/\Omega^2)^{1/3}$ and $OD_b = r_b/l_a$, with l_a being the attenuation length for the probe field in the absence of EIT (inversely proportional to the atomic density).

There are several points worth noting. First, Eq. (10.15) implies that the particle propagates as a (zero momentum) plane wave at $r \to \pm\infty$. The relative phase difference between these two plane waves $\psi_{SP}(z = \infty)$(before the collision) and $\psi_{PS}(z = \infty)$(after the collision) indicates that the interaction imprints a phase of $\pm\pi/2$ for positive and negative C_α, respectively. Second, this wavefunction has vanishingly small amplitude when $|r - r'| < r_s$. Therefore, the bright state polaritons or $5P_{3/2}$ states will not be populated when $OD_b \gg 1$, consistent with our initial assumptions. Finally, we note that the imprinted phase $\pm\pi/2$ is independent of the precise value of experimental parameters such as $\Omega, \bar{g}, \gamma$ or $V_{ex}(r - r')$. The only requirement for the phase being unchanged is that the integrated interaction $\phi(z)$ diverges as z approach to zero. While this is approximately satisfied in the regime of large OD_b, more careful analysis is necessary for small OD_b, as we provide later in Appendix H.2.

10.2.2 Symmetry protection of the phase

The fact that the phase shift acquired in a collision between two polaritons is robustly $\pi/2$, independent of the precise experimental parameters, can be understood in terms of symmetries of the effective Hamiltonian describing the scattering process. To derive this, we start with the effective Schrödinger equation from the previous section:

$$i\partial_\tau \Psi = \left[i\sigma^z v_g \partial_z + V(z)\sigma^x\right]\Psi \equiv \hat{H}_{\text{ex}}\Psi, \tag{10.16}$$

where z is the distance between two particles, Ψ is the two-component wavefunction $\Psi = (\psi_{SP}, \psi_{PS})^T$, and τ is the effective time in the center-of-mass frame defined by $\partial_\tau = \partial_t + (v_g/2)\partial_R$. We find that this effective Hamiltonian $\hat{H}_{\text{ex}}$ has three symmetries $\hat{\mathbb{T}}$, $\hat{\mathbb{P}}$, and $\hat{\mathbb{C}}$, whose action on the wavefunction is defined by:

$$\hat{\mathbb{T}} = \sigma^x\hat{\mathbb{K}}, \quad \hat{\mathbb{P}} = \sigma^z\hat{\mathbb{K}}, \quad \hat{\mathbb{C}} = -i\sigma^y, \tag{10.17}$$

where $\hat{\mathbb{K}}$ is complex conjugation. We refer to these symmetries as time-reversal, particle-hole, and chiral symmetries (respective) in analogy to those of fermionic particles. Note that three operators are related by $\hat{\mathbb{C}} \equiv \hat{\mathbb{T}}\hat{\mathbb{P}}$ as in the case of free fermions. The symmetry of the exchange process is defined by the commutation and anti-communtation relations of $\hat{H}_{\text{ex}}$ with these operators, where one can easily check that

$$\hat{\mathbb{T}}\hat{H}_{\text{ex}} = \hat{H}_{\text{ex}}\hat{\mathbb{T}}, \quad \hat{\mathbb{P}}\hat{H}_{\text{ex}} = -\hat{H}_{\text{ex}}\hat{\mathbb{P}}, \quad \hat{\mathbb{C}}\hat{H}_{\text{ex}} = -\hat{H}_{\text{ex}}\hat{\mathbb{C}}. \tag{10.18}$$

These symmetries imply that if Ψ is an eigenstate of H_{ex} with energy E, then $\hat{\mathbb{T}}\Psi$, $\hat{\mathbb{P}}\Psi$, $\hat{\mathbb{C}}\Psi$ are also eigenstates with energy E, $-E$, and $-E$, respectively. Here, we are most interested in a propagating wave at energy $E = 0$, where any linear combination of these states are still an eigenstate with zero energy. Let us assume $\Psi_0 = (f(z), g(z))^T$ is such an eigenstate.

As the interaction $V(z)$ diverges at $z = 0$ and vanishes at $z \to \infty$, we know $f(z)$ and $g(z)$ have to vanish at $z = 0$ and converge at large z to a plane wave with zero momentum (i.e., a constant). Without loss of generality, we set $f(\infty) = 1$ and $g(\infty) = t$, where t is the complex transmission coefficient. From the time-reversal symmetry, it follows that the wavefunction $\Psi_1 \equiv t^*\Psi_0 - \hat{\mathbb{T}}\Psi_0 = [t^*f(z) - g^*(z), t^*g(z) - f^*(z)]^T$ is an eigenstate, where the first component vanishes as $z \to \infty$. Using the conservation of the probability current densities at $z = 0$ and $z = \infty$, one finds that the second component must also vanish, implying that the transmission probability is unity $|t|^2 = 1$. It follows that, to the extent that the above symmetries are perfectly satisfied, the transmission through the medium in the presence of the exchange interaction is perfectly lossless.

Similarly, using the particle-hole and chiral symmetries, one can define $\Psi_2 \equiv \Psi_0 + \hat{\mathbb{P}}\Psi_0$ and $\Psi_3 \equiv t\Psi_0 - \hat{\mathbb{C}}\Psi_0$, each of which implies $t + t^* = 0$ and $t^2 + 1 = 0$, respectively. Thus the combination of the particle-hole and chiral symmetries ensures that the scattering phase of the collision is $\pm\pi/2$.

Symmetry	Properties	Action	Consequence
Time-reversal	anti-unitary $\hat{\mathbb{T}}\hat{H} = \hat{H}\hat{\mathbb{T}}$	$\psi(r, r') \mapsto \psi^*(r', r)$ or $\sigma^x\hat{\mathbb{K}}$	$\lvert t\rvert^2 = 1$
Particle-hole	anti-unitary $\hat{\mathbb{P}}\hat{H} = -\hat{H}\hat{\mathbb{P}}$	$\psi(r, r') \mapsto \text{sgn}(r' - r)\psi^*(r, r')$ or $\sigma^z\hat{\mathbb{K}}$	$t + t^* = 0$
Chiral	unitary $\hat{\mathbb{C}}\hat{H} = -\hat{H}\hat{\mathbb{C}}$	$\psi(r, r') \mapsto -\text{sgn}(r' - r)\psi(r', r)$ or $-i\sigma^y$	$t^2 = -1$

Table 10.1: Summary of symmetries and their consequences. The operator $\hat{\mathbb{K}}$ indicates complex-conjugation.

Table 10.1 summarizes the symmetry properties of our collision process and their consequences.

Interestingly, if $V_{ex}(z)$ does not diverge at $z = 0$, this symmetry argument is broken due to the boundary condition $\lim_{z\to 0} f(z) = \lim_{z\to 0} g(z)$. If $f(0) = g(0) \neq 0$ satisfies the boundary condition, $\hat{\mathbb{C}}\Psi$ or $\hat{\mathbb{P}}\Psi$ cannot, breaking the symmetries. When $V(0)$ diverges, the value of $|\Psi(0)|$ vanishes and the symmetry is restored, providing a robust phase shift.

10.3 Scattering resonances and bound states for strongly interacting Rydberg polaritons

In this section, we provide a theoretical framework describing slow-light polaritons interacting via atomic Rydberg states. We use a diagrammatic method to analytically derive the scattering properties of two polaritons. We identify new parameter regimes where polariton-polariton interactions are *repulsive*. Furthermore, in the regime of *attractive* interactions, we identify multiple two-polariton bound states, calculate their dispersion, and study the resulting scattering resonances. Finally, the two-particle scattering properties allow us to derive the effective low-energy many-body Hamiltonian. This theoretical platform is applicable to ongoing experiments.

10.3.1 Introduction

Weak interactions of photons with each other are the basis for many applications of light signals in areas such as optical communication. However, many other applications in classical and quantum communication, computation, and metrology would greatly benefit from tunable photon-photon interactions. Moreover, photon-photon interactions at the level of individual quanta could pave the way to the realization of exotic strongly corre-

lated photonic states [279, 280, 281]. A typical approach to achieve strong two-photon interactions relies on confining photons to high-finesse cavities [282, 283, 284]. An alternative approach towards this goal has recently emerged using Rydberg slow-light polaritons [252, 254, 285, 255, 286, 287, 257, 239].

The key idea [243] is to combine electromagnetically induced transparency (EIT) [278, 288] with the strong interaction between Rydberg atoms [181]. Both phenomena have been well-studied in the past: it has been demonstrated that photons can be slowed down and stored in atomic gases using EIT [289, 290, 291], while recent experiments on Rydberg atoms have demonstrated the strong interaction and the associated blockade of Rydberg excitations [292, 293, 294, 295, 296, 255, 297]. In the Rydberg-EIT system, a photon entering the atomic gas is converted into a slow-light polariton with a substantial admixture of the Rydberg state. It is the latter admixture that maps the Rydberg-Rydberg interaction onto an effective interaction between slow Rydberg polaritons. Within this approach, a single-photon source [255] and switch [298] was realized, the photon blockade [287] and the formation of bound states of Rydberg polaritons [257] has been demonstrated, and atom-photon entanglement was observed [299].

10.3.2 Diagrammatic approach

Here, we derive the scattering properties and bound-state structure of Rydberg polaritons in one dimension. Our analysis uses diagrammatic techniques and provides a rigorous theoretical framework for analyzing a variety of problems in Rydberg-polariton systems. This framework allows us to analytically derive the effective interaction potential between two Rydberg polaritons and to identify a regime with a purely repulsive interaction. We de-

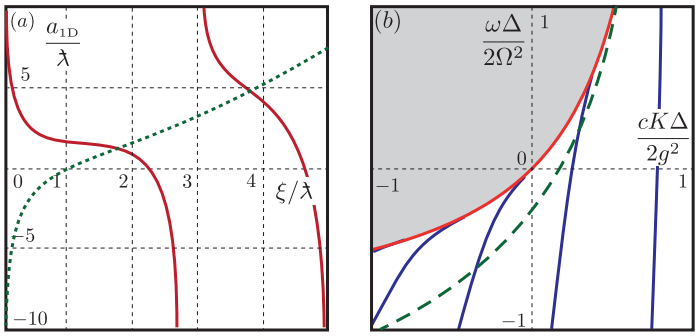

Figure 10.5: (a) Low-energy scattering length a_{1D}: for attractive interactions (solid line), we obtain scattering resonances associated with the appearance of additional bound states for increasing interaction strength ξ/λ; $\lambda = \hbar\sqrt{|\bar{\chi}/\alpha m|}$. For repulsive interactions (dashed line), we find a single zero crossing. (b) Two-polariton spectrum for $\Omega \ll |\Delta| \lesssim g$: For weak interactions $\xi/\lambda = 0.5$ (dashed line), we obtain a single bound state below the continuum of scattering states, whereas for strong interactions $\xi/\lambda = 5$ (solid lines), we observe the existence of several bound states.

rive the low-energy scattering length and find the appearance of resonances, see Fig. 10.5; we expect the corresponding tunability of the scattering length to play the role that Feshbach resonances play in ultra-cold atomic gases [300]. Moreover, we identify multiple two-polariton bound states for attractive interactions and determine their dispersion relation. This understanding paves the way for a microscopic derivation of the many-body theory for Rydberg polaritons in the dilute regime.

Before proceeding we note that first steps towards a many-body theory for Rydberg polaritons in one dimension have already been taken [281]. However, a full description of the system – including the short-range and finite-energy effects relevant to ongoing experiments [287, 257] – is limited to extended numerical simulations [285, 301], which can treat only a small number of interacting photons.

Model and key results.—We consider photons inside an atomic ensemble propagating in one-dimension under EIT conditions, where the atomic ground state is coupled to a

Rydberg state via an intermediate level denotes as p-state. We introduce the electric field operators $\psi_e^\dagger(z)$ and $\psi_e(z)$, creating and annihilating a photon at position z, respectively. If the atomic density is much higher than the photon density, the excitations of atoms are well-described by the bosonic field operators $\psi_p^\dagger(z)$ and $\psi_s^\dagger(z)$. Here, $\psi_p^\dagger(z)$ describes the atomic excitation into the p-state, while $\psi_s^\dagger(z)$ generates a Rydberg excitations. We then obtain the non-interacting part of the microscopic Hamiltonian under the rotating-wave approximation in the rotating frame

$$H_0 = \hbar \int dz \begin{pmatrix} \psi_e \\ \psi_p \\ \psi_s \end{pmatrix}^\dagger \begin{pmatrix} -ic\partial_z & g & 0 \\ g & \Delta & \Omega \\ 0 & \Omega & 0 \end{pmatrix} \begin{pmatrix} \psi_e \\ \psi_p \\ \psi_s \end{pmatrix}. \tag{10.19}$$

Here, g denotes the collective coupling of the photons to the matter via the excitation of ground state atoms into the p-level, while Ω denotes the Rabi frequency of the control field between the p-level and the Rydberg state. Note that the kinetic energy of the photons $-i\hbar\partial_z$ only accounts for the deviation from the EIT condition. We introduced the complex detuning $\Delta = \delta - i\gamma$, which accounts the detuning δ of the control field and the decay rate 2γ from the p-level. Throughout our analysis, we assume $|\delta| \gg \gamma$, thus providing the results in the limit $\gamma = 0$. Then, the inclusion of a finite decay rate γ is obtained by an analytical continuation in $\Delta = \delta - i\gamma$. The interaction between the Rydberg levels is described by

$$H_{\text{rr}} = \frac{1}{2} \int dz dz' V(z - z') \psi_s^\dagger(z) \psi_s^\dagger(z') \psi_s(z') \psi_s(z). \tag{10.20}$$

In the following, we focus on a van der Waals interaction $V(r) = C_6/r^6$. The microscopic Hamiltonian $H_0 + H_{\text{rr}}$ describes three bosonic fields with a non-interacting quadratic part and a quartic interaction. Such systems have been extensively studied in the past using

diagrammatic methods, *cf.* Ref. [302]. However, it is important to stress that the quadratic Hamiltonian exhibits a rather unconventional form, as the only dynamics is given by the light velocity of the photon. It is this property, together with the conservation of total energy $\hbar\omega$ and total momentum $\hbar K$, that is crucial to our analysis and gives rise to novel phenomena.

In order to understand the many-body properties of the system, we will analyze the scattering properties and bound-state structure for two polaritons. The main idea is to derive the scattering length a_{1D}, which in turn allows for the description of the many-body theory in terms of a pseudo-potential. This approach is in analogy to cold atomic gases, where it is extremely successful [300].

The description of two polaritons requires, in the most general case, a nine-component, two-particle wavefunctions $\psi_{\alpha\beta}(z, z')$ with $\alpha, \beta \in \{e, p, s\}$, which denotes the amplitude of finding particles in states α and β at z and z', respectively [285]. To utilize the conservation of energy and momentum, we rewrite $\psi_{\alpha\beta}$ in the center-of-mass $R = (z + z')/2$ and relative $r = z - z'$ coordinates and parametrize it in terms of temporal and spatial Fourier components (ω, K), leaving r the only degree of freedom. Using the diagrammatic techniques, we find that the quantum dynamics of the two polaritons is well captured by a Schrödinger-like equation for a single component

$$\hbar\bar{\omega}\psi(r) = \left[-\frac{\hbar^2}{m}\partial_r^2 + \alpha V_{\text{eff}}(r)\right]\psi(r), \tag{10.21}$$

with the effective potential and polariton mass

$$V_{\text{eff}}(r) = \frac{V(r)}{1 - \bar{\chi}(\omega)V(r)}, \qquad m = \hbar\frac{(g^2 + \Omega^2)^3}{2c^2 g^2 \Delta\Omega^2}. \tag{10.22}$$

Here, $\hbar\bar{\omega}(K, \omega)$ is the energy due to the relative motion, and the dimensionless parameter

$\alpha(K,\omega)$ can be interpreted as the overlap of the polaritons with the Rydberg state. The effective interaction potential is renormalized as the interaction shifts the two Rydberg states out of resonance, when two polaritons approach each other. This behavior is captured by a single parameter $\bar{\chi}(\omega)$. The wavefunction $\psi(r)$ is related to the two-body wavefunctions via $\psi(r) = \psi_{ss}(r)[1-\bar{\chi}V(r)]$, where the amplitude $\psi_{ss}(r)$ to find two Rydberg states vanishes at distances shorter than the blockade radius $\xi = (|C_6\bar{\chi}|)^{1/6}$. In addition, the wavefunction $\psi(r)$ is proportional to the electric field amplitude $\psi_{ee}(r)$. Equation (10.21) is valid in several relevant regimes, including the low-momentum and low-energy regime, and the far-detuned regime as discussed below. For vanishing $\omega = 0$, Eq. (10.21) reproduces the steady state results obtained in Refs [285, 257].

We start with the *low-momentum and low-energy regime*, which allows us to analytically derive the low-energy scattering length $a_{\,1\mathrm{D}}$. The characteristic energy scale is given by $\omega_c = \min\{|\Delta|, 2\Omega^2/|\Delta|\}$ and the corresponding characteristic momentum is $q_c = \omega_c/v_g$ with $v_g = \Omega^2/(\Omega^2+g^2)c$ the slow light velocity. At low energies $|\omega| \ll \omega_c$ and momenta $|K| \ll q_c$, the expressions for $\bar{\omega}$ and α are in leading order

$$\bar{\omega} = \omega - v_g K, \qquad \alpha = \frac{g^4}{(g^2+\Omega^2)^2}. \tag{10.23}$$

In this limit, Eq. (10.21) provides the intuitive result: $\bar{\omega}$ is the difference between the total energy ω and the kinetic energy $v_g K$ of the center-of-mass motion, and α is the square of the probability to find a polariton in the Rydberg state. Furthermore, the amplitude for the electric field takes the form $\psi_{ee} = \Omega^2/g^2\psi$. At the same time, $\bar{\chi}$ reduces to

$$\hbar\bar{\chi} = \frac{\Delta}{2\Omega^2} - \frac{1}{2\Delta}, \tag{10.24}$$

which exhibits a zero crossing for $\Omega = \pm\Delta$ with an associated sign change. Therefore, it is possible to realize effectively *repulsive* polariton-polariton interactions for $\Omega > |\Delta|$

with $C_6\delta > 0$ (the latter condition avoids a singularity in V_{eff}). This surprising behaviour is related to the modification of frequency-dependant part of susceptibility of proximal polaritons. It is in contrast to the far off-resonant regime ($\Omega \ll |\Delta|$), where the combination of polariton mass and effective interaction always leads to an effective attraction [257]. In this regime, we observe a transition from a negative to a positive 1D scattering-length $a_{\,1\text{D}}$ for increasing interactions, see Fig. 10.5(a). The interaction strength is conveniently expressed by the dimensionless parameter $\xi/\lambda\!\!\!^{-}$ with the blockade radius $\xi = (|C_6\bar{\chi}|)^{1/6}$ and $\lambda\!\!\!^{-} = \sqrt{|\hbar^2\bar{\chi}/(\alpha m)|}$ the de Broglie wavelength associated with the depth/height of the effective potential. Then, we obtain the asymptotic behavior $a_{\,1\text{D}} = -(3/\pi)\lambda\!\!\!^{-2}/\xi$, valid for weak interactions with $\xi/\lambda\!\!\!^{-} \ll 1$, where the interaction potential can be replaced by a δ-function. Note that for $\gamma = 0$, the scattering length is negative, while for a finite decay rate $\gamma > 0$, the analytical continuation of the scattering length reduces to $a_{\,1\text{D}} = (3/\pi)(-\bar{\chi}^5/C_6)^{1/6}(\hbar^2/\alpha m)$ and gives rise to an imaginary contribution accounting for losses from the p-level during the collision. For increasing interactions, eventually a zero crossing of $a_{\,1\text{D}}$ appears, and we obtain the positive scattering length $a_{\,1\text{D}} \approx 0.7\,(\alpha m C_6/\hbar^2)^{1/4}$, where the full tail of the van der Waals interaction dominates.

In the *attractive* regime $\Omega < |\Delta|$ with $C_6\delta < 0$, the system generally gives rise to bound states. Note that bound states can be identified by negative values of $\bar{\omega}$. For weak interaction $\xi < \lambda\!\!\!^{-}$, a single bound state is present, and we recover the expression for the scattering length $a_{\,1\text{D}} = (3/\pi)\lambda\!\!\!^{-2}/\xi$, which is now positive. For increasing interactions $\xi > \lambda\!\!\!^{-}$, additional bound states will appear. Each additional bound state is associated with a resonance in the scattering length in analogy to Feshbach resonances in cold atomic gases [300]. The exact determination of the scattering length $a_{\,1\text{D}}$ requires the full treatment

of the effective interaction potential $V_{\text{eff}}(r)$; the latter is easily achieved numerically, see Fig. 10.5(a). It clearly demonstrates that we can tune the scattering length to arbitrary values by controlling the single parameter ξ/λ, which defines the strength of the interaction potential.

In general, the bound states will violate the condition of low energy and are thus more appropriately studied next in the *far-detuned regime* with $\Omega \ll |\Delta|$, which is valid for all momenta K with the weak constraint on the energy $|\omega| \ll |\Delta|$. In this regime, we obtain $\hbar\,\bar{\chi}(\omega) = (\omega + 2\Omega^2/\Delta)^{-1}$, and the blockade radius reduces to $\xi = (|C_6\Delta/2\Omega^2|)^{1/6}$, while the analytic but lengthy expressions for $\bar{\omega}$ and α are presented in Appendix H. In the experimentally most interesting regime of slow light $g \gg \Omega$ with $g \gtrsim |\Delta|$, we find

$$\alpha = \frac{1 - \frac{cK\Delta}{2g^2}}{\left(1 + \frac{\omega\Delta}{2\Omega^2}\right)^2}, \tag{10.25}$$

while the expression for the energy $\bar{\omega}$ takes the form

$$\frac{\bar{\omega}\Delta}{2\Omega^2} = \frac{\frac{\omega\Delta}{2\Omega^2}}{1 + \frac{\omega\Delta}{2\Omega^2}} - \frac{1 + 2\frac{\omega\Delta}{2\Omega^2}}{1 + \frac{\omega\Delta}{2\Omega^2}}\,\frac{cK\Delta}{2g^2} + \left(\frac{cK\Delta}{2g^2}\right)^2. \tag{10.26}$$

Finally, the relation to the electric field amplitude ψ_{ee} is again closely related to the wavefunction ψ via $(g^2 - cK\Delta/2)\psi_{ee} = (\Omega^2 + \omega\Delta/2)\psi$. It is important to stress that, in this limit, the diagrammatic result agrees with the approach utilizing adiabatic elimination, see Appendix H.

The effective equation Eq. (10.21) allows us to derive the bound states and their group velocity in addition to the scattering states. The spectrum is shown in Fig. 10.5(b): it exhibits a continuum of scattering states as well as bound states. Note that the interaction potential as well as $\bar{\omega}$ depend on the energy ω, and therefore the bound-state energies have to be determined self-consistently. The dimensionless parameter measuring the strength of

the interaction reduces to $\xi/\lambda\!\!\!^{-} = \xi g^2/|\Delta|c$ and is related to the resonant optical depth per blockade radius $\kappa_\xi = 2\xi|\Delta|/\lambda\!\!\!^{-}\gamma$. Then for weak interactions $\xi/\lambda\!\!\!^{-} < 1$, we recover a single bound state, which is well described by replacing the effective interaction potential by a δ-function. For increasing interaction strength $\xi/\lambda\!\!\!^{-} > 1$, we observe the appearance of additional bound states. Then, the exact bound state energy requires the numerical treatment of the full effective interaction potential Eq. (10.22). The result is shown in Fig. 10.5(b) for two different interaction strengths.

Derivation and limitations.—Next, we present the microscopic derivation of Eq. (10.21) and discuss its limitations. We start by diagonalizing the non-interacting part of the Hamiltonian in momentum space obtaining the dispersion relations of three polariton modes, $H_0 = \sum_{q,\alpha\in 0,\pm 1} \epsilon_{\alpha q} \bar{\psi}^\dagger_{\alpha q} \tilde{\psi}_{\alpha q}$. Here, $\alpha \in \pm 1$ account for the two bright polariton modes, while $\alpha = 0$ denotes the dark polariton. The new field operators take the form $\tilde{\psi}_{\alpha q}$ = $\sum_{\beta\in\{e,p,s\}} U^\beta_\alpha(q)\psi_{\beta q}$ with $\alpha \in \{0, \pm 1\}$, and the inverse $\bar{U} \equiv U^{-1}$ provides $\bar{\psi}^\dagger_{\alpha q} = \sum_{\beta\in\{e,p,s\}} \bar{U}^\alpha_\beta(q)\psi^\dagger_{\beta q}$.

The two-polariton scattering properties are well accounted for by the T-matrix. As the interaction acts only between the two Rydberg states, it is sufficient to study the T-matrix for the Rydberg states alone, denoted as $T_{kk'}(K,\omega)$. Here, k is the relative momentum of the two incoming polaritons and k' the relative momentum of the outgoing polaritons. For two polaritons, the T-matrix is expressed as a resummation of all ladder diagrams, see Fig. 10.6(a), and gives rise to the integral equation [302]

$$T_{kk'}(K,\omega) = V(k-k') + \int \frac{dq}{2\pi} V(k-q)\chi_q(K,\omega)T_{qk'}(K,\omega).$$

The full pair propagator of two polaritons and its overlap with the Rydberg state takes the

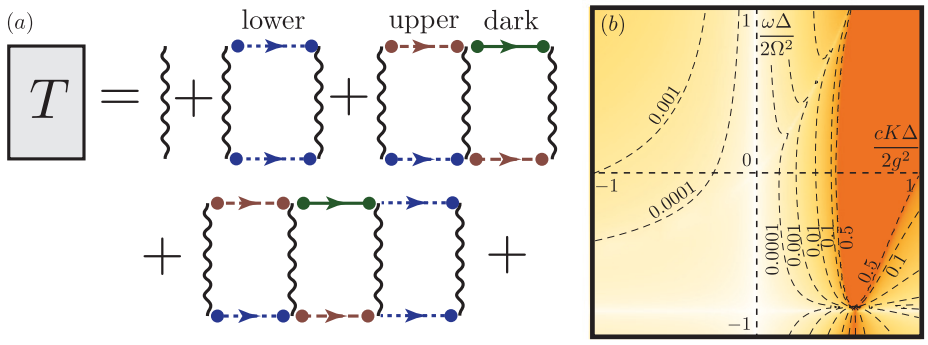

Figure 10.6: (a) Illustration of a few ladder diagrams: the interaction $V(r)$ is denoted by a wavy line, while the straight lines with an arrow are Green's functions for the three polariton modes $1/(\hbar\omega - \epsilon_\alpha + i\eta)$, and the dots mark the overlap factors U^s_α and $\bar{U}^\alpha_s$ of the polariton with the Rydberg state. (b) Parameter $\zeta(K,\omega)$ measuring the influence of the second pole for $g \gg \Omega$ and $\Omega/\Delta = 0.5$. In the low energy/momentum limit, the second pole can be safely neglected, however its influence strongly increases for $Kc\Delta/2g^2 \sim 1$.

form

$$\chi_q(K,\omega) = \sum_{\alpha,\beta\in\{0,\pm1\}} \frac{\bar{U}^\alpha_s(p)U^s_\alpha(p)\bar{U}^\beta_s(p')U^s_\beta(p')}{\hbar\omega - \epsilon_\alpha(p) - \epsilon_\beta(p') + i\eta}, \tag{10.27}$$

with $q = (p-p')/2$ and $K = p + p'$. It is a special property of our polariton Hamiltonian that the pair propagation reduces to three terms,

$$\chi_q = \bar{\chi} + \frac{\alpha}{\hbar\bar{\omega} - \hbar^2q^2/m + i\eta} + \frac{\alpha_{\rm B}}{\hbar\bar{\omega}_{\rm B} - \hbar^2q^2/m + i\eta}. \tag{10.28}$$

Here, $\bar{\chi}(\omega)$ accounts for the saturation of the pair propagation at large momenta $q \to \pm\infty$ and takes the form

$$\bar{\chi}(\omega) = \frac{1}{\hbar}\frac{\Delta - \frac{\omega}{2} - \frac{\Omega^2}{\Delta-\omega}}{\omega\left(\Delta - \frac{\omega}{2}\right) + 2\Omega^2}. \tag{10.29}$$

The second term in Eq. (10.28) is the pole structure for the propagation of the two incoming polaritons. This term reduces to the propagator of a single massive particle, where α and $\bar{\omega}$ depend on the center-of-mass momentum K and total energy ω. The latter defines the relative momentum $k = \pm\sqrt{m\bar{\omega}/\hbar}$ of the incoming scattering states. Finally, the

last term accounts for a second pole, describing the phenomenon of resonant scattering of two incoming polaritons into a different outgoing channel, *e.g.*, the conversion of two dark polaritons into an upper and a lower bright polariton. The influence of the second pole is measured by the dimensionless parameter $\zeta(K,\omega) = \sqrt{|(\bar{\omega}\alpha_{\rm B}^2)/(\bar{\omega}_{\rm B}\alpha^2)|}$. Especially, $\zeta(K,\omega)$ is strongly suppressed in the two regimes discussed above; an illustration demonstrating the strong suppression is shown Fig. 10.6(b), while the analytical expressions are provided in Appendix H. In these cases the second pole can be dropped in leading order in the small parameter $\zeta \ll 1$. The saturation $\bar{\chi}$ can be eliminated by introducing the effective interaction potential $V_{\rm eff}(r)$ given in Eq. (10.22). Then, the equation for the T-matrix reduces to

$$T_{kk'} = V_{\rm eff}(k-k') + \int \frac{dq}{2\pi} V_{\rm eff}(k-q)\, \frac{\alpha}{\hbar\bar{\omega} - \hbar^2 q^2/m}\, T_{qk'}.$$

Consequently the T-matrix describes a system of a single massive particle in the effective interaction potential $V_{\rm eff}$ with the relative coordinate as the degree of freedom and is fully described by the Schrödinger equation in Eq. (10.21). The relation $\psi(r) = \psi_{ss}(r)[1 - \bar{\chi}V(r)]$ follows from the relation between the T-matrix and the scattering wave function $\psi_{ss}(r)V(r) = \int dk' e^{irk'} T_{kk'}/(2\pi) = \psi(r)V_{\rm eff}(r)$.

Discussion and Outlook.—The full understanding of the scattering properties allows us to derive the *low energy many-body Hamiltonian for Rydberg polaritons*. Here, the fundamental assumption is that each scattering process of the polaritons is independent of each other. This condition is satisfied in the dilute regime $n_d\, r_0 \ll 1$, where the density n_d of Rydberg polaritons is low compared to the range r_0 of the interaction potential. The latter is determined either by the blockade radius or the van der Waals length, *i.e.*, $r_0 = \max\{\xi, (|\alpha m C_6|/\hbar^2)^{1/4}\}$. Then, the interaction is fully determined by the scattering

length $a_{\,1\mathrm{D}}$ via the one-dimensional pseudo-potential $V_{1\mathrm{D}} = -2\hbar^2/m a_{\,1\mathrm{D}}\delta(r)$ [303], and the many-body theory reduces to the Hamiltonian

$$H = \int dx \left[\psi_d^\dagger \left(-i\hbar v_g \partial_z - \frac{\hbar^2}{2m}\partial_z^2 \right) \psi_d - \frac{2\hbar^2}{m a_{\,1\mathrm{D}}} \psi_d^\dagger \psi_d^\dagger \psi_d \psi_d \right],$$

with $\psi_d^\dagger$ (ψ_d) denoting the bosonic field operator creating (annihilating) a Rydberg polariton. Here we can control the scattering length $a_{\,1\mathrm{D}}$ by the strength of the interactions, see Fig. 10.5(a). We can therefore study continuously the crossover from a Lieb-Liniger gas at $a_{\,1\mathrm{D}} < 0$ to the Super-Tonks-Girardeaux gas at $a_{\,1\mathrm{D}} > 0$ by tuning the parameters through a zero crossing of the scattering length [304, 305, 306]. In contrast to cold atomic gases [307, 308], the zero crossing of the scattering length is not associated with losses in the system.

Finally, we point out that a complementary derivation of an effective low-energy theory can also be achieved at high densities, if the interaction is dominated by the purely repulsive part of the van der Waals interaction, as proposed in Ref. [281]. This theory is of interested in the parameter regime with $1/(|\alpha m C_6|/\hbar^2)^{1/4} < n_{\,1\mathrm{D}} < q_c, 1/|\xi|$; note that here we provide a microscopic derivation for the short distance behavior. We have demonstrated that this regime is most interesting to study when $\Delta \approx \pm\Omega$ and $C_6\delta > 0$, where $\bar{\chi}$ is strongly suppressed, and the effective interaction reduces to the pure van der Waals repulsion $V_{\mathrm{eff}}(r) = C_6/r^6$. This scenario allows one to observe the crossover into a regime where crystalline correlations dominate the ground state.

Experimental implications.—The microscopic analysis presented here has several implications for experiments. First, the existence of a parameter regime with a purely repulsive interaction will give rise to photon anti-bunching for the two-photon correlations in an experimental setup similar to that of Ref. [257]. The experimental requirements are

strong Rabi frequency $\Omega \gtrsim |\Delta|$, $q_c\xi < 1$ for the low momentum regime, and $\gamma \ll |\delta|$ to distinguish the repulsion from losses. In turn, the analysis of the bound-state structure allows for the determination of the group velocity. As can be seen in Fig. 10.5(b), the group velocity of the bound states is larger than the slow light velocity, and the bound states will travel ahead of the continuum. This will allow one to spatially separate the bound photon pairs in a pulsed experiment. Finally, the scattering length defines the phase shift two polaritons pick up during a collision; it has been proposed to use such collisions to realize photonic two-qubit gates [252, 285]. Here, the predicted zero-crossing of the scattering length corresponds to the optimal π-phase shift. A direct measurement of these resonances is possible in a setup with frequency difference $\Delta\omega$ and spatially-resolved detection of the polaritons inside the medium. Therein, the correlation function in the relative coordinate will oscillate with a wavevector $\Delta k = \Delta\omega/v_g$. The maxima of these oscillations will shift for increasing scattering length by a phase ϕ via $\cot(\phi) = -a_{\,1\mathrm{D}}\Delta k$. The details of these observations depend on the experimental setup and on the precise boundary conditions but can be efficiently addressed within the presented framework.

Chapter 11

Universal Photonic Quantum Computation via Time Delayed Feedback

We propose and analyze a deterministic protocol to generate two-dimensional photonic cluster states using a single quantum emitter via time-delayed quantum feedback. As a physical implementation, we consider a single atom or atom-like system coupled to a 1D waveguide with a distant mirror, where guided photons represent the qubits, while the mirror allows the implementation of feedback. We identify the class of many-body quantum states that can be produced using this approach and characterize them in terms of 2D tensor network states.

11.1 Introduction

Quantum information processing with optical photons is being actively explored for the past two decades [309, 310]. However, despite a number of conceptual [311] and technological breakthroughs [312, 313, 314], the probabilistic nature of quantum gates limits the scalability of linear optical systems. Here we show that one can deterministically generate photonic states with the full power of universal quantum computation using quantum control of a single emitter in combination with time delayed coherent quantum feedback [315, 316, 317]. Our approach is motivated by recent experimental progress demonstrating high-fidelity generation of single photons [313, 318] and deterministic quantum operations between single photons and emitters [319, 320, 321] in various systems [183, 322, 323, 324, 325, 326]. We present an explicit protocol to create a 2D cluster state [327] with a single atomic or atom-like emitter coupled to photonic waveguide. The delayed feedback is introduced by reflecting part of the emitted light field back onto the emitter. Our approach allows for deterministic generation of complex photonic entangled states, and opens new avenues to photonic quantum computation and quantum simulation using minimal resources already available in current state-of-the-art experiments.

Time delayed feedback is a powerful tool in several areas of science and engineering [315]. In what follows we show that delayed coherent quantum feedback can be used as a resource to generate quantum entanglement, and already in its most basic form may enable universal quantum computation. We focus on quantum optical systems, where it was shown previously that multipartite entanglement between photonic qubits can be generated by a single emitter in a sequential emission process [328, 329, 330]. We demonstrate that the entanglement structure of the resultant state can be qualitatively enriched using

time delayed quantum feedback. While photons emitted in a generic sequential process are entangled only in a one-dimensional way, characterized by so called matrix product states (MPS) [331], we show below that delayed feedback leads to higher-dimensional entanglement structure captured by so called projected entangled pair states (PEPS) [332]. Significantly, while MPS have limited use for quantum computation and simulation, as they can be efficiently simulated classically, PEPS contain states that serve as resource for universal measurement based quantum computation (MBQC) [327]. The difference is rooted in the Markovian nature of the sequential emission process that severely restricts the class of achievable states. In contrast, time delayed quantum feedback renders the system non-Markovian, introducing an effective quantum memory that we harness to create a universal resource.

11.2 Generating photonic 2D cluster state

The fundamental building block of our approach is a single, driven quantum emitter ($\mathcal{Q}$) coupled to a 1D waveguide and a distant mirror as depicted in Fig. 11.1(a). Our protocol consists of a repeated excitation of this quantum emitter leading to an emission of a train of photons pulses into the waveguide, encoding qubits via the absence ($|0\rangle_k$) or presence ($|1\rangle_k$) of a photon in the k-th pulse. The mirror feeds these photons back to the emitter with a time delay τ, such that the photons can interact with the emitter more than once [Fig. 11.1(b)]. In this way, the emitter can create correlations not only between subsequently emitted photons, but also between photon pulses separated by the time delay τ. Effectively this leads to a two dimensional entanglement structure as we discuss now for the specific example of the 2D cluster state [see also Fig. 11.1(c)].

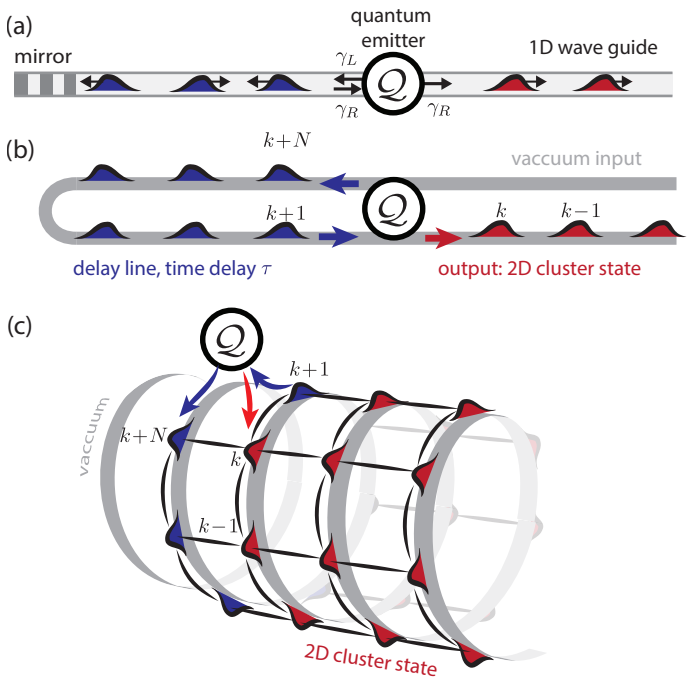

Figure 11.1: Schematic setting. (a) A quantum emitter $\mathcal{Q}$ is coupled to a 1D wave-guide that is terminated on one side by a (distant) mirror. (b) In each time step k, $\mathcal{Q}$ can emit a phtoton $(k+N)$ towards the mirror, i.e. into a delay line and interact with a photon k returning from the delay line, and exiting at the output port. (c) Visualization of the resulting entanglement structure: wrapping the photon channel displayed in (b) around a cylinder with the proper circumference (equivalent to the time delay τ), it can be seen that in each time step $\mathcal{Q}$ interacts with two photons that are neighboring along the artificial, second dimension. Therefore, as time progresses, $\mathcal{Q}$ creates entanglement between neighboring photonic qubits, both in the physical and the artificial dimension.

For concreteness, we focus on an emitter (representing $\mathcal{Q}$) with an internal structure depicted in Fig. 11.2(a), supporting two metastable states $|g_1\rangle \equiv |0\rangle_{\mathcal{Q}}$ and $|g_2\rangle \equiv |1\rangle_{\mathcal{Q}}$, which can be coherently manipulated by a classical field $\Omega_1(t)$. The emitter can be excited from $|g_2\rangle$ to a state $|e_L\rangle$ using a laser with Rabi frequency $\Omega_2(t)$. Following each excitation the atom will decay to $|g_2\rangle$ emitting a photon into the waveguide. For now, we assume that the atom-photon coupling is chiral [333] such that every such photon is emitted unidirectionally, i.e. to the left in Fig. 11.1(a) (see however below). Finally, another excited state

$|e_R\rangle$, degenerate with $|e_L\rangle$, couples to the right moving photons reflected from the mirror. We denote the corresponding decay rates by γ_L and γ_R.

Protocol – Our protocol starts by first generating 1D cluster states of left-propagating photons [328]. To this end, the atom is initially prepared in the state $|0\rangle_{\mathcal{Q}}$. Then, a rapid $\pi/2$-pulse is applied on the atomic qubit, followed by a π-pulse on the $|g_2\rangle \rightarrow |e_L\rangle$ transition [Fig. 11.2(a,b)]. The subsequent decay from state $|e_L\rangle$ to $|g_2\rangle$ results in entanglement between the atom and the emitted photon, i.e. $|0\rangle_{\mathcal{Q}}|0\rangle_1 + |1\rangle_{\mathcal{Q}}|1\rangle_1$. Repeating this pulse sequence for n times leads to a train of photonic qubits in the form of 1D cluster state. An analogous scheme has been demonstrated in an experiment using a quantum dot [330], following a seminal proposal by Lindner and Rudolph [328].

Remarkably, the 2D cluster state is generated from exactly the same sequence if we take into account the effect of the mirror and the scattering of the reflected photons from the atom. We are interested in the situation where the time delay τ is so large that the k-th photon interacts for the second time with the atom between the generation of the $(k{+}N{-}1)$-th and $k+N$-th photon. This is achieved, for example, by setting $\tau = (N-1/2)T$ [with T the protocol period; see Fig. 11.2(b)]. Crucially, if the atom is then in the state $|g_2\rangle$, the returning photon is resonantly coupled to the $|g_2\rangle \rightarrow |e_R\rangle$ transition, picking up a scattering phase shift of π without any reflection [333]. In contrast, if the atom is in state $|g_1\rangle$, or the photon mode is empty, there is no interaction. This process implements a controlled σ^z gate

$$\hat{Z}_{\mathcal{Q},k} = |0\rangle_{\mathcal{Q}}\langle 0| \otimes \mathbb{1}_k + |1\rangle_{\mathcal{Q}}\langle 1| \otimes \sigma_k^z \tag{11.1}$$

entangling the atom and the k-th photon. In turn, the subsequently generated $k+N$-th photon inherits this entanglement, thereby giving rise to an effective 2D entanglement

structure [Fig. 11.1(c)].

Formally, the protocol can be interpreted as a sequential application of gates $\hat{X}_{\mathcal{Q},k+N}\hat{Z}_{\mathcal{Q},k}\hat{H}_{\mathcal{Q}}$, on the atom and photonic qubits k and $k+N$, on the initial trivial state $|0\rangle_{\mathcal{Q}}\bigotimes_k|0\rangle_k$ [Fig. 11.2(c,d)]. Here $\hat{H}_{\mathcal{Q}}=\frac{1}{\sqrt{2}}(\sigma^z_{\mathcal{Q}}+\sigma^x_{\mathcal{Q}})$ and $\hat{X}_{\mathcal{Q},k}=|0\rangle_{\mathcal{Q}}\langle 0|\otimes\mathbb{1}_k+|1\rangle_{\mathcal{Q}}\langle 1|\otimes\sigma^x_k$. One can show, that after $(M+1)\times N$ turns this gives exactly the 2D cluster state on a $M\times N$ square lattice with shifted periodic boundary conditions [see Appendix I]:

$$|\psi_{\mathcal{C}_{2D}}\rangle=\left(\prod_{k=1}^{N(M+1)}\hat{X}_{\mathcal{Q},k+N}\hat{Z}_{\mathcal{Q},k}\hat{H}_{\mathcal{Q}}\right)|0\rangle_{\mathcal{Q}}\bigotimes_k|0\rangle_k\,. \tag{11.2}$$

Universal quantum computation [334] can be performed by sequentially measuring each photonic qubit directly at the output port, e.g. using another atom as a high fidelity measurement device. This can be implemented using pulse shaping techniques [Fig. 11.3(a)], allowing for a perfect absorption of each photon by the second atom [335, 336].

Experimental requirements – Photons generated in this pulsed scheme have a finite bandwidth $\mathcal{B}$. To realize the controlled phase gate (11.1) this bandwidth must be small, i.e., $\mathcal{B}\ll\gamma_R$ [333]; otherwise, the wave packet is distorted when scattered by the atom, reducing the gate fidelity, $\mathcal{F}_Z$ [Fig. 11.3(c)]. Narrow-bandwidth photons, and high fidelity gates can be obtained by shaping the temporal profiles, eliminating the error to first order in $\mathcal{B}/\gamma_R$ [Fig. 11.3(c) and Appendix I].

Second, the information capacity of the feedback loop is bounded by the number of photons in the delay line, N. In order to well distinguish two consecutive photons, one can only generate them at a rate $1/T\ll\mathcal{B}$ [see Fig. 11.3(d)]. Therefore, the requirement for narrow-bandwidth photons is competing with the effective size of the emergent, second dimension N. Thus, a high fidelity implementation requires the hierarchy $N\sim\tau/T\ll$

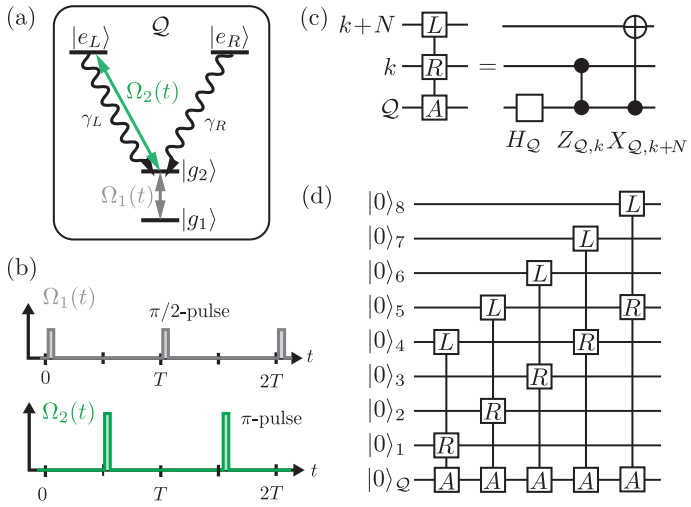

Figure 11.2: Protocol to generate the photonic 2D cluster state. With the level structure (a) and periodic, pulsed coherent drive (b) the setup in Fig.11.1(a) leads to 2D cluster state of photons in the output. During each step $k = 1, 2, \ldots$ (of duration T) the pulse (b) sequence realizes a unitary involving the emitte $\mathcal{Q}$ (A), and two photonic qubits, k and $k + N$ [realized by a right (R) and left (L) moving photon respectively], with $N = 3$ in (d). The corresponding circuit diagram is shown in (c,d). Each step consists of a Hadamard gate $\hat{H}_\mathcal{Q}$, and a controlled phase gate $\hat{Z}_{\mathcal{Q},k}$ between the atom an the photon qubit k returning from the delay line, followed by a controlled-NOT gate $\hat{X}_{\mathcal{Q},k+N}$ (see text).

$\tau\mathcal{B} \ll \gamma_R\tau$. Note that τ can be dramatically enhanced e.g. via a dispersive slow-light medium [337].

Apart from these fundamental considerations, experimental imperfections will eventually limit the achievable size of the cluster state. One of the most important challenges is photon loss in atom-photon interactions, often quantified by the so-called cooperativity $\eta_j = \gamma_j/\Gamma_j$ ($j = L, R$), where Γ_j denotes emission rate into unguided modes from state $|e_j\rangle$. Amplitude attenuation in the waveguide and finite photon detection can be accounted for by a renormalized Γ_j. Large, high-fidelity cluster states can be obtained in the regime $\eta_j \gg 1$, where the achievable system sizes scale as $NM \lesssim (1/\eta_L + 2/\eta_R)^{-1}$ [Fig. 11.3(e)]. High cooperativities have been demonstrated in nanophotonic experiments

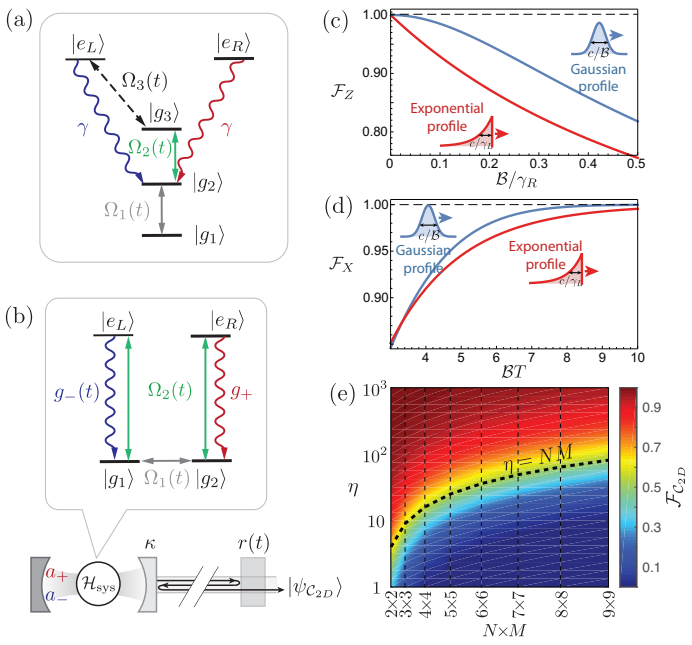

Figure 11.3: Modified setups and effects of imperfections. (a) Exciting the atom via a third stable state $|g_3\rangle$ in a Raman-type configuration, one can shape the profile of the emitted photon wave-packet. In the limit $|\Omega_3(t)| \ll \gamma$ an adiabatic elimination of the excited state $|e_L\rangle$ leads to the same effective dynamics as in Fig. 11.2(b), but with a renormalized and dynamically controllable, effective decay rate $\gamma_L(t) = |\Omega_3(t)|^2/(2\gamma)$. (b) Modified setup to generate the 2D cluster state in a cavity QED setting with photon qubits encoded in polarization degrees of freedom and without the requirement of chiral coupling. (c) Fidelity of the controlled phase gate for a photon with Lorentzian (red) or Gaussian (blue) spectrum [see also Appendix I]. (d) Analogously, fidelity of photon generation as a function of the protocol period T. (e) Effect of photon loss: Fidelity of the generated state ρ (with $\eta_L = \eta_R = \eta$) and the 2D cluster states of size $N \times M$, $\mathcal{F}_{\mathcal{C}_{2D}} = \sqrt{\langle\psi_{\mathcal{C}_{2D}}|\,\rho\,|\psi_{\mathcal{C}_{2D}}\rangle}$.

with neutral atoms and solid-state emitters [321, 322].

Finally, we note that chiral coupling is not essential in realizing the above protocol. For example, in a cavity QED setting [321, 320], the delayed feedback can be introduced by a distant, switchable mirror [Fig. 11.3(b)]. There, proper control of the mirror can ensure that each generated photon interacts exactly twice with the emitter. Moreover, in such a setting one can encode qubit states in photon polarizations rather than number degrees of

freedom, allowing the detection of photon loss errors.

11.3 Tensor networks from photons

To completely characterize the class of achievable photonic states using the setup in Fig. 11.1(a), we turn to a more abstract description of the dynamics (see also Appendix I). Formally, the quantum system $\mathcal{Q}$ generates an output state by sequential unitary interaction with two qubits k and $k+N$ on a 1D array, representing the photonic qubits. Assuming that the qubits are initialized in the state $|0\rangle$, this reduces to a map

$$\hat{U}[k] = \sum_{i,a,b,c,d} U[k]^{i}_{a,b,c,d} \, |i,a,b\rangle \langle c,0,d| \,, \tag{11.3}$$

where $|i,a,b\rangle \equiv |i\rangle_k |a\rangle_{k+N} |b\rangle_{\mathcal{Q}}$ denotes a state with k-th and $k+N$-th qubits and $\mathcal{Q}$ in states i, a, b, respectively. Repeated application of such maps produces a quantum state $|\Psi(k)\rangle$, describing $\mathcal{Q}$ and the string of photonic qubits after k steps:

$$|\Psi(k)\rangle = \hat{U}[k] \, |\Psi(k-1)\rangle = \prod_{j=1}^{k} \hat{U}[j] \, |\Psi(0)\rangle \,. \tag{11.4}$$

Given the initial state, the wavefunction is entirely specified by the tensors $U[j]^{i}_{a,b,c,d}$ ($j = 1 \ldots k$), and in particular, it can be expressed as a contraction of the 2D tensor network shown in Fig. 11.4(b) (see Appendix I). This reveals a deep relation between output states of systems with delayed coherent quantum feedback and 2D tensor network states. The unitarity of our protocol requires the tensors to satisfy

$$\sum_{i,a,b} U^{i}_{a,b,c,d} (U^{i}_{a,b,c',d'})^{*} = \delta_{c,c'} \delta_{d,d'} . \tag{11.5}$$

Physically, this isometric condition reflects the deterministic and sequential nature of the protocol. Importantly, every 2D tensor network state (or PEPS) that can be brought into a

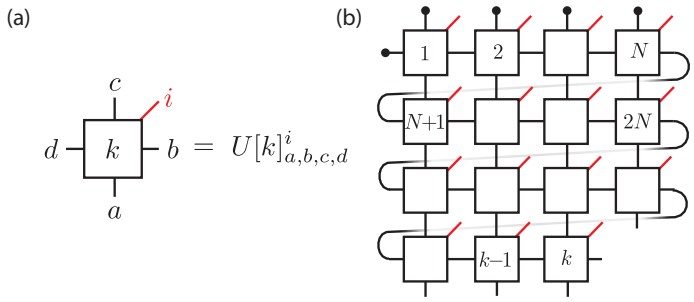

Figure 11.4: Tensor network representation of the generated states. (a) Graphical representation of the rank-5 tensors $U[k]^i_{a,b,c,d}$.The "physical index" i denotes the state of the qubit k, the "horizontal bonds" b and d run over internal degrees of freedom of $\mathcal{Q}$, and "vertical bonds" a and c enumerate the quantum states of input into and output from the delay line, respectively. (b) Representation of the state (11.4) in terms of these tensors. Connected lines indicate contractions, red open lines denote physical indices corresponding to the states of qubits in the output. In the top row the tensors are contracted with the initial state of $\mathcal{Q}$ and the vacuum state for the first N qubits in the string, as indicated by the black circles. Open legs at the bottom correspond to the state of the qubits in the delay line after step k, and the open line on the bottom right, corresponds to the state of $\mathcal{Q}$.

form respecting (11.5) can be constructed in this setting with a single quantum emitter and delayed feedback. Per construction we showed that this includes universal resources for MBQC, but it also allows to create exotic 2D states of light, exhibiting topological order such as string-net states [338] or the ground state of Kitaev's toric code Hamiltonian [339], see Appendix I.

11.4 Outlook

Our work can be extended in several ways, including the addition of multiple delay lines, leading to tensor networks in higher dimensions. This is of relevance for fault tolerant implementations of MBQC using 3D cluster states [327]. Additionally, on can envisage implementing variants of MBQC that can tolerate up to 50% of counterfactual errors due

to photon loss [340]. Finally, besides nanophotonic setups our 'single-atom quantum computer' can be implemented with microwave photons in circuit QED [323, 325], phonons or surface-acoustic waves [341].

Appendix A

Supporting Material of Chapter 2

A.1 Materials and Methods

A.1.1 Sample Fabrication

The diamond sample used in this work (type-Ib, $\sim$4 mm in diameter) was grown via high pressure and high temperature (HPHT), at 5.5 GPa and 1350 ^{o}C, using a Fe-Co alloy as a solvent. The main source of paramagnetic impurities was provided by substitutional nitrogen atoms in the neutral charge state (P1 centers) at a concentration of $\sim$100 ppm. A diamond plate of thickness $\sim$1 mm was obtained via laser cutting and polishing. To obtain NV centers, high energy electron irradiation was performed at $\sim$2 MeV with a flux of 1.3-1.4$\cdot 10^{13}$ e$\cdot$cm$^{-2}\cdot$s^{-1} and in-situ annealing at 700-800 ^{o}C up to a total fluence of 1.4$\cdot 10^{19}$ cm^{-2} (total time of 285 hrs). Additional annealing at 1000 ^{o}C for 2 hrs in vacuum was performed after half as well as after the full irradiation time. This process resulted in the diamond with NV centers of a concentration $\sim$45 ppm, corresponding to $\sim$5 nm

of average separation and $\sim (2\pi)$ 420 kHz dipole-dipole interaction strength. To control the region of optical excitation, we used angle etching to create a beam-shaped piece of diamond, of 20 μm length and $\sim$300 nm width, and transferred it onto our coplanar waveguide [36].

A.1.2 Optical Setup

As shown in Fig. A.1A, the optical setup consists of a home-built confocal microscope with a Nikon Plan Fluor 100x oil immersion objective (NA = 1.3). The sample is mounted on a xyz-piezoelectric stage in the focal plane of the microscope. Excitation of the ensemble of NV centers is performed by illuminating a green laser ($\lambda = 532$ nm) with average power less than 50 μW. Short laser pulses are generated by an acousto-optic modulator (AOM) from Isomet in a double pass configuration. The $\lambda/2$-waveplate at the objective allows the control over the polarization of excitation light. NV centers emits fluorescence into the phonon sideband (630-800 nm), which is isolated from the excitation laser by a dichroic mirror. An additional 650 nm long-pass filter further suppresses the detection of unwanted signal. After passing a pinhole the collection beam is then focused onto a single photon counting avalanche photodiode (APD) to achieve detections with confocal resolution.

To probe the spin dynamics over time, we used a pulse sequence illustrated in Fig. A.1B. We repeat the same pulse sequence twice, but include an extra π-pulse right before the read-out at end of the second sequence. The photon-count difference between the two read-outs allows us to measure the NV polarization, while being insensitive to changes in the background fluorescence due to charge dynamics [27].

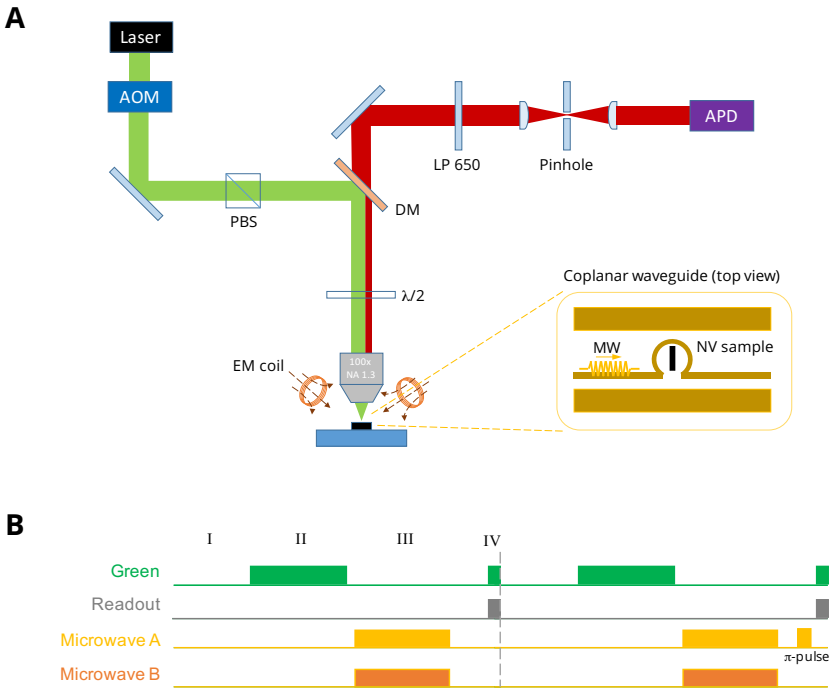

Figure A.1: **Schematic of the Optical Setup and the Pulse Sequence.** (**A**) Green and red lines indicate the optical paths (excitation: green, collection: red). An acousto-optic modulator (AOM) is used to control green laser duration. A dichroic mirror (DM) spectrally filters out the fluorescence from NV centers for electronic spin state readout. A 650 nm long pass filter additionally helps to filter fluorescence emission, corresponding to the phonon sideband (PSB) of NV centers. A 5-μm pinhole is used in combination with a single photon counting avalanche photodiode (APD) to achieve confocal detection. A polarizing beam splitter (PBS) is used to polarize the excitation beam. With the addition of a $\lambda/2$ waveplate we get control over the incident green polarization onto the diamond sample. The sample is placed ontop of a coplanar microwave (MW) structure in the shape of an omega (inset). Three electromagnetic coils are used to create a static magnetic field up to $\sim$300 Gauss in an arbitrary direction. (**B**) Typical experimental sequence used to measure NV dynamics. I: charge equilibration; II: spin polarization; III: experimental sequence; IV: spin readout.

A.1.3 Microwave Setup

To coherently control the electronic spin states of NV centers we deliver microwaves to the sample through an impedance-matched coplanar waveguide fabricated on a glass coverslip. An omega-shaped microstructure (with a inner diameter 20 μm) at the center of

the waveguide allows us to achieve Rabi frequencies up to $\sim(2\pi)$ 100 MHz. In Fig. A.2, we illustrate the schematic diagram of the microwave control system. In order to have full control over two groups of NV centers with different transition frequencies, we employ two independent microwave circuits. In each circuit, a RF signal generator (Rohde & Schwarz SMIQ06B) produces the main driving frequency; an IQ mixer (Marki IQ1545LMP) generates pulsed signals; a low-pass microwave filter (Mini-Circuits VLF-3000+) suppresses unwanted higher-order harmonics of fundamental frequencies; and a DC block (Picosecond 5501a) additionally isolates the signals from low-frequency noises. After separately amplified (ZHL-16W-43+), two RF signals are then combined by a power combiner (Mini-Circuits ZFRSC-42-S+) and delivered to our sample. The inset of Fig. A.2 depicts the detailed configuration of analog inputs (AI) connected to the IQ mixers. An arbitrary waveform generator (The Tektronix AWG7052) defines the duration and the phase of the pulses with a temporal resolution of 1 ns. For fine tuning of the voltage offset on the I and Q ports, a DC voltage is applied to the AWG signal. The addition of a 10-dB attenuator between the voltage source and the combiner suppresses unwanted reflections (see inset of Fig. A.2).

A.1.4 Magnetic Field Setup

For an external magnetic field, we use three water-cooled electromagnetic (EM) coils, which can provide a B-field up to $\sim$300 Gauss in an arbitrary orientation (see Fig. A.1A and A.3A).

As shown in Fig. A.3B, we calibrate the magnetic field by recording electron spin resonance (ESR) spectra at various values of currents in the coils; since the Hamiltonian of a NV center in the presence of a magnetic field is known, the magnetic field at the posi-

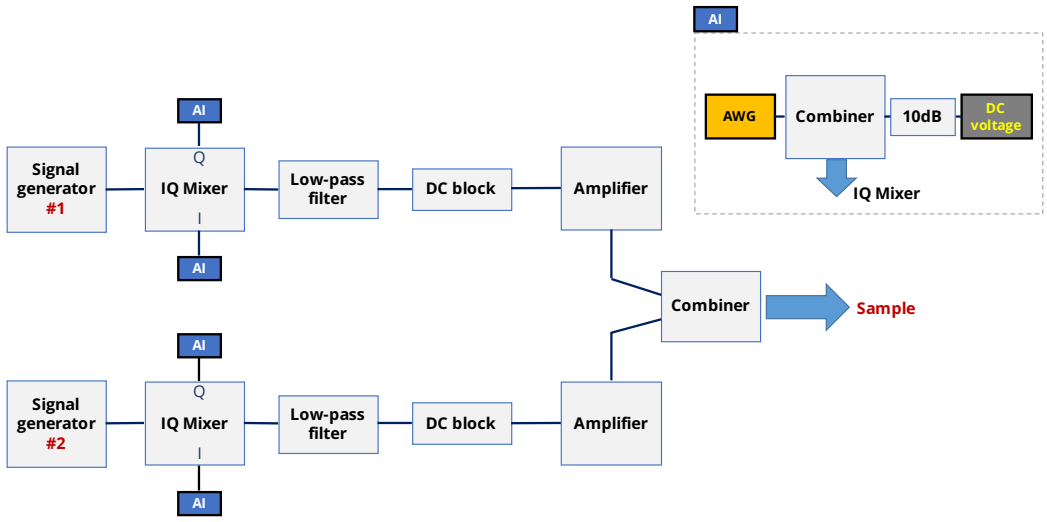

Figure A.2: **Schematic of the Microwave Control Setup.** Two sets of independent microwave circuits are used to achieve full control over two separate groups of NV centers at different transition frequencies. A 3 GHz low-pass filter suppresses unwanted higher-order harmonics. The two microwave paths are separately amplified to avoid saturation and then combined and sent to the diamond sample. In order to precisely control the microwave pulse length as well as phase, each path is sent through an IQ mixer controlled by an arbitrary waveform generator (AWG) output. The inset shows the detailed configuration of analog inputs connected to the IQ mixers used to define microwave pulse length and phase. In order to finely tune the voltage offset of the I and Q port, to achieve high isolation, a DC voltage source is combined with the AWG signal. The addition of an attenuator allows the suppression of unwanted reflections.

tion of our sample can be extracted from transitions frequencies of NV centers. For this process we utilize all four groups $\{A, B, C, D\}$ of NV centers oriented in different crystallographic axes of diamond lattice, e.g., A = [111], B = $[\bar{1}\bar{1}1]$, C = $[1\bar{1}\bar{1}]$, and D = $[\bar{1}1\bar{1}]$ (see Fig. A.3C). Fig. A.3D shows an ESR spectrum when the B-field is aligned along [111] direction; group A exhibits the largest Zeeman splitting, while the other groups B, C, and D become degenerate. In Fig. A.3E, the direction of an external B-field is perpendicular to the sample surface, i.e., B $\|$ [001], resulting in four degenerate groups.

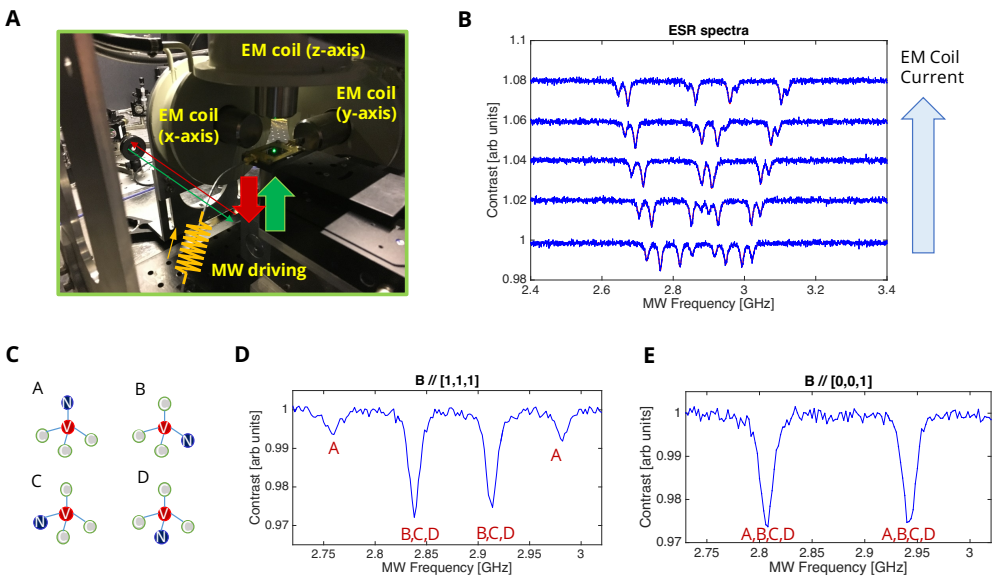

Figure A.3: **Magnetic Field Calibration and Control. (A)** Three electromagnetic (EM) coils are located in the vicinity of the diamond sample in order to provide an external magnetic field (B-field) in an arbitrary direction with an amplitude up to ∼300 Gauss. **(B)** To calibrate the coil's magnetic field, electron spin resonance (ESR) spectra are recorded for different values of coil currents. **(C)** The diamond lattice allows for four different crystallographic orientations of NV centers. The different groups A, B, C, and D of NV centers are characterized by their N-V axis orientations, i.e., A = [111], B = $[\bar{1}\bar{1}1]$, C = $[1\bar{1}\bar{1}]$, and D = $[\bar{1}1\bar{1}]$. **(D)** Measured ESR spectrum for the B-field aligned along the [111] direction. Group A exhibits the largest Zeeman splitting (highest projected $B_{||}$) because the spin quantization axis of group A is parallel to the chosen B-field. **(E)** Measured ESR spectrum for the B-field aligned along the [001] direction. Due to the [100] cutting direction of the diamond, all 4 NV groups form the same angle to the surface. With the external B-field being perpendicular to the sample surface, this leads to groups A-D having degenerate B field projections.

A.2 Characterization of Experimental System

A.2.1 On-site Potential Disorder

The ESR linewidth of an NV ensembles is influenced by multiple factors. To discuss and estimate their contributions we introduce the ground state hamilitonian of the electronic

spin state of a single NV center:

$$H = \left(\hbar\Delta_0 + d_{||}E_{||}^z\right) S_z^2 + \gamma_{NV}(\vec{S}\cdot\vec{B}) - d_\perp\left[E_\perp^x\left(S_xS_y + S_yS_x\right) + E_\perp^y\left(S_x^2 - S_y^2\right)\right], \tag{A.1}$$

where S_x, S_y and S_z denote the spin-1 matrices and $\hbar$ the reduced Planck constant; $\Delta_0 \approx (2\pi)2.87$ GHz, γ_{NV} = (2π) 2.8 MHz G^{-1}, $d_\parallel$ = (2π) 0.35 Hz cm V^{-1} and $d_\perp$ = (2π) 17 Hz cm V^{-1} are the zero field splitting, the gyromagnetic ratio, axial and perpendicular components of the ground triplet state permanent electric dipole moment of a NV center [342]. $B_{\parallel(\perp)}$ and $E_{\parallel(\perp)}$ are projection of the effective magnetic and electric field parallel (perpendicular) to the NV axis. To a leading order, we ignore the effect of the perpendicular magnetic field noise $\delta B_\perp$, since it influence less on the spin coherence than the parallel one $\delta B_\parallel$, owing to the large zero field splitting.

To account for effects of the local NV environment we include in $B_{||}$ and $E_{||(\perp)}$ on-site potential disorders originating from randomly distributed magnetic fields due to nuclear spins (i.e. ^{13}C or ^{14}N) and paramagnetic impurities (i.e. P1 centers) as well as fields caused by local electric fields and lattice strain. To quantify the different contributions to the ESR linewidth, we conduct Ramsey spectroscopy in distinct basis states as listed in Fig. A.4A. Since each basis has a well defined sensitivity to different physical noise sources, our Ramsey measurements provide insight into the local environment of the NV centers. Table A.1 lists the effects of magnetic and electric field noise on free induction decay of several different basis states. Figure A.4 shows the outcome of Ramsey spectroscopy in the five different bases defined in A.1 .

As seen in the table A.1, each coherent superposition can effectively probe different types of noise components, enabling us to quantify the relative strengths of the on-site

Definition	Wavefunction	Precession rate	Noise	$1/T_2^*$
$\|\psi_1\rangle$	$(\|0\rangle + \|1\rangle)/\sqrt{2}$	$\gamma_{NV}B_\parallel$ + $d_\parallel E_\parallel$	$\delta B_\parallel, \delta E_\parallel$	$\pi[\Gamma_{B_\parallel} + \Gamma_{E_\parallel}]$
$\|\psi_2\rangle$	$(\|0\rangle + \|-1\rangle)/\sqrt{2}$	$\gamma_{NV}B_\parallel$ + $d_\parallel E_\parallel$	$\delta B_\parallel, \delta E_\parallel$	$\pi[\Gamma_{B_\parallel} + \Gamma_{E_\parallel}]$
$\|\psi_3\rangle$	$(\|1\rangle + \|-1\rangle)/\sqrt{2}$	$2\gamma_{NV}B_\parallel$	$\delta B_\parallel$	$2\pi\Gamma_{B_\parallel}$
$\|\psi_4\rangle$	$(\|0\rangle + \|D\rangle)/\sqrt{2}$	$d_\parallel E_\parallel$ + $d_\perp E_\perp$	$\delta E_\parallel, \delta E_\perp$	$\pi[\Gamma_{E_\parallel} + \Gamma_{E_\perp}]$
$\|\psi_5\rangle$	$(\|0\rangle + \|B\rangle)/\sqrt{2}$	$d_\parallel E_\parallel$ + $d_\perp E_\perp$	$\delta E_\parallel, \delta E_\perp$	$\pi[\Gamma_{E_\parallel} + \Gamma_{E_\perp}]$

Table A.1: Five different basis states used for characterizing the local on-site disorder. The dark ($|D\rangle \equiv (|1\rangle - |-1\rangle)/\sqrt{2}$) and bright states ($|B\rangle \equiv (|1\rangle + |-1\rangle)/\sqrt{2}$) are prepared by applying an off-axis magnetic field perpendicular to an NV symmetry axis. Γ is a noise source-dependent inhomogeneous broadening contributing to the linewidth of the ESR.

potential disorder. Using the identity $\Gamma = 1/\pi T_2^*$ and the relations given in the last column of table A.1, we can estimate a value for the different noise sources $\Gamma_{B_\parallel}$, $\Gamma_{E_\parallel}$, and $\Gamma_{E_\perp}$. The discrepancy in T_2^* between $|\psi_1\rangle$ and $|\psi_2\rangle$ (as well as $|\psi_4\rangle$ and $|\psi_5\rangle$) in experimental data is presumably due to frequency-dependent field noise. By averaging these results, we can extract the three inhomogeneous broadening factors as $\Gamma_{B_\parallel}$ = 3.78(3) MHz, $\Gamma_{E_\parallel}$ = 2.18(8) MHz and $\Gamma_{E_\perp}$ = 4.30(13) MHz. The measured ESR linewidth $\Gamma_{\text{meas}} = \sqrt{8\ln 2}W \approx 9.4$ MHz (see Fig. 2.1D) roughly agrees up to a factor of $\sim$1.5 with the calculated $\Gamma_{\text{calc}} \approx 6.0$ MHz. According to this analysis, the random on-site disorder in our sample seems to result from both electric and magnetic fields with comparable weights.

A.2.2 Estimation of NV Density and Dipolar Interaction Strength

Due to the high density of NVs within our sample, the spin-echo coherence time is limited by interactions, as discussed in the main text. In particular, using the double electron-electron resonance (DEER) sequence presented in Fig. 2A in the main text, we verified experimentally that the additional dephasing of group A indeed originates from interactions with group B. Fig. A.5 shows a measurement result of the DEER sequence in which

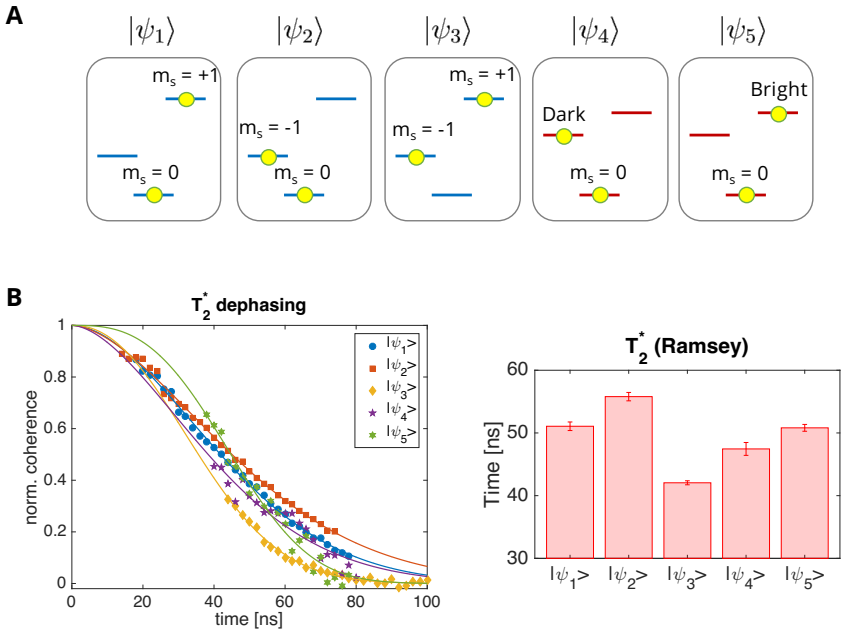

Figure A.4: T_2^* **and** T_2 **Measurements of different Basis States.** **(A)** Different initial conditions used for coherence measurements. By aligning the magnetic field parallel (perpendicular) to the NV axis, the eigenbasis for the spin state of NV centers becomes $\{|m_s = 0\rangle, |m_s = +1\rangle, |m_s = -1\rangle\}$ ($\{|m_s = 0\rangle, |Dark\rangle, |Bright\rangle\}$), where Bright and Dark states are defined as even and odd combination of the original bare spin states $|m_s = -1\rangle$ and $|m_s = +1\rangle$. **(B)** Ramsey spectroscopy data and extracted decay timescale for different initial states.

we probe the relative spin-echo amplitude at a fixed time τ as a function of driving frequency of group B. It shows a clear resonance when $\omega = \omega_0^B$, indicating that inter-group interactions between group A and B lead to enhanced dephasing.

To quantitatively analyze the dependence of decoherence rate on the spin density, we study the dynamics of interacting spins using the exact diagonalization method with the effective Hamiltonian of Eq. (A.24). Comparing the numerical result to the experimental data allows us to extract the density of NV spins in our sample.

Specifically, we simulate the time evolution of 12 NV spins under a spin echo pulse

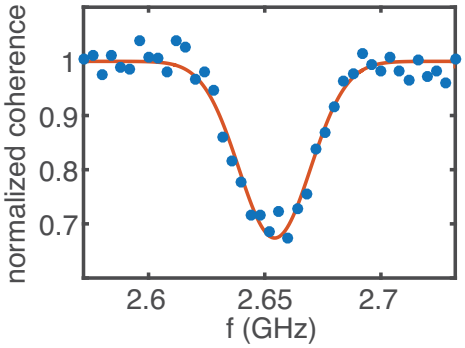

Figure A.5: **Intra-group Interaction Probed via Double Electron-Electron Resonance.** The relative, normalized spin echo coherence time at a fixed time τ as a function of driving frequency of group B.

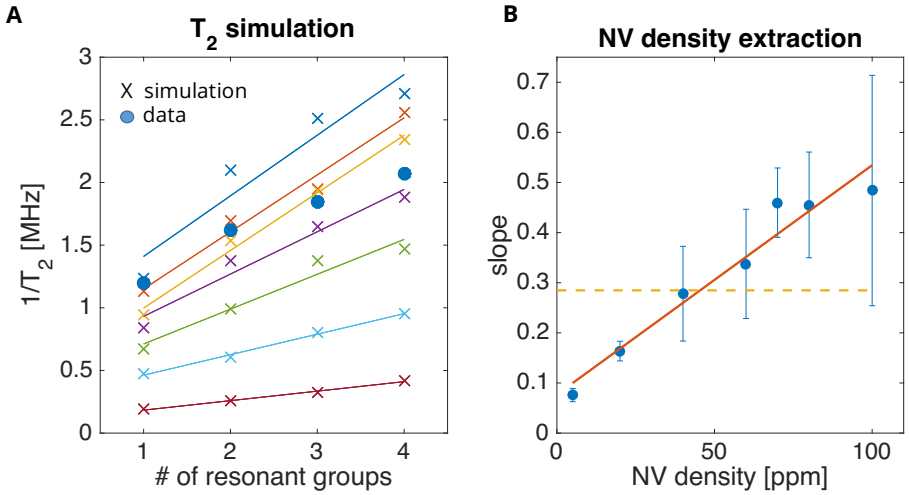

Figure A.6: **NV Density Extraction via Spin Echo Simulation.** **(A)** Comparison of the spin echo simulation results at different concentrations (crosses) to the measured data (circles). The total NV concentrations selected for the simulation are 5, 20, 40, 60, 70, 80 and 100 ppm. Solid lines are linear fits to the simulation to extract both γ_b and γ_0 in the main text. **(B)** The NV concentration can be extracted by comparing the slopes (γ_0) taken from the numerical simulations to the extracted slope of the experiment data (orange dashed line).

sequence protocol. The total NV concentrations selected for simulations are 5, 20, 40, 60, 70, 80 and 100 ppm. We averaged over ∼500 realizations of positional disorder, resulting

in a single smooth coherence curve under the spin echo sequence. We fit the coherence decay with a simple exponential function and extract the decoherence rate, $\gamma_T \equiv 1/T_2$. Fig. A.6A summarizes the spin echo simulation results as a function of the number of resonant NV groups (effective density), where a linear dependence of γ_T is identified for all the density values. We model the decoherence rate as $\gamma_T(\nu) = \gamma_b(\nu) + \nu\gamma_0(\nu)$, where ν is the number of resonant NV groups, γ_b and γ_0 are density-dependent, bare and dipolar interaction-induced dephasing rates, respectively. Such linear dependence of γ_T on ν is also confirmed in the experiment (see Fig. 2B in main text). By comparing γ_0 between the experiment and the simulation, we estimate the NV density in our sample to be $\sim$45 ppm (see Fig. A.6B).

A.2.3 Inhomogeneity of the Microwave Field

Hartmann-Hahn resonances rely on the exact matching of Rabi frequencies of two driving fields $\Omega_A = \Omega_B$. Hence, stable and precise control of the driving strength is essential in our experiments. To this end, we estimate the inhomogeneity of our microwave driving field, by measuring the decay time of Rabi oscillations at various driving strengths (Fig. A.7).

In an ideal case, the lifetime of Rabi oscialltions generally increases due to suppression of disorder (T_2^*). At higher driving strength ($W_{\text{eff}} \sim \delta^I$) this lifetime should saturate due to the effect of Ising interaction. In our measurements however we observe a slight decrease in lifetime at high driving strengths, which is well explained by a 1.1% variation in Rabi frequency. We attribute this variation to spatial inhomogeneity in the driving field. With the strongest driving in our measurement $\Omega = (2\pi)$ 32 MHz, this effect leads to a spread

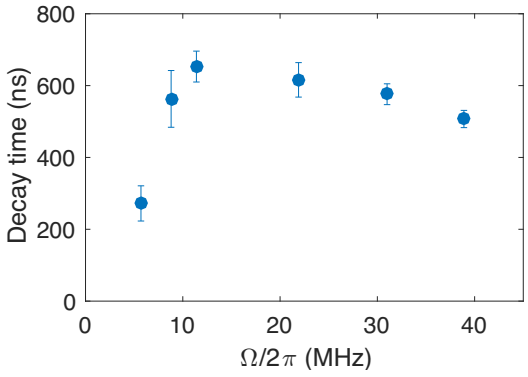

Figure A.7: **Rabi Oscillation Measurement.** Decay time of Rabi oscillations as a function of Rabi frequency Ω.

in Rabi frequencies of $\sim (2\pi)$ 0.3 kHz. While it is still smaller than the effective disorder $\sim (2\pi)$ 0.6 kHz, such an inhomogeniety ultimately limits the maximum driving strength of our thermalization experiments.

A.3 Effective Hamiltonian of a Driven System

In this section, we derive the effective Hamiltonian for a driven, dipolar interacting spin ensemble. The main idea is to work in a frame that is rotating along each NV group's quantization axis at corresponding driving frequency (ω_0^A and ω_0^B for group A and B, respectively). If the difference between ω_0^A and ω_0^B is large compared to the interaction strength, then one can ignore exchange interactions between spins from different groups (secular approximation). This results in distinct forms of intra- and inter-group interactions. We project the original Hamiltonian into two-level systems, and derive the effective Hamiltonian.

We start with the Hamiltonian for dipolar interacting NV centers

$$H = \sum_i H_i^0 + \sum_i H_i^d(t) + \sum_{ij} H_{ij}^{dd}, \tag{A.2}$$

where H_i^0 is a single particle Hamiltonian for a spin at site i, $H_i^d(t)$ is time-dependent driving, and H_{ij}^{dd} is the magnetic dipole-dipole interaction between spins at sites i and j. The first term H_i^0 includes Zeeman coupling to an external magnetic field, the zero field splitting of a NV center, and any other disordered potentials arising from couplings to paramagnetic impurities as described in the main text. In our experiments, dominant contributions for H_i^0 come from the zero-field splitting $\sim (2\pi)\ 2.87$GHz and Zeeman field projected along the quantization axis (a few hundred MHz), which are two orders of magnitude larger than the rest of the couplings. Setting $\hbar = 1$, we can write

$$H_i^0 \approx (\Delta_0 + \delta_{0,i}) \left(\hat{c}_i \cdot \vec{S}_i\right)^2 + (\Delta_B(\hat{c}_i) + \delta_{B,i}) \left(\hat{c}_i \cdot \vec{S}_i\right) \tag{A.3}$$

where $\vec{S}_i$ are spin-1 vector operators, $\hat{c}_i$ is the unit vector along the quantization axis of the spin, $\Delta_0 = (2\pi)\ 2.87$ GHz is the zero-field splitting, $\Delta_B(\hat{c}_i)$ is the Zeeman splitting along $\hat{c}_i$, and $\delta_{0,i}$ and $\delta_{B,i}$ are on-site disorder potentials. If the external magnetic field $\vec{B}$ is oriented in a way that $\Delta_B(\hat{c}_i)$ for different groups are sufficiently separated (compared to the driving strength), one can effectively address distinct groups independently. Below we assume such a case and consider resonant driving of two groups A and B using microwave frequencies $\omega_0^{A(B)} = \Delta_0 - \Delta_B(\hat{c}_{A(B)})$. The Hamiltonian for such driving is given as $H_i^d(t) = \gamma_{NV} \vec{B}_{\text{MW}} \cdot \vec{S}_i \cos(\omega_0 t)$, where γ_{NV} is the gyromagnetic ratio of the NV center, and $\vec{B}_{\text{MW}}$ is the microwave field vector. Now moving into the rotating frame with unitary transformation $U(t) = \exp\left[-i\left(\sum_i \Delta_0(\hat{c}_i \cdot \vec{S}_i)^2 + \Delta_B(\hat{c}_i)(\hat{c}_i \cdot \vec{S}_i)\right) t\right]$ and applying

rotating wave approximations, we obtain the effective single particle Hamiltonian

$$\bar{H}_i = U^\dagger(t)\left[H_i^0 + H_i^d(t)\right]U(t) - iU^\dagger\frac{d}{dt}U \tag{A.4}$$

$$= (\delta_{0,i} + \delta_{B,i})\left|1\right\rangle\left\langle 1\right| + (\delta_{0,i} - \delta_{B,i})\left|-1\right\rangle\left\langle -1\right| + \frac{\Omega}{2}\left(\left|-1\right\rangle\left\langle 0\right| + h.c.\right), \tag{A.5}$$

where $\{\left|1\right\rangle, \left|0\right\rangle, \left|-1\right\rangle\}$ is the basis of spin states along its quantization axis and Ω is the Rabi frequency of the driving.

The effective interaction among spins can be obtained in a similar way as follows. We start with the dipole-dipole interaction between spin-i and spin-j

$$H_{ij}^{dd} = -\frac{J_0}{r^3}\left(3\left(\vec{S}_i\cdot\hat{r}\right)\left(\vec{S}_j\cdot\hat{r}\right) - \vec{S}_i\cdot\vec{S}_j\right), \tag{A.6}$$

where $J_0 = (2\pi)\ 52\ \text{MHz}\cdot\text{nm}^3$ and $\vec{r}$ is the relative position between two spins. In the rotating frame, we obtain the effective interaction by replacing $\vec{S}_i \mapsto U^\dagger(t)\vec{S}_i U(t)$. Since we are interested in the interaction in the basis of each NV's own quantization axis, we first explicitly rewrite $\vec{S}_i$ in terms of (S_i^x, S_i^y, S_i^z) in a coordinate system where $\hat{z}_i$ is parallel to the quantization axis $\hat{c}_i$

$$\bar{H}_{ij}^{dd} = U^\dagger(t)H_{ij}^{dd}U(t) = -J_0/r^3\Big[\left(3\left(\hat{r}\cdot\hat{x}_i\right)\left(\hat{r}\cdot\hat{x}_j\right) - \hat{x}_i\cdot\hat{x}_j\right)S_i^xS_j^x \tag{A.7}$$

$$+\left(3\left(\hat{r}\cdot\hat{y}_i\right)\left(\hat{r}\cdot\hat{y}_j\right) - \hat{y}_i\cdot\hat{y}_j\right)S_i^yS_j^y \tag{A.8}$$

$$+\left(3\left(\hat{r}\cdot\hat{x}_i\right)\left(\hat{r}\cdot\hat{y}_j\right) - \hat{x}_i\cdot\hat{y}_j\right)S_j^xS_j^y \tag{A.9}$$

$$+\left(3\left(\hat{r}\cdot\hat{y}_i\right)\left(\hat{r}\cdot\hat{x}_j\right) - \hat{y}_i\cdot\hat{x}_j\right)S_i^yS_j^x \tag{A.10}$$

$$+\left(3\left(\hat{r}\cdot\hat{z}_i\right)\left(\hat{r}\cdot\hat{z}_j\right) - \hat{z}_i\cdot\hat{z}_j\right)S_i^zS_j^z\Big] \tag{A.11}$$

$$+H_{\text{rest}}, \tag{A.12}$$

where H_{rest} contains all the other terms of the form $S^xS^z, S^yS^z, S^zS^x, S^zS^y$.

We now perform rotating wave approximations. This is very well justified because the typical strength of the interaction is much weaker than the driving frequency $J_0/r^3 \sim (2\pi)\ 0.4$ MHz $\ll \omega_0^{A,B} \sim (2\pi)\ 2.5$ GHz. First, we note that S^x and S^y operators are rapidly oscillating in time while S^z remains invariant, $[S_i^z, U(t)] = 0$. Therefore, every term in H_{rest} may be safely ignored. Then, introducing

$$g_{ij}^{+} = \frac{1}{2}\Big[3\,(\hat{r}\cdot\hat{x}_i)\,(\hat{r}\cdot\hat{x}_j) - \hat{x}_i\cdot\hat{x}_j + 3\,(\hat{r}\cdot\hat{y}_i)\,(\hat{r}\cdot\hat{y}_j) - \hat{y}_i\cdot\hat{y}_j\Big] \tag{A.13}$$

$$g_{ij}^{-} = \frac{1}{2}\Big[3\,(\hat{r}\cdot\hat{x}_i)\,(\hat{r}\cdot\hat{x}_j) - \hat{x}_i\cdot\hat{x}_j - 3\,(\hat{r}\cdot\hat{y}_i)\,(\hat{r}\cdot\hat{y}_j) + \hat{y}_i\cdot\hat{y}_j\Big] \tag{A.14}$$

$$h_{ij}^{+} = \frac{1}{2}\Big[3\,(\hat{r}\cdot\hat{x}_i)\,(\hat{r}\cdot\hat{y}_j) - \hat{x}_i\cdot\hat{y}_j + 3\,(\hat{r}\cdot\hat{y}_i)\,(\hat{r}\cdot\hat{x}_j) - \hat{y}_i\cdot\hat{x}_j\Big] \tag{A.15}$$

$$h_{ij}^{-} = \frac{1}{2}\Big[3\,(\hat{r}\cdot\hat{x}_i)\,(\hat{r}\cdot\hat{y}_j) - \hat{x}_i\cdot\hat{y}_j - 3\,(\hat{r}\cdot\hat{y}_i)\,(\hat{r}\cdot\hat{x}_j) + \hat{y}_i\cdot\hat{x}_j\Big] \tag{A.16}$$

$$q_{ij} = 3\,(\hat{r}\cdot\hat{z}_i)\,(\hat{r}\cdot\hat{z}_j) - \hat{z}_i\cdot\hat{z}_j, \tag{A.17}$$

we can simply rewrite

$$\bar{H}_{ij}^{dd} \approx -J_0/r^3\big[g_{ij}^{+}(S_i^xS_j^x + S_i^yS_j^y) + h_{ij}^{-}(S_i^xS_j^y - S_i^yS_j^x) + q_{ij}S_i^zS_j^z \tag{A.18}$$

$$+ g_{ij}^{-}(S_i^xS_j^x - S_i^yS_j^y) + h_{ij}^{+}(S_i^xS_j^y + S_i^yS_j^x)\big]. \tag{A.19}$$

Here, g^+ and h^- terms correspond to "flip-flop" type transitions, exchanging one unit of spin polarization,

$$(S_i^xS_j^x + S_i^yS_j^y) = |{+}0\rangle\langle 0{+}| + |{+}{-}\rangle\langle 00| + |00\rangle\langle -{+}| + |0{-}\rangle\langle -0| + h.c. \tag{A.20}$$

$$(S_i^xS_j^y - S_i^yS_j^x) = i\big(\,|{+}0\rangle\langle 0{+}| + |{+}{-}\rangle\langle 00| + |00\rangle\langle -{+}| + |0{-}\rangle\langle -0|\,\big) + h.c. \tag{A.21}$$

In addition, owing to the strong anharmonic level structure, we may also ignore flip-flop transitions between levels with large energy differences, e.g. terms such as $|{+}{-}\rangle\langle 00|$. Finally, we ignore the terms in Eq. (A.19) as they correspond to double flip-up or flip-down

and rapidly oscillate in time. After these approximations, the effective interaction becomes

$$\bar{H}_{ij}^{dd} \approx -J_0/r^3 \left[\left(g_{ij}^{+} + i h_{ij}^{-} \right) |+0\rangle \langle 0+| + |0-\rangle \langle -0| + h.c. + q_{ij} S_i^z S_j^z \right]. \tag{A.22}$$

Now we divide into two cases depending on whether spins i and j belong to the same group or to different groups. In the former case, the quantization axes coincide, and we can simplify $h_{ij}^{-} = 0$, $g_{ij}^{+} = \frac{1}{2}(1 - 3\cos^2\theta)$, and $q_{ij} = -(1 - 3\cos^2\theta)$ with $\cos\theta \equiv \hat{z} \cdot \hat{r}$. In the latter case, the flip-flop terms are again rapidly oscillating, and only the Ising interaction $S_i^z S_j^z$ remains, resulting in

$$\bar{H}_{ij}^{dd} \approx \begin{cases} -\frac{J_0 q_{ij}}{r^3} \left(-\frac{|+0\rangle\langle 0+| + |0-\rangle\langle -0| + h.c.}{2} + S_i^z S_j^z \right) & \text{same group} \\ -\frac{J_0 q_{ij}}{r^3} S_i^z S_j^z & \text{different groups} \end{cases}. \tag{A.23}$$

These interactions as well as the single particle terms conserve the total population of spins in $|+\rangle$. Therefore, once the system is initialized into a state with no population in $|+\rangle$, the dynamics remains in the manifold spanned by $|-\rangle$ and $|0\rangle$. Projecting $\sum_i \bar{H}_i + \sum_{ij} \bar{H}_{ij}^{dd}$ into this manifold, we obtain the Hamiltonian for an effective two-level system. Introducing spin-1/2 operators $\vec{s}$ for two levels $|-\rangle$ and $|0\rangle$, we obtain $H_T = H_A + H_B + H_{AB}$, where

$$H_{A(B)} = \sum_{i \in A(B)} \left[(\delta_{0,i} - \delta_{B,i}) s_i^z + \Omega_{A(B)} s_i^x \right] + \sum_{i,j \in A(B)} \frac{J_0 q_{ij}}{r_{ij}^3} \left(s_i^x s_j^x + s_i^y s_j^y - s_i^z s_j^z \right), \tag{A.24}$$

$$H_{AB} = -\sum_{i \in A, j \in B} \frac{J_0 q_{ij}}{r_{ij}^3} s_i^{z_A} s_j^{z_B}, \tag{A.25}$$

up to a constant.

Finally, we remark one particularly interesting aspect of this Hamiltonian in the dressed-state basis, i.e., quantization along s_i^x. With sufficiently strong driving, s_i^x becomes a good spin polarization basis, and one can rewrite the interactions in terms of $s^{\pm} = s^y \pm i s^z$, wherein the intra-group interaction becomes $\propto s_i^x s_j^x + (s_i^+ s_j^+ + s_i^- s_j^-)/2$ and the inter-group

interaction $\propto (s_i^+ s_j^- + s_i^+ s_j^+ + h.c.)$. Here, we find that spin exchange terms ($s_i^+ s_j^- + h.c.$) are missing in the intra-group interaction. Omitting the energy non-conserving terms such as $s_i^+ s_j^+$ (secular approximation with a strong driving strength Ω), we obtain the effective Hamiltonian described in the main text.

A.4 Resonance Counting Theory

In this section, we provide a detailed study of the single particle resonance counting theory. We will first focus on the case of quenched on-site potential disorder, deriving the disorder-dependent power-law relaxation presented in the main text. Then, we generalize the result to the case when disordered potentials are time-dependent.

A.4.1 Disorder-dependent Power-law Decay

As discussed in the main text, we estimate the survival probability of a single spin excitation based on a simple counting argument. At time t, we compute the probability $\mathrm{Pr}(k;t)$ that the central spin is connected to $k-1$ other spins via a network of resonances, as defined in the main text. Assuming that the population of the excitation is equally shared among a resonating cluster, the survival probability is given as

$$P(t) \approx \sum_{k=1}^{\infty} \frac{1}{k} \mathrm{Pr}(k;t). \tag{A.26}$$

reducing our problem to the computation of $\mathrm{Pr}(k;t)$. Below we will show that the dominant contributions arise from $k=1$, suggesting that finding a single resonant partner is usually enough to delocalize the spin excitation over the entire sample.

In general, the exact calculation of $\Pr(k;t)$ is difficult. This is because the connectivity of the resonance network is correlated due to the spatial structure (d-dimensional Euclidean space) as well as a given assignment of random on-site potentials, e.g., if spin pairs (a,b) and (b,c) are pair-wise resonant, it is likely that the pair (a,c) is also resonant, etc. However, the qualitative behavior of $\Pr(k;t)$ can still be well-understood by ignoring these correlations. In such a case, we may assume that the number of resonant partners ℓ for a spins is drawn from a probability distribution $p(\ell)$ and that this process can be iterated for each partner. We note that such a process may not terminate, in which case the central excitation becomes delocalized over a macroscopic number of spins. We first compute $p(\ell)$ as a function of time t. For $\ell = 0$, a spin of interest (spin-i) must not have any resonating spins at any distance from r_{min} to $R(t) \equiv (J_0 t)^{1/3}$, where r_{min} is the short-distance cut-off. Hence, $p(0;t)$ is given as a product of probabilities:

$$p(0;t) = \prod_{r_{\text{min}} \le r < R(t)} \left(1 - 4\pi n r^2 dr \frac{\beta J_0 / r^3}{W_{\text{eff}}}\right) \tag{A.27}$$

$$= \exp\left[-\int_{r_{\text{min}}}^{R(t)} \frac{4\pi n Q_{\text{res}}}{r} dr\right] \tag{A.28}$$

where $4\pi n r^2 dr$ is the probability of finding a spin at distance r, and $Q_{\text{res}} = \beta J_0/(W_{\text{eff}} r^3)$ is the probability that the spin resonates with the spin-i. Defining $\lambda(t) = 4\pi Q_{\text{res}}(\ln R(t) - \ln r_{\text{min}})$, we obtain $p(0;t) = \exp[-\lambda(t)]$. Similarly, we can calculate $p(\ell;t)$ for $\ell > 0$, and obtain $p(\ell;t) = \frac{1}{\ell!}(\lambda(t))^{\ell} e^{-\lambda(t)}$, which is the Poisson distribution with mean $\lambda(t)$.

To show that the dominant contribution of Eq. (A.26) arises from the $k = 1$ term, we consider the probability of the termination of the resonance finding process, P_{term}. It satisfies the self-consistency equation

$$P_{\text{term}} = e^{-\lambda} + \sum_{\ell=1}^{\infty} \frac{\lambda^{\ell} e^{-\lambda}}{\ell!} (P_{\text{term}})^{\ell}, \tag{A.29}$$

where the first term corresponds to the case where the initial spin does not have any resonance up to time t, while the second term implies the termination of each sub-graph generated from ℓ resonant spins. For sufficiently large λ, P_{term} becomes small, and its contribution is dominated by the first term ($\ell = 0$). In our case, $\lambda(t)$ is a function of time which diverges in the limit $t \to \infty$. As we are interested in the late time dynamics, we may consider the first term only. In terms of $\Pr(k;t)$, this corresponds to approximating $\Pr(k;t) \sim 0$ for $k > 2$. Finally, noting that that $\Pr(k = 1;t) = p(0;t)$, we recover the expression in the main text.

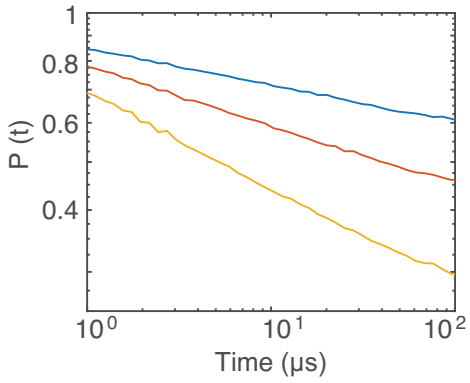

Figure A.8: **Single-particle simulation of power-law dynamics.** Blue, red, and yellow curve correspond to $\Omega = (2\pi)$ 3, 8, and 20 MHz, respectively. For the simulations, we use 10^4 spins and average over more than 10^3 disorder realizations.

We numerically test the analytic resonance counting that predicts the power-law decay dynamics. In the limit of single-particle excitation, the survival probability $P(t) = |\langle\psi(t)|\psi(0)\rangle|^2$ can be computed at any time t after the time evolution of a system under H_{eff} (See Eq. (1) in the main text). Considering physically relevant parameters used in the experiments, we verify such power-law decay dynamics for up to 10^4 spins as shown in Fig. A.8. Moreover, we confirm the extracted power-law exponent is inversely proportional

to effective disorder W_{eff} (Fig. 4C in the main text), further substantiating the thermalization mechanism based on rare resonances. The power-law exponents extracted from the simulations are summarized in Fig. A.12A.

A.4.2 Interplay between Dimensionality and long-range Interaction

The critical nature of a disordered dipolar spin ensemble in three dimensions originates from the interplay between long-range interactions and dimensionality. To see this, we can generalize the resonance counting analysis for a situation in which a single particle excitation is located in a d-dimensional spin system with long-range coupling decaying as $1/r^{\alpha}$. In such a setting, the survival probability $P(t)$ can be expressed as,

$$P(t) = \exp\left[-\int_{r_{\text{min}}}^{R(t)} nS_d r^{d-1} \frac{\beta J_0/r^{\alpha}}{W_{\text{eff}}} dr\right] \tag{A.30}$$

$$= \exp\left[-\frac{nS_d \beta J_0}{W_{\text{eff}}} \int_{r_{\text{min}}}^{R(t)} r^{d-\alpha-1} dr\right], \tag{A.31}$$

where S_d is the surface area of the d-dimensional volume. In fact, the argument of $P(t)$, $\int_{r_{\text{min}}}^{R(t)} r^{d-\alpha-1} dr$, is associated with the probability of finding a resonance up to the distance $R(t)$ reachable at time t. Hence, when the dimensionality d is larger (smaller) than the interaction strength α, the above integral diverges (converges) as $R(t)$ becomes large, which implies delocalization (localization) of the single particle excitation. In the critical case where d is equal to α, the resonance probability increases at a slow logarithmic rate, resulting in the power-law relaxation of the initial spin state as derived in Eq. (2) in the main text. In the limit of single particle excitations we therefore associate our system dynamics to such criticality behavior. However, due to the presence of many-spin excitations, much richer dynamics may appear at longer times. We attribute the deviation of power-law

dynamics at late times observed in our experiments to this effect.

A.4.3 Time-dependent Disorder

Now we consider the case of time-dependent disorder. For concreteness, we assume that the on-site potential disorder is given as a sum of a static and a dynamical disorder potential, $\tilde{\delta}_i(t) = \tilde{\delta}_i^s + \tilde{\delta}_i^d(t)$, where the static part $\tilde{\delta}_i^s$ (dynamical part $\tilde{\delta}_i^d(t)$) is random with zero mean and standard deviation W_s (W_d). While $\tilde{\delta}_i^s$ is time-independent, the dynamical component $\tilde{\delta}_i^d(t)$ changes over time by uncorrelated jumps at a rate $\Gamma = 1/\tau_d$. Here, we focus on an experimentally relevant regime where $W_s \gg W_d \gtrsim nJ_0 > 1/\tau_d$.

As already mentioned in the main text, we modify the resonance criteria as follows. Two spins at sites i and j are on resonance at time t if: (1) *at any point in time* $t' < t$, their energy mismatch is smaller than their dipolar interaction strength, $|\tilde{\delta}_i(t') - \tilde{\delta}_j(t')| < \beta J_{ij}/r_{ij}^3$, and (2) the interaction occurs within the time-scale t, $J_{ij}/r_{ij}^3 > 1/t$. While the second part of the condition is unchanged, the first part now captures that a pair may be brought into resonance by spectral jumps. Under the hierarchy of $W_s \gg W_d \gtrsim nJ_0 > 1/\tau_d$, the condition (1) can be approximated by two independent events: (a) the static energy mismatch is small enough, $|\tilde{\delta}_i^s - \tilde{\delta}_j^s| < W_d$, and (b) the dynamical energy mismatch is smaller than the coupling strength, $|\tilde{\delta}_i^d(t') - \tilde{\delta}_j^d(t')| < \beta J_{ij}/r_{ij}^3$ at some time $t' < t$. In combination, the condition (1) is satisfied with the probability

$$P_{\text{res}}(r,t) \approx \frac{W_d}{W_s}\left(1 - e^{-\frac{\beta J_0/r^3}{W_d}\frac{t}{\tau_d}}\left(1 - \frac{\beta J_0/r^3}{W_d}\right)\right) \tag{A.32}$$

which is the product of probabilities for conditions (a) and (b). For the second factor, we used the probability that the initial configuration is off-resonant, $(1 - \frac{\beta J_0/r^3}{W_d})$, and the probability that none of the subsequent spectral jumps brings them into resonance $e^{-\frac{\beta J_0/r^3}{W_d}\frac{t}{\tau_d}}$.

We note that, in practice, one should use $\max(0, 1-\beta J_0/W_d r^3)$ instead of $(1-\beta J_0/W_d r^3)$ since a probability cannot be less than zero. Finally, the survival probability is obtained by requiring no resonance at every distance r up to $R(t) = (J_0 t)^{1/3}$

$$\overline{P(t)} = \exp\left[-\int_{r=r_0}^{R(t)} 4\pi n r^2 P_{\text{res}}(r,t) dr\right], \tag{A.33}$$

where r_0 is the short distance cut-off of the NV separations. We use the cut-off distance $r_0 \sim 1.4$ nm, at which the corresponding dipole-dipole interaction is $J_0/r_0^3 \sim (2\pi)\ 20$ MHz. Due to dipole blockade, a pair of NV centers closer than r_0 cannot be addressed by microwave driving of Rabi frequency $\Omega \sim (2\pi)\ 20$ MHz, which we use for initial preparations of spin states. Those spins do not participate in the spin exchange dynamics due to large energy mismatch. We note that, $\lim_{\Gamma\to 0} P_{\text{res}}(r,t) \to Q_{\text{res}}(r) = \beta J_0/(W_s r^3)$ and the Eq. (A.33) correctly reduces to the disorder-dependent power-law decay. In the presence of a small but finite $\Gamma = 1/\tau_d$, integrating Eq. (A.33) using Eq. (A.32) yields,

$$\overline{P(t)} = P_1(t) P_0(t), \tag{A.34}$$

where

$$P_1(t) = \exp\left[-\frac{4\pi n}{3}\frac{W_d}{W_s}\left\{J_0(t-t_0) - J_0(te^{-\frac{\beta}{W_d\tau_d}} - t_0 e^{-\frac{t}{t_0}\frac{\beta}{W_d\tau_d}})\right\}\right] \tag{A.35}$$

$$P_0(t) = \exp\left[-\frac{4\pi n J_0\beta}{3W_s}\left\{(1+t/\tau_d)\mathcal{G}[0, \frac{\beta}{W_d\tau_d}] - (1+t/\tau_d)\mathcal{G}[0, \frac{t}{t_0}\frac{\beta}{W_d\tau_d}]\right\}\right]. \tag{A.36}$$

Here $\mathcal{G}$ is an incomplete Gamma function. In the limit of the hierarchy $W_s \gg W_d \gtrsim nJ_0 > 1/\tau_d$, we can simplify:

$$P_1(t) \approx C_1 \exp\left[-\frac{4\pi n}{3}\frac{W_d}{W_s}\left(J_0 t(1 - e^{-\frac{\beta}{W_d\tau_d}})\right)\right] \tag{A.37}$$

$$\approx C_1 \exp\left[-\frac{4\pi n J_0\beta}{3W_s}\frac{t}{\tau_d}\right] \tag{A.38}$$

$$\equiv C_1 \exp[-t/T^*], \tag{A.39}$$

where C_1 is a time-independent prefactor and

$$T^* = \frac{3W_s\tau_d}{4\pi nJ_0\beta} \propto \frac{W_s\tau_d}{nJ_0}. \tag{A.40}$$

Similarly, $P_0(t)$ can also be simplified as,

$$P_0(t) \approx C_2 \exp\left[-\frac{4\pi nJ_0\beta}{3W_s}\left\{\mathcal{G}[0, \frac{\beta}{W_d\tau_d}] - \mathcal{G}[0, \frac{t}{t_0}\frac{\beta}{W_d\tau_d}]\right\}\right] \tag{A.41}$$

$$\approx C_2' \exp\left[-\frac{4\pi nJ_0\beta}{3W_s}\ln(t/t_0)\right] \tag{A.42}$$

$$= C_2'(t/t_0)^{-\frac{4\pi nJ_0\beta}{3W_s}}. \tag{A.43}$$

Here we used the approximation $\mathcal{G}(0, z) \approx -\ln(z) + \gamma + \mathcal{O}(z)$ for $z \ll 1$. Once again, we rediscover the power-law decay (Eq. (A.43)) predicted in the main text, but now only up to a finite time T^*:

$$\overline{P(t)} = P_1(t)P_0(t) \propto e^{-t/T^*}t^{-\frac{4\pi nJ_0\beta}{3W_s}}. \tag{A.44}$$

Therefore, according to the Eq. (A.44), the weak time-dependent disorder results in a multiplicative exponential correction to the power-law decay up to $t < T^*$, beyond which the thermalization accelerates substantially. Furthermore, our theory model predicts that T^* is linearly proportional to the static disorder strength W_s, which is consistent with our observations (See Fig. 3D and Fig. 4D in the main text).

A.5 Detailed Analysis of Thermalization Experiments

A.5.1 Effective Disorder Control under Spin-locking Conditions

To investigate the interplay between disorder and interaction experimentally, it is required to tune both disorder and interaction in a controlled way. In our experiments, we

rely on a spin-locking technique in which both the energy spacing and the on-site disorder of a spin ensemble can be controlled in a continuous fashion.

As discussed in the main text, spin-locking allows us to prepare spins in the dressed state basis. In the new basis, the energy eigenstates are $|\pm\rangle \approx (|m_s = 0\rangle \pm |m_s = -1\rangle)/\sqrt{2}$ and are split by an effective Rabi frequency of a spin-lock field, $\Omega_{\text{eff}} = \sqrt{\Omega^2 + \delta^2}$, where Ω is the driving strength and δ is the on-site disorder in the bare frame. Owing to a random distribution of δ, the new level spacing Ω_{eff} is also a random variable. Therefore, an effective disorder under the spin-locking condition can be defined as,

$$W_{\text{eff}} \equiv \sqrt{\text{Var}[\Omega_{\text{eff}}]} = \sqrt{E[\Omega^2 + \delta^2] - E[\sqrt{\Omega^2 + \delta^2}]^2}, \tag{A.45}$$

where $\text{Var}[X]$ and $E[X]$ are the variance and expectation value of a random variable X. Since the disorder in the bare frame follows a Gaussian distribution with a standard deviation W, the expectation values can be expressed as

$$E[\Omega^2 + \delta^2] = \frac{1}{\sqrt{2\pi W^2}} \int_{-\infty}^{+\infty} d\delta \; [\Omega^2 + \delta^2] e^{-\delta^2/2W^2} \tag{A.46}$$

$$E[\sqrt{\Omega^2 + \delta^2}] = \frac{1}{\sqrt{2\pi W^2}} \int_{-\infty}^{+\infty} d\delta \; \sqrt{\Omega^2 + \delta^2} e^{-\delta^2/2W^2}. \tag{A.47}$$

In the case of weak driving ($\Omega \ll \delta$), $W_{\text{eff}} \approx \sqrt{\text{Var}[\delta]} = W$; namely, the effective disorder is almost equal to that in the bare frame. However, as the driving strength Ω increases we find $W_{\text{eff}} \approx \sqrt{\text{Var}[\frac{\delta^2}{2\Omega}]} = \frac{W^2}{\sqrt{2}\Omega}$. Hence, the effective disorder W_{eff} can be tuned by adjusting the Rabi frequency Ω in the dressed state basis.

We note that the probability distribution of Ω_{eff} is highly asymmetric, which may lead to small corrections to our counting argument at a quantitative level. To this end, for our numerical computations, we use an alternative definition of W_{eff} which is consistent with our resonance counting argument. Recall that two spins at site i and j with separation r are

defined to be on resonance when $|\tilde{\delta}_i - \tilde{\delta}_j| < \beta J_0/r^3$ and that we assumed this occurs with probability $Q_{\text{res}} \propto (J_0/r^3)/W_{\text{eff}}$. Therefore, the effective disorder strength W_{eff} should be defined in the same way from the full distribution of Ω_{eff}. More specifically, we compute the probability $q(\xi)$ that two independent random variables $\tilde{\delta}_i$ and $\tilde{\delta}_i$ satisfy $|\tilde{\delta}_i - \tilde{\delta}_j| < \xi$ for a small parameter ξ. In the limit of $\xi \ll W^2/\sqrt{2}\Omega$, the probability $q(\xi)$ is linearly proportional to ξ. Then, we define the effective disorder as $W_{\text{eff}} \equiv \lim_{\xi \to 0} \xi/q(\xi)$. Fig. A.9 shows the dependence of W_{eff} as a function of Ω. In the limit of large Ω, the effective disorder scales as $W_{\text{eff}} \propto 1/\Omega$, as expected.

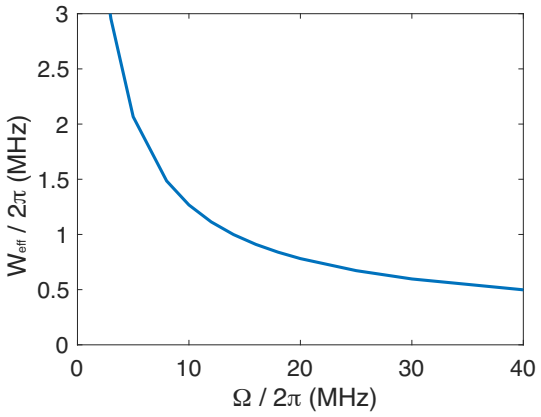

Figure A.9: **Effective disorder under spin locking conditions.** Based on the resonance counting argument, the effective disorder W_{eff} can be computed as a function of the Rabi frequency Ω.

A.5.2 Effects of Incoherent Dynamics

In our Hartman-Hahn experiments, the spin dynamics are governed by both coherent cross-relaxation and incoherent depolarization. These two effects have qualitatively different dependence on the driving strength and can be clearly distinguished in our observations.

To perform a detailed analysis of the results presented in the main text, we focus on the coherent dynamics by normalizing our data at the Hartman-Hahn resonance $\Omega_A = \Omega_B$ via a sufficiently detuned case $|\Omega_A - \Omega_B| \gg nJ_0$, at which the spin relaxations are dominated by incoherent dynamics (Fig. A.10, blue line). Such normalization can be justified only if the two effects are independent and multiplicative. This is the case if the incoherent dynamics are induced by an independent Markovian noise, which results in an exponential and multiplicative factor $e^{-\gamma t}$. In our experiment, however, we observe a stretched exponential $e^{-\sqrt{t/T}}$ decay profile from incoherent dynamics (Fig. 2D in the main text). Below, we explain why such incoherent decays are still factorizable.

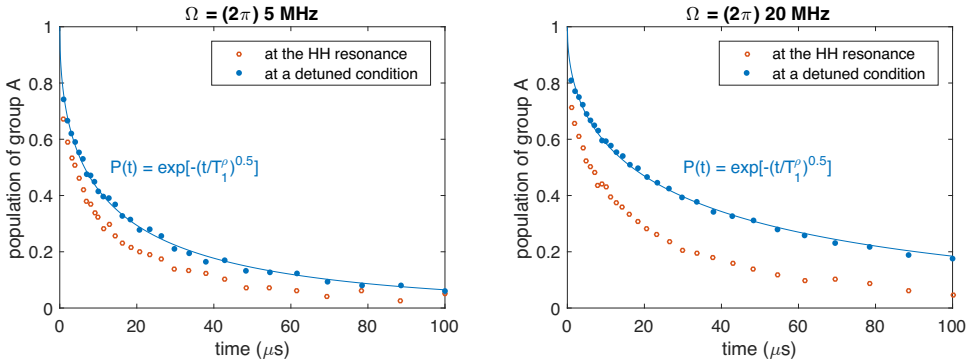

Figure A.10: **Unnormalized experimental Data.** Two data sets with different common Rabi frequencies of $\Omega = (2\pi)$ [5, 20] MHz are presented at the Hartmann-Hahn resonance (red) and at the far-detuned case (blue). For the detuned signal, a stretched exponential of power 0.5 is fitted to the data.

Our incoherent dynamics can be modeled as follows. (See Ref. [27] for more details). Each spin at site i undergoes incoherent depolarization at rate γ_i. This rate γ_i is determined by the microscopic local environment of the spin and follows a random distribution

$\rho(\gamma; T_1^\rho)$, such that the ensemble averaged polarization decays as a stretched exponential

$$e^{-\sqrt{t/T_1^\rho}} = \int_0^\infty \rho(\gamma; T_1^\rho) e^{-\gamma t} d\gamma. \tag{A.48}$$

The analytical expression as well as the microscopic origin of the distribution $\rho(\gamma; T_1^\rho)$ are presented in Ref. [27]. At the Hartman-Hahn condition, both the incoherent process and the coherent cross-relaxation lead to depolarization (see Fig. A.10). Hence, at time t, the rate of depolarization for spin-i is given by $\dot{p}_i(t) = -[\gamma_i + f_i(t)]p_i(t)$, where $f_i(t)$ is the rate of cross-relaxation (which generally depends on the state of other spins). This cross-relaxation, once averaged over an ensemble, leads to a power-law decay as derived in the previous section. The differential equation for the polarization is exactly solvable with the solution $p_i(t) = e^{-\gamma_i t} e^{\int_0^t f_i(t')dt'}$, where one finds a multiplicative exponential factor $e^{-\gamma_i t}$. Crucially, this effect is still factorizable, even after ensemble averaging:

$$\langle p_i(t) \rangle_{\text{ensemble}} = \int_0^\infty \rho(\gamma; T_1^\rho) e^{-\gamma_i t} d\gamma \left\langle e^{\int_0^t f_i(t')dt'} \right\rangle_{\text{ensemble}} \propto e^{-\sqrt{t/T_1^\rho}} \cdot t^{-\eta}, \tag{A.49}$$

where η is the disorder dependent exponent derived in the main text. Physically, this factorization arises because the microscopic environment for each spin, which determines coherent as well as incoherent dynamics, is random and independent. For this reason, in the experiment, we normalize the polarization decay at the Hartmann-Hahn resonance (Fig. A.10, red line) by the incoherent decay at the far-detuned case (Fig. A.10, blue line).

A.5.3 Dependence of Thermalization Dynamics on Spin Bath Polarization

In Fig. A.11, the theory prediction from Eq. (A.33) is compared with experimental data for various Rabi frequencies and two different initial polarizations of group B spins. The

functional profiles of the decay are consistent with power laws for over a decade, followed by accelerated, though still sub-diffusive relaxation at late times. In the power-law regime, we find that the power-law decay exponents depend on the initial polarization of group B spins (Fig. A.12A). This is consistent with our theory; for single-particle dynamics, we expect that the power-law exponent scales as $\sim nJ/W_{\text{eff}}$, where n is the density of oppositely polarized spins. Indeed, when group B is initially unpolarized, the exponents are decreased by a factor of two compared to the fully polarized case, consistent with our theory at a quantitative level.

To characterize the late-time acceleration of the polarization decay, we use the time-dependent model where the pair-resonance counting criteria are modified as discussed in the previous section. By fitting the experimental data to our model using a Monte-Carlo (MC) optimization, we extract the parameters of the dynamical disorder strength W_d and spectral diffusion time $\tau_d = 1/\Gamma$. Here, we assume W_d as a global fit parameter which is independent from Ω; this is because we expect W_d to be predominantly determined by the mean-field interaction strength. In contrast, τ_d may in principle be dependent on Ω since the fluctuations of the Ising mean-field potential depend on the thermalization speed and hence also on the effective disorder strength tuned by Ω. To this end, we performed two independent MC optimizations where we (i) treat W_d as global (Ω-*independent*) and τ_d as local (Ω-*dependent*) variables (Fig. A.11A), or instead (ii) fix both parameters as global variables (Fig. A.11B). For the static effective disorder, we use the theory-predicted values $W_s \sim W^2/\Omega$ (as described previously). Naturally, owing to the larger number of fit parameters, a global W_d with local τ_d variation (Fig. A.11A) shows better agreement than a global W_d together with with global τ_d (Fig. A.11B). In the latter case, extracted fit

parameters W_d and τ_d are $(2\pi)\ 46 \pm 14$ kHz and $43 \pm 9\ \mu s$, respectively.

In the former case (Fig. A.11A), the extracted dynamical disorder $W_d \sim (2\pi)\ 0.5$ MHz is consistent with the expected strength of the Ising interaction, suggesting that spin-spin interactions play an important role for the time-dependent disorder. Furthermore, τ_d is also consistent with the observed NV depolarization timescale, including contributions from both coherent cross-relaxation and incoherent spin depolarization. We note that in the fully polarized case the extracted values for τ_d are smaller than those in the unpolarized case (Fig. A.12B). We speculate that this could be due to faster coherent spin-exchange dynamics in the former case, giving rise to a faster fluctuation in δ^I, responsible for the accelerated thermalization dynamics at late times.

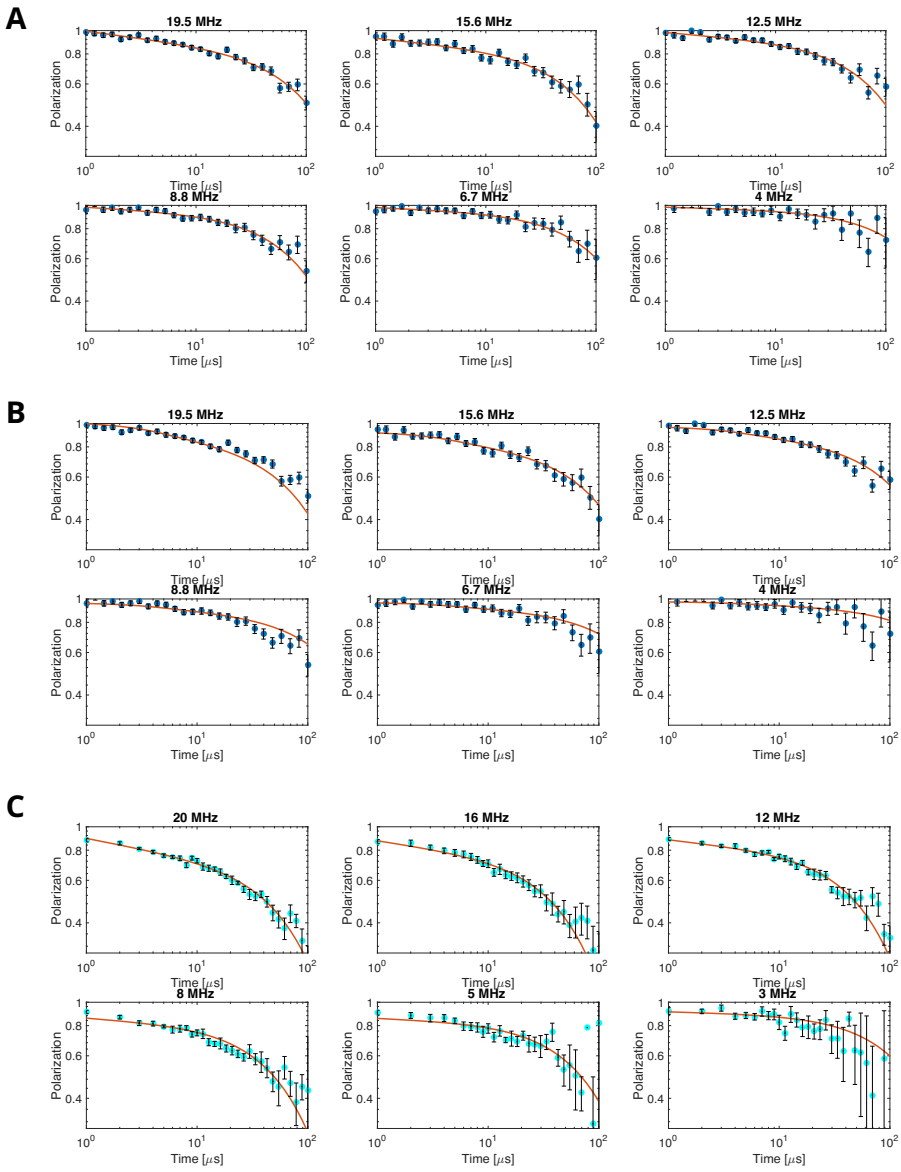

Figure A.11: **Polarization decay of a NV ensemble under Hartmann-Hahn conditions.** An initially polarized group A spin ensemble interacts with **(A,B)** unpolarized and **(C)** fully polarized group B. Solid lines are theoretical fits based upon a time-dependent disorder model with extracted parameters (W_d, τ_d) via a Monte-Carlo optimization. In **(A,C)**, the spectral diffusion time τ_d is dependent on the Rabi frequency, while in **(B)** τ_d is independent of the applied Rabi frequency. The dynamical disorder strength W_d is a Ω-independent, global variable in all three cases.

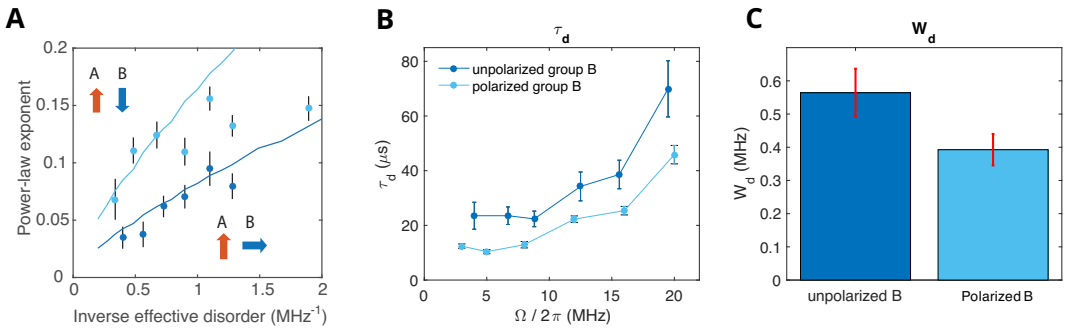

Figure A.12: **Fitted parameters of the time-dependent disorder model extracted from a Monte-Carlo optimization.** **(A)** Exponents of the power-law decay of group A polarization with oppositely polarized (light blue) and unpolarized (dark blue) group B as a function of inverse effective disorder. Solid lines correspond to numerical simulation results. **(B)** The extracted τ_d as a function of Rabi frequency. Light and dark blue point corresponds to fully oppositely polarized and unpolarized group B spin states, respectively. **(C)** The extracted dynamical disorder W_d. All errorbars are evaluated from the standard deviation of the optimized parameter after running 10 independent Monte-Carlo runs.

Appendix B

Supporting Material of Chapter 3

B.1 Methods

B.1.1 Experimental sequence.

Initial polarization of NV centers into $|m_s = 0\rangle$ is performed via laser illumination at a wavelength of 532 nm, a power of $50\ \mu$W and a duration of 100 μs. Subsequent application of a microwave $-\pi/2$ pulse along the $\hat{y}$ axis is used to coherently rotate the spin ensemble into $|+\rangle = (|m_s = 0\rangle + |m_s = -1\rangle)/\sqrt{2}$. The spins are then subjected to continuous driving at a Rabi frequency $2\pi \times 54.6\,$MHz along the $\hat{x}$ axis for a duration τ_1. This so-called spin-locking technique suppresses two-spin (flip-flip and flop-flop) processes, owing to energy conservation, and decouples spins from their environment[53]. In our sample, this technique leads to spin lifetimes of $T_1^\rho \approx 60\ \mu$s[27]. Finally, we apply a short microwave pulse along the $\hat{y}$ axis over an angle $\theta \approx \pi$. We repeat this Floquet cycle with various values of θ, controlled by changing the Rabi driving strength as well as the pulse duration. The

imperfection in microwave manipulations (for initialization into $|+\rangle$ as well as rotation angles θ) amounts to 0.9%, arising from a combination of spatial inhomogeneity of the driving field (0.8%) as well as on-site potential disorder (0.6%). Following a coherent time evolution, the spin state of the NV ensemble is optically detected by applying a final $\pi/2$ pulse along the $\hat{y}$ axis and measuring the population difference in the $|m_s = 0\rangle$ and $|m_s = -1\rangle$ basis. The polarization is defined as $P = \mathcal{P}_0 - \mathcal{P}_{-1}$ with $\mathcal{P}_a$ denoting the population in spin state a, and is determined by calibrating the NV fluorescence using a Rabi oscillation contrast measurement. To avoid heating of the sample, resulting in drifts in the Rabi frequency, a waiting time of $600 - 900\,\mu$s is implemented before the sequence is repeated. The minimum spacing between microwave pulses is maintained at 1 ns.

To understand the effect of different initial states on the DTC phase, we replaced the initial $-\pi/2$ pulse with a $-\pi/3$ pulse. This results in the preparation of a global spin state, which is rotated from the $\hat{x}$ axis by $\pi/6$. Despite this change, the measured lifetime of the DTC order ($47.6 \pm 2.4\,\mu$s) agrees well with that of the polarized spin state ($49.2 \pm 3.3\,\mu$s), demonstrating that DTC order is insensitive to the initial state.

B.1.2 Experimental identification of phase boundary.

To identify the position of the phase boundary in our experiment, we define the crystalline fraction f as $f = |S(\nu = \frac{1}{2})|^2 / \sum_\nu |S(\nu)|^2$. Error bars in f are calculated via error propagation in consideration of the noise floor in the Fourier spectrum; each measured

spectrum contains a background noise level σ_n, resulting in a variation of f as,

$$\delta f = f\sqrt{\left(\sigma_n/|S(\nu=\frac{1}{2})|^2\right)^2 + \left(N\sigma_n/\sum_\nu |S(\nu)|^2\right)^2 - 2N\sigma_n^2/\left(|S(\nu=\frac{1}{2})|^2\sum_\nu |S(\nu)|^2\right)}, \tag{B.1}$$

where $N = 50$ is the number of points in the Fourier spectrum. This gives rise to an uncertainty in the crystalline fraction: $f \in [f-\delta f, f+\delta f]$ (Fig. 3a). To extract the phase boundary, we use a phenomenological, super-Gaussian function

$$F_{\tau_1}(\theta) = \begin{cases} f_{\tau_1}^{\max} \exp\left[-\frac{1}{2}\left(\frac{|\theta-\theta_0|}{\sigma_-}\right)^p\right] & , \theta \le \theta_0 \\ f_{\tau_1}^{\max} \exp\left[-\frac{1}{2}\left(\frac{|\theta-\theta_0|}{\sigma_+}\right)^p\right] & , \theta \ge \theta_0 \end{cases} \tag{B.2}$$

where $\sigma_\pm$, θ_0, p are the characteristic width, central position and the power of the super-Gaussian fit, and $f_{\tau_1}^{\max}$ is the maximum value of the crystalline fraction for a given duration τ_1. The proposed function naturally captures the observed asymmetry in the phase boundary. We define the phase boundary as the rotation angle $\theta_\pm$ at which $F_{\tau_1}(\theta_\pm)$ = 0.1; that is, $\theta_\pm = \theta_0 \pm \sigma_\pm \left[2\ln(f_{\tau_1}^{\max}/0.1)\right]^{\frac{1}{p}}$. Errors in the phase boundary are derived from the fit uncertainties.

B.1.3 Theoretical description.

As a variational ansatz, we consider the time evolution of a homogeneous product state of the form $|\Psi\rangle = |\psi_0\rangle^{\otimes N}$ with $|\psi_0\rangle = \cos(\theta_0/2)\,|+\rangle + \sin(\theta_0/2)e^{i\phi_0}\,|-\rangle$, where $|\pm\rangle = (|m_s=0\rangle \pm |m_s=-1\rangle)/\sqrt{2}$. The qualitative behavior does not change even if we allow spins to be oriented in different directions. An approximate eigenstate for the time evolution over two periods is obtained by solving the equation for a single spin, $|\psi_0\rangle = e^{-i\theta S^y}e^{i\phi_i S^x}e^{-i\theta S^y}e^{-i\phi_i S^x}\,|\psi_0\rangle$ with a self-consistently determined $\phi_i = \bar{J}_i \langle\psi_0|\, S^x\, |\psi_0\rangle$ where

$\bar{J}_i = \sum_j J_{ij}/r_{ij}^3$ is the total strength at site i. The sign of ϕ_i is flipped in the second evolution as the spin polarization along the $\hat{x}$ direction alternates in each cycle. Note that we have ignored the effects of the on-site disorder potential Δ_i, interactions during global rotations and rotations induced by Ω_x. This is justified due to the high microwave driving strength $\Omega_{x(y)} \gg W$ and $\Omega_x \tau_1$ being integer multiples of 2π. (The effects of on-site disorder are fully included in the numerical computations.) A non-trivial solution ($\theta_0 \neq \pm\pi$) is obtained if the first two rotations result in a vector that is rotated by π along the $\hat{y}$ axis (Fig. 3d), which is satisfied when $\phi_0 = m\pi - \phi_i/2$ with $m \in \mathbb{Z}$ and $\cot\theta_0 = -(-1)^m \tan(\theta/2)\sin(\phi_i/2)$. Solving for $\cos^2\theta_0$ yields

$$\cos^2\theta_0 = \frac{\tan^2(\theta/2)\sin^2(\phi_i/2)}{1+\tan^2(\theta/2)\sin^2(\phi_i/2)}. \tag{B.3}$$

Using $\phi_i = \bar{J}_i\tau_1\cos\theta_0$, one can show that a solution exists only when $|\tan(\theta/2)\bar{J}_i\tau_1/4| > 1$, implying that $|\theta - \pi| < |\bar{J}_i\tau_1/2|$ in the vicinity of $\theta \approx \pi$. The linear dependence of the phase boundary is consistent with the phase diagram provided in Ref. [49]. As long as a solution exists, small variations in θ correspond to a smooth deformation of the closed trajectory. Therefore, the existence of such a closed path stabilizes the time-crystalline phase. We emphasize that such a $2T$-periodic path is a consequence of interactions; without the change of sign in ϕ_i, the eigenstates of the unitary evolution over one or two periods coincide, and therefore, unless the rotation angle is fine-tuned, T-periodic motion cannot be broken into a $2T$ period. The eigenstates of unitary evolution over one period can be obtained as even and odd linear combinations, $(|\Psi\rangle \pm e^{-i\epsilon_i}U_1|\Psi\rangle)/\sqrt{2}$, where $U_1 = \otimes_i(e^{-i\theta S_i^y}e^{-i\phi_i S_i^x})$, and the quasi-energy eigenvalue is given by $e^{i2\epsilon_i} = \langle\Psi|(U_1)^2|\Psi\rangle$.

To estimate the phase boundary, we numerically solve the self-consistency equation. Here, we include the effects of on-site disorder potential Δ_i in all four rotations as well

as the disorder in $\bar{J}_i$ arising from the random positions of NV centers. The distribution of $\bar{J}_i$ is simulated for 1000 spins, randomly distributed in three dimensions with an average separation r_0 and minimum cutoff distance $r_{\text{min}} = 3$ nm (limited by NV-NV electron tunneling[27]). Instead of $\cos(\theta_0)$, we solve for a self-consistent distribution for $\cos(\theta_0)$, where $\langle S^x \rangle$ is defined as the mean of the distribution. The average order parameter $\langle \cos^2 \theta_0 \rangle$ is computed for various values of τ_1 and θ and compared with a threshold value of 0.1 in order to identify the phase boundary. The experimental and numerical phase boundaries are asymmetric about $\theta = \pi$. We attribute this to the inherently asymmetric distribution of the effective rotation angle, $\theta_i \approx \tau_2 \sqrt{\Omega_y^2 + \Delta_i^2 + \bar{J}_i^2}$, which causes the transition to occur earlier for positive deviations $\theta - \pi$.

While we assumed ϕ_i to be a classical variable in this analysis, the interaction induced rotation angle is an operator $\hat{\phi}$ that exhibits quantum fluctuations and leads to non-trivial quantum dynamics. Under such dynamics, spins get entangled, resulting in mixed state density matrices. These effects cannot be ignored in the case of long interaction times, effectively limiting the present description. We believe that the diminished range of θ in the experimentally obtained phase diagram (Fig. 3b) is related to this effect.

B.1.4 Rotary echo sequence.

Certain features similar to DTC order could potentially arise from spatially inhomogeneous microwave driving along the $\hat{x}$ axis during the spin-locking sequence. This leads to variations in the effective, single-particle disorder in the dressed state basis, which could give rise to an effective self-correcting dynamical decoupling that might resemble DTC order [51]. In particular, in the spin-locking sequence, spins precess along the axis

$(\Omega_x(r_i) + \bar{J}_i)\hat{x} + \Delta_i\hat{z}$, with effective Rabi frequency $\Omega_{x,i}^{\text{eff}} = \sqrt{(\Omega_x(r_i) + \bar{J}_i)^2 + \Delta_i^2}$, where $\Omega_x(r_i)$ is the spatially inhomogeneous Rabi frequency, $\bar{J}_i$ is the mean-field Ising interaction, and Δ_i characterizes the quasi-static on-site disorder. In the case of strong driving ($\Omega_x \gg \Delta_i, \bar{J}_i$), this precession axis is determined by Ω_x and spins undergo dephasing dominated by global microwave inhomogeneities. If the net rotation during one spin-locking cycle is an odd integer multiple of π, this could accidentally lead to an XY-sequence[51] that may result in $2T$-periodicity. In our measurements, we always choose τ_1 as an integer multiple of $2\pi/\Omega_x$ to minimize such effects.

Although it has been shown theoretically that disorder alone is insufficient (in the absence of interactions) for stabilizing DTC order[46, 47, 48, 49], to experimentally demonstrate that the accidental decoupling is not responsible for the observed DTC ordering, we implement a "rotary echo" sequence, wherein after half the interaction time τ_1 the microwave driving is flipped from Ω_x to $-\Omega_x$ (Extended Data Fig. 1a). In the limit of strong driving, such a sequence eliminates the phase acquired between the two dressed states for each spin, regardless of the exact value of Ω_x. As shown in Extended Data Fig. 1b, the lifetimes of the DTC order are nearly identical between the cases of the rotary echo and continuous $+\hat{x}$ driving. Moreover, the rotary echo spin polarization maintains a larger amplitude at late times, excluding the possibility of self-correcting dynamical decoupling as the origin of the observed DTC order.

B.1.5 Markovian dephasing effects on discrete time crystalline order.

The presence of the sub-harmonic peak at $\nu = 1/2$ at small values of $\theta - \pi$ can, in principle, also be explained based on fast Markovian dephasing in the dressed state basis.

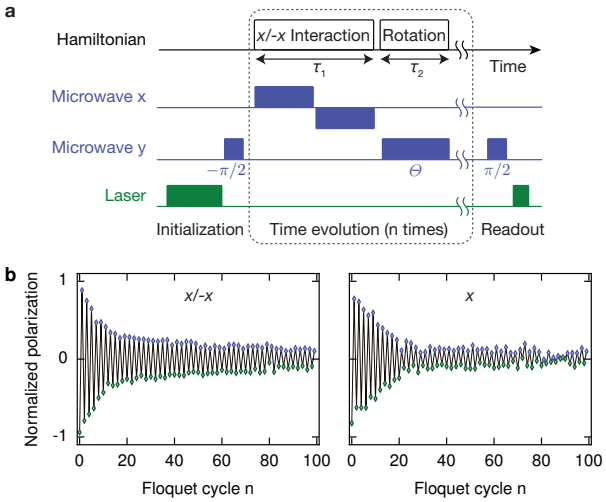

Figure B.1: **Effect of rotary echo sequence.** **a** Experimental sequence: during the interaction interval τ_1, the phase of the microwave driving along $\hat{x}$ is inverted after $\tau_1/2$. **b** Comparison of time traces of $P(nT)$ in the presence (left) and absence (right) of an $\hat{x}$/-$\hat{x}$ rotary echo sequence at similar τ_1 and θ (left: $\tau_1 = 379$ ns, $\theta = 0.979\pi$; right: $\tau_1 = 384$ ns, $\theta = 0.974\pi$). The rotary echo leads to more pronounced $2T$-periodic oscillations at long time. The microwave frequencies used in the rotary echo sequence are $\Omega_x = 2\pi \times 52.9$ MHz and $\Omega_y = 2\pi \times 42.3$ MHz.

Indeed, for sufficiently fast dephasing, coherences along both $\hat{y}$ and $\hat{z}$ will be eliminated after each rotation, R_y^θ. Thus, the only evolution that remains is the population dynamics along $\hat{x}$, which exhibits 2T-periodicity from the alternating sign. Microscopically, such strong dephasing could potentially originate from either dipolar interactions between the spins or from coupling to an external (Markovian) environment.

Intuitively, the result of such dephasing can be understood as an "effective" projective measurement of polarization along $\hat{x}$ in each Floquet cycle, reminiscent of the quantum Zeno effect. In order to quantify and distinguish such dephasing-induced sub-harmonic rigidity, we consider the dynamics (over one Floquet period) of a single spin undergoing Markovian dephasing, with super-operator $\hat{\mathcal{D}}[\rho] = -\frac{\gamma}{2}(\rho - 4S^x \rho S^x)$ and dephasing rate γ. Assuming $\theta - \pi \ll 1$, evolution falls into two well known limits. In the under-damped

limit (weak dephasing), $S(\nu)$ exhibits two Lorentzian peaks at $\nu = \pm\eta$ with a linewidth set by $\gamma\tau_1$, where τ_1 is the spin-locking duration and $\cos(2\pi\eta) = \cos\theta(1 + e^{\gamma\tau_1})/2$. In the over-damped limit (strong dephasing), $S(\nu)$ (at late times) exhibits a peak at $\nu = 1/2$ with a linewidth (in Floquet units)

$$\Gamma \approx \frac{(\theta - \pi)^2}{2\tanh(\gamma\tau_1/2)}. \tag{B.4}$$

These over-damped oscillations of the spin polarization exhibit sign flips between the even and odd cycles, leading to a sub-harmonic Fourier response reminiscent of DTC order.

While strong Markovian dephasing can indeed result in a $\nu = 1/2$ sub-harmonic peak, we observe three distinct experimental signatures clearly showing that our observations are not governed by this effect. First, the linewidth, Γ (Eq. 5), of the sub-harmonic peak should be quadratically sensitive to the deviation of θ from π. This is in stark contrast with our experimental observations shown in Fig. 2d, where this linewidth Γ is essentially independent of θ within the DTC phase. Second, according to the dephasing model (Eq. 5), the lifetime of the 3T-periodic DTC order is expected to be longer than that of the 2T-periodic DTC order owing to enhanced dephasing (from a lack of spin-locking) in the bare basis[27]. However, we observe the exact opposite behavior. Finally, Markovian dephasing requires an effective environment with a relatively fast sub-μs correlation time. This is also inconsistent with our experimental observations. In particular, we performed Rabi oscillation decay measurements with a rotary echo sequence, resulting in a lower bound of $1.5\,\mu$s on the Markovian dephasing time T_2. This time scale still includes contributions from static on-site disorder and interactions, and thus the Markovian dephasing rate is, in fact, significantly slower than this. Indeed, we have independently extracted the typical timescales of disorder fluctuations in our system[53], and we find that they are similar

($60\,\mu$s) to depolarization timescale under spin-locking dynamics. Effects resulting from such slow dephasing should be completely negligible within a typical Floquet period. Thus, we conclude that fast dephasing alone does not explain the observed DTC order.

At the same time, in the time crystalline order description based on interacting spin models[46, 47, 48, 49], the time crystalline order is expected to be robust and is not expected to exhibit any functional dependence on the angle θ, in complete agreement with experimental observations. This is also the case for our self-consistent description. We finally note that the interplay between coherent interactions and dephasing could potentially play a role in stabilizing DTC order at longer interaction times. Detailed understanding of such mechanisms require further theoretical investigation.

B.1.6 Derivation of Effective Hamiltonian for $\mathbb{Z}_3$ symmetry breaking phase.

Using microwave driving resonant with two different transitions (Fig. 4a), we realize dynamics involving all three spin states and observe a robust $3T$-periodic time-crystalline order. The unitary matrix of the time evolution during the fundamental period T is given as

$$U_3 = e^{-i\sum_i(\sigma^i_{-1,0}+\sigma^i_{0,-1})\theta/2} e^{-i\sum_i(\sigma^i_{+1,0}+\sigma^i_{0,+1})\theta/2} e^{-iH_2\tau}, \tag{B.5}$$

where $\sigma^i_{a,b} \equiv |m_s = a\rangle \langle m_s = b|$ for spin-i and $H_2 = H_{\text{dis}} + H_{\text{int}}$ is the effective Hamiltonian of NV centers for all three spin states including on-site disorder potentials $H_{\text{dis}} = \sum_i \Delta^+_i \sigma^i_{+1,+1} + \Delta^-_i \sigma^i_{-1,-1}$ and dipolar interactions for spin-1 particles[53]

$$H_{\text{int}} = \sum_{ij} \frac{J_{ij}}{r^3_{ij}} \left[-\frac{\sigma^i_{+1,0}\sigma^j_{0,+1} + \sigma^i_{-1,0}\sigma^j_{0,-1} + h.c.}{2} + (\sigma^i_{+1,+1} - \sigma^i_{-1,-1})(\sigma^j_{+1,+1} - \sigma^j_{-1,-1}) \right]. \tag{B.6}$$

We note that this Hamiltonian is obtained in the rotating frame under the secular approximation. The Hamiltonian H_2 conserves the total population in any of the three spin states, $\mathcal{P}_a = \sum_i \sigma^i_{aa}$ with $a \in \{0, \pm 1\}$. If each microwave pulse realizes a π pulse ($\theta = \pi$), their combination results in a cyclic transition $R^\pi_3 : |m_s = +1\rangle \mapsto -|m_s = -1\rangle \mapsto i\,|m_s = 0\rangle \mapsto |m_s = +1\rangle$, and the population $\mathcal{P}_a$ becomes periodic over three periods. Under such evolution, the effective Hamiltonian over three periods is given by $D^\pi_3 = [H_2 + (R^\pi_3)^{-1} H_2 R^\pi_3 + (R^\pi_3)^{-2} H_2 (R^\pi_3)^2]/3$, in which on-site disorders average to zero, and the interactions are modified to

$$D^\pi_3 = \sum_{ij} \frac{J_{ij}}{r^3_{ij}} \left[\sum_a \sigma^i_{aa} \sigma^j_{aa} - \frac{1}{3} \sum_{a \neq b} \sigma^i_{ab} \sigma^j_{ba} \right]. \tag{B.7}$$

The first term describes Ising-like interactions that shift energy when any pair of spins are in the same state, and the second term corresponds to spin-exchange interactions that allow polarization transport. These additional exchange interactions may lead to a shorter lifetime of the DTC order as compared to that of the $\nu = 1/2$ DTC order. For small perturbations in the microwave pulse angle $\epsilon = \theta - \pi$, the effective dynamics, to leading order, are governed by

$$D^{\pi+\epsilon}_3 \approx D^\pi_3 + \frac{\epsilon}{3\tau} \sum_j \left(\sigma^j_{+1,0} + \sigma^j_{-1,0} + i\sigma^j_{+1,-1} + h.c. \right), \tag{B.8}$$

which explicitly breaks the conservation laws for $\mathcal{P}_a$.

B.2 Details on technical procedure

In this section, we present the details on the technical procedure used to rotate the depolarization inducing Hamiltonian

$$H(t) = \sum_{ij} \frac{J_{ij}}{r_{ij}^3} S_i^x S_j^x + \epsilon \sum_i S_i^y \sum_n \delta(t - n^- \tau_1), \tag{B.9}$$

into an effective Hamiltonian $H'(t)$.

As mentioned in the main text, because of the disorder in the interactions, single spin-flip processes, effected by the action of a single operator S_i^y (i.e. the off-diagonal $O(\epsilon)$ term in Eq. (B.9)), are typically not resonant and do not induce significant depolarization. One has to consider other channels for depolarization which are of higher order in ϵ, such as two, three, spin-flip processes, and inquire if they are resonant processes – if so, then the dominant channel of decay is the one that governs the asymptotic behavior of depolarization dynamics.

The purpose of the transformation we employ is thus to extract the terms that give rise to dominant depolarization processes: we will rotate the original Hamiltonian in such a way that off-diagonal terms that generate non-resonant processes are 'integrated out', giving a resulting effective Hamiltonian $H'(t)$ whose leading order off-diagonal terms generate resonant proceses. In our system, it will turn out that the dominant decay channel is given by two spin-flip processes.

B.2.1 Rotating the Hamiltonian

To that end, let us perform this transformation in detail. We write the unitary time evolution operator $U(t) = \mathcal{T}e^{-i\int_0^t H(t')dt'}$, generated by Eq. (B.9), as

$$U(t) = Q(t)\tilde{U}(t)Q^\dagger(0), \tag{B.10}$$

where we have yet to define the unitary $Q(t)$. With this decomposition, $\tilde{U}(t)$ is given by

$$\tilde{U}(t) = \mathcal{T}e^{-i\int_0^t H'(t)dt}, \tag{B.11}$$

i.e. it is generated by a rotated time-dependent Hamiltonian (via the Schrodinger equation):

$$H'(t) = Q(t)^\dagger \left(H_0 + \epsilon V \sum_n \delta(t - n^- \tau_1) - i\partial_t \right) Q(t), \tag{B.12}$$

where

$$H_0 = \sum_{ij} \frac{J_{ij}}{r_{ij}^3} S_i^x S_j^x, \tag{B.13}$$

$$V = \sum_i S_i^y. \tag{B.14}$$

Here $J_{ij} = J_0 q_{ij}$ where $q_{ij} = -(1 - 3(\hat{z} \cdot \hat{r}_{ij})^2)$ encodes the angular dependence of the interactions between spins (i, j), as in Ref. [18].

We will pick $Q(t)$ to be time-periodic; then because $Q(n\tau_1) = Q(0)$, the expected value of observables as a function of time, such as the polarization (of one site) $S_i^x(n\tau_1)$, is given by

$$\begin{aligned}
\langle\psi|S_i^x(n\tau_1)|\psi\rangle &= \langle\psi|U^\dagger(n\tau_1)S_i^x U(n\tau_1)|\psi\rangle \\
&= \langle\tilde{\psi}|\tilde{U}^\dagger(n\tau_1)\tilde{S}_i^x\tilde{U}(n\tau_1)|\tilde{\psi}\rangle, \\
|\tilde{\psi}\rangle &= Q^\dagger(0)|\psi\rangle \\
\tilde{S}_i^x &= Q^\dagger(0)S_i^x Q(0),
\end{aligned} \tag{B.15}$$

where $|\psi\rangle$ is the initial state which we take to be polarized in the x-direction. In other words, $Q(0)$ is just some static rotation that rotates both the state and observable.

If in addition $Q(0)$ is a 'small' rotation (as we will choose, and to be made precise below), then both the state and observable are close to the unrotated ones,$|\tilde{\psi}\rangle \approx |\psi\rangle$ and $\tilde{S}_i^x \approx S_i^x$, and one can conclude that

$$\langle\psi|S_i^x(n\tau_1)|\psi\rangle \approx \langle\psi|\tilde{U}^\dagger(n\tau_1)S_i^x\tilde{U}(n\tau_1)|\psi\rangle. \tag{B.16}$$

That is, the time dependence (and consequently, depolarization) is completely captured in $\tilde{U}(t)$ and hence, $H'(t)$, the rotated effective Hamiltonian.

B.2.2 Choosing the rotation $Q(t)$

Now let us construct $Q(t)$, which we write as $Q(t) = e^{\epsilon\Omega(t)}$, where ϵ is explicitly the small parameter and $\Omega(t)$ a periodic anti-Hermitian operator. Expanding Eq. ($B.12$) we get

$$\begin{aligned} H'(t) = H_0 &+ \epsilon\left(V\sum_n \delta(t-n^-\tau_1) - [\Omega, H_0] - i\partial_t\Omega\right) \\ &+ \epsilon^2\left(\frac{1}{2}[\Omega,[\Omega,H_0]] - [\Omega,V]\sum_n\delta(t-n^-\tau_1) + \frac{i}{2}[\Omega,\partial_t\Omega]\right) \\ &\cdots . \end{aligned} \tag{B.17}$$

Utilizing a procedure similar to Ref. [65], we equate the order ϵ piece to 0 with the constraint that $\Omega(t)$ is time-periodic. Note that this transformation is distinct from the transformations employed in Refs. [66, 67] to generate effective Hamiltonians in high-frequency driven systems. There, the small parameter was the inverse of the driving frequency ω, but here, in anticipation that we will take into account the disorder in the interactions, the small parameter is served by ϵ, the strength of the off-diagonal perturbation to H_0. Decomposing

$\Omega(t)$ in terms of its Fourier modes $\Omega(t) = \sum_n \Omega^{(n)} e^{in\omega_0 t}$, where $\omega_0 = 2\pi/\tau_1$, and using the fact the Fourier transform of the Dirac comb $\sum_n \delta(t - n^- \tau_1)$ is $\frac{1}{\tau_1}\sum_n e^{-in\omega_0 t}$, the equation that the n-th Fourier mode has to obey is

$$\frac{V}{\tau_1} - [\Omega^{(n)}, H_0] + \omega_0 n \Omega^{(n)} = 0. \tag{B.18}$$

In the basis of the eigenstates $|s\rangle$ of H_0 which are product states in the x-direction, we can therefore write the solution as

$$\langle s'|\Omega^{(n)}|s\rangle = \frac{\langle s'|V|s\rangle}{(E_s - E_{s'} - n\omega_0)\tau_1}. \tag{B.19}$$

Note that since $V = \sum_i S_i^y$, the eigenstates s and s' representing spin configurations in the matrix element of $\Omega^{(n)}$ can only differ by one spin-flip. If $|s\rangle$ and $|s'\rangle$ differ at the Ith spin,

$$E_s - E_{s'} = 2\sum_{j\neq I} \frac{J_{jI}}{r_{jI}^3} S_j^x(s) S_I^x(s), \tag{B.20}$$

where $S_j^x(s)$ represents the S^x component of the jth spin for the configuration $|s\rangle$, which for the starting state is just $+\frac{1}{2}$.

Because of the disorder in J_{ij}/r_{ij}^3 (accorded for by the random positions and relative angles between the spins), resonances (i.e. terms where the denominator ≈ 0) are controlled, provided

$$\frac{\epsilon}{\tau_1} \ll \min_{m\in\mathbb{Z}} \left| \left(2\sum_{i\neq J} \frac{J_{iJ}}{r_{iJ}^3} S_i^x(s) S_J^x(s) - m\omega_0 \right) \right|. \tag{B.21}$$

This gives us a condition that our perturbative procedure should work only for

$$\epsilon < \min(W, \omega_0)\tau_1, \tag{B.22}$$

where W^2 is the variance of the interactions,

$$W^2 = \left\langle 4 \left(\sum_{i\neq J} \frac{J_{iJ}}{r_{iJ}^3} S_i^x(s) S_J^x(s) \right)^2 \right\rangle. \tag{B.23}$$

The angular brackets represent averaging over different spins i, and we have used the fact that the mean is 0. In that case, the corresponding fraction of spins that are resonant is then small, and goes as $\sim \frac{\epsilon}{\min(W,\omega)\tau_1}$.

B.2.3 Effective Hamiltonian

The rotated Hamiltonian (B.17) then becomes

$$H'(t) = H_0 - \frac{\epsilon^2}{2}[\Omega(t), V] \sum_n \delta(t - n^- \tau_1) + \cdots . \tag{B.24}$$

Let us concentrate on the second term and look at its matrix elements. This is

$$-\frac{\epsilon^2}{2\tau_1}\langle s'| \sum_{n,m} [\Omega^{(m)}, V]|s\rangle e^{i\omega_0(m+n)t}. \tag{B.25}$$

Now $\Omega^{(m)}$ and V are sums of terms which each individually flip a single spin, so $|s\rangle$ and $|s'\rangle$ can differ by either only zero spin flips (i.e. $|s'\rangle = |s\rangle$) or two spin flips ($|s'\rangle = |s_{IJ}\rangle$) where s_{IJ} stands for the spin configuration s with the I-th and J-th spins flipped. The diagonal process (zero spin flips) leads to a renormalization of the energy of H_0, while the off-diagonal process where V flips spin I and $\Omega^{(m)}$ flips spin J results in the matrix element

$$\begin{aligned} &- \frac{\epsilon^2}{2\tau_1} \sum_{m,n} \langle s_{IJ}|\Omega_J^{(m)} V_I - V_I \Omega_J^{(m)}|s\rangle e^{i\omega_0(m+n)t} \\ =& - \frac{\epsilon^2}{2\tau_1} \sum_{m,k} e^{i\omega_0 kt} \left(\langle s_{IJ}|\Omega_J^{(m)}|s_I\rangle - \langle s_J|\Omega_J^{(m)}|s\rangle \right). \end{aligned} \tag{B.26}$$

The term in the parenthesis is

$$\begin{aligned}
&- \frac{1}{(E_{s_I} - E_{s_{IJ}} - m\omega_0)\tau_1} + \frac{1}{(E_s - E_{s_J} - m\omega_0)\tau_1} \\
&= - \frac{1}{(2\sum_{i\neq I,J} \frac{J_{iJ}}{r_{iJ}^3} S_i^x(s) S_J^x(s) - 2\frac{J_{IJ}}{r_{IJ}^3} S_I^x(s) S_J^x(s) - m\omega_0)\tau_1} \\
&\quad + \frac{1}{(2\sum_{i\neq J} \frac{J_{iJ}}{r_{iJ}^3} S_i^x(s) S_J^x(s) - m\omega_0)\tau_1} \\
&\approx - \frac{4\frac{J_{IJ}}{r_{IJ}^3} S_I^x(s) S_J^x(s)}{\tau_1 \left(2\sum_{i\neq J} \frac{J_{iJ}}{r_{iJ}^3} S_i^x(s) S_J^x(s) - m\omega_0\right)^2},
\end{aligned} \tag{B.27}$$

where $\omega_0 = 2\pi/\tau_1$.

Using this, we can thus write the rotated Hamiltonian (B.24) in operator form:

$$\begin{aligned}
H'(t) \approx H_0 + \sum_{IJ} \frac{A_{IJ} J_{IJ}}{r_{IJ}^3} (S_I^+ S_J^+ + h.c.) \sum_n \delta(t - n^- \tau_1) \\
+ O(\epsilon^3),
\end{aligned} \tag{B.28}$$

where $S_I^+ \equiv S_I^y + iS_I^z$ is the spin raising operator in the S_I^x basis for spin I, A_{IJ} is the coefficient of the interactions between two spins (I, J), given by

$$\begin{aligned}
A_{IJ} = \left(\frac{\epsilon^2}{\tau_1^2}\right) \sum_m \frac{-2S_I^x(s) S_J^x(s)}{\left(2\sum_{i\neq J} \frac{J_{iJ}}{r_{iJ}^3} S_i^x(s) S_J^x(s) - m\omega_0\right)^2} \\
+ (I \leftrightarrow J).
\end{aligned} \tag{B.29}$$

This effective Hamiltonian gives Eqs. (5, 13) and (14) in the main text. Note that technically speaking, Eqs. (B.27) when written in operator form would also give flip-flop terms $S_I^+ S_J^- + h.c.$. However, because we are ultimately interested in the dynamics of depolarization beginning from an initial polarized state in the $\hat{x}$ direction, and moreover such flip-flop terms are polarization conserving, they do not contribute to depolarization and so we drop them in the effective Hamiltonan.

Depending on the two limits of high or low frequencies ($\omega_0 \gg W$ or $\omega_0 \ll W$ respectively), A_{IJ} has qualitatively different behaviors. Its scaling behavior with respect to ϵ and τ_1 can be extracted in those limits, which is Eq. (6) in the main text. Thus, this gives rise to different behaviors for the depolarization rate in the two limiting cases, and can ultimately be used to determine the phase boundary of the critical time crystal, as was done in the main text.

B.3 Numerical procedure to extract decay rate and phase boundary

In this section, we describe the numerical procedure used to 1) determine the decay rate Γ as a function of the perturbation ϵ, and 2) obtain the phase diagram of the critical DTC shown in the main text.

Assuming that the initial state is polarized in the x-direction, we first generated the probability distribution $P(h_I)$ of h_I, which is the mean-field potential field felt by spin I, i.e. $h_I = \frac{1}{2}\sum_{j\neq I} \frac{J_{Ij}}{r_{Ij}^3}$. Here $J_{ij} = J_0 q_{ij}$ and $q_{ij} = -(1 - 3(\hat{z}\cdot\hat{r}_{ij})^2)$ encodes the angular dependence of two spins (i, j). We modeled this by uniformly distributing $N = 2000$ spins in a 3-torus of linear dimension $L = 60$ nm, with a minimum (UV) distance cut-off $r_{\text{UV}} = 3$ nm, and caculating for each spin h_i. Such a choice of parameters gives a particle density of $n_0 = 9.26 \times 10^{-3}$ nm^{-3}. Using $J_0 = 2\pi \times 52$ Mhz nm^{-3} as in the experiments, we can characterize this distribution by its variance W^2, which gives $W = 4.49$ Mhz.

From this distribution, we then drew two values (h_I, h_J), provided that they are each

not resonant. That is, we discarded values if

$$\frac{\epsilon/\tau_1}{|h_{I/J} - m\omega_0|} > \alpha_1 \text{ for all } m \in \mathbb{Z}, \tag{B.30}$$

where α_1 is some fixed $O(1)$ number. We determined this number from the condition that along the line $W\tau_1 = |\epsilon|$ where our perturbative analysis holds, at least 80% of the spins are not resonant. In the region where $W\tau_1 > \epsilon$, this implies that $> 80\%$ of the spins are off-resonant. In our simulation, $\alpha_1 = 3.7$. Then, (h_I, h_J) represent the mean-field potentials felt by spins I and J respectively.

Next, we estimated the probability that the two spins (I, J) a distance r apart form a resonant pair. In principle this is obtained by comparing the effective hopping $J_{\text{eff}}(r) \equiv A_{IJ}J_{IJ}/r^3$, against the minimum quasi-energy gap Δ. Here

$$A_{IJ}J_{IJ} \sim -\left(\frac{\epsilon^2}{\tau_1^2}\right) J_0 \overline{q_{IJ}} \sum_m \left(\frac{1}{(h_I - m\omega_0)^2} + \frac{1}{(h_J - m\omega_0)^2}\right) \tag{B.31}$$

and $\Delta \approx \min_m |h_I + h_J - m\omega_0|$. The bar over the angular dependence q_{ij} represents the typical angular dependence; this can be derived analytically and gives $\overline{q_{ij}} = 2/\sqrt{5}$. In other words, for a fixed r, if

$$\frac{J_{\text{eff}}(r)}{\Delta} > \alpha_2, \tag{B.32}$$

where α_2 is another order one number, then this spin pair is resonant. We take $\alpha_2 = 3.4$.

In practice, we make a simplifying assumption that for large enough r, which we call d, the probability of finding two spins a distance r apart which are resonant is small and is simply proportional to $J_{\text{eff}}(r)/\alpha_2\Delta \propto 1/r^3$ (we have numerically checked this assumption holds).

Then, one can simplify the counting of resonant pairs by just estimating the the probability $\mathcal{P}$ of finding two spins some fixed distance d apart. We generate 4000 pairs (I, J),

and count the number of pairs that satisfy Eq. (B.32) for $r = d$; the fraction of such pairs is $\mathcal{P}$. To get the probability of resonant pairs at distances $R > d$, we can then just multiply $\mathcal{P}$ by the factor $(d/r)^3$. In the simulations, we obtain d as the distance for which the last step of Eq. B.27 is justified, that is, if $W \sim J_0\overline{q_{ij}}/d^3$, which gives $d = 4.02$ nm for the parameters we have used.

Having determined $\mathcal{P}$, we extracted the decay rate $\Gamma(\epsilon, \tau_1)$. The survival of polarization probability is given by a power law $P(t) = (t/t_0)^{-q}$ where $q \propto \mathcal{P}$. This can be derived as the product of probabilities of having no resonant spins at each distance $[r, r + dr]$ up to $R(t) = (J_0 t)^{1/3}$ [18]:

$$P(t) = \prod_{r=r_{\text{UV}}}^{R(t)} \left(1 - 4\pi n_0 r^2 dr \frac{\overline{A_{IJ}J_{IJ}}}{d^3\alpha_2\Delta}\frac{d^3}{r^3}\right) = (t/t_0)^{-q}\,, \tag{B.33}$$

where

$$\begin{aligned} q &= \frac{4\pi n_0 d^3}{3}\left(\frac{\overline{A_{IJ}J_{IJ}}}{\alpha_2\Delta d^3}\right), \\ t_0 &= \frac{r_{\text{UV}}^3}{J_0}. \end{aligned} \tag{B.34}$$

The factor in the parenthesis $\left(\frac{\overline{A_{IJ}J_{IJ}}}{\alpha_2\Delta d^3}\right)$ is the probability $\mathcal{P}$, and hence we see $q \propto \mathcal{P}$.

The dimensionless decay rate per Floquet cycle Γ can then be obtained from $\Gamma(\epsilon, \tau_1) = 1/n^*(\epsilon, \tau_1)$ where $n^*(\epsilon, \tau_1)$ is the number of Floquet cycles such that $P(t)$ drops to some fixed threshold $1/A$. Solving $P(n^*\tau_1) = 1/A$ for n^* yields

$$\Gamma(\epsilon, \tau_1) = \frac{\tau_1}{t_0}e^{-\beta/\mathcal{P}}, \tag{B.35}$$

where

$$\beta = \frac{3\log(A)}{4\pi n_0 d^3}. \tag{B.36}$$

We take $A = 10$; physically this corresponds to the situation where the polarization drops to 10% of its starting value.

Lastly, to get the phase diagram, we estimated the phase boundary of the time crystal as the contour in the ϵ-τ_1 plane satisfying $\Gamma(\epsilon, \tau_1) = \Gamma_* = 1/100$. In other words, the phase boundary demarcates the regions in ϵ-τ_1 parameter space having significant decay after 100 Floquet cycles or not. The choice of 100 Floquet cycles was picked to match the experimental observations. Referring to Fig. 2 in the main text, one sees the linear ($\tau_1 \propto |\epsilon|$) phase boundary for small τ_1, and also the 'closing up' of the phase boundary, $\tau_1 \propto 1/\epsilon^2$, for large τ_1, as predicted by our theory.

Appendix C

Supporting Material of Chapter 4

C.0.1 The effect of disorder on spin correlation lengths

Our protocols introduced in the main text utilize quantum phase transitions to develop long-range spin correlations. In an ideal case, the spin correlation length ξ reaches the linear system size at the critical point, and our initialization step prepares Greenberger-Horne-Zeilinger (GHZ) states, allowing Heisenberg limited quantum sensing. In the presence of disorder, however, ξ may be limited as the disorder can prevent the propagation of spin correlations by localizing quasi-particle excitations. In turn, the limited spin correlations lead to diminished sensitivity enhancement compared to Heisenberg limit. In this section, we quantify such an effect for a spin chain with nearest neighbor Ising interactions.

For concreteness, we assume that the transverse field strength at each spin is weakly disordered $\Omega_i = \Omega + \delta\Omega_i$, where Ω is the average field strength and $\delta\Omega_i$ is a random variable uniformly distributed from $[-W/2, W/2]$. Likewise, we assume that the interaction strength $J_i = J + \delta J_i$ is also random, where δJ_i is uniformly distributed from $[-W, W]$.

Without loss of generality, the imperfection and disorder in the spin rotation angle $\delta\theta_i$ can be absorbed as a part of $\delta\Omega_i$ in the effective Hamiltonian description.

In order to quantify the localization length ξ_{loc} of quasi-particles at the critical point, we numerically diagonalize our effective Hamiltonian. More specifically, our effective Hamiltonian during the initialization step, $D = -\sum_i J_i S_i^z S_{i+1}^z - \sum_i \Omega_i S_i^x$, can be mapped to a quadratic fermionic Hamiltonian using Jorndan-Wigner transformation: $c_i^\dagger = \left(\prod_{j=1}^{i-1} 2S_i^x\right)(S_i^z - iS_i^y)$ and $c_i = \left(\prod_{j=1}^{i-1} 2S_i^x\right)(S_i^z + iS_i^y)$. This leads to $D = \sum_{ij} \begin{pmatrix} c_i^\dagger & c_i \end{pmatrix} H_{ij} \begin{pmatrix} c_j & c_j^\dagger \end{pmatrix}^T$, where the single particle Hamiltonian H_{ij} can be written as

$$H_{ij} = \delta_{ij} \begin{pmatrix} -\frac{\Omega_i}{2} & 0 \\ 0 & \frac{\Omega_i}{2} \end{pmatrix} + \frac{1}{8}\delta_{i+1,j} \begin{pmatrix} J_i & J_i \\ -J_i & -J_i \end{pmatrix} + \frac{1}{8}\delta_{i,j+1} \begin{pmatrix} J_j & -J_j \\ J_j & -J_j \end{pmatrix}. \quad \text{(C.1)}$$

We consider an even number of particles up to $N = 3000$ in the even parity sector $P = 1$ with a periodic boundary condition (which corresponds to the anti-periodic boundary condition for free fermions, i.e. $c_{N+1} = -c_1$). We numerically diagonalize the single particle H_{ij} at the critical point $\Omega = J/2$.

As a proxy for an inverse localization length ξ_{loc}^{-1}, we compute the average inverse participation ratio $\xi_{\text{loc}}^{-1} \approx IPR = \langle \sum_i |\psi_i|^4 \rangle$, where ψ_i is the quantum amplitude of an eigenstate at site-i, and $\langle\cdot\rangle$ denotes averaging over 50 disorder realizations and over 50 energy eigenstates (closest to zero energy) per disorder realization. As shown in Fig. C.1, the localization length scales as $\xi_{\text{loc}}^{-1} \sim (W/J)^\mu$ with the numerically extracted exponent $\mu \approx 1.49$.

As mentioned in the main text, the effect of disorder can become favorable during the spectroscopy step. Without disorder, domain wall excitations in one dimension are mobile, which hinders coherent accumulation of phase information over long time. If the localization lengths during the measurement step ($\Omega = 0$) are much shorter than those at the critical

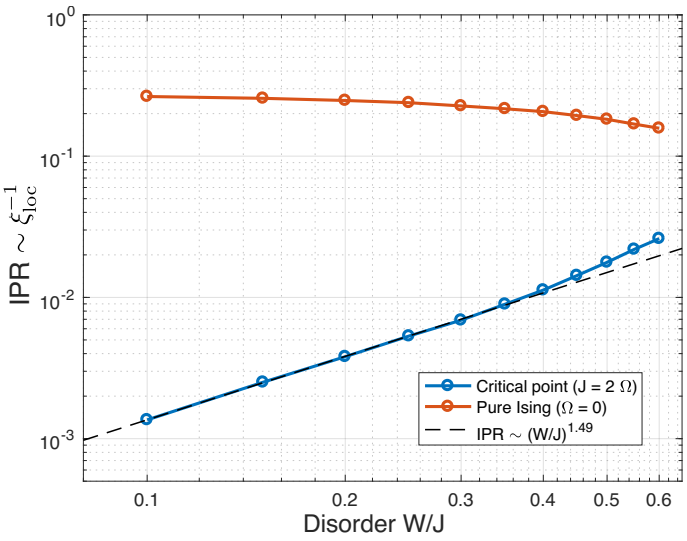

Figure C.1: Inverse participation ratio as a function of disorder strength W/J. At the phase transition point ($\Omega = J/2$), the spatial extents of localized quasi-particle excitations are larger in orders of magnitudes than those during the measurement step ($\Omega = 0$). During the measurement step, the tight localization of quasi-particles is favorable for a stable accumulation of phase information.

point, domain wall excitations become immobile, allowing more stable accumulation of the phase information from the signal. Repeating the numerical calculations at $\Omega = 0$, we find that the localization length is indeed multiple orders of magnitude shorter during the measurement step than at the phase transition point (Fig. C.1). We note that, in our numerical calculations, two types of disorder (δJ_i and $\delta\Omega_i$) are characterized by the same disorder strength W. However, in realistic settings, disorder in J is often much stronger than that of Ω, since the dominant source of disorder arises from random positioning of spins, which is even more favorable for our protocol.

C.0.2 Broad-band sensing using correlated spin states

The detection of a weak signal at an unknown frequency requires a highly sensitive spectroscopic method with a large bandwidth. Such technique is often needed in the study of fundamental physics such as the detection of gravitational waves or weakly interacting massive particles. In a conventional spectroscopic method, the increase in bandwidth entails the decrease in detection sensitivity. For example, as discussed in the main text, the standard quantum limit (SQL) of N non-interacting particles leads to the sensitivity scaling

$$\delta B^{-1} \sim \sqrt{NTT_2}, \tag{C.2}$$

where δB is the minimum detectable signal strength, T_2 is the duration of each measurement cycle, and T is the total integration time. The bandwidth $\delta\omega$ of this method is Fourier limited to the measurement duration $\delta\omega \sim 1/T_2$, leading to the relation between the bandwidth and the signal sensitivity

$$\delta\omega/(\delta B)^2 \sim NT \quad \text{(conventional method in SQL)}. \tag{C.3}$$

By utilizing quantum entanglement, the bandwidth of the detection can be increased while maintaining the same signal sensitivity. In our method, we utilize interactions to develop quantum entanglement among $\chi \gg 1$ spins (i.e. $\chi = \xi^d$ in d-dimensional systems), and the sensitivity scales

$$(\delta B')^{-1} \sim \sqrt{NT\bar{T}_2\chi}, \tag{C.4}$$

where $\bar{T}_2$ is the relevant coherence time of the correlated spin state and can be generally shorter than the coherence time T_2 of individual spins. In particular, when each constituent spin is coupled to an independent noise bath $\bar{T}_2 \sim T_2/\chi$, which can offset the sensitivity

gain in Eq. (C.4). Nevertheless, the sensing bandwidth of our method is determined by the duration of each measurement cycle, $\delta\omega' \sim 1/\bar{T}_2$, leading to the relation

$$\delta\omega'/(\delta B')^2 \sim \chi NT \quad \text{(quantum correlated method)}. \tag{C.5}$$

Therefore, one can improve the detection bandwidth by a factor of χ while maintaining the same sensitivity.

When our protocols are used, the number of correlated spins χ is also determined from the maximum coherence time $\bar{T}_2$ (or more precisely by $T_p \lesssim \bar{T}_2$). Since χ itself affects $\bar{T}_2$, χ has to be computed self-consistently:

$$\chi = \xi^d = \left((J\bar{T}_2)^{\nu/(1+z\nu)}\right)^d = (JT_2)^{d\nu/(1+z\nu)}/\chi^{d\nu/(1+z\nu)} \tag{C.6}$$

$$\Rightarrow \chi^{\frac{1+z\nu+d\nu}{1+z\nu}} = (JT_2)^{d\nu/(1+z\nu)} \tag{C.7}$$

$$\Rightarrow \chi = (JT_2)^{d\nu/(1+z\nu+d\nu)}. \tag{C.8}$$

For example, in the case of dipolar interactions ($J_{ij} \sim J_0/r_{ij}^3$) in a two dimensional array, the phase transition can be described by the mean-field theory with the critical exponents $\nu = 1$ and $z = 1/2$, leading to $\chi \sim \xi^2 \sim (JT_2)^{4/7}$. In a realistic setting, however, the noise bath often exhibits spatial correlations, which can modify the simple estimates provided in this section. As we discuss in the next section, magnetic field fluctuations with microscopic origins such as dipolar spin impurities can exhibit spatial anti-correlations, which is favorable for our purposes.

C.0.3 Spatial correlation of magnetic field noise from a dipole

When multiple spins are entangled, the coherence time $\bar{T}_2$ of the collective spin state may be different from the coherence time T_2 of constituent particles. More specifically,

when each spin is coupled to an *independent* noise bath, the coherence time of χ spins in the Greenberger-Horne-Zeilinger (GHZ) state, $|G_{\pm}\rangle = (|\uparrow\rangle^{\otimes\chi} \pm |\downarrow\rangle^{\otimes\chi})/\sqrt{2}$, is reduced to $\bar{T}_2 = T_2/\chi$, offsetting the potential sensitivity improvement in Eq. (4) in the main text. In realistic settings, however, this simplified analysis is not valid since external noises at different spins often exhibit correlations. Such correlations are particularly relevant in high density electronic or nuclear spin ensembles, where the decoherence arises dominantly from local sources such as interactions of sensing spins with nearby magnetic dipoles of different species.

In this section, we show that the magnetic noise generated from a fluctuating dipole (fluctuator) exhibits spatial anti-correlations at short distances. Such anti-correlations lead to a relatively longer coherence $\bar{T}_2$ compared to T_2/χ, allowing sensitivity improvements for methods utilizing entangled spin states in realistic experiments. To be concrete, we begin our analysis by considering a single sensing spin interacting with a single fluctuator, which creates an effective magnetic field noise $\vec{B}(t)$ at the position of the spin. The coherence time of the sensing spin is determined from the spectral density function: $1/T_2 \propto S^{zz}(\omega_s)$, where ω_s is the probing frequency defined in the main text, and

$$S^{\mu\nu}(\omega) \equiv \int e^{i\omega t} \langle B^{\mu}(t) B^{\nu}(0) \rangle dt. \tag{C.9}$$

When multiple spins and fluctuators are located far from one another, the noise fields at distant positions originate from different fluctuators; in such case, one may assume that spins are coupled to their own noise bath, leading to the relation $\bar{T}_2 = T_2/\chi$ discussed above. However, when the spacing between sensing spins becomes comparable to, or even shorter than typical distances to fluctuators, the noise fields at nearby spins originate from the same fluctuator and can be correlated. Such spatial correlations play an important role

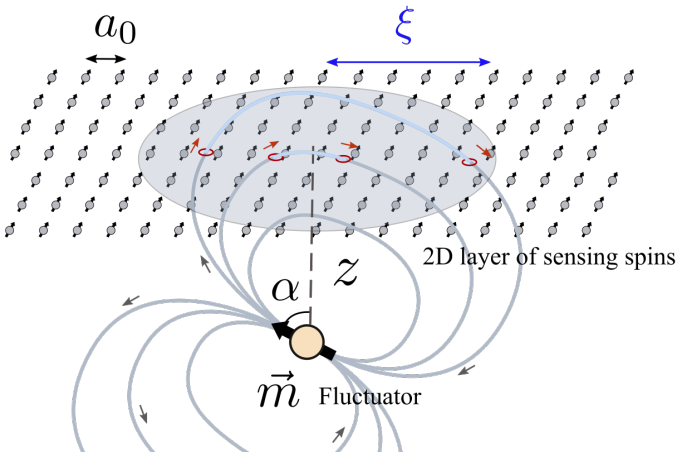

Figure C.2: Schematic diagram depicting a single dipole located at distance z from the sensing layer.

in determining the coherence time of GHZ states since the collective spins state interacts with its environment via the effective magnetic field noise

$$\vec{B}_{\text{eff}}(t) = \sum_i \vec{B}(\vec{r}_i, t), \tag{C.10}$$

where $\vec{B}(\vec{r}_i, t)$ is the magnetic field experienced by a single spin positioned at $\vec{r}_i$. The corresponding spectral density function

$$S^{\mu\nu}_{\text{eff}}(\omega) = \int e^{i\omega t} \sum_{ij} \langle B^\mu(\vec{r}_i, t) B^\nu(\vec{r}_j, 0)\rangle dt, \tag{C.11}$$

which sensitively depends on the spatial correlations, i.e. $\langle B^\mu(\vec{r}_i, t) B^\nu(\vec{r}_j, 0)\rangle$ for $i \neq j$. In order to quantify the spatial correlation, we consider a single magnetic dipole $\vec{m}$ located at a distance z from a two-dimensional array of sensing spins with average spacing a_0 (see Fig. C.2). The fluctuator creates a classical magnetic field $\vec{B}(\vec{r}_i)$, and we compute the

effective field experienced by the collective spin with correlation length ξ (see Fig. C.2):

$$\vec{B}_{\text{eff}} = \sum_i \vec{B}(\vec{r}_i) \approx \frac{1}{a_0^2} \iint \vec{B}(\vec{r}) d\vec{r} \tag{C.12}$$

$$= \frac{\mu_0}{4\pi a_0^2} \iint \left(\frac{3\vec{r}(\vec{m}\cdot\vec{r})}{r^5} - \frac{\vec{m}}{r^3} \right) d\vec{r} \tag{C.13}$$

$$= \frac{\mu_0}{4a_0^2} \frac{\xi^2}{\left(z^2+\xi^2\right)^{3/2}} \left(2m_z\hat{z} - m_q\hat{q}\right), \tag{C.14}$$

where the integration is performed over the area that covers correlated spins and $m_z = m\cos\alpha$ and $m_q = m\sin\alpha$ are the projections of the dipole moment in the vertical $\hat{z}$ and planar $\hat{q}$ directions, respectively. The corresponding spectral density scales as

$$S_{\text{eff}}^{\text{corr}} \sim \left(\frac{\mu_0 m}{a_0^2}\right)^2 \frac{\xi^4}{(z^2+\xi^2)^3}. \tag{C.15}$$

We note that when $z \ll \xi$, the noise density $S_{\text{eff}}^{\text{corr}}$ is strongly suppressed. Intuitively, this suppression arises from the spatial profile of the magnetic field created from a dipole moment, as depicted in Fig. C.2. In order to obtain the total noise density coming from multiple flucuators at different depths, we need to integrate $S_{\text{eff}}^{\text{corr}}$ over all $z \in (0, \infty)$:

$$\int_0^\infty S_{\text{eff}}^{\text{corr}} n_z dz \sim \frac{(\mu_0 m)^2}{a_0^4} \frac{n_z}{\xi}, \tag{C.16}$$

where the n_z is the linear density of fluctuators along the perpendicular direction $\hat{z}$. We neglect the integration along $\hat{x}$ and $\hat{y}$ directions due to the symmetry.

This result should be compared to a fiducial spectral density $S_{\text{eff}}^{\text{uncorr}}$ in the absence of spatial correlations, i.e. assuming $\langle B^\mu(\vec{r}_i,t)B^\nu(\vec{r}_j,0)\rangle = 0$ for $i \neq j$. This condition is equivalent to the assumption that each spin is coupled to an independent noise source. For a single classical dipole at depth z,

$$S_{\text{eff}}^{\text{uncorr}} \sim \sum_i |B(\vec{r}_i)|^2 \approx \frac{1}{a_0^2} \iint |\vec{B}(\vec{r})|^2 d\vec{r} \sim \frac{(\mu_0 m)^2}{a_0^2} \left(\frac{1}{z^4} - \frac{1}{(z^2+\xi^2)^2} \right). \tag{C.17}$$

Integrated over the entire depth $z \in (a_0, \infty)$,

$$\int_{a_0}^{\infty} S_{\text{eff}}^{\text{uncorr}} n_z dz \sim \frac{(\mu_0 m)^2}{a_0^2} \frac{n_z}{\xi^3} \int_{x=a_0/\xi}^{\infty} \left(\frac{1}{x^4} - \frac{1}{(1+x^2)^2} \right) dx \tag{C.18}$$

$$\sim \frac{(\mu_0 m)^2 n_z}{a_0^5} \sim \frac{\xi}{a_0} \int_0^{\infty} S_{\text{eff}}^{\text{corr}} n_z dz, \tag{C.19}$$

where we assumed that a fluctuator cannot be located closer than the spacing a_0. We find that, for a sufficiently large correlation length, $\xi \gg a_0$, the integrated noise density of the correlated case is indeed smaller by a factor a_0/ξ compared to the uncorrelated case. This result implies that the effective coherence time

$$\bar{T}_2 \sim (T_2/\chi)(\xi/a_0) \sim T_2/\sqrt{\chi}. \tag{C.20}$$

Finally, from Eq. (C.4), the sensitivity scales

$$(\delta B')^{-1} \sim \sqrt{NT\bar{T}_2\chi} \tag{C.21}$$

$$\sim \sqrt{NTT_2}\chi^{1/4}. \tag{C.22}$$

We note that this sensitivity is strictly better than SQL despite the presence of local magnetic noise sources.

C.0.4 Sensitivity enhancement for magnetic field imagers

In this section, we estimate the amount of sensitivity enhancement for magnetic field imagers when our protocols are used. A (quasi) two-dimensional array of electronic spins such as nitrogen vacancy (NV) color centers can be used to image a spatially resolved AC magnetic field profile [73, 76, 77]. Since quantum states of NV centers are optically read-out, the spatial resolution of this method is given by the diffraction limit of the optical wavelength $d \sim \lambda/2 \approx 250\,\text{nm}$, and can be further improved via sub-wavelength imaging

techniques [343]. Therefore, in order to achieve high precision AC magnetic field sensing without compromising the spatial resolution, the length scale of the probe volume should not exceed d. At such length scale, however, dipolar interactions among electronic spins, $J_{\text{dd}} \sim J_0/d^3 \approx (2\pi)\,3.3\,\text{Hz}$, is already significant compared to the maximum coherence time of a NV center $T_2 \approx 500\,\text{ms}$ at low temperature (77 K) [344]. This implies that one cannot utilize more than one NV center per probe volume for the purpose of AC field sensing without affecting diffraction limited spatial resolution. Even at room temperature with the coherence time $T_2 \approx 3\,\text{ms}$, the separation among NV centers have to be at least $r_{\text{min}} \approx 100\,\text{nm}$ in order to avoid interaction-induced decoherence. This allows one to use at most $N_0 \approx 6$ NV centers per probe volume with the corresponding enhancement in signal-to-noise ratio $\sqrt{N_0} \approx 3$ at best in the conventional SQL.

Our protocols dramatically alleviate aforementioned limitations. The minimum distance among NV centers are not bounded by dipolar interactions, allowing much higher particle density. In this case, the minimum distance is restricted only by the length scale of electronic orbitals of NV centers, which is the order of a few nm. Assuming a single layer of NV centers, one expects to achieve $N_1 \approx 2500$ particles per probe volume. This already allows about a factor of 50 enhancement in sensitivity at 77 K and about 20 at room temperature even without accounting for the effects of quantum correlations.

When the coherence time of the sensing spin is limited by correlated magnetic noises, e.g. generated by proximal fluctuating dipoles, our protocol can provide additional sensitivity enhancement as discussed in the previous section. In the case of two-dimensional array of spins, this sensitivity enhancement amounts to a factor of $\chi^{1/4}$ in Eq. (C.22). χ can be estimated self-consistently similar to Eq. (C.8). Figure C.3 summarizes the sensitivity

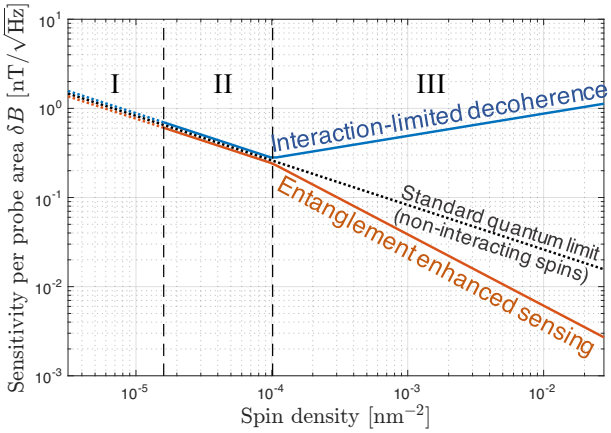

Figure C.3: Sensitivity scaling of a magnetic field imager as a function of spin sensor (NV center) density. Regime I: the magnetic field imaging is limited by spin separation. Regime II and III: the spatial resolution is diffraction limited at optical wavelength $\lambda \sim 500\,\text{nm}$. When conventional methods are used with a high density spin ensemble (regime III), the coherence time is shortened by interactions, deteriorating the sensitivity δB. In our method, such limitation is circumvented; rather, the interactions are used to further enhance the sensitivity by generating entangled many-body quantum states. This estimate assumes two-dimensional arrays of dipolar interacting spin ensembles with a single-spin coherence time $T_2 \sim 3\,\text{ms}$ and the diffraction-limited probe area $\sim (\lambda/2)^2$. We assume that the dominant source of decoherence is due to local magnetic field noise created by proximal dipolar magnetic impurities. Such magnetic noises exhibit spatial correlations and allow sensitivity improvement beyond standard quantum limit when correlated spin states are used.

enhancement in this scenario as a function of spin density.

Appendix D

Supporting Material of Chapter 5

D.1 Generalized Gell-Mann matrices

In the main text, we parametrize interactions using a set of trace orthonormal matrices $\{\lambda_\mu\}$. Here, for completeness, we present explicit expressions of $\{\lambda_\mu\}$ for $d = 2$ and $d = 3$. For $d > 3$, we provide a general method for constructing $\{\lambda_\mu\}$.

For $d = 2$ (qubits) the operator basis $\{\lambda_\mu\}$ coincides with Pauli matrices:

$$\lambda_1 = \sigma^x = \begin{pmatrix} 0 & 1 \\ 1 & 0 \end{pmatrix}, \quad \lambda_2 = \sigma^y = \begin{pmatrix} 0 & -i \\ i & 0 \end{pmatrix}, \quad \lambda_3 = \sigma^z = \begin{pmatrix} 1 & 0 \\ 0 & -1 \end{pmatrix}. \quad \text{(D.1)}$$

As required, these matrices satisfy the trace orthonormality $\mathrm{tr}\,(\lambda_\mu \lambda_\nu) = 2\delta_{\mu\nu}$ and, together with identity $\mathbb{1}_2$, form a basis for two dimensional Hermitian matrices. For $d = 3$ (spin-1

particles or qutrits), we choose $\{\lambda_\mu\}$ as so-called Gell-Mann matrices:

$$\lambda_1 = \begin{pmatrix} 0 & 1 & 0 \\ 1 & 0 & 0 \\ 0 & 0 & 0 \end{pmatrix}, \quad \lambda_2 = \begin{pmatrix} 0 & 0 & 0 \\ 0 & 0 & 1 \\ 0 & 1 & 0 \end{pmatrix}, \quad \lambda_3 = \begin{pmatrix} 0 & 0 & 1 \\ 0 & 0 & 0 \\ 1 & 0 & 0 \end{pmatrix}, \tag{D.2}$$

$$\lambda_4 = \begin{pmatrix} 0 & -i & 0 \\ i & 0 & 0 \\ 0 & 0 & 0 \end{pmatrix}, \quad \lambda_5 = \begin{pmatrix} 0 & 0 & 0 \\ 0 & 0 & -i \\ 0 & i & 0 \end{pmatrix}, \quad \lambda_6 = \begin{pmatrix} 0 & 0 & -i \\ 0 & 0 & 0 \\ i & 0 & 0 \end{pmatrix}, \tag{D.3}$$

$$\lambda_7 = \begin{pmatrix} 1 & 0 & 0 \\ 0 & -1 & 0 \\ 0 & 0 & 0 \end{pmatrix}, \quad \lambda_8 = \frac{1}{\sqrt{3}} \begin{pmatrix} 1 & 0 & 0 \\ 0 & 1 & 0 \\ 0 & 0 & -2 \end{pmatrix}. \tag{D.4}$$

Again, these matrices are traceless and orthonormal (normalized to $\mathrm{tr}\,(\lambda_\mu \lambda_\mu) = 2$), and form a basis for three dimensional Hermitian matrices together with the identity $\mathbb{1}_3$. Note that three matrices in the first and the second lines are purely real and imaginary, respectively, and the last two matrices are real and diagonal. For a generic d, we construct $m = d^2 - 1$ matrices in the following way. Let E_{ij} be a matrix with an element 1 at the i-th row and j-th column and zeros elsewhere. We define first $d(d-1)/2$ matrices as

$$\lambda_\mu = E_{i_\mu, j_\mu} + E_{j_\mu, i_\mu} \quad \text{for } \mu \in \{1, 2, \ldots, d(d-1)/2\}, \tag{D.5}$$

where (i_μ, j_μ) enumerates all possible $d(d-1)/2$ combinations of $i < j$ pairs. The next $d(d-1)/2$ matrices are similarly defined as

$$\lambda_\mu = -iE_{i_\mu, j_\mu} + iE_{j_\mu, i_\mu} \quad \text{for } \mu \in \{d(d-1)/2 + 1, \cdots, d(d-1)\}. \tag{D.6}$$

Finally, the remaining $d-1$ matrices are real, diagonal, and defined as

$$\lambda_\mu = \frac{1}{\sqrt{k_\mu(k_\mu-1)/2}}\left(\sum_{i=1}^{k_\mu-1} E_{ii} - (k_\mu-1)E_{k_\mu,k_\mu}\right) \quad \text{for } \mu \in \{d(d-1)+1,\ldots,d^2-1\}, \tag{D.7}$$

where k_μ enumerates $\{2,3,\cdots,d\}$. These matrices are traceless by construction, and their orthonormality can be checked by explicit computation.

D.2 Dynamical decoupling of dipolar interactions among spin-1 particles

In this section, we provide the details of dipolar interactions among spin-1 particles and their decoupling by using our 6-pulse sequence. We start with a generic Hamiltonian of the form $H = \sum_i H_i^{(1)} + \sum_{ij} H_{ij}^{\text{d-d}}$, where $H_i^{(1)}$ is a single spin Hamiltonian for a particle i and $H_{ij}^{\text{d-d}}$ is a pairwise dipolar interaction for a particle pair i and j

$$H_{ij}^{\text{d-d}} = -\frac{J_0}{r_{ij}^3}\left(3\left(\vec{S}_i\cdot\vec{r}_{ij}\right)\left(\vec{S}_j\cdot\vec{r}_{ij}\right)/r_{ij}^2 - \vec{S}_i\cdot\vec{S}_j\right) \tag{D.8}$$

with the interaction strength J_0, the relative position of the pair $\vec{r}_{ij}$, and the spin-1 vector operators $\vec{S}_i = (S_i^x, S_i^y, S_i^z)$. In the absence of single particle terms, the dipolar interactions can be efficiently suppressed by a sequence of $SO(3)$ spin rotations. This can be understood by rewriting the interactions as $H_{ij}^{\text{d-d}} = -(J_0/r_{ij}^3)\sum_{\mu\nu} S_i^\mu T_{\mu\nu} S_j^\nu$ with a rank-2 tensor

$$T = \begin{pmatrix} -1 & 0 & 0 \\ 0 & -1 & 0 \\ 0 & 0 & 2 \end{pmatrix}, \tag{D.9}$$

where we have chosen $\hat{z} \equiv \vec{r}_{ij}/r_{ij}$ without the loss of generality. As well-known in the nuclear magnetic resonance (NMR) community, the tensor T can be symmetrized to zero upon three $SO(3)$ rotations, effectively decoupling the interaction [57].

In contrast, under the presence of strong single particle terms, the form of interactions can be effectively modified, making it impossible to decouple them only using $SO(3)$ rotations. More specifically, we consider strongly anharmonic energy levels of spin-1 particles characterized by a Hamiltonian $H_i^{(1)} = hS_i^z + \Delta(S_i^z)^2$, where the first term typically arises from Zeeman coupling to external magnetic field and the second term naturally occurs when spin symmetries are broken, e.g., by quadrupolar couplings for nuclear spins or by spin-spin couplings for nitrogen vacancy color centers (NV) in diamond. In the limit of strong anharmonicity $|h|, |\Delta|, |h \pm \Delta| \gg J_0/r_{ij}^3$, as satisfied by most of experiments with solid state NMR or high density NV ensembles, the conservation of energy suppresses some of spin exchange processes in $H_{ij}^{\text{d-d}}$. The resultant effective interactions can be obtained in the interacting picture with a transformation

$$H_{\text{eff}}(t) = U_0^{-1}(t) H U_0(t) - i U_0^{-1}(t) \frac{\partial}{\partial t} U_0(t), \tag{D.10}$$

where $U_0(t) = \exp\left[-i\left(\sum_i hS_i^z + \Delta(S_i^z)^2\right)t\right]$. Ignoring energy non-conserving terms (secular approximations), the effective interactions become $H_{\text{eff}} \approx \sum_{ij} \frac{J_0}{r^3}(1-3\cos^2\theta) \sum_{\mu\nu} C_{\mu\nu}^{\text{eff}}\, \lambda_\mu \otimes$

λ_ν with $\cos\theta = \hat{z}\cdot\vec{r}/|\vec{r}|$ and

$$C^{\text{eff}} = -\frac{1}{4}\begin{pmatrix} 1 & 0 & 0 & 0 & 0 & 0 & 0 & 0 \\ 0 & 1 & 0 & 0 & 0 & 0 & 0 & 0 \\ 0 & 0 & 0 & 0 & 0 & 0 & 0 & 0 \\ 0 & 0 & 0 & 1 & 0 & 0 & 0 & 0 \\ 0 & 0 & 0 & 0 & 1 & 0 & 0 & 0 \\ 0 & 0 & 0 & 0 & 0 & 0 & 0 & 0 \\ 0 & 0 & 0 & 0 & 0 & 0 & -1 & -\sqrt{3} \\ 0 & 0 & 0 & 0 & 0 & 0 & -\sqrt{3} & -3 \end{pmatrix}. \tag{D.11}$$

Identifying $J_{ij} \equiv -(J_0/r_{ij}^3)(1-3\cos^2\theta)$ reduces H_{eff} to the expression given in the main text. We note that C^{eff} is traceless and hence allows a complete suppression by a pulse sequence.

In order to find a decoupling pulse sequence, we use our algorithm presented in the main text. We assume that the set of available unitaries $\mathcal{U}$ is limited to composite pulses made out of up to four $\pm\pi$ and $\pm(\pi/2)$-pulses: we define a set of elementary operations $\mathcal{E} = \{\mathbb{1}_3, e^{\pm i\frac{\pi}{2}X_a}, e^{\pm i\pi X_a}, e^{\pm i\frac{\pi}{2}Y_a}, e^{\pm i\pi Y_a}\}$ with $X_a = \lambda_a/2$ and $Y_a = (\lambda_{a+3})/2$ ($a \in \{1,2,3\}$) and construct composite pulses $\mathcal{U} = \{u = x_1x_2x_3x_4 | x_1, x_2, x_3, x_4 \in \mathcal{E}\}$. Using a linear programming routine built-in `Mathematica`, we find a set of 6 unitary rotations that

average C^{eff} to zero:

$$u_1 = e^{-i\frac{\pi}{2}X_3}e^{-i\frac{\pi}{2}Y_3}e^{-i\pi X_1}e^{i\frac{\pi}{2}Y_3}e^{i\frac{\pi}{2}X_3}, \tag{D.12}$$

$$u_2 = e^{-i\frac{\pi}{2}X_3}e^{-i\frac{\pi}{2}Y_3}e^{-i\pi Y_2}e^{i\frac{\pi}{2}Y_3}e^{i\frac{\pi}{2}X_3}, \tag{D.13}$$

$$u_3 = e^{-i\frac{\pi}{2}Y_3}e^{i\frac{\pi}{2}X_3}e^{i\frac{\pi}{2}Y_3}e^{i\frac{\pi}{2}X_3}, \tag{D.14}$$

$$u_4 = e^{-i\frac{\pi}{2}Y_3}e^{i\frac{\pi}{2}X_3}e^{-i\pi X_1}e^{i\frac{\pi}{2}Y_3}e^{i\frac{\pi}{2}X_3}, \tag{D.15}$$

$$u_5 = e^{-i\frac{\pi}{2}Y_3}e^{i\frac{\pi}{2}X_3}e^{-i\pi Y_2}e^{i\frac{\pi}{2}Y_3}e^{i\frac{\pi}{2}X_3}, \tag{D.16}$$

$$u_6 = \mathbb{1}_3. \tag{D.17}$$

The corresponding pulse sequence $p_i = u_i u_{i-1}^{\dagger}$ is given as

$$p_1 = e^{-i\frac{\pi}{2}X_3}e^{-i\frac{\pi}{2}Y_3}e^{-i\pi X_1}e^{i\frac{\pi}{2}Y_3}e^{i\frac{\pi}{2}X_3}, \tag{D.18}$$

$$p_2 = e^{-i\frac{\pi}{2}X_3}e^{-i\frac{\pi}{2}Y_3}e^{-i\pi Y_2}e^{i\pi X_1}e^{i\frac{\pi}{2}Y_3}e^{i\frac{\pi}{2}X_3}, \tag{D.19}$$

$$p_3 = e^{-i\frac{\pi}{2}Y_3}e^{i\frac{\pi}{2}X_3}e^{i\pi Y_2}e^{i\frac{\pi}{2}Y_3}e^{i\frac{\pi}{2}X_3}, \tag{D.20}$$

$$p_4 = e^{-i\frac{\pi}{2}Y_3}e^{i\frac{\pi}{2}X_3}e^{-i\pi X_1}e^{-i\frac{\pi}{2}X_3}e^{i\frac{\pi}{2}Y_3}, \tag{D.21}$$

$$p_5 = e^{-i\frac{\pi}{2}Y_3}e^{i\frac{\pi}{2}X_3}e^{-i\pi Y_2}e^{i\pi X_1}e^{-i\frac{\pi}{2}X_3}e^{i\frac{\pi}{2}Y_3}, \tag{D.22}$$

$$p_6 = e^{-i\frac{\pi}{2}X_3}e^{-i\frac{\pi}{2}Y_3}e^{i\pi Y_2}e^{-i\frac{\pi}{2}X_3}e^{i\frac{\pi}{2}Y_3}. \tag{D.23}$$

The numerical simulation presented in the main text is based on the exact diagonalization of the time evolution over one period $U_T = P_6 e^{-iH_d T/6} P_5 \dots P_1 e^{-iH_d T/6}$, where $P_i \equiv p_i^{\otimes N}$ for $N = 6$ particles.

We note that the order of u_i is not important within our approximations. Therefore, by rearranging the order of u_i, one can significantly simplify the corresponding pulse sequence p_i'. Also, once a composite pulse p_i' is identified as a sequence of elementary operations, one can further "compress" it using algebraic identities of $SU(d)$ group. For instance, the

above dynamical decoupling can be also achieved via the following sequence

$$p_1' = e^{i\pi \frac{X_1+X_2}{\sqrt{2}}} \tag{D.24}$$

$$p_2' = e^{-i\pi \frac{Y_1+X_2}{\sqrt{2}}} \tag{D.25}$$

$$p_3' = e^{i\frac{\pi}{2}Y_3} e^{i\frac{\pi}{4}S_z} \tag{D.26}$$

$$p_4' = e^{i\pi \frac{X_1+Y_2}{\sqrt{2}}} \tag{D.27}$$

$$p_5' = e^{-i\pi \frac{X_1-Y_2}{\sqrt{2}}} \tag{D.28}$$

$$p_6' = (p_3')^{-1}. \tag{D.29}$$

In experiments with NMR or high density NV ensembles, the pulses p_1', p_2', p_4', and p_5' can be implemented by simultaneous microwave driving of two transitions with appropriate phase choices while p_3' and p_6' can be realized by using AC stark shifts and two-photon Raman transitions. Also, p_3' and p_6' can be decomposed to four short pulses as provided in the figure in the main text.

D.3 Symmetrizing a pulse sequence

In this work we approximate the effective Hamiltonian by truncating the Magnus expansion to zeroth order. However, given any pulse sequence, one can always improve it such that the effective Hamiltonian is also correct up to the first order. For a pulse sequence $\{P_1, \ldots P_k\}$ followed by free evolutions $\{\tau_1, \ldots, \tau_k\}$, the first order correction in the Magnus expansion is given by

$$H_{\text{eff}}^{(1)} = -\frac{i}{2T} \sum_{i>j} [\tau_i \bar{H}_i, \tau_j \bar{H}_j], \tag{D.30}$$

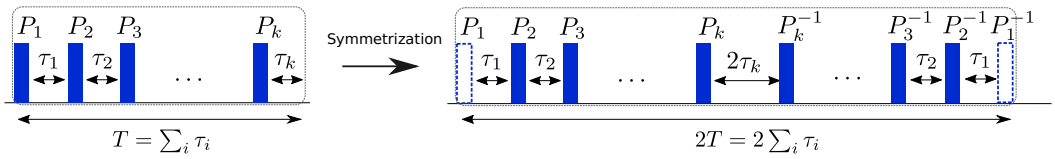

Figure D.1: Symmetrization of a pulse sequence. Any finite pulse sequence can be symmetrized such that the first order correction in Magnus expansion vanishes. When k-pulse sequence is symmetrized, the total duration of the pulse is doubled and the number of pulses becomes $2k-2$.

where $\bar{H}_i = U_i^\dagger H U_i$ with $U_i = P_i P_{i-1} \dots P_1$ as defined in the main text. The key idea is to appropriately *symmetrize* a pulse sequence such that $H_{\text{eff}}^{(1)}$ exactly vanishes. More specifically, we now consider a modified pulse sequence of total period $2T$, where the evolution in the first half remains the same while the pulses in the second half is time reversed [see Fig. D.1]:

$$U_{\text{sym}}(2T) = P_1^{-1} e^{-iH\tau_1} P_2^{-1} e^{-iH\tau_2} \dots P_k^{-1} e^{-iH\tau_k}\ e^{-iH\tau_k} P_k \dots e^{-iH\tau_2} P_2 e^{-iH\tau_1} P_1. \quad \text{(D.31)}$$

In the toggling frame, $U_{\text{sym}}(2T)$ can be written as

$$U_{\text{sym}}(2T) = e^{-i\bar{H}_1\tau_1} e^{-i\bar{H}_2\tau_2} \dots e^{-i\bar{H}_k\tau_k} e^{-i\bar{H}_k\tau_k} \dots e^{-i\bar{H}_2\tau_2} e^{-i\bar{H}_1\tau_1}, \quad \text{(D.32)}$$

where one finds that every $\bar{H}_i$ appears twice, each in the first (A) and the second (B) half of the period in reversed orders. For convenience let us denote the pair of $\bar{H}_i$ as $\bar{H}_i^A$ and $\bar{H}_i^B$ depending on their positions. Now the first order correction becomes

$$H_{\text{eff}}^{(1)} = -\frac{i}{4T}\left(\sum_{i>j\in A}[\tau_i\bar{H}_i^A, \tau_j\bar{H}_j^A] + \sum_{i<j\in B}[\tau_i\bar{H}_i^B, \tau_j\bar{H}_j^B] + \sum_{i\in B, j\in A}[\tau_i\bar{H}_i^B, \tau_j\bar{H}_j^A]\right) \quad \text{(D.33)}$$

$$= -\frac{i}{4T}\left(\left[\sum_{i\in B}\tau_i\bar{H}_i^B, \sum_{j\in A}\tau_j\bar{H}_j^A\right]\right) = 0, \quad \text{(D.34)}$$

where the cancellation in the second line is due to the reversed order of indices in B. Note that, in practice, the last pulse, P_1^{-1}, in a symmetrized sequence is immediately compensated by the first pulse, P_1, from the next period. Therefore, the number of pulses is generally $2(k-1)$ while the total time duration is exactly doubled to $2T$.

D.4 Phase diagram of $H(p,q)$

The classification of symmetry-protected topological (SPT) phases for bosonic one dimensional systems has been extensively studied [345, 346, 215], and their detections based on numerical methods are also well known [347, 147]. In particular, we note that Prakash *et al* in Ref. [147] investigate the phases of Hamiltonians $H'(r,q)$ that are closely related to our model $H(p,q)$:

$$H'(r,q) = H_1 + rH_2' + qH_3, \tag{D.35}$$

where H_1 and H_3 are the same as in our case and

$$H_2' = \sum_i (S_i^x S_{i+1}^x)^2 + (S_i^y S_{i+1}^y)^2 + (S_i^z S_{i+1}^z)^2. \tag{D.36}$$

When $r = 0$ this model coincides with our case with $p = 0$. In Ref. [147], Prakash *et al* predicts that $H'(r = 0, q)$ with $|q| < 1/2$ belongs to a topologically non-trivial phase (the phase C in their Fig. 1) that is equivalent to the AKLT phase. Also, they show that there are two adjacent, distinct topological phases for $r > 0$ (the phases B and D in their Fig. 1). The ground states of these phases respect all symmetries, namely A_4 spin rotations, lattice translations, and inversion, but they are distinguishable by $U(1)$ phases that their wavefunctions acquire upon the action of a 120° rotation $a \in A_4$. More specifically, we

consider a translationally-invariant, infinite-size matrix product state Γ^i_{ab} for each ground state (with a physical index $i \in \{0, \pm 1\}$, and bond indices $a, b \in \{1, \dots D\}$), and study its transformation under the action of internal symmetry group elements $g \in A_4$:

$$\sum_j u(g)_{ij} \Gamma^j_{ab} = \sum_{a'b'} \chi(g) V^{-1}(g)_{aa'} \Gamma^i_{a'b'} V(g)_{b'b}, \tag{D.37}$$

where $u(g)_{ij}$ is the unitary representation of a local spin rotation by $g \in A_4$, $\chi(g) \in U(1)$ is an overall phase factor that a wavefunction acquires, and $V(g)$ is a projective representation of A_4 with a complex phase ω, i.e., $V(g_1)V(g_2) = \omega(g_1, g_2)V(g_1 g_2)$. When ω is non-trivial, the corresponding phase is topologically non-trivial as in the case of phases B, C, and D in Ref. [147]. The three phases are, however, distinguished by $\chi(g)$; while the phase C has $\chi(a) = 1$, phases B and D have $\chi(a) = e^{\pm i 2\pi/3}$.

In our case, the phase diagram looks different from Fig. 1 in Ref. [147] owing to a different parametrization of Hamiltonians. Nevertheless, its qualitative features remain similar, and the phase diagram exhibits three SPT phases I, II, and III adjacent to one another. We identify the phases I, II, and III with the phases C, B and D in Ref. [147], respectively. Below, we verify this claim by using both exact numerical computation of ground states and ITEBD algorithm [348].

D.4.1 Exact numerical results

We exactly compute the ground states of Hamiltonian $H(p, q)$ for systems with up to $N = 14$ spins under periodic boundary conditions. The ground states are obtained by finding the largest eigenvalue of $-H(p, q) + C$ with a sufficiently large constant C and its corresponding eigenvector. The phase of a state is identified using the following quantities: $A_a \equiv \langle\psi| u(a)^{\otimes N} |\psi\rangle$, $A_x \equiv \langle\psi| u(x)^{\otimes N} |\psi\rangle$, $t \equiv \langle\psi| \mathcal{T} |\psi\rangle$, $f \equiv \langle\psi| \mathcal{P} |\psi\rangle$, and the energy

gap ΔE to the first excited state, where $u(a) = e^{i\frac{2\pi}{3}(S^x+S^y+S^z)/\sqrt{3}}$ and $u(x) = e^{i\pi S^x}$ are generators a and x of the internal symmetry group A_4, the operator $\mathcal{T}$ is the translation by one lattice site, and the operator $\mathcal{P}$ is the spatial inversion of spin indices. When the absolute values of these quantities are unity, the corresponding symmetry is respected by the wavefunciton $|\psi\rangle$.

In order to find the phase diagram, we first consider ground states of a relatively small system size $N = 10$ and compute A_a, A_x, t, p, and ΔE for ~ 1000 different parameters (p, q) randomly spread in the range $p \in [0, 2]$ and $q \in [-1/2, 1/2]$. The absolute values of $|A_a|$, $|A_x|$, $|t|$, and $|p|$, are shown in Fig. D.2(a), where we find that all symmetries are respected in almost entire range of parameters except $p \gtrsim 1$ and $-0.1 \lesssim q| \lesssim 0.1$. As we will discuss in details below, this domain of "symmetry broken" regime is due to the effects of finite system sizes, rather than being a distinct phase. From closings of energy gaps as well as the complex phase $\phi = \mathrm{Im}\left[\log\left(A_a\right)\right]$, we clearly identify three distinct phases, I, II, and III [see Fig. D.2(b)].

In order to extract the phase transition points, we perform finite size scaling analysis. We obtain the ground state energies $E^{(N)}(p, q)$ of up to $N = 14$ spins along two cuts at $p = 3/2$ and $3/4$ with $q \in [-0.4, 0.4]$. We compute the first and the second derivatives of energy density $E = E^{(N)}/N$ with respect to the parameter q, and extract the phase transition points q_c from discontinuities in $\partial E/\partial q$, or peaks in $\partial^2 E/\partial q^2$. We note that extracted q_c are sensitive to N mod 3. This is natural since the fiducial SPT phases are distinguished only by a complex phase $\chi \in \{1, e^{\pm i2\pi/3}\}$ which is periodic in 3; for a system of N spins, the many-body wavefunction acquires total phase χ^N, which is a function of N mod 3. For example, when N is an integer multiple of 3, the ground states in the three

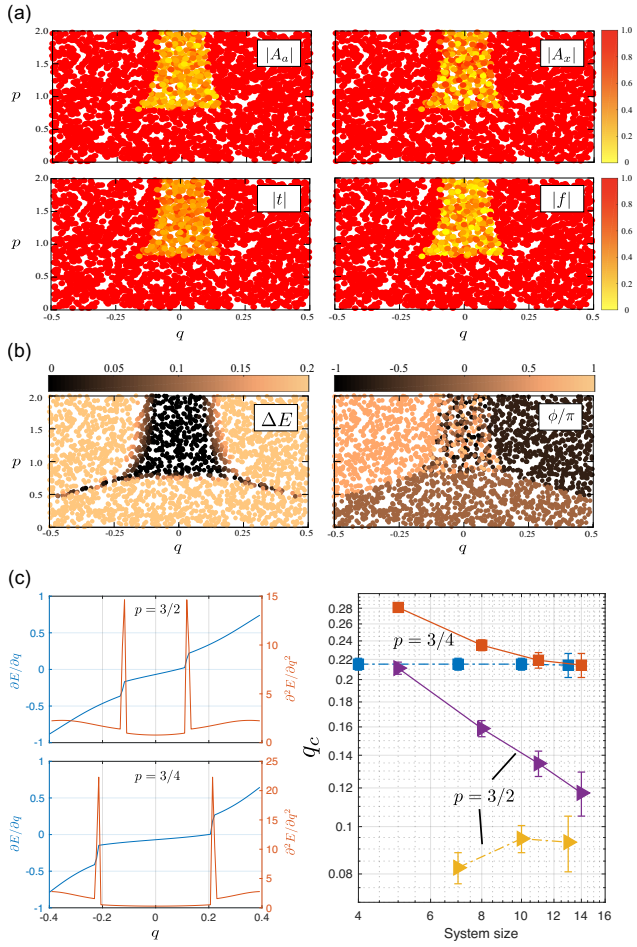

Figure D.2: Results of exact numerical computations. (a) The absolute values of $|A_a|$, $|A_x|$, $|t|$, and $|f|$ for $p \in [0, 2]$ and $q \in [-1/2, 1/2]$ with $N = 10$. The ground state respects all symmetries except for near the phase transition points. (b) The energy gap ΔE and the phase of $|A_a|$ for $p \in [0, 2]$ and $q \in [-1/2, 1/2]$ with $N = 10$. One clearly finds three separated phases. (c) Extraction of phase transition points using the first and second derivative of ground state energy as a function of q for a fixed value of p. Left: the first and second derivatives of energy density $E \equiv E^{(N)}/N$ for a system of $N = 14$ spins. Discontinuities in the first derivative or peaks in the second derivative are used as critical points q_c. Right: finite size scaling of the extracted critical points. Squares and triangles correspond to extracted critical points for two different cuts $p = 3/4$ and $3/2$, respectively. Due to the periodicity of χ (order 3), the estimated critical points are sensitive to N mod 3. For this reason, we plot separate scaling curves for different N mod 3 and omit N which are integer multiples of 3.

phases are not distinguishable by the complex phase, and we do not expect sharp phase transitions in our numerics with small system sizes.

For $p = 3/4$, one always finds two phase transitions at $\pm q_c$ which converge to non-zero values in increasing system sizes [Fig. 1(c) right]. In contrast, for $p = 3/2$, the critical point q_c decreases with system sizes, suggesting that the phase transition may occur directly from phase II to phase III in the thermodynamic limit.

D.4.2 ITEBD

We further confirm the phase diagram using an independent numerical method based on translationally-invariant, infinite-size matrix product states (iMPS). In order to find a ground state, we generally follow ITEBD algorithm introduced in Ref. [348] with a bond dimension $D = 60$. The iMPS Γ starts as a random product state. In every iteration, the state is updated after an imaginary time evolution $U_\tau = e^{-\tau\, H(p,q)}$, where we choose the small time step $\tau = 1/60$. After 300 repetitions, the updated Γ is taken as an approximate ground state.

A SPT phase is identified by studying how Γ transforms under the 120° spin rotation $a \in A_4$. Such information is contained the transfer matrix [347, 147]

$$T^{\alpha'\beta'}_{\alpha\beta} = \sum_{ij} u(a)_{ij} \Gamma^j_{\alpha\beta} (\Gamma^i_{\alpha'\beta'})^*, \tag{D.38}$$

where $i, j \in \{\pm 1, 0\}$ are physical indices and $\alpha, \alpha', \beta, \beta' \in \{1, \dots D\}$ are virtual (bond) indices [see Fig. D.3(a)]. Since we are interested in an infinite system, we only consider an eigenvalue η of the $T^{a'b'}_{ab}$ with the largest absolute value; if $|\eta| = 1$ the state Γ is invariant under the action of a, and otherwise the state breaks the symmetry. Also, in the case of symmetry unbroken phases, η coincides with $\chi(a)$, allowing us to distinguish the three

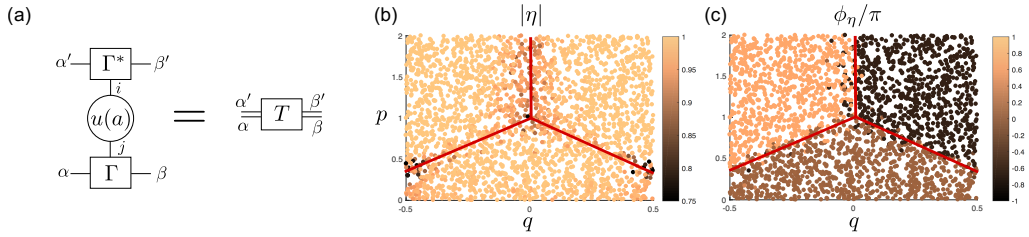

Figure D.3: ITEBD numerical calculations. (a) Diagrammatic representation of a transfer matrix $T^{\alpha'\beta'}_{\alpha\beta}$. (b-c) Absolute values $|\eta|$ and its phase ϕ_η as a function of (p, q). The red lines are guides to eyes, for estimated phase boundaries.

SPT phases. Figure D.3 (b) and (c) show $|\eta|$ and $\phi_\eta = \mathrm{Im}[\log(\eta)]$ for $p \in [0, 2]$ and $q \in [-1/2, 1/2]$. Clearly, we find three distinct phases separated by red lines. Near the phase boundaries, $|\eta|$ deviates from 1, probably owing to the finite bond dimension D, but there is little evidence for the existence of a symmetry broken phase.

D.5 Engineering of $H(p, q)$

In this section, we show that the Ising Hamiltonian $H_I = \sum_i S^z_i S^z_{i+1}$ can be engineered into $H(p, q)$ for a range of (p, q) satisfying $2|q| < p < 2 - 2|q|$. In fact, it is sufficient to show that $H(p, q)$ can be engineered for four points $(p_A, q_A) = (2, 0)$, $(p_B, q_B) = (1, -1/2)$, $(p_C, q_C) = (0, 0)$, and $(p_D, q_D) = (1, 1/2)$ by four pulse sequences. This is because any $H(p, q)$ with (p, q) in the convex hull of those points can be also engineered by concatenating the pulse sequences.

We first start by rewriting the given Ising interactions in a C representation:

$$C_I = \begin{pmatrix} 0 & 0 & 0 & 0 & 0 & 0 & 0 & 0 \\ 0 & 0 & 0 & 0 & 0 & 0 & 0 & 0 \\ 0 & 0 & 0 & 0 & 0 & 0 & 0 & 0 \\ 0 & 0 & 0 & 0 & 0 & 0 & 0 & 0 \\ 0 & 0 & 0 & 0 & 0 & 0 & 0 & 0 \\ 0 & 0 & 0 & 0 & 0 & 0 & 0 & 0 \\ 0 & 0 & 0 & 0 & 0 & 0 & \frac{1}{4} & \frac{\sqrt{3}}{4} \\ 0 & 0 & 0 & 0 & 0 & 0 & \frac{\sqrt{3}}{4} & \frac{3}{4} \end{pmatrix}. \tag{D.39}$$

Likewise, the C-representations of four target interactions are given as

$$C_A = \frac{1}{2}\begin{pmatrix} 1 & -1 & 0 & 0 & 0 & 0 & 0 & 0 \\ -1 & 1 & 0 & 0 & 0 & 0 & 0 & 0 \\ 0 & 0 & 2 & 0 & 0 & 0 & 0 & 0 \\ 0 & 0 & 0 & 1 & -1 & 0 & 0 & 0 \\ 0 & 0 & 0 & -1 & 1 & 0 & 0 & 0 \\ 0 & 0 & 0 & 0 & 0 & 2 & 0 & 0 \\ 0 & 0 & 0 & 0 & 0 & 0 & \frac{3}{2} & -\frac{\sqrt{3}}{2} \\ 0 & 0 & 0 & 0 & 0 & 0 & -\frac{\sqrt{3}}{2} & \frac{1}{2} \end{pmatrix}, \tag{D.40}$$

$$C_B = \frac{1}{2}\begin{pmatrix} 1 & 0 & 0 & -1 & 0 & 0 & 0 & 0 \\ 0 & 1 & 0 & 0 & 1 & 0 & 0 & 0 \\ 0 & 0 & 1 & 0 & 0 & 0 & 0 & 0 \\ -1 & 0 & 0 & 1 & 0 & 0 & 0 & 0 \\ 0 & 1 & 0 & 0 & 1 & 0 & 0 & 0 \\ 0 & 0 & 0 & 0 & 0 & 1 & -\frac{1}{2} & -\frac{\sqrt{3}}{2} \\ 0 & 0 & 0 & 0 & 0 & -\frac{1}{2} & 1 & 0 \\ 0 & 0 & 0 & 0 & 0 & -\frac{\sqrt{3}}{2} & 0 & 1 \end{pmatrix}, \tag{D.41}$$

$$C_C = \frac{1}{2}\begin{pmatrix} 1 & 1 & 0 & 0 & 0 & 0 & 0 & 0 \\ 1 & 1 & 0 & 0 & 0 & 0 & 0 & 0 \\ 0 & 0 & 0 & 0 & 0 & 0 & 0 & 0 \\ 0 & 0 & 0 & 1 & 1 & 0 & 0 & 0 \\ 0 & 0 & 0 & 1 & 1 & 0 & 0 & 0 \\ 0 & 0 & 0 & 0 & 0 & 0 & 0 & 0 \\ 0 & 0 & 0 & 0 & 0 & 0 & \frac{1}{2} & \frac{\sqrt{3}}{2} \\ 0 & 0 & 0 & 0 & 0 & 0 & \frac{\sqrt{3}}{2} & \frac{3}{2} \end{pmatrix}, \tag{D.42}$$

$$C_D = \frac{1}{2}\begin{pmatrix} 1 & 0 & 0 & 1 & 0 & 0 & 0 & 0 \\ 0 & 1 & 0 & 0 & -1 & 0 & 0 & 0 \\ 0 & 0 & 1 & 0 & 0 & 0 & 0 & 0 \\ 1 & 0 & 0 & 1 & 0 & 0 & 0 & 0 \\ 0 & -1 & 0 & 0 & 1 & 0 & 0 & 0 \\ 0 & 0 & 0 & 0 & 0 & 1 & \frac{1}{2} & \frac{\sqrt{3}}{2} \\ 0 & 0 & 0 & 0 & 0 & \frac{1}{2} & 1 & 0 \\ 0 & 0 & 0 & 0 & 0 & \frac{\sqrt{3}}{2} & 0 & 1 \end{pmatrix} \tag{D.43}$$

The strengths of isotropic components are given as $s_I = 1$, $s_A = 5$, $s_B = 4$, $s_C = 3$, and $s_D = 4$, which fix the rescaling parameters $\beta_a = s_I/s_a$. As in the case of decoupling spin-1 dipolar interactions, we assume that the set of available unitaries $\mathcal{U}$ is limited to composite pulses made out of up to four $\pm\pi$ and $\pm(\pi/2)$-pulses. Then, we use a linear programming routing built-in `Mathematica`. In each case, we find a 15-pulse sequence with $\beta_A^* = 1/5$ for C_A, a 12-pulse sequence with $\beta_B^* = 1/4$ for C_B, a 6-pulse sequence with $\beta_C^* = 1/3$ for C_C, and a 13-pulse sequence with $\beta_D^* = 1/4$ for C_D. These maximum β_a^* saturate the

required inequalities $\beta_a^* \geq s_I/s_a$ in all four cases.

Appendix E

Supporting Material of Chapter 6

E.1 Methods

Numerical methods and details—Here, we provide full numerics for our protocol in both the spin-1 model in Eq. (1) and the generic Heisenberg spin-1/2 model with random fields (Eq. 9). The general outline of the demonstration is the following. First, for a given realization of a disordered Hamiltonian we numerically identify two qubit- and bus-type excitations, located at positions L and R. Second, we compute the effective interaction strength between qubits either with or without off-resonant coupling to the bus excitations. Third, we repeat this process for various distances separating L and R and average the interaction strength over 500 realizations. Below, we provide the details of this process for both spin-1 and spin-1/2 models, always setting the lattice spacing $a = 1$.

For the spin-1 model, we exactly diagonalize a system of 14 spins (Eq. 1) with $\Delta_0 = 25, \Delta = 15, h_0 = h = 0.02$, and $t = 1$. The Hamiltonian conserves total z-magnetization, $\sum_i S_i^z$. Therefore, we only need to diagonalize a few relevant symmetry sectors of the

Hilbert space, namely, systems with up to four spin excitations starting from the spin polarized state $|G\rangle$. A single qubit excited state at position i is identified as the energy eigenstate with the largest overlap with $S_i^x |G\rangle$ where S_i^x is the spin flip operator at position i. We denote the eigenstate with a single excitation at position L as $\left|\phi^L\right\rangle$. In this simulation we choose $L = 3$. Similarly, we identify eigenstates with single qubit excitations at various positions $R = 8$, 9, 10, 11, and 12th site and denote them as $\left|\phi^R\right\rangle$. The eigenstates with two qubit excitations $\left|\phi^{LR}\right\rangle$ and bus excitations at L(or R) are also identified in a similar way from $S_R^x \left|\phi^L\right\rangle$ and $S_L^x \left|\phi^L\right\rangle$(or $S_R^x \left|\phi^R\right\rangle$), respectively. The off-resonant driving on the left qubit has been implemented by transforming the Hamiltonian into the rotating frame with a rotating wave approximation. The time-dependent driving on the right qubit has been numerically integrated over one period, and then the long time dynamics is studied in the Floquet basis. As discussed in the main text, the effective interaction strength between the MBL qubits is directly calculated from energy eigenvalues,

$$\delta_I \equiv E_{LR} - E_L - E_R + E_G. \tag{E.1}$$

This is also the case for the driven hamiltonian in the Floquet basis, where energies are defined via logarithms of unitary evolution. The average interaction strength as a function of distance is shown in Fig. E.1a. We confirm the exponential decay of the bare interaction strength δ_I with a length scale $\xi_1 \approx 0.53$ (blue solid line), which agrees with our simple theoretical estimate $\left(\log \frac{\Delta}{t}\right)^{-1} \approx 0.5$. When the qubits are driven, the interaction is enhanced by several orders of magnitude (red dash-dot line and green dotted line). Moreover, we observe that the enhanced interaction strength scales quadratically in Ω/δ (see Fig. E.1b), confirming the off-resonant dressing picture presented in Eq. (7) of the main text.

We use a similar technique to simulate a system of 16 spins in the Heisenberg model,

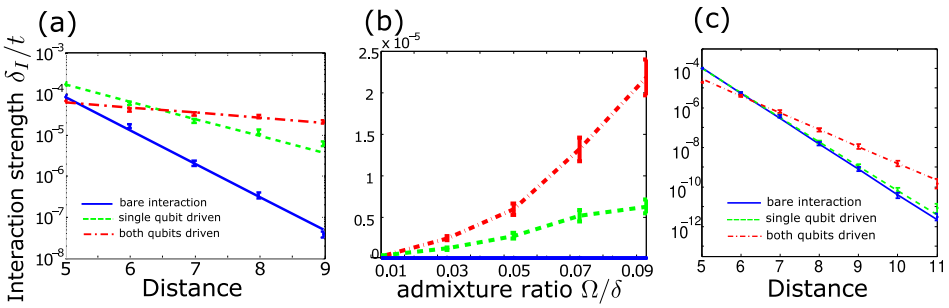

Figure E.1: Effective interaction strength. (a) Interaction strength decays more weakly when either one or both qubits are off-resonantly coupled to the bus excitations. (b) The enhanced interaction strength is quadratic in the ratio of Rabi frequency to detuning Ω/δ as expected for off-resonant dressing. (c) Effective interaction strength decay for the random field Heisenberg model.

with $t = 1$ and $\Delta = 7.5$. Again, the simulation supports up to four excitations from the polarized state $|G\rangle$. Unlike our spin-1 model, the qubit excitations are identified by their energy eigenvalues; single spin excitations with the highest and the lowest energies are used as $\left|\phi^L\right\rangle$ and $\left|\phi^R\right\rangle$ depending on their relative positions. A single excitation with either high or low energy is expected to have a short localization length. Therefore, coupling to any subsequent excitations will, on average, enhance the effective interaction. Note that our criteria of identifying qubit- and bus-excitations can be further optimized to achieve a stronger interaction enhancement. We estimate the positions of qubit excitations $p_{L(R)}$ by maximizing $|\left\langle\phi^{L(R)}\right| S^x_{p_{L(R)}} |G\rangle|$, and then identify bus excitations from $S^x_{p_L+1}\left|\phi^L\right\rangle$ and $S^x_{p_R-1}\left|\phi^R\right\rangle$, i.e. nearest subsequent excitations. The effective interaction strength as a function of distance is shown in Fig. E.1c. Again, we confirm that the enhancement is exponentially large at long distances. We emphasize that this model does not have 'engineered' localization lengths as in the spin-1 model.

The typical localization lengths of qubit and bus excitations can be obtained from the

slopes in Fig. E.1c, yielding $\xi_1 \sim 0.34$ (blue solid line) and $\xi_2 \sim 0.50$ (red dash-dot line). These values are consistent with the probability distribution of localization lengths studied in the next section.

Variation of localization lengths—Here, we provide numerics showing that a variation in localization lengths always exists in the localized phase of the random field Heisenberg model (this variation is of course most pronounced near the transition).

First, to work in the localized phase, we estimate the criticial disorder Δ/t for the many-body localization phase transition for various spin excitation densities (relative to the polarized state $|G\rangle$). We follow the method used in Ref. [13], and calculate the fraction of dynamical polarization at infinite temperature. The result is summarized in the left panel of Fig. E.2. We confirm that the transition occurs at $\Delta/t \sim 5$ for high densities, consistent with previous results for small system sizes [13]. At low densities, the critical disorder is smaller, approaching the limit of the Anderson localization criteria in 1D $\Delta/t \to 0$.

We study the variation of localization lengths under various conditions. Here, we *define* the localization length of excitations with respect to a particular a many-body eigenstate in the following way. First, we exactly diagonalize a system of 12 spins, choosing an arbitrary energy eigenstate with total spin up density $n_s = \sum_i \langle \left(S_i^z + \frac{1}{2}\right) \rangle / N$ and define it as our logical ground state $|\mathcal{G}\rangle = |00\rangle$. Then, we choose two "probing positions" $L_p = 2$ or 4 and $R_p = 9$ or 11 and identify all possible computational basis states (*viz.* $|01\rangle$, $|10\rangle$, and $|11\rangle$) as energy eigenstates that have large enough overlap with $S_R^+ |00\rangle$, $S_L^+ |00\rangle$, and $S_L^+ S_R^+ |00\rangle$; we also impose that these states satisfy the consistency condition $|\langle 11| S_L^+ |01\rangle|, |\langle 11| S_R^+ |10\rangle| > c$ with a threshold $c = 0.01$. The relative differences in the energy eigenvalues of these states *defines* the interaction strength δ_{int} and the localiza-

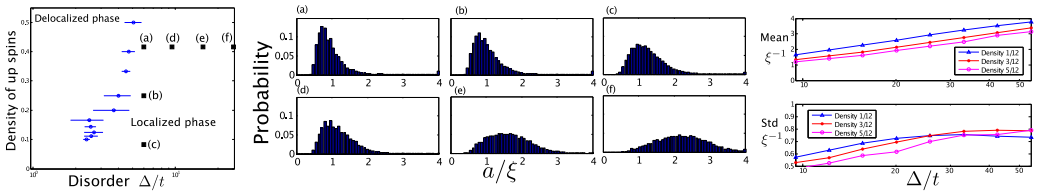

Figure E.2: Variation in the localization lengths. Left: the phase diagram of the random field Heisenberg spin-1/2 model as a function of spin density and disorder. Middle: histograms of the inverse localization length for parameters shown in the left panel. Right: mean and standard deviation of the inverse localization length in the strong disorder regime.

tion length ξ by

$$d/\xi \equiv -\log\left(\frac{|\delta_{\text{int}}|}{t}\right) = -\log\left(\frac{|E_{11} - E_{10} - E_{01} + E_{00}|}{t}\right) \tag{E.2}$$

where E_{ab} is the energy eigenvalue for $|ab\rangle$ and the distance between two excitations d is computed in the same way as in the previous section. We repeat this process for different logical ground states and disorder realizations; various values of n_s and Δ/t are shown as black squares (a-f) in Fig. E.2(left). For each case, the histogram of inverse localization lengths is shown in the middle panel of Fig. E.2. Note that we have chosen to histogram $1/\xi$ rather than ξ because the Jacobian induces long tails in ξ.

The mean of the inverse localization length increases with both decreasing spin density and increasing disorder strength. It may seem that the variance of the distribution is also increasing with disorder strength in (a), (d), (e), and (f); however, this behavior does not continue at larger disorder strengths. Rather, as shown in the right panel of Fig. E.2, the standard deviation saturates near $\Delta/t \sim 30$ while the mean continues to increase.

Initialization and DEER sequences— Here, we provide the detailed protocol for initializing the system into an effective many-body eigenstate using a combination of DEER

(double electron electron resonance) spin echo and efficient quantum phase estimation [180, 182]. We assume that the quantum state of the system is initially in an unknown superposition of many-body eigenstates. Our goal is to efficiently prepare a quantum state such that the coherence of qubit excitations and their interactions is maintained for sufficiently long times. In doing so, we only use local operators and projective measurements limited to the accessible region of size ℓ. We assume that we can start by preparing the small local regions $L(R)$ into their respective local eigenstates $\left|0_{L(R)}\right\rangle$ (e.g. eigenstates of τ^z spin operators within the region) [168].

The state of the full system can be written in the τ^z basis as

$$|\psi_0\rangle = \sum_M c_M \left|0_L\right\rangle \otimes |M\rangle \otimes \left|0_R\right\rangle \tag{E.3}$$

where M enumerates all (exponentially many) possible configurations for the uninitialized regions. Then, we perform local spectroscopy in each region (L and R) in order to estimate the energy of a single excitation at the center of the region. Due to the diagonal interactions in the MBL phase, the spectral lines for these excitations are broadened by at most $\sim t \exp\left(-l/\xi_2\right)$. With $\ell \gg \xi_2$, one can resolve and manipulate individual localized excitations in each region within a timescale $\sim t^{-1}$. We choose a single excitation in each region to use as our MBL qubits. These qubit excitations interact with spins in the rest of the chain and therefore dephase over a time scale $T \sim t^{-1} \exp\left(\ell/\xi_2\right)$. This dephasing can in principle be refocused by the spin echo sequence considered in Fig. E.3a [180].

For coherent interactions between MBL qubits, one needs to further initialize the system, since the interaction strength δ_I depends on the configuration M of the uninitialized region. For a specific M, the interaction can be written as $\delta_I = \delta_{LR} + \delta_{LMR}$ [168]. Here, one can understand δ_{LR} as the direct interaction between the two excitations while δ_{LMR} is

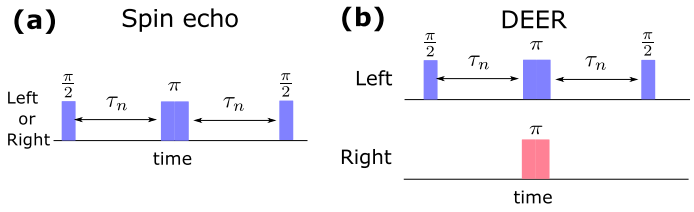

Figure E.3: Spin echo pulse sequences. (a) The dephasing of the left MBL qubit can be refocused via a simple Hahn echo. (b) a modified spin echo sequence (DEER) isolates the dephasing of the left MBL qubit induced by interactions $\delta_I = \delta_{LR} + \delta_{LMR}$.

the contribution provided by all of the multi-body interactions mediated by τ-spins in the uninitialized region. It is this dependence of δ_I on M that that prevents the coherent interaction between MBL qubits [180]. Interestingly, this problem can be solved by precisely measuring δ_I (to within $\delta\omega$) since the measurement serves as a quantum non-demolition measurement for the configuration of the uninitialized region. Note that this simple solution is only possible due to the lack of thermalization in the MBL phase.

For the measurement of δ_I, we consider a modified spin echo sequence, known as DEER, as depicted in Fig. E.3b [180]. This sequence refocuses the dephasing of the left MBL qubit induced by all but the MBL qubit on the right [180]. Each measurement of δ_I projects the many-body state of the system into a superposition of a few eigenstates that share the values of δ_I consistent with the measurement outcomes. Note that we do *not* require the preparation of a unique eigenstate as long as the prepared state enables coherent interactions between MBL qubits up to a desired time scale $T \sim \delta\omega^{-1}$. Repeating the DEER sequence (followed by measurements of the left MBL qubit) with a free evolution time τ_n measures the phase shift $\delta_I \tau_n$ modulo 2π. Therefore, by varying the free evolution time $\tau_n = 2^{-n}/\delta\omega$ with $n = 0, 1, 2, \ldots$, one can efficiently measure δ_I up to the desired precision $\delta\omega$ [182]. This particular sequence of τ_n is chosen such that the protocol mini-

$1-\mathcal{F}_1$	Gaussian	Lorentzian
$\ell < \xi_1$	$\exp[-2\mathcal{E}/\delta\omega]$	$(\delta\omega/\mathcal{E})^2$
$\ell > \xi_1$	$(\ell/\xi_1) \times (\delta\omega/\mathcal{E})$	$(\ell/\xi_1) \times (\delta\omega/\mathcal{E})$

Table E.1: Fidelity of one-qubit gates for finite spectral and spatial resolution under various conditions. Two different types of spectral profiles arise from different origins: Gaussian from inhomogeneous broadening, including the effects of the bare un-enhanced interaction, and Lorentzian from homogeneous broadening, e.g., extrinsic decoherence processes.

mizes the total evolution time and is well described in Ref. [182]. The total measurement time $\sum \tau_n$ scales linearly with the inverse of the desired resolution $T_{\text{init}} = \eta\delta\omega$, where a constant of order unity $\eta > 2$ accounts for the repetition of the $n = 0$ step due to projection noise.

Fidelity estimates— Here ,we analyze the fidelity of single qubit and gates under various conditions. The single qubit fidelity depends on both (i) whether the broadened spectral lines have power-law tails (e.g., a Lorentzian) or fall off more rapidly (e.g., a Gaussian) and (ii) how the spatial resolution ℓ compares with ξ_1. When $\ell \lesssim \xi_1$, local level repulsion ensures that there are no levels within the local spectral gap $\mathcal{E}$ of the targeted level that couple to the external driving field; when $\ell > \xi_1$, approximately $\delta\omega/\mathcal{E}$ levels per localization length are within the spatial extent of the driving, where $\delta\omega \sim 1/T_2$ is the spectral resolution. Moreover, when the linewidth is Lorentzian, the dominant imperfections are due to nearby transitions that use the tails $\sim (\delta\omega/\mathcal{E})^2$ of the Lorentzian (spectral imperfection); whereas, for rapidly decaying tails, the dominant imperfections are due to distant, exponentially weak lines that are within $\delta\omega$ of the targeted line (spatial imperfection). Fidelities in the four cases are summarized in Table E.1.

We now focus on the fidelity of two qubit gates and derive Eq. (12) in the main text, which we present here again for convenience,

$$\mathcal{F}_2 \simeq 1 - (t/\Gamma)^{-1+\xi_1/\xi_2^{eff}} \tag{E.4}$$

where Γ is an effective decoherence rate and ξ_2^{eff} is an effective localization length for bus excitations.

In general, the fidelity of a two qubit gate is given as

$$1 - \mathcal{F}_2 \simeq \frac{\max(\Gamma, \delta_I)}{\delta_I^{\text{driven}}} \tag{E.5}$$

where the numerator is the rate of decoherence due to either external imperfections or bare dephasing interactions, while the denominator is the strength of the enhanced interaction. One can always optimize d such that $\delta_I(d_{\text{opt}}) = \Gamma$. Then, using $\delta_I^{\text{driven}} \sim te^{-d_{\text{opt}}/\xi_2^{\text{eff}}}$, one can obtain Eq. (12). The dominant contributions to Γ and ξ_2^{eff} vary under differing conditions. First, ξ_2^{eff} is either ξ_2 or $\xi' \approx a\sqrt{tT_2}$ depending on the spectral resolution. When $1/T_2$ is larger than the typical energy spacing of bus-type excitations $\mathcal{E}_2$, one necessarilly couples a single MBL qubit with multiple excitations. In this case, the spatial extent of the qubit is broadened in the same way as that of a bound state coupled to a multi-particle contiuum of effective mass $m^* \approx 1/ta^2$, leading to $\xi' \approx \sqrt{T_2/m^*} \approx a\sqrt{tT_2}$ [183, 184, 185]. The effective decoherence rate Γ is limited by the rate of population loss as well as the extrinsic decoherence scale, $\Gamma = \max(\Gamma_{\text{loss}}, 1/T_2)$, where Γ_{loss} can be estimated using Fermi's golden rule

$$\Gamma_{loss} \sim \frac{1/T_2}{1/T_2^2 + \Delta^2} \left(\frac{l}{\xi_2}\Omega\right)^2 \frac{\Delta}{\mathcal{E}_2}. \tag{E.6}$$

The first factor comes from the Lorentzian spectrum, the second from the effective coupling strength, and the last from the density of bus excitation states. In order to maximize the size

of the dressed qubit, Δ needs to be as small as possible, limited only by $1/T_2$. Therefore, we set $\Gamma \sim 1/(T_2^2\mathcal{E}_2)\,(l/\xi_2)^2$, wherein the corresponding optimal spacing is given by $d_{\text{opt}} = \xi_1 \ln[tT_2 \min(1, T_2\mathcal{E}_2\xi_2^2/l^2)]$. There is a cross over at $l^2/T_2 = \mathcal{E}_2\xi_2^2$; when $l^2/T_2 > \mathcal{E}_2\xi_2^2$ the loss error limits the fidelity, and d_{opt} has to be relatively small in order to to avoid long gate operation times. For $l^2/T_2 < \mathcal{E}_2\xi_2^2$, the spectral lines of the bus-excitations are not resolved, but the fidelity remains limited by the number of gate operations within a decoherence window. Thus, one finds

$$1 - \mathcal{F}_2 \simeq (tT_2)^{-1+\xi_1/\xi'}. \tag{E.7}$$

We can estimate the fundamental limit of our protocol by considering a system optimized for our purposes viz. a system that supports different types of excitations with $\xi_2/\xi_1 \to \infty$ with perfect spatial resolution and finite decoherence time $T_2 < \infty$. In this case the optimal fidelity is achieved from Eq. (E.7). Consequently, in the limit $\xi_2 \to \infty$ and $\xi_1 \to a$, we obtain $\mathcal{F}_2^{opt} \simeq 1 - (tT_2)^{-1+\frac{1}{\sqrt{tT_2}}}$ as presented in the main text.

Appendix F

Supporting Material of Chapter 7

F.1 Numerical verification of effective Hamiltonian

In the main text, we have argued that the dynamics under U_F in Eq. (1) can be well approximated by an effective Hamiltonian H^*_{eff} up to an exponentially long time $t^* \sim \exp(\omega_0/J)$, and that H^*_{eff} can be obtained from a systematic series expansion. More specifically, it can be shown that H^*_{eff} can be obtained from Magnus series expansion of the form

$$H^*_{\text{eff}} = H^{(0)}_{\text{eff}} + H^{(1)} + H^{(2)} + \cdots + H^{(n_*)}, \tag{F.1}$$

where each high order term has decreasing (local) norm by a factor J/ω_0, providing additional corrections required for approximating longer time evolution. This series expansion converges exponentially up to the maximum order $n_* \sim O(\omega_0/J)$, which determines the longest time scale $t^* \sim \exp(n_*)$ during which the energy absorption can be neglected. While this statement has been analytically proved in Ref. [59, 81, 144, 100], it can be also explicitly confirmed from numerical simulations.

In this section, we numerically verify the validity of the effective Hamiltonian H^*_{eff} of

the Floquet unitary U_F in the main text. For this, we first exactly compute the Floquet unitary U_F in Eq. (1) with $\theta = \pi$ for a system of $N = 14$ spin-1/2 particles. Then, independently, we also construct the corresponding effective Hamiltonian

$$H_{\text{eff}}^{(k)} \equiv H_{\text{eff}}^{(0)} + \sum_{\ell=1}^{k} H^{(\ell)} \tag{F.2}$$

from the Magnus expansion of the time-dependent Hamiltonian in the toggling frame [Eq. (4)-(5) in the main text] by truncating at a finite order k. Then, the time-evolutions under $(U_F)^2$ and $\exp\left[-i2\tau H_{\text{eff}}^{(k)}\right]$ are compared using the fidelity

$$\mathcal{F}[2n] \equiv \left| \text{tr}\left[(U_F)^{2n} e^{i2n\tau H_{\text{eff}}^{(k)}} \right] \right| / D, \tag{F.3}$$

where D is the dimension of the Hilbert space. Note that we only compare the time-evolution over even number of Floquet cycles since the Hamiltonian in the toggling frame is periodic in 2τ. Also, we only diagonalize the total magnetization $\sum_i S_i^z = 0$ sector for numerical efficiency. The fidelity $\mathcal{F}$ is equal to unity if and only if two unitary evolutions are identical. Hence, the deviation of $\mathcal{F}$ from 1 serves as a conservative measure for the error in the effective Hamiltonian $H_{\text{eff}}^{(k)}$.

Figure F.1 shows our numerical results for four different truncation order k with the driving period $\tau = 2\pi/(7J)$ averaged over more than 400 disorder realizations. We find that the fidelity $\mathcal{F}$ deviates from 1 starting from a time scale that exponentially grows in k. This numerical demonstration strongly corroborates that the effective Hamiltonian can be indeed obtained from a perturbation series, which in our case converges to a MBL phase by design, c.f. Eq. (4) in the main text. We note that this numerical computation is possible only for $k \leq n_*$, beyond which the Magnus expansion is not guaranteed to converge. However, even in such cases, the perturbation series introduced in Ref. [65] can be still

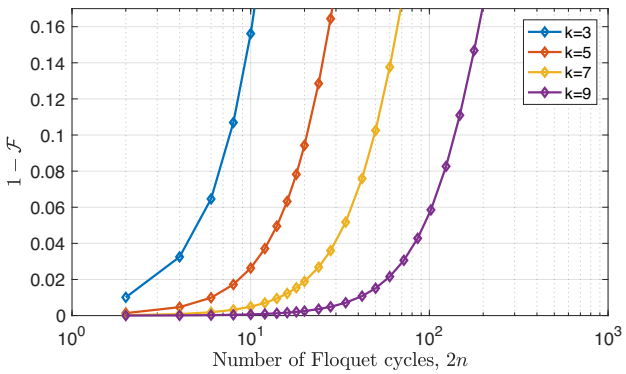

Figure F.1: Numerical verification of the effective Hamiltonian. The fidelity $\mathcal{F}$ deviates from 1 only after a long time that exponentially increases with k.

used to prove the convergence. Here, the crucial necessary condition is that $H_{\text{eff}}^{(k)}$ belongs to a MBL phase with an exponentially small probability of resonances, e.g. Eq. (11) in Ref. [65]. In our case, the smallness of the resonance probability has been shown in Eq. (8) of the main text.

Appendix G

Supporting Material of Chapter 9

G.1 Matrix product state representation of AKLT states

The ground states of AKLT Hamiltonian can be exactly represented by matrix product states (MPS). More specifically, for a system of n spin-1 particles, the unnormalized AKLT ground states can be written as

$$|G_{ab}\rangle = |A^n_{ab}\rangle = \sum_{\{s_i\}} \langle a|A^{(s_1)}A^{(s_2)}\cdots A^{(s_n)}|b\rangle \, |s_1 s_2 \cdots s_n\rangle \,, \tag{G.1}$$

where $s_i \in \{|m_z = \pm 1\rangle \,, |m_z = 0\rangle\}$ runs over three spin projections of particles at site i, and $a, b \in \{\uparrow, \downarrow\}$ specify the edge states of $|G_{ab}\rangle$. Here and below, the notation $|A^n_{ab}\rangle$ indicates translational-invariant MPS of n particles with open boundary condition specified by a and b, and $|A^n\rangle$ denotes the state with periodic boundary condition, i.e. $|A^n\rangle = \sum_a |A^n_{aa}\rangle$. In this way, one can conveniently rewrite the quantum state of an n-particle system as a linear superposition of composite systems, each with m and $n-m$ particles, i.e. $|A^n_{ab}\rangle = \sum_c |A^m_{ac}\rangle \left|A^{n-m}_{cb}\right\rangle$. In the canonical form [214], the explicit MPS representation of

AKLT states is given by

$$A^{(+)} = \sqrt{\frac{2}{3}}\sigma^{+}, \quad A^{(0)} = -\sqrt{\frac{1}{3}}\sigma^{z}, \quad A^{(-)} = -\sqrt{\frac{2}{3}}\sigma^{-}. \tag{G.2}$$

In this representation, the many-body overlap between two AKLT states with different boundary conditions can be straightforwardly computed. More explicitly, using the transfer matrix [214], we obtain

$$\langle A^{n}_{ab}|A^{n}_{a'b'}\rangle = \langle ab| \begin{pmatrix} \frac{1}{2}(1+\epsilon^n) & 0 & 0 & \epsilon^n \\ 0 & \frac{1}{2}(1-\epsilon^n) & 0 & 0 \\ 0 & 0 & \frac{1}{2}(1-\epsilon^n) & 0 \\ \epsilon^n & 0 & 0 & \frac{1}{2}(1+\epsilon^n) \end{pmatrix} |a'b'\rangle\,, \tag{G.3}$$

where $|ab\rangle\,, |a'b'\rangle \in \{\uparrow\uparrow, \uparrow\downarrow, \downarrow\uparrow, \downarrow\downarrow\}$ and $\epsilon \equiv -1/3$. We note that this MPS is injective (see section G.7.1 and Ref. [214]).

G.2 Effective Liouvillian

Our proposal for preparing AKLT states uses only one type of jump operator, e.g. $c = |00\rangle\langle{+}{+}|$. The dissipative dynamics due to this jump operator is $\mathcal{L}_0 = \Gamma \sum_i \mathcal{D}[c^{(i)}]$, where i enumerates the pair of neighboring sites $(i, i+1)$. Our key idea is to use coherent global manipulations, corresponding to operations in the symmetry group, so as to effectively realize additional jump operators. This can be achieved either by periodically applying pulsed global spin rotations (symmetry operations), or by continuously rotating the spins.

In the first, multi-pulse sequence approach, we apply pulses $V_\theta = (e^{i\theta S_y})^{\otimes n}$, separated by interval of τ each. Then in the rotating frame, we have the time-dependent Liouvillian:

$$\mathcal{L}_{\text{MP}}(t) = (V_\theta^\dagger)^k \mathcal{L}_0 V_\theta^k \quad \text{for} \quad k\tau \le t < (k+1)\tau. \tag{G.4}$$

Suppose we choose $\theta = 2\pi/\ell$ for some integer ℓ, then this dynamics is periodic with period $\ell\tau$, since $V_{2\pi/\ell}^{\ell} = \mathbb{1}$. In the limit of fast pulses $\tau \ll 1/\Gamma$, we can use the first-order Magnus expansion to derive a simpler, effective time-independent Liouvillian that approximate the dynamics:

$$\bar{\mathcal{L}}_{\text{MP}} = \frac{1}{\ell\tau}\int_0^{\ell\tau} \mathcal{L}_{\text{MP}}(t)dt = \frac{\Gamma}{\ell}\sum_i \sum_{\alpha=0}^{\ell-1} \mathcal{D}[\bar{c}_\alpha^{(i)}], \tag{G.5}$$

where $\bar{c}_\alpha = (V_{2\pi/\ell}^\dagger)^\alpha c V_{2\pi/\ell}^\alpha$.

Alternatively, we may employ a continuous wave approach by introducing a time-independent Hamiltonian $H_{\text{CW}} = \omega\sum_i S_i^y$. Then in the rotating frame, we have $c(t) = e^{i\omega t S_y} c e^{-i\omega t S_y}$, and

$$\dot{\rho} = \mathcal{L}_{\text{CW}}(t)\rho \equiv \Gamma\sum_i \mathcal{D}[c^{(i)}(t)]\rho. \tag{G.6}$$

In this frame, the dynamics is periodic with period $2\pi/\omega$. Again, we compute the effective time-independent Liouvillian

$$\bar{\mathcal{L}}_{\text{CW}} = \frac{\omega}{2\pi}\int_0^{2\pi/\omega} \mathcal{L}_{\text{CW}}(t)dt = \sum_i \sum_{\beta=0}^{\ell-1} \Gamma_\beta \mathcal{D}[\bar{c}_\beta^{(i)}], \tag{G.7}$$

obtained by time-averaging (first-order Magnus expansion) as an approximation. The effective jump operator $\bar{c}_\beta$ in the standard form of Liouvillian can be obtained by diagonalizing the superoperator acting on the space of density operator. More explicitly, we diagonalize a Hermitian matrix $L = U^\dagger \Lambda U$, whose entries $L_{ii',jj'}$ are given by

$$L_{ii',jj'} \equiv \left\langle ij|\frac{\omega}{2\pi}\int_0^{2\pi/\omega} dt\, \Gamma c^*(t)\otimes c(t)|i'j'\right\rangle = \sum_\beta U^*_{\beta,ii'}\Lambda_\beta U_{\beta,jj'} \equiv \left\langle ij|\sum_\beta \Gamma_\beta \bar{c}_\beta^*\otimes\bar{c}_\beta|i'j'\right\rangle \tag{G.8}$$

We can read off $\Gamma_\beta = \Lambda_\beta$, and $\bar{c}_\beta = \sum_{k,k'} U_{\beta,kk'}|k\rangle\langle k'|$. For our example choice of $c(t=0) = |00\rangle\langle++|$, we obtain $\ell = 9$ independent jump operator after evaluating the integral and diagonalizing, each with rate $\Gamma_\beta/\Gamma = 7/32$, 3/16, 3/16, 1/8, 1/8, 1/16, 1/16, 1/64, 1/64.

G.3 Uniqueness of steady states

In this section, we provide detailed proofs that our proposed $\bar{\mathcal{L}}_{\text{MP}}$ and $\bar{\mathcal{L}}_{\text{CW}}$ have AKLT states as unique steady states, for $n \geq 2$ under open boundary condition, and $n \geq 4$ under periodic boundary condition.

G.3.1 Open Boundary Condition

Although the proof for open boundary condition has been sketched in the main text, here we provide more detailed analysis. We prove by induction. Let us denote $\mathcal{L}_i = \sum_{\alpha=0}^{\ell-1} \Gamma_\alpha \mathcal{D}[\bar{c}_\alpha^{(i)}]$ as the Liouvillian acting only on sites i and $i+1$, and $\mathcal{L}_{[n]} = \sum_{i=1}^{n-1} \mathcal{L}_i$. The base case of $n = 2$ can easily be checked numerically or by exact calculations. The inductive hypothesis is that $\mathcal{L}_{[n]}$ only has AKLT states $|A_{ab}^n\rangle$ as steady states. Assume for the sake of contradiction that there exist other steady states for $\mathcal{L}_{[n+1]}$ on $n+1$ particles. This means that there exists a subspace $\mathcal{S}$ where $c_\alpha^{(i)}\mathcal{S} \subseteq \mathcal{S}$ for any i and α, and $\mathcal{S} \perp G \equiv \text{span}\{|A_{ab}^{n+1}\rangle\}$ [221]. This assumption implies that $f(\{\bar{c}_\alpha^{(i)}\})\,|\psi\rangle \in \mathcal{S}$ for any $|\psi\rangle \in \mathcal{S}$ and any polynomial $f(\cdot)$ of the jump operators. Now, let $\rho_{\mathcal{S}}$ be a steady state supported by $\mathcal{S}$, so that $\text{range}(\rho_{\mathcal{S}}) \subseteq \mathcal{S}$. Then let us perform the infinite time evolution $\rho_\infty = \lim_{t\to\infty} \exp(\mathcal{L}_{[n]}t)\rho_{\mathcal{S}}$, which is a steady state of $\mathcal{L}_{[n]}$. Consider any state $|\psi\rangle \in \text{range}(\rho_\infty)$.

On one hand, by our inductive hypothesis, any steady state of $\mathcal{L}_{[n]}$ must look like an AKLT state on the first n particles. Hence, we can write $|\psi\rangle = \sum_{abs} \psi_{abs}\,|A_{ab}^n\rangle\,|s\rangle$, where $s \in \{+, 0, -\}$. On the other hand, we must have $|\psi\rangle \in \mathcal{S}$ since $\mathcal{L}_{[n]}$ contains the same jump operators found in $\mathcal{L}_{[n+1]}$ that leave $\mathcal{S}$ invariant by assumption. Let us denote $f_\mu = \bar{c}_\mu$ for $\mu = 0, \ldots, \ell-1$, and $f_\mu = \mathbb{1}$ for $\mu = \ell$. By the assumption that $f_\mu^{(n)}\,|\psi\rangle \in \mathcal{S} \perp G$, we require that for any $p, q \in \{\uparrow, \downarrow\}$ and $0 \leq \mu \leq \ell$, the following set of linear equations for

ψ_{abs} must be true:

$$0 = \left\langle A^{n+1}_{pq} | f^{(n)}_{\mu} | \psi \right\rangle \tag{G.9}$$

$$= \sum_{abs} \psi_{abs} \left\langle A^{n+1}_{pq} | f^{(n)}_{\mu} (|A^{n}_{ab}\rangle |s\rangle) \right\rangle \tag{G.10}$$

$$= \sum_{abcrs} \psi_{abs} \left\langle A^{n-1}_{pr} | A^{n-1}_{ac} \right\rangle \times \left\langle A^{2}_{rq} | f_{\mu} | A^{1}_{cb} \right\rangle |s\rangle$$

$$= \sum_{abs} B^{abs}_{pq\mu} \psi_{abs} \equiv \boldsymbol{B}\vec{\psi}, \tag{G.11}$$

where $\vec{\psi}$ is a 12-dimensional vector and $\boldsymbol{B}$ is a $4(\ell+1)$-by-12 matrix. The matrix elements of $\boldsymbol{B}$ given by $B^{abs}_{pq\mu} = \sum_{cr} \left\langle A^{n-2}_{pr} | A^{n-2}_{ac} \right\rangle \times \left\langle A^{2}_{rq} | f_{\mu} | A^{1}_{cb} \right\rangle |s\rangle$ can be calculated analytically, since the first factor comes from diagonalizing the transfer matrix, and the second factor is computed in a small 9-dimensional Hilbert space. Now if $\det(\boldsymbol{B}^{\dagger}\boldsymbol{B}) \neq 0$, then the matrix $\boldsymbol{B}$ has full rank, indicating that we only have the trivial solution $\psi_{abs} = 0$. Then, by contradiction, $\mathcal{S}$ cannot exists, and $\left|A^{n+1}_{ab}\right\rangle$ are the unique steady states of $\mathcal{L}_{[n+1]}$.

Therefore, it only remains to compute $\det(\boldsymbol{B}^{\dagger}\boldsymbol{B})$ for $\mathcal{L}$ in our proposals. Let us first consider $\bar{\mathcal{L}}_{\text{MP}}$, with $\ell = 5$ corresponding to rotation pulses with $\theta = 2\pi/5$. For this, we explicitly find

$$\det(\boldsymbol{B}^{\dagger}\boldsymbol{B}) = \frac{5^8(x+3)^6(x-1)^2(3x+1)^6(x^2+27)^2(x^2-6x+45)^3}{2^{40}9^{13}x^{24}}, \quad x \equiv (-3)^n \tag{G.12}$$

It's easy to see that this is only zero for $n = 0, \pm 1$, so our inductive proof holds for $n \geq 2$. For $\bar{\mathcal{L}}_{\text{CW}}$, which has $\ell = 9$, we find

$$\det(\boldsymbol{B}^{\dagger}\boldsymbol{B}) = \frac{13(x+3)^6(x-1)^2(3x+1)^6(5x^2-6x+153)^2(13x^2-66x+549)(65x^2-342x+2781)}{2^{20}7^4 9^{17}x^{24}}$$

where we again denote $x \equiv (-3)^n$. This is also only nonzero when $n = 0, \pm 1$, proving that the steady states of $\bar{\mathcal{L}}_{\text{MP}}$ and $\bar{\mathcal{L}}_{\text{CW}}$ are unique for $n \geq 2$.

This proof naturally suggests a method to prepare an AKLT state with specified edge states instead of a mixture of the four $|A^{n}_{ab}\rangle$ under open boundary condition. For instance,

$\left|A^n_{\uparrow\uparrow}\right\rangle$ can be deterministically prepared by adding two jump operators: $c_L = |0\rangle\langle -|_1$ on the left edge and $c_R = |0\rangle\langle +|_n$ on the right. In this case, it is easy to see that any linear combination of four ground states $|A^n_{ab}\rangle$ can further decay into $\left|A^n_{\uparrow\uparrow}\right\rangle$, which becomes the unique steady state.

G.3.2 Periodic Boundary Condition

The uniqueness proof for periodic boundary condition builds on the result for open boundary condition, and is very similar in spirit. Let the Liouvillian under periodic boundary condition be $\mathcal{L}^{\circ}_{[n]} = \mathcal{L}_{[n]} + \mathcal{L}_{n,1}$, where $\mathcal{L}_{n,1} = \sum_{\alpha=0}^{\ell-1} \Gamma_\alpha \mathcal{D}[\bar{c}^{(n,1)}_\alpha]$ acts on sites n and 1. Assume for the sake of contradiction that there exists a steady state of $\mathcal{L}^{\circ}_{[n]}$ other than $|A^n\rangle = \sum_a |A^n_{aa}\rangle$, supported by a subspace $\mathcal{S} \perp |A^n\rangle$. Let $\rho_{\mathcal{S}}$ be such a steady state, on which we perform the infinite time evolution to obtain $\rho_\infty = \lim_{t\to\infty} \exp(\mathcal{L}_{[n]}t)\rho_{\mathcal{S}}$. Note ρ_∞ is a steady state of $\mathcal{L}_{[n]}$. Again, consider any state $|\psi\rangle \in \mathrm{range}(\rho_\infty) \subseteq \mathcal{S}$.

From our results for open boundary condition, we know that we can write $|\psi\rangle = \sum_{ab} \psi_{ab} |A^n_{ab}\rangle$. Additionally, we must have $f(\{\bar{c}^{(i,i+1)}_\alpha\}) |\psi\rangle \in \mathcal{S}$ for any polynomial $f(\cdot)$ of jump operators. It turns out that unlike in the case of open boundary condition, polynomials of degree one are not sufficient to demonstrate uniqueness of steady states. Instead, let us consider polynomials of the form $f^{(n,1)}_\mu f^{(n-1,n)}_\nu f^{(n,1)}_\lambda$, where $f_\mu = \bar{c}_\mu$ for $\mu = 0, \ldots, \ell - 1$

and $f_\mu = \mathbb{1}$ for $\mu = \ell$. Hence, we have the following set of linear equations for ψ_{ab}:

$$\begin{aligned} 0 = & \quad \left\langle A^n | f_\mu^{(n,1)} f_\nu^{(n-1,n)} f_\lambda^{(n,1)} | \psi \right\rangle & \text{(G.14)} \\ = & \quad \textstyle\sum_{ab} \psi_{ab} \left\langle A^n | f_\mu^{(n,1)} f_\nu^{(n-1,n)} f_\lambda^{(n,1)} | A^n_{ab} \right\rangle & \text{(G.15)} \\ = & \quad \textstyle\sum_{ab} B^{ab}_{\mu\nu\lambda} \psi_{ab} = \boldsymbol{B}\vec{\psi}, \end{aligned}$$

$$\begin{aligned} \text{where} \quad B^{ab}_{\mu\nu\lambda} = & \quad \textstyle\sum_{cdpqr} (\langle A^1_{pq}| \left\langle A^{n-3}_{qr}\right| \left\langle A^2_{rp}| \right) f_\mu^{(n,1)} f_\nu^{(n-1,n)} f_\lambda^{(n,1)} (|A^1_{ac}\rangle \left| A^{n-3}_{cd} \right\rangle |A^2_{db}\rangle) \\ = & \quad \textstyle\sum_{cdqr} \left\langle A^{n-3}_{qr} | A^{n-3}_{cd} \right\rangle \times \left\langle A^3_{rq} | (\mathbb{1} \otimes f_\mu)(f_\nu \otimes \mathbb{1})(\mathbb{1} \otimes f_\lambda) | A^2_{db} \right\rangle |A^1_{ac}\rangle & \text{(G.16)} \end{aligned}$$

Here, $\vec{\psi}$ is a 4-dimensional vector, and $\boldsymbol{B}$ is a $(\ell+1)^3$-by-4 matrix. For $\bar{\mathcal{L}}_{\text{MP}}$ with $\ell = 5$, we find

$$\det(\boldsymbol{B}^\dagger \boldsymbol{B}) = \frac{5^9 7^3 (x+3)^2 (x+27)^6}{2^{33} 3^{15} x^8}, \quad x \equiv (-3)^n. \tag{G.17}$$

And similarly, for $\bar{\mathcal{L}}_{\text{CW}}$, which has $\ell = 9$, we find

$$\det(\boldsymbol{B}^\dagger \boldsymbol{B}) = \frac{5 \times 283^2 (x+3)^2 (x+27)^6}{2^2 7^5 3^{17} x^8}, \quad x \equiv (-3)^n. \tag{G.18}$$

Both of these vanish only when $n = 1, 3$. Thus, the steady states of $\bar{\mathcal{L}}_{\text{MP}}$ and $\bar{\mathcal{L}}_{\text{CW}}$ are unique for $n \geq 4$. The fact that they vanish for $n = 3$ corroborates numerical simulations that also demonstrate the existence of undesired steady states for $n = 3$ under periodic boundary condition.

G.4 Details of our numerical simulation

We simulate the dissipative dynamics $\mathcal{L} = \sum_\mu \Gamma_\mu \mathcal{D}[c_\mu]$ using the stochastic wavefunction method [240]. In this approach, the wavefunction $|\psi(t)\rangle$ continuously evolves under the effective non-Hermitian Hamiltonian $H_{\text{eff}} = H - i \sum_\mu \Gamma_\mu c_\mu^\dagger c_\mu / 2$ and stochastically undergoes quantum jumps c_μ at a rate $\langle \psi | \Gamma_\mu c_\mu^\dagger c_\mu | \psi \rangle$. Physical observables are extracted from

an ensemble of wavefunction trajectories obtained from independent simulations. Compared to direct numerical integrations of quantum master equations, this method allows simulation of systems with larger number of particles. In order to simulate a maximally mixed initial state (or equivalently an infinite temperature ensemble), we sample a random product state in the S_z-basis as the initial state $|\psi_\alpha(0)\rangle$ for the α-th simulation. For each small time step δt, the state $|\psi_\alpha(t)\rangle$ evolves stochastically according to either

- $|\psi_\alpha(t+\delta t)\rangle \propto c_\mu |\psi_\alpha(t)\rangle$ with probability $\delta p_\mu = \langle \psi_\alpha(t)|\Gamma_\mu c_\mu^\dagger c_\mu|\psi_\alpha(t)\rangle \, \delta t$, or
- $|\psi_\alpha(t+\delta t)\rangle \propto e^{-iH_{\text{eff}}\delta t}|\psi_\alpha(t)\rangle$ with probability $1-\sum_\mu \delta p_\mu$.

We choose δt so that $\delta p = \sum_\mu \delta p_\mu \ll 1$. Since this process is stochastic, we average over a sufficiently large number N_{traj} of trajectories to estimate the values of observables:

$$\left\langle \hat{\mathcal{O}} \right\rangle = \text{tr}[\hat{\mathcal{O}}\rho(t)] \simeq \frac{1}{N_{\text{traj}}} \sum_{\alpha=1}^{N_{\text{traj}}} \left\langle \psi_\alpha(t)|\hat{\mathcal{O}}|\psi_\alpha(t)\right\rangle . \tag{G.19}$$

For the numerical data presented in the main text, we average over up to $N_{\text{traj}} = 1000$ trajectories, and statistical uncertainties are estimated using the bootstrapping technique [349]. For relatively large system sizes $n > 8$, numerical computations of exact many-body wavefunctions are impractical. Instead, we store the wavefunction in MPS representation, and simulate the evolution using the time-evolving block decimation algorithm [241]. Since we are dissipatively preparing AKLT states that have bond dimension $D = 2$, we find that restricting the maximum bond dimension of our MPS wavefunction to $D \leq 15$ is sufficient, as truncation errors are found to be $< 5 \times 10^{-5}$ in all simulations. This algorithm allows us to simulate systems with up to $n = 25$ spins.

During our simulated evolution, we monitor two observables: (1) energy density $\langle H_{\text{AKLT}}\rangle /(n-1)$ and (2) fidelity of state preparation $\mathcal{F} = \langle P_G\rangle$ where P_G is the projector onto AKLT

ground states. Note that since our simulation in the main text is for the open boundary condition, there are four degenerate ground states that are all accepted as output; we define our fidelity $\mathcal{F}$ to be the sum of overlap with each accepted state. Another widely used measure on quantum states, trace distance [350], cannot be applied in this context, because it measures how close a state is to another (target) state, not to a subspace of such states. Even in a situation where the target state is a single pure state, e.g. under periodic boundary condition, the trace distance T is bounded by our fidelity $\mathcal{F}$ through $1-\sqrt{\mathcal{F}} \leq T \leq \sqrt{1-\mathcal{F}}$. In our numerics where the system size goes up to $n = 25$, the computational cost of calculating the density matrix and trace distance would also be prohibitively expensive. Lastly, this fidelity $\mathcal{F}$ coincides with the success probability of state preparation, which is a physically meaningful metric.

G.5 Detailed analysis of Rydberg-EIT implementation proposal

In this section, we derive the effective dissipative interaction between two nearby particles for our Rydberg-EIT implementation scheme introduced in the main text. Consider two particles interacting via the Rydberg shift $H_{\text{int}} = U\left|rr\right\rangle \bar{r}\bar{r}$. Their effective (non-Hermitian) Hamiltonian under the Rydberg-EIT scheme proposed in the main text is

$$\begin{aligned} H_{\text{eff}} &= \sum_{j=1}^{2}\left[(g|+\rangle\langle e| + \Omega|r\rangle\langle e| + h.c.) - i\frac{\gamma}{2}\left|e\right\rangle\bar{e}\right]_j + U\left|rr\right\rangle\left\langle rr\right| \\ &= \sum_{j=1}^{2}\left[\Delta(|B\rangle\langle e| + h.c.) - i\frac{\gamma}{2}\left|e\right\rangle\left\langle e\right|\right]_j + U\left|rr\right\rangle\left\langle rr\right|, \end{aligned} \tag{G.20}$$

where $\Delta = \sqrt{\Omega^2 + g^2}$, $|D\rangle = (\Omega\,|+\rangle - g\,|r\rangle)/\Delta$ is the EIT-dark state, and $|B\rangle = (g\,|+\rangle + \Omega\,|r\rangle)/\Delta$ a state orthogonal to $|D\rangle$ that we call EIT-bright state. Now consider a general two-particle wavefunction $|\psi\rangle = \sum_a c_{aa}\,|aa\rangle + \sum_{a<b} c_{ab}(|ab\rangle + |ba\rangle)/\sqrt{2}$, where we've restricted ourselves to working in the symmetric subspace. Then the equations of motion for the coefficients are

$$i\dot{c}_{DD} = \frac{g^4 U}{\Delta^4} c_{DD} - \frac{\sqrt{2} g^3 \Omega U}{\Delta^4} c_{DB} + \frac{g^2 \Omega^2 U}{\Delta^4} c_{BB} \tag{G.21}$$

$$i\dot{c}_{De} = -i\frac{\gamma}{2} c_{De} + \Delta c_{DB} \tag{G.22}$$

$$i\dot{c}_{DB} = \frac{2 g^2 \Omega^2 U}{\Delta^4} c_{DB} + \Delta c_{De} - \frac{\sqrt{2} g^3 \Omega U}{\Delta^4} c_{DD} - \frac{\sqrt{2} g \Omega^3 U}{\Delta^4} c_{BB} \tag{G.23}$$

$$i\dot{c}_{ee} = -i\gamma c_{ee} + \sqrt{2}\Delta c_{eB} \tag{G.24}$$

$$i\dot{c}_{eB} = -i\frac{\gamma}{2} c_{eB} + \sqrt{2}\Delta(c_{ee} + c_{BB}) \tag{G.25}$$

$$i\dot{c}_{BB} = \frac{\Omega^4 U}{\Delta^4} c_{BB} + \sqrt{2}\Delta c_{eB} - \frac{\sqrt{2} g \Omega^3 U}{\Delta^4} c_{DB} + \frac{g^2 \Omega^2 U}{\Delta^4} c_{DD}. \tag{G.26}$$

In the limit of $U \ll g, \Omega, \gamma$, or $g \ll \Omega, \gamma, U$, and assuming we start initially with $|\psi\rangle = |DD\rangle$, we can adiabatically eliminate the fast dynamics involving coefficients $\{c_{ab}\}$ other than c_{DD}. This procedure can be effectively achieved by setting $\dot{c}_{ab} = 0$ for $ab \neq DD$, allowing us to obtain

$$i\dot{c}_{DD} = U_{DD} c_{DD} \quad \text{where} \quad U_{DD} = \frac{g^4}{\Delta^4} \frac{U}{1 + i\chi U} \quad \text{and} \quad \chi = \frac{\Omega^2(\Omega^2 + (1 + 3g^2/\Delta^2)\gamma^2/4)}{\Delta^4 \gamma}. \tag{G.27}$$

Here, $\mathrm{Re}[U_{DD}]$ is the interaction-induced energy shift, and $\Gamma_{DD} = -2\mathrm{Im}[U_{DD}]$ is the two-body effective decay rate.

A more general version of adiabatic elimination for open system can be found in Ref. [244], which allows us to obtain effective jump operators. Consider original jump operators of the form $L_{s,j} = |s\rangle\langle e|_j$, corresponding to the spontaneous decay from excited

state $|e\rangle$ to one of the three hyperfine ground state $|s\rangle$ for $s \in \{+, 0, -\}$ in atom j. Note that in practice, the excited state can also decay into other hyperfine ground states, which can then be repumped to the excited state using additional lasers. We denote the decay rate corresponding to $L_{s,j}$ as γ_s, where $\gamma_+ + \gamma_0 + \gamma_- = \gamma$. Then we can compute the effective jump operators:

$$L_{s,1}^{\text{eff}} = |s\tilde{e}\rangle\langle DD|, \quad L_{s,2}^{\text{eff}} = |\tilde{e}s\rangle\langle DD|, \quad \text{each with rate} \quad \frac{\gamma_s}{2\gamma}\Gamma_{DD}, \tag{G.28}$$

and $|\tilde{e}\rangle \propto \frac{\Omega\gamma}{2\Delta}|B\rangle - i\Omega|e\rangle - \frac{g\gamma}{\Delta}|D\rangle$. Note $|\tilde{e}\rangle$ will further decay through the original jump operator $L_{s,j}$. Assuming we are in the regime $\gamma \gg \gamma_s\Gamma_{DD}/2\gamma$ so that $|\tilde{e}\rangle$ is a short-lived intermediate state, we can approximate the overall effective dynamics with jump operators of the form $L_{ss'}^{\text{eff}} = |ss'\rangle\langle DD|$ for $s, s' \in \{+, 0, -\}$. Note while we only need the jump operator $L_{00}^{\text{eff}} = |00\rangle\langle DD|$ to ensure AKLT states are unique steady states of the engineered dissipative dynamics, the extra effective jump operators do not affect the steady states and can help to more quickly depopulate the undesired states.

G.6 Detailed analysis of parallelized protocol

G.6.1 Non-Hermitian time evolution

In this section, we use the stochastic wavefunction formalism for open system dynamics. Namely, we define an effective non-Hermitian Hamiltonian $H_{\text{eff}} = H - i\sum_\mu \Gamma_\mu c_\mu^\dagger c_\mu/2$, where H is the hamiltonian of the system and $c^{(i)}$ are quantum jump operators. A system evolves under H_{eff} until it undergoes quantum jump $|\psi\rangle \mapsto c_\mu|\psi\rangle$ at a rate $\langle\psi|\Gamma_\mu c_\mu^\dagger c_\mu|\psi\rangle$. In our protocol to prepare AKLT states, $H = 0$ since we work in the rotating frame. Hence, H_{eff} is anti-Hermitian and thus diagonalizable with eigenvalues $\lambda_\alpha = -i\gamma_\alpha/2$.

It is assumed that our desired states are "dark states", which are eigenvectors with zero imaginary part of the eigenvalue. For simplicity and illustrative purpose, let us also assume there just one dark state $|0\rangle$ with eigenvalue $\lambda_0 = 0$, and the rest of the eigenvalues are sorted by $0 < \gamma_1 \leq \gamma_2 \leq \cdots$. Let us decompose the initial state in the eigenbasis $|\psi_0\rangle = \sum_\alpha c_\alpha |\alpha\rangle = c_0 |0\rangle + c_1 |1\rangle + \cdots$. The evolution under H_{eff} yields the following unnormalized state

$$\left|\tilde{\psi}(t)\right\rangle \equiv e^{-iH_{\text{eff}}t} |\psi_0\rangle = c_0 |0\rangle + c_1 e^{-\gamma_1 t/2} |1\rangle + \cdots . \tag{G.29}$$

The probability of undergoing no quantum jump over a time duration T is

$$p_0(T) = \left\langle \tilde{\psi}(T)|\tilde{\psi}(T)\right\rangle = |c_0|^2 + |c_1|^2 e^{-\gamma_1 T} + \cdots \geq |c_0|^2 = |\langle 0|\psi_0\rangle|^2 . \tag{G.30}$$

Conditioned on such an event, the fidelity of the quantum state preparation is

$$\mathcal{F}(T) = |\langle 0|\psi(T)\rangle|^2 = \frac{\left|\left\langle 0|\tilde{\psi}(T)\right\rangle\right|^2}{\left\langle \tilde{\psi}(T)|\tilde{\psi}(T)\right\rangle} = \frac{|c_0|^2}{|c_0|^2 + |c_1|^2 e^{-\gamma_1 T} + \cdots} = 1 - \mathcal{O}(e^{-\gamma_1 T}) \quad \text{if} \quad |c_0|^2 > 0, \tag{G.31}$$

where we find that the fidelity exponentially approaches to unity. This allows for effective "cooling" of the system into the desired state when there is no quantum jump for $T \gg 1/\gamma_1$, which occurs with probability $p_0 \simeq |\langle 0|\psi_0\rangle|^2$.

G.6.2 Success probability of connection

Consider an arbitrary initial state of two unentangled length-m chains of AKLT states, $|\psi_0\rangle = \mathcal{N}_0(\sum_b \alpha_b |A^m_{ab}\rangle) \otimes (\sum_c \beta_c |A^m_{cd}\rangle)$, where $\vec{\alpha}, \vec{\beta} \in \mathbb{C}^2$ characterizes the edge states at the interface, and $\mathcal{N}_0$ is normalization constant. We want to cool this state into the desired state of $\left|\psi^{2m}_f\right\rangle = \mathcal{N}_f |A^{2m}_{ad}\rangle$ by turning on the jump operators acting at the interface (i.e.

spin m and $m+1$). The success probability of connection is the probability of undergoing no quantum jumps for sufficiently long time, which can be computed using Eq. (G.3) to be

$$p \simeq \left|\left\langle \psi_f^{2m} | \psi_0 \right\rangle\right|^2 = \frac{|\vec{\alpha}\cdot\vec{\beta}|^2}{2|\vec{\alpha}|^2|\vec{\beta}|^2} + \mathcal{O}(\epsilon^m), \quad \text{where} \quad \epsilon = -1/3. \tag{G.32}$$

If the edge states $\vec{\alpha}, \vec{\beta}$ are random vectors in $\mathbb{C}^2$, we have on average $p \simeq 1/4$. When the edge states are aligned, i.e. $\vec{\alpha} \parallel \vec{\beta}$, we obtain the maximum success probability of $p_{\text{max}} = 1/2$.

In the case of failure, it turns out that quantum jumps affect the success probability of subsequent connections, which in fact vanishes for our protocol unless we perform quantum feedback by applying a global spin rotations to one of the chains. In our protocol, the jump operators are of the form $c_\theta = V_\theta^{\dagger\otimes 2}|\phi\rangle\langle{+}{+}|V_\theta^{\otimes 2}$, where $V_\theta = e^{i\theta S_y}$. In the event of a quantum jump c_θ, the state after discarding the two spins at the interface is $|\psi_1\rangle = \mathcal{N}_1(\sum_{b'} \tilde{\alpha}_{b'} \left|A^{m-1}_{ab'}\right\rangle) \otimes (\sum_{c'} \tilde{\beta}_{c'} \left|A^{m-1}_{c'd}\right\rangle)$, where $\tilde{\alpha}_{b'} = \sum_b \langle{+}|V_\theta|A^1_{b'b}\rangle\, \alpha_b$ and $\tilde{\beta}_{c'} = \sum_c \langle{+}|V_\theta|A^1_{cc'}\rangle\, \beta_c$. Then we find

$$\vec{\tilde{\alpha}}\cdot\vec{\tilde{\beta}} = \sum_{b'} \tilde{\alpha}_{b'}\tilde{\beta}_{b'} = \sum_{bc} \left\langle {+}{+} | V_\theta^{\otimes 2} | A^2_{cb} \right\rangle \alpha_b \beta_c = 0. \tag{G.33}$$

This is zero regardless of initial states α_b and β_c, due to the fact that $V_\theta^\dagger \otimes V_\theta^\dagger\, |{+}{+}\rangle$ has total angular momentum $J = 2$ and thus zero overlap with AKLT state $|A^2_{cb}\rangle$. Hence, the success probability of the next connection attempt is $p' \simeq |\left\langle \psi_f^{2m-2} | \psi_0 \right\rangle|^2 = \mathcal{O}(\epsilon^m)$, which vanishes for a large system size. In fact, this vanishing success probability can be traced back to the bond-inversion symmetry of AKLT states, which we discuss further in Sec. G.7.4. Remarkably, we can restore the success probability to its maximum value p_{max} by applying a global π-rotation $U = e^{i\pi S_y}$ to all spins in one of the two chains (same

rotational axis as V_θ). In other words, we attempt the next connection on the state

$$|\psi_1'\rangle = U^{\otimes m-1} \otimes \mathbb{1}^{\otimes m-1} |\psi_1\rangle = \mathcal{N}_1 \left(\sum_{b'} (u^\dagger \vec{\tilde{\alpha}})_{b'} \left| A^{m-1}_{u^\dagger a, b'} \right\rangle \right) \otimes \left(\sum_{c'} \tilde{\beta}_{c'} \left| A^{m-1}_{c'd} \right\rangle \right). \quad \text{(G.34)}$$

Note that since U is part of the $\mathrm{SO}(3)$ symmetry of AKLT states, its action can be represented as a rotation of edge states through $u = e^{-i\pi\sigma_y/2}$ (see Sec. G.7.2). One can check by explicit computation that $u^\dagger \vec{\tilde{\alpha}} \parallel \vec{\tilde{\beta}}$, regardless of the initial state α_b and β_c or the type of quantum jump occurred in the previous attempt. Hence, the new state $|\psi_1'\rangle$ will have the maximum success probability of connection $p_{\max} = 1/2$, up to exponential corrections.

We now provide a more intuitive explanation on why success probability vanishes after any quantum jump, and why applying U works to restore the maximum success probability. We can interpret the dynamics under $\mathcal{L} = \mathcal{D}[c_\theta]$ as a continuous measurement of whether the pair of spins have $J_\theta = +2$, where $J_\theta = e^{-i\theta J_y} J_z e^{i\theta J_y}$. To be more specific, consider four spin-1 particles $\vec{S}_1, \ldots, \vec{S}_4$, and imagine that we are performing a connection between site 2 and 3 by continuously measuring $\vec{J} = \vec{S}_2 + \vec{S}_3$. Now we "decompose" each spin-1 as if it is made out of two spin-$\frac{1}{2}$ particles: $\vec{S}_i = \vec{s}_{i,L} + \vec{s}_{i,R}$. It is known [148] that AKLT state can be constructed by starting with singlet bonds of virtual spin-$\frac{1}{2}$ particles where $s_{i,R} + s_{i+1,L} = 0$, and then imposing the constraint that $s_{i,L} + s_{i,R} = 1$ are in one of the triplet states corresponding to the physical spin-1 states. The detection of a quantum jump c_θ in a failed connection attempt implies $J_\theta = 2$, which is only possible if $s^\theta_{2L} = s^\theta_{2R} = s^\theta_{3L} = s^\theta_{3R} = +\frac{1}{2}$. Due to the singlet bond conditions, this automatically implies $s^\theta_{1R} = s^\theta_{4L} = -\frac{1}{2}$. Subsequently, when we retry the connection with site 1 and 4, the overlap with AKLT state is zero since the two virtual spin-$\frac{1}{2}$ particles are in the state $\left|s^\theta_{1R} = -\frac{1}{2}\right\rangle \left|s^\theta_{4L} = -\frac{1}{2}\right\rangle$ that has no overlap with the desired singlet bond state $\left|+\frac{1}{2}\right\rangle \left|-\frac{1}{2}\right\rangle - \left|-\frac{1}{2}\right\rangle \left|+\frac{1}{2}\right\rangle$. Now, applying U to one of the chains, say the first chain, flips s^θ_{1R} so that the resultant state is $\left|+\frac{1}{2}\right\rangle \left|-\frac{1}{2}\right\rangle$.

This has overlap of 1/2 with the singlet state, restoring our success probability to roughly 1/2.

As stated in the main text, this protocol is robust against changes in the rotation axis; if the rotational axis deviates from the xy-plane by angle φ, then the above procedure to restore the success probability (by applying π-rotation around the new axis) yield a subsequent success probability of $\frac{1}{2}\cos^2\varphi$.

G.6.3 Effect of imperfect quantum jump detection

In realistic experiments, the detection of quantum jumps often entails imperfections. The presence of such imperfections affects our protocol by (i) not heralding the failure of connection of two chains (false-positive), and (ii) incorrectly heralding failure when the connection has been successful (false-negative). The former may arise due to imperfect detection efficiency, and the latter due to the dark counts in the detector. As mentioned in the main text, our parallelized protocol can still have an efficient scaling even when such imperfect quantum jump detection is accounted for. In the false-negative scenario, we can still discard affected particle pairs and continue the procedure, but we have to adopt an ideal case success probability lower than p_{max} (see below). To minimize the occurrence of false-positives, we propose two methods that address detector inefficiency. In the following analysis, let us denote the detector efficiency to be $1-\eta$, the dark count rate r, and the ideal case success probability p.

Success probability after false-negative "failure"— We showed previously in Sec. G.6.2 that the maximum success probability of connection of $p_{\text{max}} = 1/2$ can be recovered for the subsequent attempt after a failed connection (via detection of quantum jumps), if we

discard the affected particles and apply a global π-rotation $U = e^{i\pi S_y}$ to one of the remaining chains. However, this is not the case if the quantum jump detector has only received a dark count, i.e. the failure is a false-negative, and the connection has in fact succeeded. After a dark count is registered, the experimenter will unwittingly discard the particles at the original interface, apply U, and retry the connection anyways. If we consider the density matrix of the remaining pair of chains, we can see that their edge states at the interface are essentially randomized in a maximally mixed state, which would intuitively yield a success probability $p \approx 1/4$ in the attempt to connect them. More precisely, if k particles were discarded in each original chain of length n starting from interface (i.e. $2k$ particles in the middle of the connected chain of length $2n$), the success probability of connecting the two chains of length $n - k$ can be computed to be

$$p = \frac{1}{4}(1 - \epsilon^{2k}) + \mathcal{O}(\epsilon^n), \tag{G.35}$$

where $\epsilon = -1/3$. In particular, when $k = 1$, $p \simeq 2/9$.

Method 1— The first method to address false-positives from detector inefficiency is to only use jump operators of the form $c = |{+}{+}\rangle\langle{+}{+}|$ for the connection. Once a quantum jump occurs, the state will continue to undergo quantum jumps indefinitely, creating a much larger signal and effectively larger detection efficiency. Consequently, the detector inefficiency can be exponentially suppressed by the time τ_c of having the jump operators turned on. Let τ_0 be the time-scale in which a single quantum jump would occur. In this case, the probability of diagnosing a successful connection and keeping the result is given by the probability of not detecting any quantum jumps over time τ_c

$$p_{\text{succ}} = \Pr\{\text{keep}\} = p(1-r\tau_0)^{\tau_c/\tau_0} + (1-p)\eta^{\tau_c/\tau_0} = p(1-r\tau_0)^{\tau_c/\tau_0}(1+a\tilde{\eta}^{\tau_c/\tau_0}), \tag{G.36}$$

where we denoted $a \equiv (1-p)/p$ and $\tilde{\eta} = \eta/(1-r\tau_0)$. The fidelity is the conditional probability that the diagnosed success was a truly successful connection

$$\mathcal{F} = \Pr\{\text{success}|\text{keep}\} = \frac{p(1-r\tau_0)^{\tau_c/\tau_0}}{p(1-r\tau_0)^{\tau_c/\tau_0} + (1-p)\eta^{\tau_c/\tau_0}} = \frac{1}{1+a\tilde{\eta}^{\tau_c/\tau_0}} \tag{G.37}$$

Note we can only achieve a fidelity arbitrarily close to 1 if $\tilde{\eta} < 1$, i.e. when the detector efficiency is larger than the dark count probability $1-\eta > r\tau_0$. In order to achieve a final error of $\mathcal{E}$ for a system size of n from initial chains of length n_0, where n/n_0 connections are necessary, we need $1-\mathcal{F} \leq n_0\mathcal{E}/n$, and consequently $\tau_c = \mathcal{O}(\ln(n/n_0\mathcal{E})/\ln\tilde{\eta}^{-1})$. This is consistent with the $\tau_c \sim \log n$ scaling necessary in the ideal protocol. Nonetheless, our new success probability now decreases with system size n as $p_{\text{succ}} \sim \mathcal{O}(n^{-\delta})$ if dark counts are non-negligible, where $\delta = \ln(1-r\tau_0)/\ln\tilde{\eta} \approx r\tau_0/\ln\eta^{-1}$. Consider now the average time to prepare a chain of length n:

$$T(n) = T_0 + \frac{\tau_c + \tau_r(1-p_{\text{succ}})}{p_{\text{succ}}}\log_2\frac{n-n_c}{n_0-n_c} \tag{G.38}$$

where $n_c = 2(1-p_{\text{succ}})/p_{\text{succ}}$, T_0 is time to prepare initial length-n_0 chains, and τ_r is some constant time necessary to reset the edge states in the event of failure. On first sight, this would mean that our preparation time would ultimately scale polynomially instead of polylogarithmically in the infinite n limit. However, in the regime of $r\tau_0 \ll 1$, this polynomial dependence has a very small power, and its effect can be neglected if $r\tau_c \ll 1$. Hence, in practice, our protocol has an efficient, polylogarithmic scaling up to $n \ll n_{\max} = \mathcal{O}((1/\eta)^{1/r\tau_0})$, beyond which it switches to a polynomial scaling. For instance, even if single-photon detection efficiency is $1-\eta = 0.2$, then assuming a dark count rate of $r = 25$ Hz [351] and a quantum jump scattering rate of $\tau_0^{-1} \approx 1$ MHz, it takes an astronomically long chain of $n_{\max} \sim 10^{4000}$ to reach the polynomial scaling. An example scaling under these conditions is shown in Figure G.1 below.

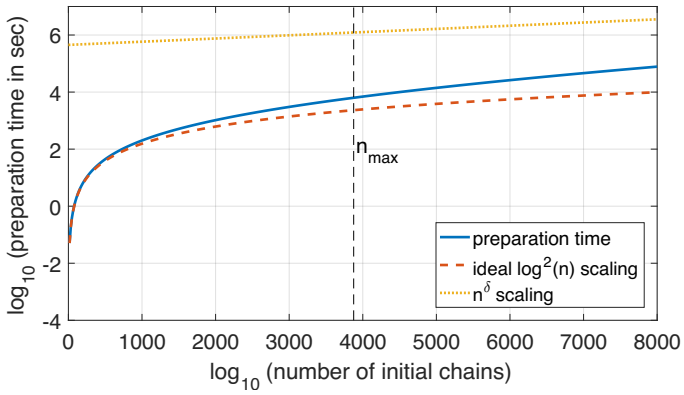

Figure G.1: Preparation time in the parallelized protocol with detector efficiency $1-\eta = 0.2$ and dark count rate $r = 25$ Hz, using jump operators of the form $c = |{+}{+}\rangle\langle{+}{+}|$ (Method 1). We also assume quantum jump rate $\tau_0^{-1} = 1$ MHz, ideal case success probability $p = 2/9$, time to discard atoms and reset edges $\tau_r = \tau_0$, and target final error $\mathcal{E} = 10^{-4}$.

Method 2— The second method for addressing detector inefficiency is to slowly turn on jump operators in the vicinity of the interface. In this way, the absence of quantum jumps further confirms that the two chains has indeed been successfully connected; since only a successful connection does not lead to any subsequent quantum jumps, any false-positive diagnosis of successful connection can be corrected. More concretely, consider a k-step scheme where we turn on jump operators to include k neighbors on each side of the original interface, one pair of neighbors at a time. At step $\ell = 1, \ldots, k$, we have jump operators on for 2ℓ particles centered at the interface, turned on for time τ_ℓ^c. If a quantum jump occurred and evaded detection at any step ℓ, we assume τ_ℓ^c is long enough so that the 2ℓ particles would have formed a connected chain of length 2ℓ. At the subsequent step $\ell+1$, the length-2ℓ chain in the middle can be connected to the two length-$(n-\ell)$ chains on both sides if we succeed by having no quantum jump, producing a fully connected chain of length $2n$. Note the success probability for steps $\ell > 1$ is roughly $p_2 = 1/2^4$. From the system size scaling found in our numerical simulations presented in the main

text, we expect to need $\tau_\ell^c \sim (2\ell)^{2.97} \approx (2\ell)^3$. Additionally, we expect the number of quantum jumps during τ_ℓ^c of step ℓ to roughly scale as $N_\ell^{\text{jump}} \approx C\tau_\ell^c$ for some constant C. Observe that this scheme allows us to obtain a fully connected chain even in the event of initial failure(s), as long as we don't have any quantum jumps at the last step. Thus, the probability of succeeding and deciding to keep the result (due to not detecting any quantum jump) is

$$\begin{aligned}\Pr\{\text{success and keep}\} = \quad & pe^{-r\sum_{\ell=1}^k \tau_\ell^c} + (1-p)\eta^{C\tau_1^c} p_2 e^{-r\sum_{\ell=2}^k \tau_\ell^c} \qquad \text{(G.39)}\\ & +(1-p)\eta^{C\tau_1^c}(1-p_2)\eta^{C\tau_2^c} p_2 e^{-r\sum_{\ell=3}^k \tau_\ell^c} + \cdots \\ = \quad & pe^{-rT_k}\left(1 + \tfrac{1-p}{p} p_2 \textstyle\sum_{s=1}^{k-1}(1-p_2)^{s-1}(\eta^C e^r)^{T_s}\right), \qquad \text{(G.40)}\end{aligned}$$

where $T_s = \sum_{\ell=1}^s \tau_\ell^c \approx Bs^4$ for some constant B. The probability of failing at the last step but still keeping the result is

$$\Pr\{\text{fail and keep}\} = (1-p)(1-p_2)^{k-1}\eta^{CT_k}. \qquad \text{(G.41)}$$

The fidelity is the conditional probability of true success given that we have kept the result:

$$\begin{aligned}\mathcal{F} \quad &= \quad \Pr\{\text{success}|\text{keep}\} = \frac{pe^{-rT_k}(1+\cdots)}{pe^{-rT_k}(1+\cdots) + (1-p)(1-p_2)^{k-1}\eta^{CT_k}} \\ &\geq \quad \frac{pe^{-rT_k}}{pe^{-rT_k} + (1-p)(1-p_2)^{k-1}\eta^{CT_k}} \approx 1 - b(1-p_2)^{k-1}\xi^{k^4}, \qquad \text{(G.42)}\end{aligned}$$

where we denoted $b = (1-p)/p$ and $\xi = (\eta^C e^r)^B$. To achieve arbitrarily good fidelity, we require $\xi < 1$, i.e. the dark count rate $r < C \ln \eta^{-1}$ needs to be sufficiently small. At the same time, the apparent "success" probability of keeping the result is $p_{\text{succ}} = \Pr\{\text{keep}\} \approx pe^{-rBk^4}$. We can carry out the same analysis as in the previous method, and a similar behavior would emerge: when the dark count rate is nonzero, the efficient polylogarithmic scaling applies until a maximum chain length of $n \ll n_{\max} = \mathcal{O}(\eta^{-C/r})$, beyond which a polynomial scaling of $\mathcal{O}(n^{\delta'})$ with $\delta' \approx r/\ln \eta^{-C}$ applies.

G.6.4 Scaling of imperfection in Rydberg-EIT implementation

Our protocol prepares AKLT states with finite fidelity when experimental imperfections are taken into account. Here, we analyze how fidelity scales as multiple chains are connected. In particular, the long-range nature of interaction in the proposed Rydberg-EIT implementation limits fidelity even in the absence of dephasing. Nevertheless, we show that by adopting the parallelized protocol, the long-range interactions only affect the initial preparation of length-n_0 chains, and such imperfection does not substantially grow in the later connection procedures. This is because the connections involve turning on the dissipative interaction on particle pairs that are spatially separated by at least n_0 particles. Since the effective decay rate scales as $\Gamma_{DD} \sim 1/R^{12}$ for the proposed implementation, the perturbative effect of long-range interaction is characterized by the very small number of $1/(n_0-1)^{12}$, which becomes even smaller in later rounds of connections. Hence, we neglect the effect of long-range interaction on the connections, and only consider how the induced errors on the states of initial chains propagate through the protocol. Let us assume we initially start with individual chains of length n_0, each with bounded error ϵ_0. At the ℓ-th level of connections, we on average double the length $n_\ell \simeq 2n_{\ell-1} - n_c$, where n_c is the expected number of particles discarded in each connection. The number of initial chains necessary to reach a final chain length of n is $L = (n-n_c)/(n_0-n_c)$, and $L-1$ connection procedures need to be performed. Hence, the final error is bounded by

$$1 - \mathcal{F} \leq L\epsilon_0 + (L-1) \times \mathcal{O}(e^{-\gamma_1 \tau_c}) \approx n\epsilon_0/n_0, \tag{G.43}$$

where we neglect the second term which can be made small compared to the first if we choose $\tau_c = \mathcal{O}(\ln n)$. As we can see, the predominant source of error is due to the imperfect initial chains, whose errors add linearly.

This linear scaling of error is indeed very favorable for *many-body state* preparation protocol. To put this in perspective, let us estimate how the effective temperature T_{eff} scales in our connection procedure. We define the effective temperature through the relation

$$\mathcal{F} = \text{tr}\left[P_G \frac{e^{-H/T_{\text{eff}}}}{\text{tr}[e^{-H/T_{\text{eff}}}]}\right] = \frac{1}{1+\int_{\Delta_{\text{gap}}}^{\infty}\rho(E)e^{-E/T_{\text{eff}}}dE} \approx 1-\int_{\Delta_{\text{gap}}}^{\infty}\rho(E)e^{-E/T_{\text{eff}}}dE, \quad \text{(G.44)}$$

where $\rho(E)$ is the density of state at energy E, and we assume that T_{eff} is sufficiently small. Now we consider connecting two length-n_1 chains at effective temperature T_1 (with errors $1-\mathcal{F}_1$). After connection, we have a chain of length $n_2 \approx 2n_1$, with bounded error $1-\mathcal{F}_2 \lesssim 2(1-\mathcal{F}_1)$. Corresponding effective temperature T_2 of the connected chain can be estimated from

$$\begin{gathered}\int_{\Delta_{\text{gap}}}^{\infty}\rho_2(E)e^{-E/T_2}dE \approx 1-\mathcal{F}_2 \lesssim 2(1-\mathcal{F}_1) \approx \int_{\Delta_{\text{gap}}}^{\infty}2\rho_1(E)e^{-E/T_1}dE \\ \implies \quad \int_{\Delta_{\text{gap}}}^{\infty}2\rho_1(E)e^{-E/T_1}dE - \int_{\Delta_{\text{gap}}}^{\infty}\rho_2(E)e^{-E/T_2}dE \gtrsim 0,\end{gathered}$$

where $\rho_1(E)$ and $\rho_2(E)$ denote the density of state for chains of length n_1 and $n_2 \approx 2n_1$, respectively. In a generic many-body interacting system, the density of state grows exponentially in system sizes. Here, we are most interested in the density of state of low-lying excitations, e.g. the first excited band, where the scaling of $\rho(E)$ can be much weaker. Ref. [352] used Bijl-Feynman single-mode approximation to deduce that there is a band of low-lying excited states with dispersion relation $E_1(k) = \frac{5}{27}(5+3\cos k)$, corresponding to magnon excitations. Therefore, we expect the number of states in the low-lying excited bands to scale at least linearly with system size, and thus $\rho_2(E) \geq 2\rho_1(E)$. Applying this to the earlier inequality, we have

$$\int_{\Delta_{\text{gap}}}^{\infty}\rho_2(E)(e^{-E/T_1}-e^{-E/T_2})dE \gtrsim 0 \quad \implies \quad T_2 \lesssim T_1. \quad \text{(G.45)}$$

Hence, the effective temperature should not increase (and can potentially decrease) after each connection procedure.

G.7 Generalization

In this section, we generalize our protocol for a broader class of translation-invariant MPS with internal symmetry. We first introduce notations and a few useful known properties of translation-invariant MPS in Sec. G.7.1, which will be referenced in subsequent sections. More detailed description and proofs of these properties can be found in Ref. [214]. We then discuss the meaning of internal symmetry of MPS in Sec. G.7.2. Lastly, we define and analyze the generalization of our protocol in Sec. G.7.3 and G.7.4.

G.7.1 Notations and useful properties of matrix product states

Any (unnormalized) translation-invariant MPS with physical dimension d and bond dimension D can be written as:

$$|A^n_{ab}\rangle = \sum_{\{s_i\}} \left\langle a|A^{(s_1)}A^{(s_2)}\cdots A^{(s_n)}|b\right\rangle |s_1 s_2 \cdots s_n\rangle \,, \tag{G.46}$$

where $s_i \in \{1, 2, \ldots, d\}$ runs over the physical spin basis for the i-th particle, and $|a\rangle, |b\rangle \in \mathbb{C}^D$ indicate the "boundary conditions" on the virtual bond level. We use the notation $|A^n_{ab}\rangle$ to indicate translational-invariant MPS of n particles with open boundary condition specified by a and b, and $|A^n\rangle$ to denote the state of a n-particle system with periodic boundary condition, i.e. $|A^n\rangle = \sum_a |A^n_{aa}\rangle$. For the case of AKLT states, we have $d = 3$ and $D = 2$. Under open boundary condition, there could be at most D^2 distinct states with different possible boundary conditions, e.g. four-fold degeneracy of AKLT states.

In general, however, these D^2 states may not be linearly independent unless the MPS is *injective* (defined below).

Canonical Form— An MPS is in a *canonical form* if the matrices have a common block diagonal structure: $A^{(s)} = \text{diag}(\lambda_1 A_1^{(s)}, \ldots, \lambda_B A_B^{(s)})$, where $0 < \lambda_\beta \leq 1$ for each block $\beta \in \{1, \ldots, B\}$. The matrices in each block must satisfy the conditions that (i) $\sum_s A_\beta^{(s)} A_\beta^{(s)\dagger} = \mathbb{1}$, (ii) a map defined as $\mathcal{E}_\beta(X) = \sum_s A_\beta^{(s)} X A_\beta^{(s)\dagger}$ has $\mathbb{1}$ as its only fixed point (unique eigenvector with unity eigenvalue), and finally (iii) $\sum_s A_\beta^{(s)\dagger} \Lambda_\beta A_\beta^{(s)} = \Lambda_\beta$ for some diagonal positive and full-rank matrices Λ_β.

Transfer Matrix— Consider the completely positive map $\mathcal{E}(X) = \sum_s A^{(s)} X A^{(s)\dagger}$, or equivalently the transfer matrix $T = \sum_s A^{(s)*} \otimes A^{(s)}$. Understanding the spectrum of this map is useful for computing the expectation value of an observable or the overlap between two quantum states, e.g. $\langle A_{ab}^n | A_{a'b'}^n \rangle = \langle aa' | T^n | bb' \rangle$ [214]. Some eigenvectors of T are $\frac{1}{\sqrt{D_\beta}} \sum_{i \in \beta} |ii\rangle$, where D_β is the dimension of the β-th block, and correspond to eigenvalues $|\lambda_\beta|^2$. Denoting the other eigenvectors of T with eigenvalues ϵ_ν as $|\nu\rangle$, we have

$$\langle A_{ab}^n | A_{a'b'}^n \rangle = \left\langle aa' \right| \left[\sum_\beta \frac{|\lambda_\beta|^2}{D_\beta} \sum_{i,j \in \beta} |ii\rangle\langle jj| + \sum_\nu \epsilon_\nu |\nu\rangle \langle \nu| \right]^n \left| bb' \right\rangle \tag{G.47}$$

$$= \sum_\beta \frac{|\lambda_\beta|^{2n}}{D_\beta} \delta_{a,b \in \beta} \delta_{aa'} \delta_{bb'} + \sum_\nu \epsilon_\nu^n \langle aa' | \nu \rangle \langle \nu | bb' \rangle . \tag{G.48}$$

Since $|\lambda_\beta|^2$ is the largest eigenvalue of each block β, typically only the first term is relevant in the limit of large n.

Parent Hamiltonian— For a sufficiently large L, the set of matrix products $\{A^{(s_1)} \cdots A^{(s_L)} : 1 \leq s_i \leq d\}$ spans the vector space of all matrices with the same block diagonal structure as the canonical form [214]. We call L the *interaction length* of the MPS. Without loss of generality, we can assume that $L = 2$. This is because otherwise we can group L sites together

to get an equivalent MPS with larger physical dimension $d' \leq d^L$, and a new interaction length $L' = 2$. The *parent Hamiltonian* of an MPS is then defined to be $H_p = \sum_i h^{(i)}$, where h is any positive semi-definite operator acting on nearest neighboring sites, whose kernel is

$$\ker(h) = \text{span}\{\left|A^2_{ab}\right\rangle : \forall a, b\}. \tag{G.49}$$

In other words, H_p imposes a condition $h^{(i)}$ for every pair of neighboring sites $(i, i+1)$, which our MPS trivially verifies (i.e. $h^{(i)} \left|A^n_{ab}\right\rangle = 0$ for all $1 \leq i \leq n-1$). Hence, H_p is a frustration-free Hamiltonian of which the MPS is a zero-energy ground state. The ground state degeneracy depends on both the boundary condition and the number of blocks in the MPS canonical form. Ref. [214] has shown that under periodic boundary condition, this degeneracy equals the number of independent blocks in the canonical form, since the ground space consists of MPS constructed from the sub-matrices from every block.

Injectivity— Often it is useful to assume a condition that the MPS is *injective*, which is satisfied in the generic case except for specific, fine-tuned MPS [214]. This injectivity condition is that the transfer matrix T has only one eigenvector corresponding to its largest eigenvalue (which we normalize to 1 in the canonical form). This also implies that there is just one block in the canonical form of the MPS. In this case,

$$\langle A^n_{ab}|A^n_{a'b'}\rangle = \langle aa'|T^n|bb'\rangle = \frac{1}{D}\delta_{aa'}\delta_{bb'} + \mathcal{O}(\epsilon_2^n), \tag{G.50}$$

where ϵ_2 is the second largest eigenvalue of $\mathcal{E}$. Additionally, this implies that the parent Hamiltonian under periodic boundary condition has the MPS as its unique ground state, and that the ground state energy is gapped in the thermodynamic limit. Under open boundary condition, D^2 distinct boundary conditions give rise to D^2 linearly independent and degenerate ground states $|A^n_{ab}\rangle$. By appropriately modifying the parent Hamiltonian terms

at the boundaries, we can break the degeneracy and make one of the D^2 states the unique ground state.

G.7.2 Internal Symmetries of MPS

We say a translation-invariant MPS defined on d-level physical spins respects an internal symmetry $\mathcal{G}$, if for some unitary representation $U : \mathcal{G} \to U(d)$, we have:

$$U_g^{\otimes n} \left|A^n_{ab}\right\rangle = \sum_{a'b'} [\chi_g]^{a'b'}_{ab} \left|A^n_{a'b'}\right\rangle \quad \text{and} \quad U_g^{\otimes n} \left|A^n\right\rangle = e^{i\theta_g} \left|A^n\right\rangle . \tag{G.51}$$

That is, a global action of the symmetry operation keeps a ground state of the MPS parent Hamiltonian in the ground space under open boundary condition, or only imprints a complex phase factor under periodic boundary condition.

Assuming the symmetry group is reasonable (either discrete or a compact connected Lie group), but without assuming injectivity, Ref. [247] showed that we can replace the action of the symmetry in the physical basis with a unitary in the virtual bond basis. More explicitly, we have

$$\sum_{s'} [U_g]_{ss'} A^{(s')} = w_g u_g A^{(s)} u_g^\dagger, \tag{G.52}$$

where $u_g = P_g v_g$, with $v_g = \bigoplus_{\beta=1}^{B} v_g^\beta$ taking on the same block diagonal structure as $A^{(s)}$, and each v_g^β a unitary in block β. P_g is a permutation amongst blocks. Lastly, $w_g = \bigoplus_\beta e^{i\varphi_g^\beta} \mathbb{1}_\beta$ is a phase factor for each block. If $\mathcal{G}$ is a compact connected Lie group, Ref. [247] showed that $P_g = \mathbb{1}$, while $g \mapsto e^{i\varphi_g^\beta}$ and $g \mapsto v_g^\beta$ are representations of $\mathcal{G}$.

For AKLT states, where $\mathcal{G} = \mathrm{SO}(3)$, the relevant representation is given by the rotations $U_g = \exp(i\vec{\alpha}_g \cdot \vec{S})$ on the spin-1 vector $\vec{S}$ for some real parameters $\vec{\alpha}_g = (\alpha_g^x, \alpha_g^y, \alpha_g^z)$. In

particular, we have

$$\sum_{s'}[U_g]_{ss'}A^{(s')} = u_g A^{(s)} u_g^\dagger \quad \Longrightarrow \quad U_g^{\otimes n}\left|A^n_{ab}\right\rangle = \left|A^n_{u_g^\dagger a, u_g^\dagger b}\right\rangle, \tag{G.53}$$

where $u_g = \exp(i\vec{\alpha}'_g \cdot \vec{\sigma}/2)$, where $\vec{\alpha}'_g = (\alpha^x_g, -\alpha^y_g, \alpha^z_g)$.

G.7.3 Generalization of our protocol

In this section, we generalize our protocol to any translation-invariant MPS with internal symmetry $\mathcal{G}$. Our goal is to design a dissipative dynamics that deterministically prepares the ground state(s) of the MPS parent Hamiltonian using a set of global coherent manipulations and a minimal number $k_{\min}$ of jump operators $\{c_1, c_2, \ldots, c_{k_{\min}}\}$, each of the form $c_\mu = |\phi_\mu\rangle\langle\psi_\mu|$ acting on neighboring pairs of particles.

Without loss of generality, we assume that the desired states are ground states of a gapped, frustration-free parent Hamiltonian $H_p = \sum_i h^{(i)}$, where $h^{(i)}$ is a translation-invariant, nearest-neighbor projector that respects the internal symmetry $\mathcal{G}$ [214, 247]. Each term h can be written in a block diagonal form, corresponding to different irreducible representations of $\mathcal{G}$. We denote the two-particle subspace that h projects onto as "bright manifold" $\mathfrak{B} \equiv \mathrm{range}(h) \subset \mathbb{C}^{d^2}$. The ground states are uniquely characterized by vanishing populations in $\mathfrak{B}$. In the H_{AKLT} example, $\mathfrak{B}$ corresponds to the $J = 2$ manifold of two neighboring spins. Similar to our protocol for AKLT, we can depopulate $\mathfrak{B}$ by employing jump operators c_μ where $\mathrm{range}(c_\mu^\dagger c_\mu) \subseteq \mathfrak{B}$. The number of jump operators can be reduced by utilizing and averaging over all symmetry rotations through $c_\mu \mapsto V_g^\dagger c_\mu V_g$, where V_g is the global unitary rotation by a group element $g \in \mathcal{G}$. Unlike in the AKLT case, the representation of $\mathcal{G}$ on $\mathfrak{B}$ may contain multiple copies of isomorphic irreducible representations in general. In such cases, the averaging of a single jump operator c_μ over $\mathcal{G}$ may not be

sufficient to depopulate the entire subspace $\mathfrak{B}$, and it becomes necessary to employ a set of multiple c_μ's.

The foremost necessary condition for the jump operators c_μ is

$$\mathfrak{B} = \mathrm{range}\left(\sum_{\mu=1}^{k_{\min}} Q_\mu\right) \quad \text{where} \quad Q_\mu = \frac{1}{|\mathcal{G}|}\sum_{g\in\mathcal{G}} V_g^\dagger c_\mu^\dagger c_\mu V_g = \frac{1}{|\mathcal{G}|}\sum_{g\in\mathcal{G}} V_g^\dagger \left|\psi_\mu\right\rangle\left\langle\psi_\mu\right| V_g. \tag{G.54}$$

In other words, the jump operators must be capable of depopulating the entire bright manifold after averaging over all symmetry operations. While here we have assumed the symmetry group $\mathcal{G}$ is finite for simplicity, the following results apply to any compact group by replacing the sum over $g \in \mathcal{G}$ by an integral over the Haar measure of $\mathcal{G}$.

To find the minimum number $k_{\min}$ of $|\psi_\mu\rangle$ (and consequently c_μ) required, it is useful to decompose V_g into direct sums of irreducible representations (irreps) $V_g = \bigoplus_r V_g^r$, where r enumerates the irreps, each with dimension d_r. This decomposition is possible because finite-dimensional unitary representations of any group are completely reducible [353]. Let us also denote $|\psi_\mu\rangle = \bigoplus_r \left|\psi_\mu^r\right\rangle$, where each $\left|\psi_\mu^r\right\rangle$ is a d_r-dimensional vector. Observe that for any $d_r \times d_{r'}$ matrix X, we can derive the following identity using Schur's Lemma [353]:

$$\frac{1}{|\mathcal{G}|}\sum_{g\in\mathcal{G}} V_g^r X V_g^{r'\dagger} = \begin{cases} 0 & \text{if } r \ncong r' \\ \frac{\mathrm{tr}(U_{rr'}^\dagger X)}{d_r} U_{rr'} & \text{if } r \cong r', \text{ i.e. } V_g^r = U_{rr'} V_g^{r'} U_{rr'}^\dagger \end{cases}, \tag{G.55}$$

where $r \cong r'$ means r is equivalent (isomorphic) to r' up to a unitary basis change. Note we can always choose a basis for the representation of V_g that absorbs $U_{rr'}$, so we assume $U_{rr'} = \mathbb{1}$ without loss of generality. Using the notation $\bigoplus_{r,r'} M_{r,r'}$ to denote the matrix whose (r,r')-th block is $M_{r,r'}$, we can write Q_μ through the above identity

$$Q_\mu = \bigoplus_{r,r'} \frac{1}{|\mathcal{G}|}\sum_{g\in\mathcal{G}} V_g^r |\psi_\mu^r\rangle\langle\psi_\mu^{r'}|^\dagger V_g^{r'\dagger} = \bigoplus_r \frac{\mathbb{1}_r}{d_r}\left\langle\psi_\mu^r|\psi_\mu^r\right\rangle + \bigoplus_{r\neq r', r\cong r'} \frac{\mathbb{1}_r}{d_r}\left\langle\psi_\mu^{r'}|\psi_\mu^r\right\rangle, \tag{G.56}$$

where the second term characterizes the possible non-zero off-diagonal blocks, which can only exists between pairs of equivalent irreps.

Since inequivalent irreps are decoupled, we for now only consider the subspace $\mathfrak{B}_r \subseteq \mathfrak{B}$ corresponding to K_r copies of irreps equivalent to irrep r ($\dim \mathfrak{B}_r = K_r d_r$). We shall also denote $Q_\mu^r = Q_\mu|_{\mathfrak{B}_r}$ as the operator Q_μ restricted to the subspace $\mathfrak{B}_r$. Observe that $|\psi_\mu\rangle$ restricted to this subspace is specified by the set of K_r vectors $\{|\psi_\mu^s\rangle \in \mathbb{C}^{d_r}\}_{s=1}^{K_r}$. When $K_r > d_r$, regardless of the choice of $|\psi_\mu\rangle$, there are $K_r - d_r$ linearly independent vectors $\vec{\beta}^j \in \mathbb{C}^{K_r}$, $j = 1, \ldots, K_r - d_r$, such that $\sum_{s=1}^{K_r} \beta_s^j \langle\psi_\mu^s| = 0$. Then any vectors of the form $|\chi\rangle = \bigoplus_{s=1}^{K_r} \beta_s^j |v\rangle$ are in the kernel of Q_μ^r for any $|v\rangle \in \mathbb{C}^{d_r}$, since one can verify $Q_\mu^r |\chi\rangle = 0$. Since there are $(K_r - d_r)d_r$ linearly independent such vectors $|\chi\rangle$, we have $\mathrm{rank}(Q_\mu^r) \leq d_r^2$. Hence, in order to fully depopulate $\mathfrak{B}_r$, we need $\dim(\mathfrak{B}_r) = \mathrm{rank}(\sum_\mu Q_\mu^r) \leq \sum_\mu \mathrm{rank}(Q_\mu^r) \leq k_{\min} d_r^2$. Because $k_{\min}$ must be an integer, we must have $k_{\min} \geq \lceil K_r/d_r \rceil$.

Note that this lower bound for $k_{\min}$ can be saturated by construction. First, we partition the K_r equivalent irreps into $\lceil K_r/d_r \rceil$ groups of no more than d_r irreps. For each group, we can assign a $|\psi_\mu\rangle$ that is nonzero only in the subspace corresponding to the irreps in the group. Lastly, we make all off-diagonal blocks vanish for each group $\mu \in \{1, \ldots, \lceil K_r/d_r \rceil\}$, by finding $\leq d_r$ mutually orthogonal vectors $|\psi_\mu^r\rangle \in \mathbb{C}^{d_r}$ such that $\langle\psi_\mu^{r'}|\psi_\mu^r\rangle = 0$ for $r \neq r'$. For a single jump operator of the form $c_\mu = |\phi_\mu\rangle\langle\psi_\mu|$, the state $|\psi_\mu\rangle$ may have supports on more than one subspaces $\mathfrak{B}_r$. Therefore, the construction of a set of jump operators $\{c_\mu\}$ to satisfy Eq. (G.54) can be done in "parallel" for all the different $\mathfrak{B}_r$ corresponding to the inequivalent set of irreps, leading to the minimum number

$$k_{\min} = \max_r \lceil K_r/d_r \rceil. \tag{G.57}$$

Here, r enumerates inequivalent irreps of $\mathcal{G}$ in $\mathfrak{B}$, K_r is the number of copies of r, and d_r is the dimension of r.

We can also consider arbitrary jump operator c_μ beyond the rank-1 form of $|\phi_\mu\rangle\langle\psi_\mu|$. For any operator c_μ, we can perform singular value decomposition to write $c_\mu = \sum_{i_\mu} \sqrt{\gamma_{i_\mu}} |\phi_{i_\mu}\rangle\langle\psi_{i_\mu}|$, where $\langle\phi_{i_\mu}|\phi_{j_\mu}\rangle = \langle\psi_{i_\mu}|\psi_{j_\mu}\rangle = \delta_{i_\mu j_\mu}$. Then $c_\mu^\dagger c_\mu = \sum_{i_\mu} \gamma_{i_\mu} |\psi_{i_\mu}\rangle\langle\psi_{i_\mu}|$ with $\gamma_{i_\mu} > 0$. Hence, the condition of Eq. (G.54) becomes a condition imposed on the set of right-singular vectors $\{|\psi_{i_\mu}\rangle : \forall \mu, i_\mu\}$, where we must have $\mathfrak{B} = \mathrm{range}(\frac{1}{|\mathcal{G}|} \sum_{g,\mu,i_\mu} \gamma_{i_\mu} V_g^\dagger |\psi_{i_\mu}\rangle\langle\psi_{i_\mu}| V_g)$. We can thus interpret the $k_{\min}$ found for rank-1 jump operators as the minimum number of independent $|\psi_{i_\mu}\rangle$'s.

Once we construct a set of c_μ's satisfying the necessary condition of Eq. (G.54), it remains to ascertain the uniqueness of steady states using our inductive proof strategy. In other words, one simply need to check whether there are non-trivial solutions to Eq. (G.11) and (G.14) for open and periodic boundary conditions. Nevertheless, for non-injective MPS, this scheme cannot break the ground state degeneracy intrinsic to the MPS parent Hamiltonian, but it can guarantee the ground states are the only non-decaying steady states.

Our Rydberg-EIT implementation proposal can be naturally adapted for more general cases. The Rydberg-EIT scheme allows us to engineer two-body jump operators of the form $c_{\text{eff}} = |s^{L1} s^{L2}\rangle\langle s^R s^R|$, where $|s^{Li}\rangle, |s^R\rangle \in \mathbb{C}^d$ are single-spin states. Unlike the case of AKLT states, the preparation of a generic symmetric MPS may require more than one ($k_{\min} \geq 2$) number of rank-1 jump operators. The implementation of multiple decay channels can be achieved, for example, by introducing extra lasers that couple (additional) hyperfine ground states to the short-lived excited state(s). By adjusting the relative strength of laser driving to each hyperfine ground state, one can engineer different EIT-dark states

that acquire a dissipative interaction. This allows us to generate a set of jump operators $\{c_\mu^{\text{eff}} = |s_\mu^{L1} s_\mu^{L2}\rangle\langle s_\mu^R s_\mu^R| : \mu = 1, ..., k_{\min}\}$ with independent $\left|s_\mu^R s_\mu^R\right\rangle$. When particles are individually addressable, one can engineer a jump operator with a more complicated right-singular vector $|\psi_\mu\rangle$, i.e. $|\psi_\mu\rangle \neq \left|s_\mu^R\right\rangle^{\otimes 2}$ for any $\left|s_\mu^R\right\rangle \in \mathbb{C}^d$. For example, if we can engineer a unitary U where $U^\dagger \left|s_\mu^R\right\rangle^{\otimes 2} = |\psi_\mu\rangle$, then applying U stroboscopically each time before turning on dissipative interaction [see Fig. 4(b)] would allow engineering of $c_\mu = |\phi_\mu\rangle\langle\psi_\mu|$.

G.7.4 Parallelized protocol for general case

In this section, we consider generalization of our parallelized protocol to prepare a translation-invariant MPS with bond dimension D and internal symmetry $\mathcal{G}$. We assume that the MPS is injective for simpler analysis. Consider an arbitrary initial state of two length-m chains of MPS, which can be written as $|\psi_0\rangle = \mathcal{N}_0 \sum_{b,c} C_{bc} |A_{ab}^m\rangle \otimes |A_{cd}^m\rangle$, where $C_{bc} \in \mathbb{C}^{D\times D}$ is some arbitrary coefficient matrix that characterizes the edge states at the interface of the chains, and $\mathcal{N}_0$ is normalization constant. If we have an initially unentangled pair of chains, we must have $C_{bc} = \alpha_b \beta_c$ for some $\vec{\alpha}, \vec{\beta} \in \mathbb{C}^D$. By turning on the jump operators acting at the interface, we can cool this state into the desired final state $\left|\psi_f^{2m}\right\rangle = \mathcal{N}_f |A_{ad}^{2m}\rangle$. Since the MPS is assumed to be injective, we can use Eq. (G.50) to find the success probability (of undergoing no quantum jumps for a sufficiently long time)

$$p \simeq \left|\left\langle \psi_f^{2m} | \psi_0 \right\rangle\right|^2 = \frac{|\text{tr}[C]|^2}{D\text{tr}[C^\dagger C]} + \mathcal{O}(\epsilon_2^m) = \frac{|\vec{\alpha}\cdot\vec{\beta}|^2}{D|\vec{\alpha}|^2|\vec{\beta}|^2} + \mathcal{O}(\epsilon_2^m) \quad \text{if} \quad C_{bc} = \alpha_b\beta_c, \tag{G.58}$$

where we wrote the expression in a more suggestive form assuming initially unentangled chains. For random states $\vec{\alpha}, \vec{\beta} \in \mathbb{C}^D$, we have on average $p \simeq 1/D^2$. The maximum success probability of $p_{\max} = 1/D$ is obtained when $\vec{\alpha} \parallel \vec{\beta}$, i.e. when the two edge

states are identical. Hence, there is a system-size-independent success probability if we attempt to connect two chains of injective MPS by turning on the jump operators for the two particles at the interface. Consequently, we can improve the scaling of preparation time of our desired MPS to $\mathcal{O}(\log^2 n)$ by connecting many pairs of chains in parallel in the same way as proposed for AKLT.

When our desired MPS also exhibits bond-inversion symmetry $\mathcal{P}$ like AKLT, we have the same issue of vanishing success probability after a quantum jump that also respects $\mathcal{P}$. In the event of a quantum jump due to a jump operator of the form $c = |\phi\rangle\langle\psi|$, the state after discarding the two particles at the interface is $|\psi_1\rangle = \mathcal{N}_1 \sum_{b',c'} \tilde{C}_{b'c'} \left|A^{m-1}_{ab'}\right\rangle \left|A^{m-1}_{c'd}\right\rangle$, where

$$\tilde{C}_{b'c'} = \sum_{bc} \langle\psi| \left(\left|A^1_{b'b}\right\rangle \otimes \left|A^1_{cc'}\right\rangle\right) C_{bc}. \tag{G.59}$$

If $|\psi\rangle$ respects bond-inversion symmetry, i.e. $\mathcal{P}|\psi\rangle = \pm|\psi\rangle$, where $\mathcal{P} = \sum_{i,j} |ij\rangle\langle ji|$, then

$$\text{tr}[\tilde{C}] = \sum_a \tilde{C}_{aa} = \sum_{abc} \langle\psi| \left(\left|A^1_{ab}\right\rangle \otimes \left|A^1_{ca}\right\rangle\right) C_{bc} \tag{G.60}$$

$$= \sum_{abc} \langle\psi| \mathcal{P} \left(\left|A^1_{ca}\right\rangle \otimes \left|A^1_{ab}\right\rangle\right) C_{bc} = \sum_{bc} \pm \left\langle\psi|A^2_{cb}\right\rangle C_{bc} = 0. \tag{G.61}$$

We find that this quantity is zero regardless of initial C_{bc}, entangled or unentangled, due to our requirement that $|\psi\rangle$ be orthogonal to the desired MPS states $|A^2_{cb}\rangle$. In fact, tr$[\tilde{C}]$ is related to the success probability of the next connection attempt: $p' \simeq \left|\left\langle\psi_f^{2m-2}|\psi_1\right\rangle\right|^2 \propto |\text{tr}[\tilde{C}]|^2 + \mathcal{O}(\epsilon_2^m) = \mathcal{O}(\epsilon_2^m)$, which is exponentially small for a large system size.

Similar to the AKLT case, we can also try to restore the success probability by applying a global symmetry operation $U_g^{\otimes m-1}$ for some $g \in \mathcal{G}$ to one of the chains. In our AKLT protocol, there is a symmetry operation $U = e^{i\pi S_y}$ whose action on the virtual bond level

$u = e^{-i\pi\sigma_y/2}$ yields $\left|\text{tr}[u^\dagger \tilde{C}]\right|^2 = \text{tr}[\tilde{C}^\dagger \tilde{C}]$, allowing us to recover the maximum success probability of $p_{\max} = 1/D$ regardless of initial state C_{bc} or which quantum jump occurred. While the existence of such an operation is not known for the general case, we can at least restore the success probability to $1/D^2$ for many injective MPS by applying a randomly chosen symmetry operation. This is because the $\{A^{(s)}\}$ matrices that generate the MPS only has one block if it is injective, and hence the symmetry operation represented on the virtual bond space u_g can be one irreducible representation of dimension D. A sufficient condition for irreducibility of u_g is given in Ref. [247], which is that U_g be irreducible and $\{A^{(s)\dagger} A^{(s')} : \forall s, s'\}$ spans the whole space of matrices. When u_g is irreducible, applying a global symmetry operation $U_g^{\otimes m-1}$ randomly chosen from the group would change any edge state $|b\rangle$ to $\frac{1}{|\mathcal{G}|}\sum_{g\in\mathcal{G}} u_g^\dagger |b\rangle \langle b| u_g = \mathbb{1}/D$. This will then yield a subsequent success probability of $1/D^2$.

Non-injective case— The analysis of generalization to non-injective cases is more subtle. Here we consider an illustrative example to prepare GHZ states: $|\text{GHZ}_\pm\rangle = (|0^n\rangle \pm |1^n\rangle)/\sqrt{2}$, which has an MPS representation with $(d, D) = (2, 2)$ given by the following matricies:

$$A^{(0)} = |\uparrow\rangle\langle\uparrow| = \begin{pmatrix} 1 & 0 \\ 0 & 0 \end{pmatrix} \quad \text{and} \quad A^{(1)} = |\downarrow\rangle\langle\downarrow| = \begin{pmatrix} 0 & 0 \\ 0 & 1 \end{pmatrix}. \tag{G.62}$$

Note this is in a canonical form, with two one-dimensional blocks. In this representation, $|\text{GHZ}_+\rangle \propto |A^n_{\rightarrow\rightarrow}\rangle = |A^n_{\leftarrow\leftarrow}\rangle$, and $|\text{GHZ}_-\rangle \propto |A^n_{\rightarrow\leftarrow}\rangle = |A^n_{\leftarrow\rightarrow}\rangle$, where $|\rightarrow\rangle = (|\uparrow\rangle + |\downarrow\rangle)/\sqrt{2}$ and $|\leftarrow\rangle = (|\uparrow\rangle - |\downarrow\rangle)/\sqrt{2}$ are possible edge configurations. This MPS has an internal symmetry group of $\mathcal{G} = \mathbb{Z}_2$, which is represented by $\{\mathbb{1}, \sigma_x^{\otimes n}\}$ acting on the system. Its parent Hamiltonian is $H_{\text{GHZ}} = \sum_i (\mathbb{1} - \sigma_z^{(i)}\sigma_z^{(i+1)})$, whose ground states

are doubly degenerate due to non-injectivity. The corresponding two-particle bright manifold is $\mathfrak{B} = \text{span}\{|\Phi_+\rangle, |\Phi_-\rangle\}$, where $|\Phi_\pm\rangle = (|01\rangle \pm |10\rangle)/\sqrt{2}$. The two states $|\Phi_\pm\rangle$ support two distinct irreducible representations of $\mathbb{Z}_2$, which are respectively the trivial and the sign representation. Hence, we can use just one jump operator of the form e.g. $c = |00\rangle (\kappa_+ \langle\Phi_+| + \kappa_- \langle\Phi_-|)$, $\kappa_\pm \neq 0$, along with the global symmetry operation $\sigma_x^{\otimes n}$, to depopulate the bright manifold and obtain $\text{span}\{|\text{GHZ}_\pm\rangle\}$ as the subspace of steady states. Now let us consider preparing $|\text{GHZ}_\pm\rangle$ in a parallelized protocol with connections and feedback. We note that unlike in the injective case, different choices of jump operator here can lead to qualitatively different outcomes. Specifically, we consider two choices of jump operators that may result in different degrees of entanglement of the final state. Firstly, consider an example choice of jump operator $c = |00\rangle\langle 01|$ (i.e. $\kappa_\pm = 1/\sqrt{2}$). While this along with the symmetry operation produces a dissipative dynamics that has $|\text{GHZ}_\pm\rangle$ as the steady states, the parallelized protocol can only produce an unentangled final state of either $|0^n\rangle \propto |\text{GHZ}_+\rangle + |\text{GHZ}_-\rangle$ or $|1^n\rangle \propto |\text{GHZ}_+\rangle - |\text{GHZ}_-\rangle$ once any quantum jump occurs, regardless of states of the initial chains. Alternatively, we may choose the jump operator $c = |00\rangle (\langle 01| + i \langle 10|)/\sqrt{2}$ (i.e. $\kappa_+ = \kappa_-^* = (1+i)/2$). In this case, suppose we start with $|0^{n_0}\rangle + |1^{n_0}\rangle$ on the initial chains of length n_0, then we can produce a maximally entangled final state of $|0^n\rangle + \zeta |1^n\rangle$ even after quantum jumps, for some $\zeta \in \{\pm 1, \pm i\}$ that we can determine from recording quantum jump history. In both cases, for an arbitrary (unentangled) initial state $|\psi_0\rangle = \sum_{a,b=0}^{1} (\alpha_a |a^m\rangle) \otimes (\beta_b |b^m\rangle)$ of two chains, the success probability of connecting them is on average $1/2$ for random $\vec{\alpha}, \vec{\beta} \in \mathbb{C}^2$. This system-size-independent success probability means the parallelized protocol for this non-injective MPS also has an efficient scaling of $\mathcal{O}(\log^2 n)$ for the preparation time.

Appendix H

Supporting Material of Chapter 10

H.1 Types of Rydberg Interactions

The interaction between two atoms in distinct levels Rydberg levels R and R' has the general form

$$V = \begin{pmatrix} V_b(r) & V_{ex}(r) \\ V_{ex}(r) & V_b(r) \end{pmatrix} \tag{H.1}$$

in the two-atom product basis $\{|RR'\rangle, |R'R\rangle\}$. Here, r is the distance between the atoms.

For levels R, R' with $\Delta L = \pm 1$, the dominant interaction will be the direct dipolar interaction $V_{ex}(r) = C_3/r^3$ [181]. Because this interaction is not diagonal in the product basis, its action is to exchange the states $|RR'\rangle$ and $|R'R\rangle$. This case describes the interaction between the $\left|100S_{1/2}, m_J = 1/2\right\rangle$ and $\left|99P_{3/2}, m_J = 3/2\right\rangle$ states used for the experiments in the main text, which feature $C_3/h = 33.4$ GHz μm^3. For these states, V_b is negligible at the relevant length scales (less than 5% of V_{ex} at $r = 20\,\mu$m), as shown in Fig.

H.1.

In contrast, for same-parity levels, the direct dipolar interaction is not allowed, so the dominant interaction is second-order, such that $V_b(r) = C_6/r^6$ and $V_{ex}(r) = \chi_6/r^6$. For states with widely separated principal quantum numbers, $|C_6| \gg |\chi_6|$. However, if the principal quantum numbers of the R, R' states are similar, $|\chi_6|$ can be comparable to $|C_6|$. When $|C_6| \gg |\chi_6|$, the interaction does not lead to exchange of Rydberg excitations, but only shifts the combined energy, as is typically assumed for Rydberg blockade (and must be true when $R = R'$). In contrast, when $|\chi_6| \approx |C_6|$ state exchange is also possible.

For the experiments described in the inset to Fig. 3, the state $\left|97S_{1/2}\right\rangle$ has $C_6/h = -114$ THz μm^6 and $\chi_6/h = -0.6$ THz μm^6, while $\left|99S_{1/2}\right\rangle$ has $C_6/h = 65.3$ THz μm^6 and $\chi_6/h = 48.7$ THz μm^6. These values are obtained from direct diagonalization of the dipole-dipole Hamiltonian for a truncated basis of states [181]. All potentials are evaluated for interatomic separation along the quantization axis, which is appropriate for the quasi-1D geometry of the experiment.

H.2 Approximate analytical solution including absorption

Here, we consider a complete model for polariton collisions that allows for the incorporation of loss and finite pulse bandwidth effects. We first use this model to derive approximate analytical expressions for the loss and phase shift for continuous-wave fields in the limits of small and large OD_b, and then consider the impact of finite pulse bandwidth.

From Eqs. (10.2) and (10.3) we can derive the following Heisenberg equations for the slowly-varying bosonic operators $\{\hat{\mathcal{E}}, \hat{\mathcal{P}}, \hat{\mathcal{S}}, \hat{\mathcal{C}}\}$:

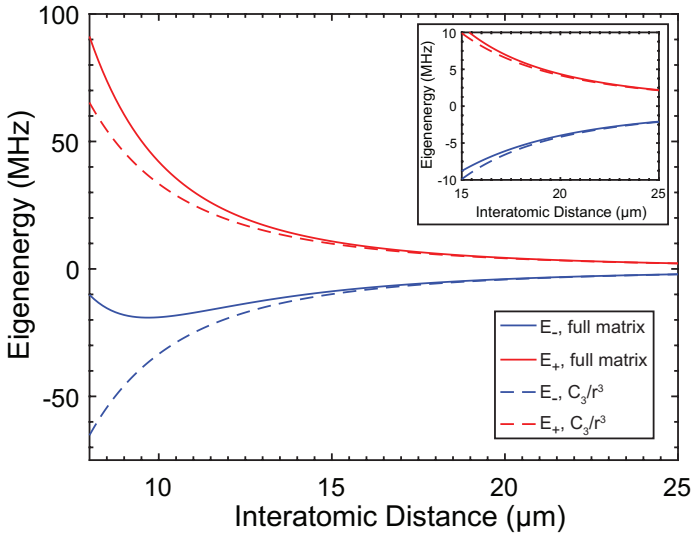

Figure H.1: Comparison of eigenenergies of a $\left|100S_{1/2}, m_J = 1/2\right\rangle$ - $\left|99P_{3/2}, m_J = 3/2\right\rangle$ atom pair using numerical diagonalization of the dipolar Hamiltonian in a basis of 2750 pairs of Rydberg levels, and a C_3/r^3 approximation (dashed lines). The positive and negative eigenenergies, E_+ and E_- (corresponding to the *gerade* and *ungerade* molecular states), are plotted as a function of the distance between the atoms r, relative to their average energy when $r \to \infty$. The C_3 approximation is accurate to better than 5% at distances greater than 20 μm, which is where the exchange interaction takes place at the highest densities used in the experiment.

$$(\partial_t + c\partial_z)\hat{\mathcal{E}}(z,t) = -i\bar{g}\hat{\mathcal{P}}(z,t) \tag{H.2}$$

$$\partial_t\hat{\mathcal{P}}(z,t) = -i\bar{g}\hat{\mathcal{E}}(z,t) - i\Omega\hat{\mathcal{S}}(z,t) - \gamma\hat{\mathcal{P}}(z,t) \tag{H.3}$$

$$\partial_t\hat{\mathcal{S}}(z,t) = -i\Omega\hat{\mathcal{P}}(z,t) - i\int \mathrm{d}z' V(z-z')\hat{\mathcal{C}}^\dagger(z',t)\hat{\mathcal{C}}(z,t)\hat{\mathcal{S}}(z',t) \tag{H.4}$$

$$\partial_t\hat{\mathcal{C}}(z,t) = -i\int \mathrm{d}z' V(z-z')\hat{\mathcal{S}}(z',t)^\dagger\hat{\mathcal{S}}(z,t)\hat{\mathcal{C}}(z',t) \tag{H.5}$$

The interaction between a single signal and gate photon can be described by the two-body wavefunction:

$$\begin{aligned}|\psi_2(t)\rangle = &\int \mathrm{d}z\mathrm{d}z' EC(z,z',t)\hat{\mathcal{E}}^\dagger(z)\hat{\mathcal{C}}^\dagger(z')|0\rangle + \int \mathrm{d}z\mathrm{d}z' PC(z,z',t)\hat{\mathcal{P}}^\dagger(z)\hat{\mathcal{C}}^\dagger(z')|0\rangle \\ &+ \int \mathrm{d}z\mathrm{d}z' SC(z,z',t)\hat{\mathcal{S}}^\dagger(z)\hat{\mathcal{C}}^\dagger(z')|0\rangle.\end{aligned} \tag{H.6}$$

Here the amplitudes $EC(z,z',t) = \langle 0|\hat{\mathcal{E}}(z)\hat{\mathcal{C}}(z')|\psi(t)\rangle$, $PC(z,z',t) = \langle 0|\hat{\mathcal{P}}(z)\hat{\mathcal{C}}(z')|\psi(t)\rangle$, and $SC(z,z',t) = \langle 0|\hat{\mathcal{S}}(z)\hat{\mathcal{C}}(z')|\psi(t)\rangle$ correspond, respectively, to a signal photon, intermediate state, or nS-Rydberg excitation at position z, with the $n'P$ spin wave stored at position z'. Their evolution equations follow by substitution into Eqs. (H.2)-(H.5), which gives

$$\begin{aligned}(\partial_t + c\partial_z)EC(z,z',t) =& -i\bar{g}PC(z,z',t) \\ \partial_t PC(z,z',t) =& -i\bar{g}EC(z,z',t) - i\Omega SC(z,z',t) - \gamma PC(z,z',t) \\ \partial_t SC(z,z',t) =& -i\Omega PC(z,z',t) - i\frac{C_3}{|z-z'|^3}SC(z',z,t).\end{aligned} \tag{H.7}$$

Transforming into the center-of-mass frame with $r = |z-z'|$ and $R = z+z'$ and Fourier transforming the resulting equations with respect to time and R ($t \to \omega$ and $R \to K$) one can derive a single equation for $\psi \equiv EC$

$$\partial_r\psi(\pm r, K, \omega) = \pm A(r,\omega)\psi(\pm r, K, \omega) \pm iB(r,\omega)\psi(\mp r, K, \omega) \tag{H.8}$$

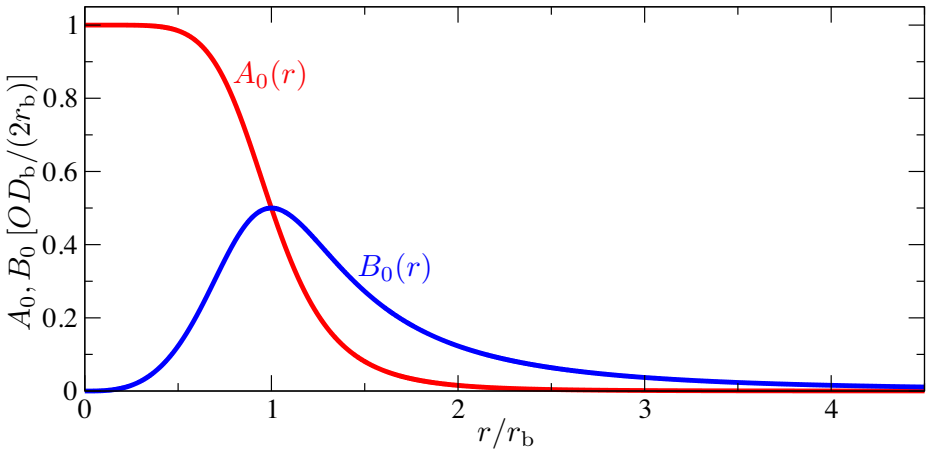

Figure H.2: Loss coefficient (red) and hopping strength (blue) as given by Eqs. (H.11) in the limit of a very slowly propagating polariton, $\omega = K = 0$.

with the complex coefficients

$$A\left(r,K,\omega\right)=i\frac{\bar{g}^{2}}{c\left(\omega-i\gamma\right)}-iK-i\frac{\omega}{c}+i\frac{\bar{g}^{2}\Omega^{2}}{c\left(\omega-i\gamma\right)^{2}}\frac{\omega-\frac{\Omega^{2}}{\omega-i\gamma}}{\left(\omega-\frac{\Omega^{2}}{\omega-i\gamma}\right)^{2}-V\left(r\right)^{2}}$$

$$B\left(r,\omega\right)=\frac{\bar{g}^{2}\Omega^{2}}{c\left(\omega-i\gamma\right)^{2}}\frac{V\left(r\right)}{\left(\omega-\frac{\Omega^{2}}{\omega-i\gamma}\right)^{2}-V\left(r\right)^{2}}. \tag{H.9}$$

Since $r \geq 0$, the wave function is defined such that $\psi(-r)$ and $\psi(+r)$ describe a signal photon propagating towards and away from the spin wave, respectively.

The advantage of such a splitting of the position-space is that the two sectors are related by the complex transmission amplitude $T(r, K, \omega) = \psi(+r)/\psi(-r)$, for which one obtains a closed equation

$$\partial_r T = 2AT + iB(1 + T^2), \tag{H.10}$$

subject to the initial condition $T(r = 0, K, \omega) = 1$. While Eq. (H.10) does not feature a general analytical solution, one can treat several important limiting cases as described below.

H.2.1 Absorptionless solution in the cw-limit

For long (quasi-continuous) signal and gate pulses we may take Eqs. (H.9) at $\omega = K = 0$ such that the coefficients become real

$$A_0(r) = A(r,0,0) = -\frac{OD_\mathrm{b}}{2r_\mathrm{b}}\frac{r_\mathrm{b}^6}{r_\mathrm{b}^6 + r^6}\,, \quad B_0(r) = B(r,0,0) = \frac{OD_\mathrm{b}}{2r_\mathrm{b}}\frac{r_\mathrm{b}^3 r^3}{r_\mathrm{b}^6 + r^6}. \tag{H.11}$$

This equation shows that $B_0(r)$ corresponds to the strength of the coherent hopping while the coefficient $A_0(r)$ causes photon loss, i.e. linearly damps the transmission amplitude in Eq.(H.10). Since $A_0 \sim r^{-6}$ drops much more rapidly that $B_0 \sim r^{-3}$ for large distances $r \gg r_\mathrm{b}$ (see Fig. H.2), we may neglect the A_0 to obtain a particularly simple solution

$$T_0(r) = \tan\left[\frac{\pi}{4} + i\int_0^r B_0(r')\mathrm{d}r'\right], \tag{H.12}$$

of Eq.(H.10). Indeed there is no absorption in this limit since $T_0(r) = \mathrm{e}^{i\varphi(r)}$. The accumulated phase of the outgoing photon

$$\varphi_0(\infty) = \mathrm{acos}\left[\cosh\left(OD_\mathrm{b}\frac{\sqrt{3}}{9}\pi\right)^{-1}\right] \underset{OD_\mathrm{b}\gg 1}{\longrightarrow} \frac{\pi}{2} - 2\mathrm{e}^{-OD_\mathrm{b}\frac{\sqrt{3}}{9}\pi}, \tag{H.13}$$

exponentially approaches $\pi/2$ for a large optical depth per blockade radius OD_b. Substituting the calculated transmission amplitude into Eq. (H.8) and using Eq. (H.10) we can also determine the actual wave function

$$\psi(\pm r) = \frac{\cosh\left[\int_0^r B_0(r')\mathrm{d}r'\right] \pm i\sinh\left[\int_0^r B_0(r')\mathrm{d}r'\right]}{\cosh\left[OD_\mathrm{b}\frac{\sqrt{3}}{18}\pi\right] - i\sinh\left[OD_\mathrm{b}\frac{\sqrt{3}}{18}\pi\right]}\psi(-\infty). \tag{H.14}$$

For large distances $r \gg r_\mathrm{b}$ we can approximate $B_0(r) \approx \frac{OD_\mathrm{b}}{2}\frac{r_\mathrm{b}^2}{r^3}$ to solve the involved integral

$$\int_0^r B_0(r')\mathrm{d}r' \approx \int_0^\infty B_0(r')\mathrm{d}r' - \frac{OD_\mathrm{b}}{2}r_\mathrm{b}^2\int_r^\infty r'^{-3}\mathrm{d}r' = OD_b\left(\frac{\sqrt{3}\pi}{18} - \frac{r_b^2}{4r^2}\right) \tag{H.15}$$

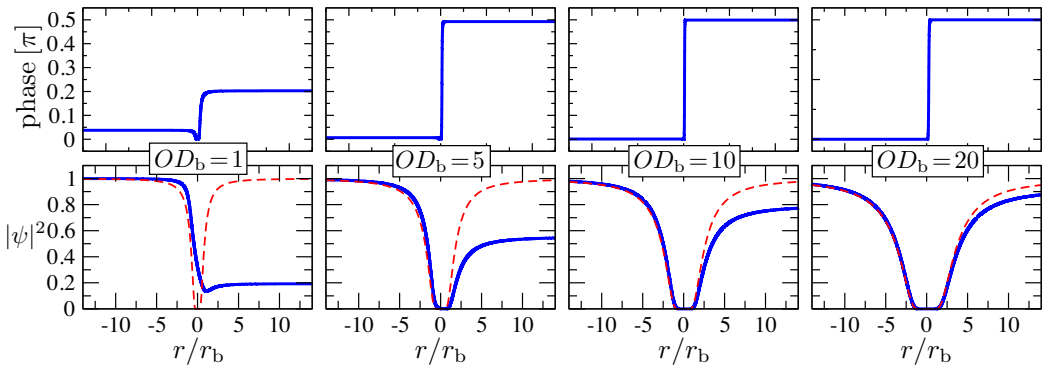

Figure H.3: Two-body phase (top) and probability density (bottom) as a function of the distance between the signal photon and the gate spin wave for different indicated values of optical depth per blockade radius, OD_b. The blue solid line shows numerical results while the red dashed line is obtained from the approximate solution Eq. (H.16).

and obtain the asymptotic solution

$$\begin{aligned}\psi(\pm r) &\underset{r\gg r_\mathrm{b}}{\approx} \frac{\cosh\left[OD_b\left(\frac{\sqrt{3}\pi}{18}-\frac{r_b^2}{4r^2}\right)\right] \pm i\sinh\left[OD_\mathrm{b}\left(\frac{\sqrt{3}\pi}{18}-\frac{r_b^2}{4r^2}\right)\right]}{\cosh\left[OD_\mathrm{b}\frac{\sqrt{3}}{18}\pi\right] - i\sinh\left[OD_\mathrm{b}\frac{\sqrt{3}}{18}\pi\right]}\psi(-\infty) \\ &\underset{OD_\mathrm{b}\gg 1}{\approx} \frac{1\pm i}{1-i}\mathrm{e}^{-OD_\mathrm{b}\frac{r_\mathrm{b}^2}{4r^2}}\psi(-\infty) \end{aligned} \tag{H.16}$$

which for $OD \gg 1$ approaches the solution given in the main text. As shown in Fig. H.3, this solution provides a reasonably good description of the numerical results already for moderate values of OD_b, while the vanishing of $\psi(r)$ for $r < r_\mathrm{b}$ provides a self-consistency test of the applied approximations. The main difference between the analytical solution and the numerical result stems from the photon losses for which we will now derive an analytical estimate.

H.2.2 Leading-order absorption

The simple solution permits us to determine the residual photon loss in the limit of large OD_b by perturbatively accounting for the amplitude decay coefficient $A_0(r)$. Using

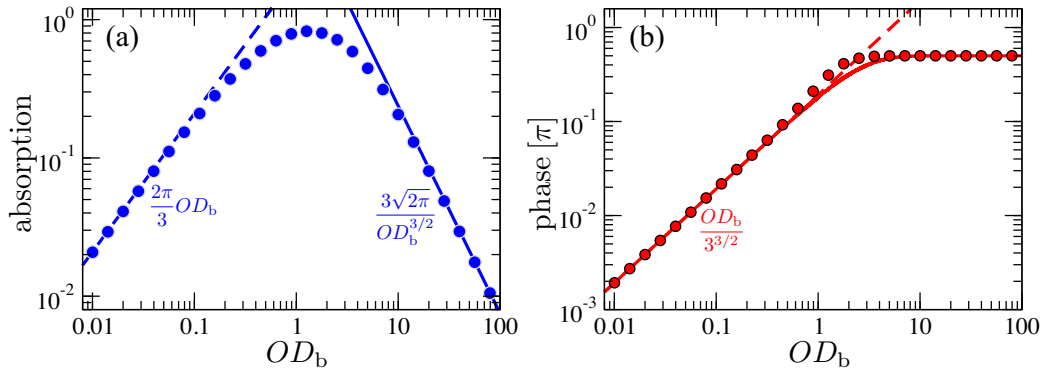

Figure H.4: (a) Signal photon absorption and (b) acquired phase as a function of OD_b. Symbols show numerical results while the solid and dashed lines show the asymptotic large-OD_b [Eqs. (H.19) and (H.16)] and small-OD_b [Eq. (H.20)] solutions, respectively.

standard perturbation theory with $A_0(r)$ as the small parameter, the leading correction to the transmission amplitude is obtained from

$$\partial_r T_1(r) = 2A_0(r)T_0(r) + iB_0(r)2T_0(r)T_1(r), \tag{H.17}$$

which subject to the boundary condition $T_1(0) = 0$ has the following solution

$$T_1(r) = 2\frac{\int_0^r A_0(z')\cosh\left[2\int_0^{z'} B_0(z'')\mathrm{d}z''\right]\mathrm{d}z'}{1 - i\sinh\left[2\int_0^r B_0(z')\mathrm{d}z'\right]} \tag{H.18}$$

Using Eq. (H.15), we can approximately solve the integrals and obtain the total transmission amplitude

$$T(\infty) \underset{OD_\mathrm{b}\to\infty}{\longrightarrow} T_0(\infty) + T_1(\infty) = i\left(1 - \frac{3\sqrt{2\pi}}{2}OD_b^{-3/2}\right), \tag{H.19}$$

which shows that the photon loss asymptotically decreases as $1 - |T|^2 = 3\sqrt{2\pi}OD_b^{-3/2}$ for large OD_b.

Similarly we can perform a perturbative expansion in the simpler limit of $OD_\mathrm{b} \ll 1$, which gives $T_0 = 1$ to zeroth order in OD_b, and

$$T(\infty) \underset{OD_\mathrm{b}\to 0}{\longrightarrow} T_0(\infty) + T_1(\infty) = 1 - \frac{\pi}{3}\left(1 - \frac{i}{\sqrt{3}}\right)OD_\mathrm{b}. \tag{H.20}$$

As shown in Fig. H.4, the derived scaling laws quantitatively reproduce our numerical results in both relevant limits.

H.2.3 Propagation effects

With the outlined formalism, the leading-order inclusion of propagation effects becomes straightforward. To this end we now consider a finite medium of constant density and length $2L$ extending from $-L$ to L. Repeating the above derivation, with A_0 replaced by $A_0 - iK - i\omega/v_{\mathrm{g}}$, gives the following asymptotic ($r > r_{\mathrm{s}}$) solution of Eq. (H.18)

$$\begin{aligned} T(r, K, \omega) &= i\left(1 - \frac{3\sqrt{2\pi}}{2} O D_b^{-3/2}\right) + 2(K + \omega/v_{\mathrm{g}})(r - \sqrt{\pi O D_b/2} r_{\mathrm{b}}) \\ &\approx i\left(1 - \frac{3\sqrt{2\pi}}{2} O D_b^{-3/2}\right) \mathrm{e}^{-2i(K+\omega/v_{\mathrm{g}})(r-\sqrt{\pi} r_{\mathrm{s}})}. \end{aligned} \tag{H.21}$$

Using the last expression in $\psi(r, K, \omega) = T(r, K, \omega)\psi(-r, K, \omega)$ and applying the free propagator, $\psi(r', K, \omega) = \mathrm{e}^{-i(K+\omega/c)(r'-r)}\psi(r', K, \omega)$ for $r, r' \gg r_{\mathrm{s}}$, then lets us Fourier transform back to time t and R and write the outgoing two-body state as

$$\psi(z = L, z', t) = i\left(1 - \frac{3\sqrt{2\pi}}{2} O D_b^{-3/2}\right) C\left(z' + \sqrt{\pi} r_s\right) E_{\mathrm{in}}\left(t - \frac{L - \sqrt{\pi} r_s}{v_g}\right) \tag{H.22}$$

in terms of the initial spin wave profile $C(z)$ and the incident signal-field mode $E_{\mathrm{in}}(t)$. We see that the dipole-dipole interaction does not cause any pulse distortion but gives rise to a homogenous spatial shift $\sqrt{\pi} r_{\mathrm{s}}$. Note that the above derivation is only accurate to leading order in the bandwidth of both photons and, thus, requires that the spatial extent of the gate spin wave and the EIT-compressed signal photon pulse are both substantially larger than r_{s}. As a consequence the ideal scenario, Eq. (H.22), eventually deviates from the exact behavior as the optical depth per blockade radius is increased to too large values (see Fig.H.5).

H.2.4 Derivation of Eq. 10.1 in the main text

Having established the vanishing of the two-body wave function for distances below $r_\mathrm{s} = \sqrt{OD_\mathrm{b}/2}r_\mathrm{b}$, we can use an asymptotic $r/r_\mathrm{b} \to \infty$ expansion of the coefficients Eq. (H.9) to simplify the propagation equations (H.8) in the limit of $OD_\mathrm{b} \gg 1$. With the definition of r_b, this is equivalent to a Taylor expansion in $V_{ex}(r)/(\Omega^2/\gamma) \ll 1$ which yields

$$A\left(K,\omega\right) \approx -iK - i\frac{\omega}{v_\mathrm{g}},\; B\left(r\right) \approx \frac{\bar{g}^2}{c\Omega^2}V_{ex}(r) \tag{H.23}$$

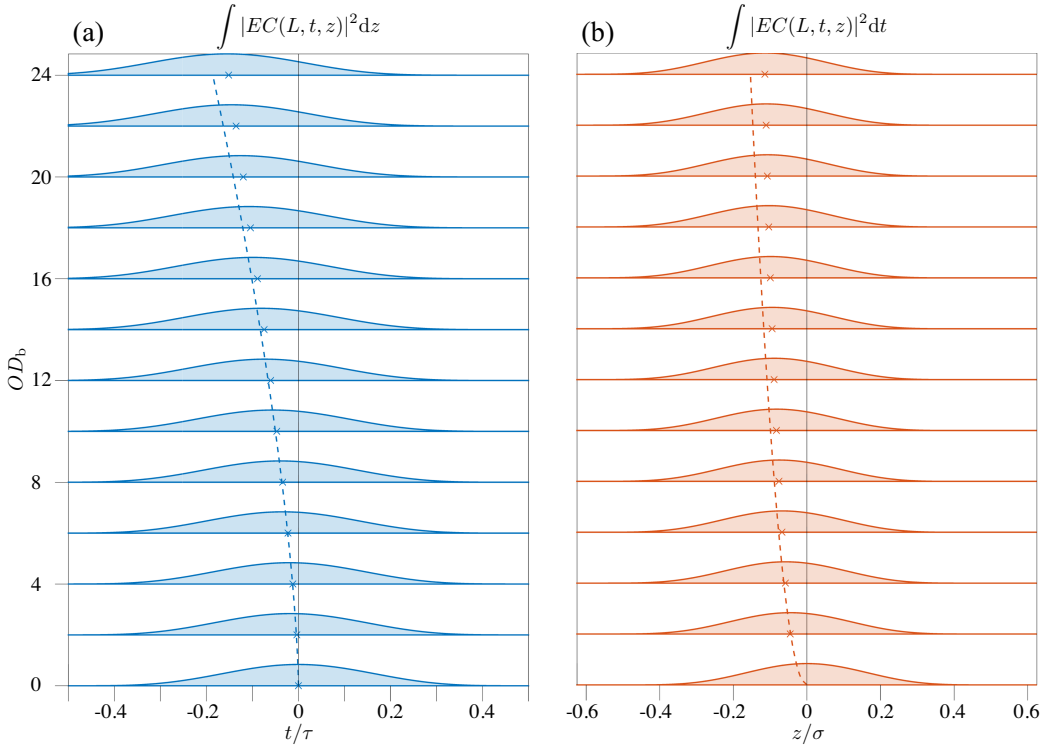

Figure H.5: (a) Transmitted signal photon intensity and (b) final probability density of the gate spin wave for different values of OD_b. The numerical simulations have been performed for a signal pulse duration of $\tau = 400(\Omega^2/\gamma)^{-1}$, a gate spin wave of length $\sigma = 40r_\mathrm{b}$, $v_\mathrm{g}/c = 0.01$ and $\Omega/\gamma = 1$. The crosses mark the numerical center of the photon pulse and spinwave density and the dashed lines show the analytical prediction Eq. (H.22).

to linear order in $\omega/(\Omega^2/\gamma)$ and $V_{ex}/(\Omega^2/\gamma)$. With these expressions Eq. (H.8) simplifies to

$$\partial_r\psi\left(\pm r,K,\omega\right)=\mp iK\psi(\pm r,K,\omega)\mp i\frac{\omega}{v_{\mathrm{g}}}\psi(\pm r,K,\omega)\pm i\frac{\bar{g}^2}{c\Omega^2}V_{ex}(r)\psi(\mp r,K,\omega) \tag{H.24}$$

Using $\bar{g}^2\gg\Omega^2$ and Fourier transforming back to t and R we thus obtain

$$\partial_r\psi(\pm r,R,t)=\pm\partial_R\psi(\pm r,R,t)\pm v_{\mathrm{g}}^{-1}\partial_t\psi(\pm r,R,t)\pm iv_{\mathrm{g}}^{-1}V_{ex}(r)\psi(\mp r,R,t) \tag{H.25}$$

and in terms of z and z'

$$\partial_t\psi(z,z',t)=-\partial_z\psi(z,z',t)-iV_{ex}(z-z')\psi(z',z,t), \tag{H.26}$$

which coincides with Eq. (10.1) of the main text. Its stationary solution, presented in the main text, agrees with Eq. (H.16), as expected.

Following these arguments, the asymptotic treatment of the wave function for $r\gg r_{\mathrm{b}}$ is equivalent to a perturbative expansion for small interactions $V_{ex}\ll\Omega^2/\gamma$. Under this condition the photon propagation can be described in terms of a dark-state polariton which follows Eq.(H.26). For $OD_{\mathrm{b}}\gg1$, the exchange-driven photon collision can thus be understood as a collision between dark-state polaritons. In contrast to previous Rydberg-EIT schemes where the van der Waals interaction inevitably causes coupling to bright state polaritons at distances $r\lesssim r_{\mathrm{b}}$, such processes are inhibited by the long-range hopping at a distance $r_{\mathrm{s}}\gg r_{\mathrm{b}}$. This mechanism is key to the observed low photon losses.

H.3 Modeling the complete experiment

Now we turn to producing a complete model for the experiment, including finite pulse duration and bandwidth effects, dephasing, and the finite size of the atomic cloud. At the

end, we present numerical simulations of this model to compare to the experimental results. To begin, we divide the experimental sequence into three stages:

A. the gate-photon storage into a nS-Rydberg spinwave and microwave transfer to a $n'P$ Rydberg state, creating a $n'P$ spinwave excitation at time $t = 0$,

B. its interaction with the incident signal photon extending from $t = 0$ to $t = T$,

C. followed by back-transfer of the gate excitation to an nS-Rydberg spin wave and subsequent retrieval ($t \geq T$),

which we will describe separately below. The timing of the different stages and associated computational steps is illustrated in Fig. H.6.

We extend the Heisenberg equations (H.2-H.5) to include dephasing and detuning terms, as well as inhomogeneous atomic density:

$$(\partial_t + c\partial_z)\hat{\mathcal{E}}(z,t) = -ig\sqrt{\rho(z)}\hat{\mathcal{P}}(z,t) \tag{H.27}$$

$$\partial_t\hat{\mathcal{P}}(z,t) = -ig\sqrt{\rho(z)}\hat{\mathcal{E}}(z,t) - i\Omega\hat{\mathcal{S}}(z,t) - \gamma\hat{\mathcal{P}}\,(z,t) \tag{H.28}$$

$$\begin{aligned}\partial_t\hat{\mathcal{S}}(z,t) = &-i\Omega\hat{\mathcal{P}}(z,t) - i[\Delta_{\mathrm{s}}(z) - i\gamma_{\mathrm{s}}]\hat{\mathcal{S}}(z,t) \\ &- i\int \mathrm{d}z' V_{ex}(z-z')\hat{\mathcal{C}}^{\dagger}(z',t)\hat{\mathcal{C}}(z,t)\hat{\mathcal{S}}(z',t)\end{aligned} \tag{H.29}$$

$$\partial_t\hat{\mathcal{C}}(z,t) = -i\Delta_{\mathrm{c}}(z)\hat{\mathcal{C}}(z,t) - i\int \mathrm{d}z' V_{ex}(z-z')\hat{\mathcal{S}}(z',t)^{\dagger}\hat{\mathcal{S}}(z,t)\hat{\mathcal{C}}(z',t) \tag{H.30}$$

The atomic density $\rho(z) = \rho_0 f(z)$ has a Gaussian $f(z) = e^{-z^2/(2\sigma^2)}$ profile along the propagation axis, with a spatial width σ and peak density ρ_0. g is the bare atom-light coupling. The position-dependent detunings $\Delta_s\,(z)$ and $\Delta_c\,(z)$ for the nS and $n'P$ states arise from interactions between ground state atoms and the excited Rydberg atoms, which

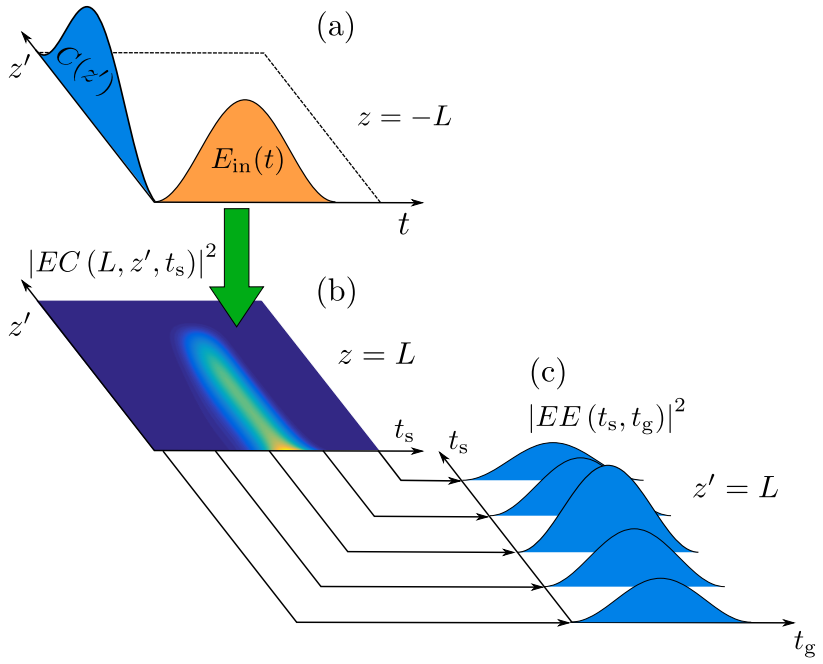

Figure H.6: Schematic illustration of photon collision sequence and involved computational steps. (a) Following the storage of a gate photon in a spin-wave mode $C(z')$, the signal photon enters the EIT medium at $(z=-L)$ with a temporal pulse envelope $E_{\rm in}(t)$. (b) During the interaction stage the correlated dynamics of the signal photon and the gate spin wave is described by the two-body amplitude $EC(z,z',t)$. Upon detection the transmitted signal photon at $z=L$ and a time t_s, the gate spinwave is left in a mode $EC(L,z',t_s)$. At each exit time t_s this amplitude is used as an initial condition for retrieval of the gate spinwave. (c) At each detection time $t_{\rm s}$ this amplitude provides the initial condition for determining the amplitude of the outgoing gate photon detected at time $t_{\rm g}$, from which we obtain the two-photon amplitude $EE(t_s,t_g)$.

vary according to the ground-state atomic density as discussed in section H.5. $\gamma_{\rm s}$ accounts for the linewidth of the nS Rydberg state.

H.3.1 Gate photon storage

The signal photon is first stored in a Rydberg spin wave in the nS state and transferred to a $n'P$ excitation as described in the main text. Since our experiment uses a weak coherent

pulse, it suffices to retain only the vacuum component, $\epsilon_{\mathrm{g}}(t)|0\rangle$ and the single-excitation component

$$|\psi_{\mathrm{g}}(t)\rangle = \int \mathrm{d}z C(z,t)\hat{\mathcal{C}}^{\dagger}(z)|0\rangle \tag{H.31}$$

of the produced spin wave state, where the amplitude $C(z, t = 0)$ denotes the mode profile of the spin wave right after storage. To simplify notation we further approximate $\epsilon_{\mathrm{g}}(t) \sim 1$.

H.3.2 Interaction stage

Due to the dipolar excitation exchange, the propagation of the subsequent signal pulse requires a two-body treatment, even though the stored $n'P$ excitation is not coupled by the classical control field Ω. Again, retaining only the vacuum and single-photon components of the incident signal pulse, the pure contribution to the total state of the system can be written as

$$|\Psi(t)\rangle = |0\rangle + |\psi_{\mathrm{g}}(t)\rangle + |\psi_{\mathrm{s}}(t)\rangle + |\psi_2(t)\rangle. \tag{H.32}$$

Impure parts resulting from the intermediate state decay do not need to be considered since the resulting spinwave decoherence precludes subsequent retrieval of the gate photon [270] and, thus, do not contribute to the observables discussed below.

The single spin wave state, $|\psi_{\mathrm{g}}(t)\rangle$ is given by Eq. (H.31) with:

$$C(z,t) = C(z,t=0)\exp[-i\Delta_{\mathrm{c}}(z)t] \tag{H.33}$$

which follows from Eq. (H.30).

The wave function of the signal photon in the absence of a stored Rydberg excitation

can be written as

$$|\psi_{\rm s}\left(t\right)\rangle = \int {\rm d}z\, E_{\rm s}(z,t)\hat{\mathcal{E}}^{\dagger}\left(z\right)|0\rangle + \int {\rm d}z\, P(z,t)\hat{\mathcal{P}}^{\dagger}\left(z\right)|0\rangle + \int {\rm d}z\, S(z,t)\hat{\mathcal{S}}^{\dagger}\left(z\right)|0\rangle\,. \tag{H.34}$$

The evolution equations for the respective amplitudes $E_{\rm s}(z,t) = \langle 0|\hat{\mathcal{E}}(z)|\psi_{\rm s}(t)\rangle$, $P(z,t) = \langle 0|\hat{\mathcal{P}}(z)|\psi(t)\rangle$, and $S(z,t) = \langle 0|\hat{\mathcal{S}}(z)|\psi(t)\rangle$ follows from Eqs. (H.27-H.29) and are given by

$$\begin{aligned}(\partial_t + c\partial_z)E_{\rm s}(z,t) &= -ig\sqrt{\rho(z)}P(z,t)\\ \partial_t P(z,t) &= -ig\sqrt{\rho(z)}E_{\rm s}(z,t) - i\Omega S(z,t) - \gamma P(z,t)\\ \partial_t S(z,t) &= -i\Omega P(z,t) - i[\Delta_{\rm s}(z) - i\gamma_{\rm s}]S(z,t)\,.\end{aligned} \tag{H.35}$$

These equations are solved numerically within a spatial range $-L \leq z \leq L$. Assuming that the signal photon initially ($t = 0$) resides outside of this region at $z < -L$ and taking $L \gg \sigma$ such that $\rho(\pm L) \approx 0$, the initial and boundary conditions are $E_{\rm s}(z,0) = P(z,0) = S(z,0) = 0$ and $E_{\rm s}(-L,t) = E_{\rm in}(t)$, where $E_{\rm in}(t)$ defines the temporal envelope of the incident signal pulse.

The two-body wavefunction is defined in Eq. (H.6). Its evolution is follows from substitution into Eqs. (H.27-H.30):

$$
\begin{aligned}
(\partial_t + c\partial_z)EC(z,z',t) =& -ig\sqrt{\rho(z)}PC(z,z',t) - i\Delta_c(z')EC(z,z',t) \\
\partial_t PC(z,z',t) =& -ig\sqrt{\rho(z)}EC(z,z',t) - i\Omega SC(z,z',t) - \gamma PC(z,z',t) \\
& - i\Delta_c(z')PC(z,z',t) \\
\partial_t SC(z,z',t) =& -i\Omega PC(z,z',t) - i[\Delta_s(z) - i\gamma_s]SC(z,z',t) \\
& - i\Delta_c(z')SC(z,z',t) - i\frac{C_3}{|z-z'|^3}SC\left(z',z,t\right). \qquad \text{(H.36)}
\end{aligned}
$$

The initial conditions for $-L \leq z, z' \leq L$ are $EC(z,z',t=0) = PC(z,z',t=0) = SC(z,z',t=0)$. Since the two-body amplitudes factorize for $z < -L$, we have the boundary condition $EC(-L,z',t) = E_{\text{in}}(t)C(z,t)$ where $C(z,t)$ is given by Eq. (H.33). The simultaneous numerical solution of Eqs.(H.33), (H.35) and (H.36), with the described initial and boundary conditions, thus yields completes knowledge about the two-body state Eq.(H.32).

A photodetector placed at $z = L$ then registers an outgoing signal photon at time t_s with a probability

$$
\langle \hat{\mathcal{E}}^\dagger(L,t_s)\hat{\mathcal{E}}(L,t_s)\rangle = \langle \Psi(t_s)|\hat{\mathcal{E}}^\dagger(L)\hat{\mathcal{E}}(L)|\Psi(t_s)\rangle \equiv \langle \tilde{\Psi}(t_s;t_s)|\tilde{\Psi}(t_s;t_s)\rangle, \qquad \text{(H.37)}
$$

where

$$
|\tilde{\Psi}(t_s;t_s)\rangle = E_s(L,t_s)|0\rangle + \int \mathrm{d}z EC(L,z,t_s)\hat{\mathcal{C}}^\dagger(z)|0\rangle. \qquad \text{(H.38)}
$$

The amplitude of the spin-wave component after signal-photon detection still picks up a phase due to the random level shift $\Delta_c(z)$, such that the state of the system at the end of the interaction stage ($t = T$) is given by

$$
|\tilde{\Psi}(T;t_s)\rangle = \epsilon_g(t_s)E_s(L,t_s)|0\rangle + \int \mathrm{d}z EC(L,z,t_s)\mathrm{e}^{-i\Delta_c(z)(T-t_s)}\hat{\mathcal{C}}^\dagger(z)|0\rangle. \qquad \text{(H.39)}
$$

H.3.3 Spinwave retrieval

Following the interaction stage, the stored $n'P$ spin wave is transferred back to an nS excitation and finally retrieved by turning the classical control field back on. The probability to detect the retrieved gate-photon at time $t_{\rm g}$ in the absence of a signal photon is given by $|E_{\rm g}(L,t_{\rm g})|^2$, where the amplitude is determined by the single-photon propagation equations

$$\begin{aligned}(\partial_t + c\partial_z)E_{\rm g}(z,t) &= -ig\sqrt{\rho(z)}P(z,t)\\ \partial_t P(z,t) &= -ig\sqrt{\rho(z)}E_{\rm g}(z,t) - i\Omega S(z,t) - \gamma P(z,t)\\ \partial_t S(z,t) &= -i\Omega P(z,t) - i[\Delta_{\rm s}(z) - i\gamma_{\rm s}]S(z,t)\ . \end{aligned} \tag{H.40}$$

subject to the initial $E_{\rm g}(-L,t) = P(-L,t) = S(-L,t) = 0$ and initial conditions $E_{\rm g}(z,T) = P(z,T) = 0$ and $S(z,T) = C(z,T)$, where $C(z,T)$ is given by Eq. (H.33).

Similarly, the amplitude of the retrieved photon after detection of a signal photon at time $t_{\rm s}$ is obtained from the evolution equations

$$\begin{aligned}(\partial_t + c\partial_z)E_2(z,t;t_{\rm s}) &= -ig\sqrt{\rho(z)}P(z,t;t_{\rm s})\\ \partial_t P(z,t;t_{\rm s}) &= -ig\sqrt{\rho(z)}E_2(z,t;t_{\rm s}) - i\Omega S(z,t;t_{\rm s}) - \gamma P(z,t;t_{\rm s})\\ \partial_t S(z,t;t_{\rm s}) &= -i\Omega P(z,t;t_{\rm s}) - i[\Delta_{\rm s}(z) - i\gamma_{\rm s}]S(z,t;t_{\rm s})\ . \end{aligned} \tag{H.41}$$

with the boundary conditions $E_2(-L,t;t_{\rm s}) = P(-L,t;t_{\rm s}) = S(-L,t;t_{\rm s}) = 0$ and initial conditions $E_2(z,T;t_{\rm s}) = P(z,T;t_{\rm s}) = 0$ and $S(z,T;t_{\rm s}) = EC(L,z,t_{\rm s})\mathrm{e}^{-i\Delta_{\rm c}(z)(T-t_{\rm s})}$ [see Eq. (H.39)]. For each signal photon detection time $t_{\rm s}$ we thus have to propagate the one-body dynamics of the gate photon to finally obtain the two-time amplitude

$$EE(t_{\rm s},t_{\rm g}) = E_2(L,t_{\rm g};t_{\rm s}) \tag{H.42}$$

for detecting both photons at times $t_\mathrm{s} < T$ and $t_\mathrm{g} > T$.

H.4 Obtaining observables from numerical simulations

In the following we describe how our observables presented in the main text are obtained from the two-time amplitude Eq. (H.42).

H.4.1 Conditioned signal photon transmission

It follows from the above discussion that the two-time correlation function

$$\langle \hat{\mathcal{E}}^\dagger(L,t_\mathrm{s})\hat{\mathcal{E}}^\dagger(L,t_\mathrm{g})\hat{\mathcal{E}}(L,t_\mathrm{g})\hat{\mathcal{E}}(L,t_\mathrm{s})\rangle = |EE(t_\mathrm{s},t_\mathrm{g})|^2 \tag{H.43}$$

is simply given by the joint probability Eq. (H.42). The signal photon transmission conditioned on detecting a gate photon is, thus, proportional to integral $\int \mathrm{d}t_\mathrm{s}\mathrm{d}t_\mathrm{g}|EE(t_\mathrm{s},t_\mathrm{g})|^2$. To calculate the relative transmission presented in the main text we have to compare this quantity to the equivalent result without interactions, for which $EE(t_\mathrm{s},t_\mathrm{g}) = E_\mathrm{s}(t_\mathrm{s})E_\mathrm{g}(t_\mathrm{g})$ [obtained from Eq. (H.35) and Eq. (H.40)], giving the conditioned relative transmission

$$T_c = \frac{\int \mathrm{d}t_\mathrm{s}\mathrm{d}t_\mathrm{g}|EE(t_\mathrm{s},t_\mathrm{g})|^2}{\int \mathrm{d}t_\mathrm{s}\mathrm{d}t_\mathrm{g}|E_\mathrm{s}(t_\mathrm{s})|^2|E_\mathrm{g}(t_\mathrm{g})|^2}, \tag{H.44}$$

shown in Fig. 3 of the main text. Similarly, we can calculate the outgoing pulse shape of the signal photon

$$I_\mathrm{s}(t) = \int \mathrm{d}t_\mathrm{g}|EE(t,t_\mathrm{g})|^2, \tag{H.45}$$

and the gate photon

$$I_\mathrm{g}(t) = \int \mathrm{d}t_\mathrm{s}|EE(t_\mathrm{s},t)|^2. \tag{H.46}$$

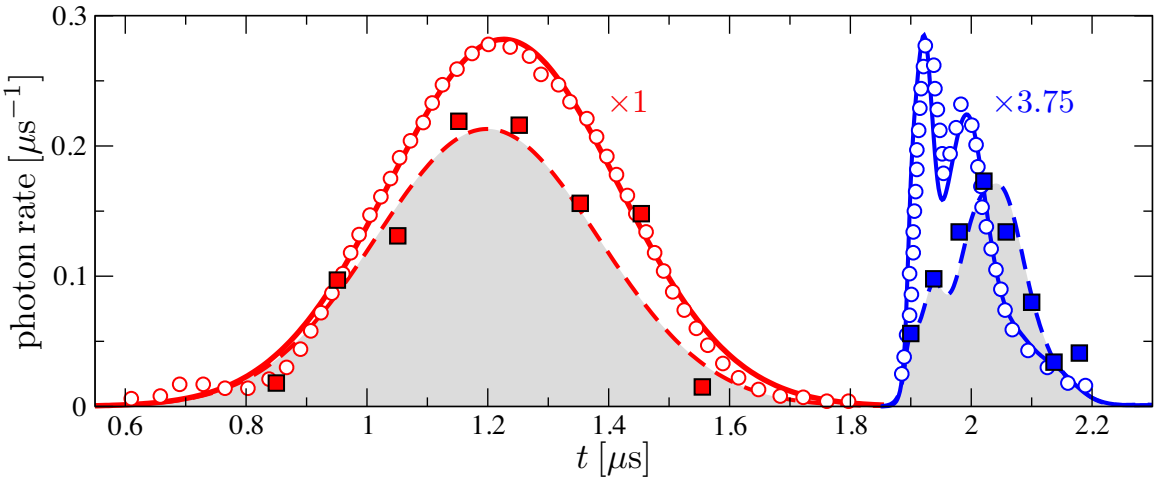

Figure H.7: Photon count rates of the signal photon (red) and retrieved gate photon (blue), measured in the presence (squares) and in the absence (circles) of dipolar excitation exchange. The experimental count rates are compared to the simulated pulse envelopes with (dashed lines, grey area) and without (solid lines) interactions. Each set of red and blue curves has been scaled by a single common factor in order to convert from the theoretical pulse envelopes to the observed count rates.

The comparison to our measured photon pulses in Fig. H.7 demonstrates that the simulations even reproduce such more sensitive observables remarkably well.

H.4.2 Acquired phase of the signal photon

In order to obtain the phase of the transmitted signal photon we superimpose the output by a reference field that does not interact with the medium, as described in the Methods. Taking the reference field to be a weak coherent pulse with a mode function $E_{\mathrm{ref}}(z,t)$, its quantum state can again be approximated by

$$|\psi_{\mathrm{ref}}(t)\rangle \approx |0\rangle + \int \mathrm{d}z E_{\mathrm{ref}}(z,t)\mathcal{E}^{\dagger}(z)|0\rangle. \tag{H.47}$$

Since all involved photon pulses are weak coherent fields, we can moreover discard any three-body contributions to the combined state $|\Psi_3(t)\rangle = |\Psi(t)\rangle|\psi_{\mathrm{ref}}(t)\rangle$, with $|\Psi(t)\rangle$ given

by Eq. (H.32). Upon detection of a signal photon at time t_s we thus get

$$\begin{aligned}\hat{\mathcal{E}}(L)|\Psi_3(t_\mathrm{s})\rangle =& \left[E_\mathrm{s}(L,t_\mathrm{s}) + E_\mathrm{ref}(L,t_\mathrm{s})\right]|0\rangle + \int \mathrm{d}z E_\mathrm{ref}(z,t_\mathrm{s})E_\mathrm{s}(L,t_\mathrm{s})\mathcal{E}^\dagger(z)|0\rangle \\ &+ \int \mathrm{d}z E_\mathrm{ref}(L,t_\mathrm{s})\left[C(z,t_\mathrm{s})\hat{\mathcal{C}}^\dagger(z) + P(z,t_\mathrm{s})\hat{\mathcal{P}}^\dagger(z) + S(z,t_\mathrm{s})\hat{\mathcal{S}}^\dagger(z)\right]|0\rangle \\ &+ \int \mathrm{d}z E_\mathrm{ref}(L,t_\mathrm{s})E_\mathrm{s}(z,t_\mathrm{s})\hat{\mathcal{E}}^\dagger(z)|0\rangle + \int \mathrm{d}z EC(L,z,t_\mathrm{s})\hat{\mathcal{C}}^\dagger(z)|0\rangle\end{aligned} \tag{H.48}$$

Taking this to be the initial state $|\bar{\Psi}_3(t=t_\mathrm{s};t_\mathrm{s})\rangle = \hat{\mathcal{E}}(L)|\Psi_3(t_\mathrm{s})\rangle$ for the description of the subsequent spin wave retrieval as described in section H.3.3, we obtain after detection of a photon at time t_g

$$\begin{aligned}\hat{\mathcal{E}}(L)|\bar{\Psi}_3(t_\mathrm{g};t_\mathrm{s})\rangle =& E_\mathrm{ref}(L,t_\mathrm{g})E_\mathrm{s}(L,t_\mathrm{s})|0\rangle + E_\mathrm{ref}(L,t_\mathrm{s})E_\mathrm{s}(L,t_\mathrm{g})|0\rangle \\ &+ E_\mathrm{ref}(L,t_\mathrm{s})E_\mathrm{g}(L,t_\mathrm{g})|0\rangle + EE(t_\mathrm{s},t_\mathrm{g})|0\rangle\end{aligned} \tag{H.49}$$

Noting that $E_\mathrm{ref}(L,t)$ and $E_\mathrm{s}(L,t)$ both vanish for $t = t_\mathrm{g} > T$, i.e. during the gate field detection window, we can drop the first line and obtain for the conditioned photon detection probability

$$\begin{aligned}\int_T^\infty \mathrm{d}t_\mathrm{g}\langle\hat{\mathcal{E}}^\dagger(L,t_\mathrm{s})\hat{\mathcal{E}}^\dagger(L,t_\mathrm{g})\hat{\mathcal{E}}(L,t_\mathrm{g})\hat{\mathcal{E}}(L,t_\mathrm{s})\rangle =& |E_\mathrm{ref}(L,t_\mathrm{s})|^2|E_\mathrm{g}(L,t_\mathrm{g})|^2 + |EE(t_\mathrm{s},t_\mathrm{g})|^2 \\ &+ 2\mathrm{Re}\left[E^*_\mathrm{ref}(L,t_\mathrm{s})E^*_\mathrm{g}(L,t_\mathrm{g})EE(t_\mathrm{s},t_\mathrm{g})\right].\end{aligned} \tag{H.50}$$

The relative phase between the signal and reference field can be read off directly from the last line. Taking the reference field amplitude to be real this phase is given by

$$\varphi(t_\mathrm{s}) = \arctan\left\{\frac{\mathrm{Im}\left[\int_T^\infty \mathrm{d}t_\mathrm{g}E^*_\mathrm{g}(L,t_\mathrm{g})EE(t_\mathrm{s},t_\mathrm{g})\right]}{\mathrm{Re}\left[\int_T^\infty \mathrm{d}t_\mathrm{g}E^*_\mathrm{g}(L,t_\mathrm{g})EE(t_\mathrm{s},t_\mathrm{g})\right]}\right\}. \tag{H.51}$$

Even in the absence of interactions, for which $EE(t_{\rm s},t_{\rm g}) = E_{\rm s}(L,t_{\rm s})E_{\rm g}(L,t_{\rm g})$, one will detect a density-dependent phase

$$\varphi_0(t_{\rm s}) = \arctan\left\{\frac{{\rm Im}E_{\rm s}(t_{\rm s})}{{\rm Re}E_{\rm s}(t_{\rm s})}\right\}. \tag{H.52}$$

which is predominantly due to the random level shifts $\Delta_{\rm s}(z)$ in Eq. (H.35). Since this phase is taken as a reference in our experiments, the calculated phase

$$\phi_{\rm c} = \int {\rm d}t[\varphi(t) - \varphi_0(t)]I_{\rm s}(t), \tag{H.53}$$

shown in Fig. 3 of the main text, is obtained by averaging the phase difference over the conditioned transmitted signal intensity given in Eq. (H.45).

H.5 Spin wave dephasing due to Rydberg-ground state atom interactions

Here we describe how we account for interactions between Rydberg and ground state atoms through the random energy shifts $\Delta_{\rm c}(z)$ and $\Delta_{\rm s}(z)$. Such interactions arise when a ground state atom is found within the electronic orbit of the Rydberg atom, and perturbs the electronic wave function of the Rydberg state through a low-energy electron-atom collision [354, 355]. The collisional electron interaction, $\hat{U}_{\rm e-a}(\mathbf{R})$, with an atom at a position $\mathbf{R}$ away from the ionic core of the Rydberg atom then couples different Rydberg states $|\alpha\rangle$, $|\beta\rangle$ (with amplitudes $\psi_{\alpha,\beta}$) with a matrix element

$$\langle\beta|\hat{U}_{\rm e-a}(\mathbf{R})|\alpha\rangle = 2\pi A_{\rm s}\psi^*_\beta(\mathbf{R})\psi_\alpha(\mathbf{R}) + 6\pi A_{\rm p}^3\left[\nabla\psi^*_\beta(\mathbf{R})\right]\cdot\left[\nabla\psi_\alpha(\mathbf{R})\right]. \tag{H.54}$$

This can be well described via a zero-range pseudopotential [354] with energy-dependent s-wave and p-wave scattering lengths, $A_{\rm s}$ and $A_{\rm p}$, respectively, whereby the electron en-

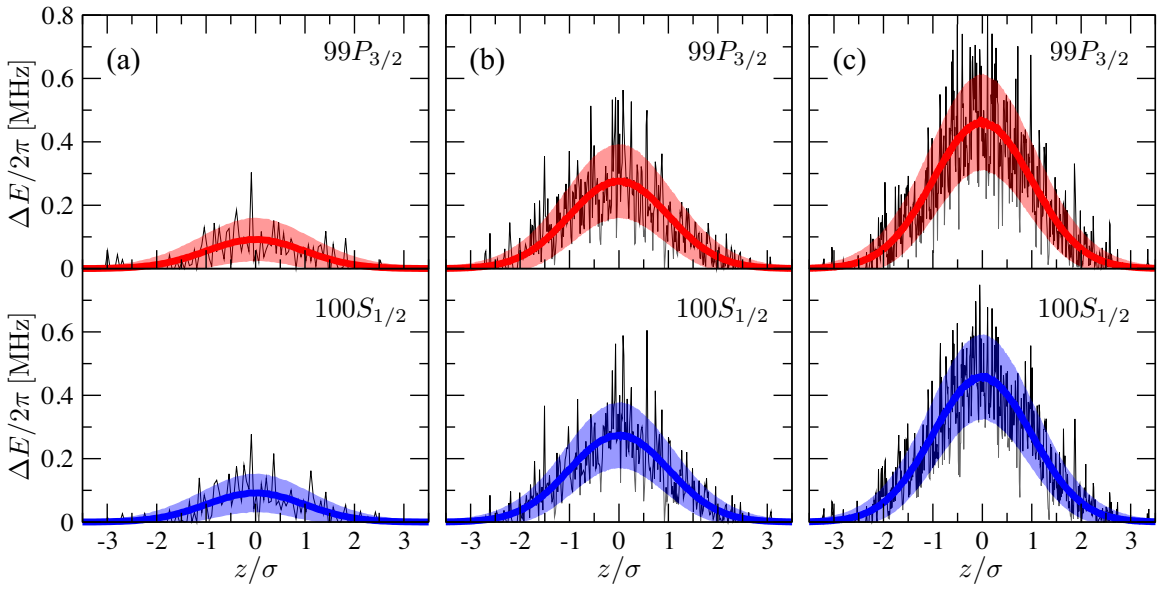

Figure H.8: Spatially fluctuating energy shifts due to interactions between Rydberg and ground-state atoms for the two relevant Rydberg states $|100S_{1/2}\rangle$ (blue) and $|99P_{3/2}\rangle$ (red) for the cloud geometry of our experiments and three different peak densities corresponding to $OD = 10$ (a), $OD = 30$ (b) and $OD = 50$ (c). The thick solid line shows the average level shift and the shaded area indicates the standard deviation of the ensemble. The individual Monte Carlo results shown by the thin black lines illustrate the strong spatial fluctuations in all cases.

ergy can be semiclassically related to the scattering center $\mathbf{R}$ [355, 356]. The shifted energy spectrum of the Rydberg atom can then be obtained by diagonalizing the underlying Hamiltonian $E_\alpha^{(0)}\delta_{\alpha,\beta} + \langle\beta|\hat{U}_{\mathrm{e-a}}(\mathbf{R})|\alpha\rangle$, where $E_\alpha^{(0)}$ is the unperturbed binding energy of the Rydberg atom in a given state $|\alpha\rangle$.

In the present situation, multiple ground state atoms may simultaneously shift a Rydberg state in the dense atomic cloud. The energy levels, $E_\alpha(\mathbf{R}_1, ..., \mathbf{R}_N)$, collectively perturbed by N atoms at positions $\mathbf{R}_i$ $(i = 1, ..., N)$ relative to the Rydberg atom core can still be straightforwardly obtained by diagonalizing the matrix $E_\alpha^{(0)}\delta_{\alpha,\beta} + \sum_{i=1}^{N}\langle\beta|\hat{U}_{\mathrm{e-a}}(\mathbf{R}_i)|\alpha\rangle$.

To calculate the resulting level shift of a delocalized Rydberg state spin wave, we randomly sample atomic positions, $\mathbf{r}_i$, according to our density distribution $\rho(z)$ within a

cylindrical volume along the light propagation axis, $\mathbf{e}_z$, assuming a constant density in the transverse direction. The spatially fluctuating energy shift $\Delta E_\alpha(z) = E_\alpha(\mathbf{r}_1 - \mathbf{e}_z z, \mathbf{r}_2 - \mathbf{e}_z z, , ...) - E_\alpha^{(0)}$ can then be calculated on the z-axis along which we solve the field propagation equations, as described in section H.3. As shown in Fig. H.8, the mean level shift follows the atomic density [357], while the spatial fluctuations for a given random configuration are comparable to the actual average shift.

For the actual calculations we repeatedly simulate the two-photon dynamics as outlined in section H.3 for a given random realization of $\Delta E_\alpha(z)$, and average the final observable over the Monte Carlo ensemble. Specifically, the conditioned transmission and the phase shown in Fig. 3 of the main text are determined as

$$T_c = \frac{\left\langle \int \mathrm{d}t_\mathrm{s}\mathrm{d}t_\mathrm{g} |EE(t_\mathrm{s}, t_\mathrm{g})|^2 \right\rangle}{\left\langle \int \mathrm{d}t_\mathrm{s}\mathrm{d}t_\mathrm{g} |E_\mathrm{s}(t_\mathrm{s})|^2 |E_\mathrm{g}(t_\mathrm{g})|^2 \right\rangle}, \tag{H.55}$$

and

$$\phi_c = \left\langle \int \mathrm{d}t [\varphi(t) - \varphi_0(t)] I_\mathrm{s}(t) \right\rangle, \tag{H.56}$$

respectively, where $\langle ... \rangle$ denotes the Monte Carlo average over the ensemble of random atom configurations. Note that the shaded areas in Fig. 3 of the main text does not reflect the statistical error of the calculated average (which is small for the 10^4 configurations used in the calculation) but indicates the extent of the classical fluctuations of T_c and ϕ_c resulting from the randomly distributed atoms in the cold gas.

In our experiments we adjust the two-photon detuning to the transmission maximum of the EIT medium in the absence of the gate spin wave. Therefore, we first calculate the average transmission spectrum to determine the frequency shift, Δ_T, induced by Rydberg-ground state atom interactions for a given optical depth OD of the medium. The detunings

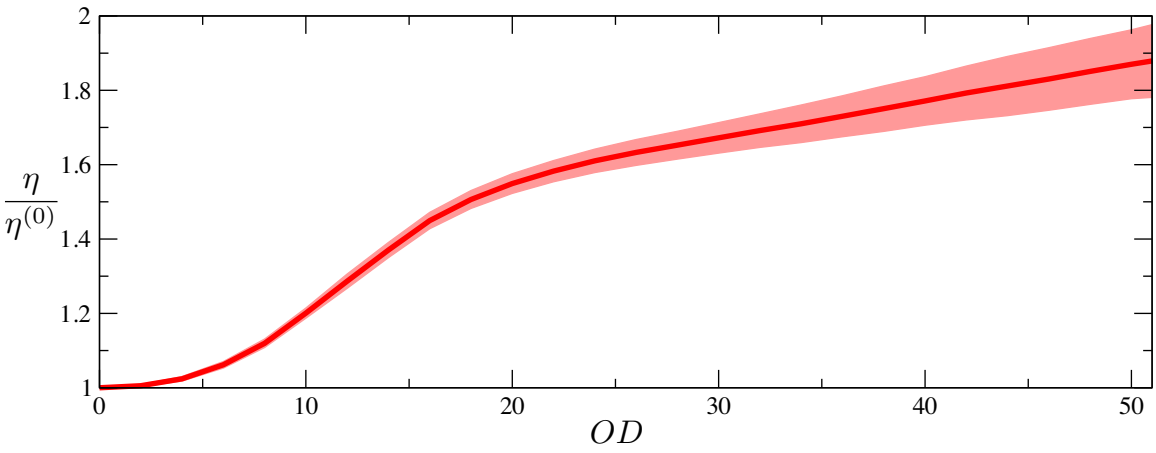

Figure H.9: The suppression, η, of the two-photon transmission by Rydberg-ground state atom interactions is significantly reduced by dipolar photon-spin wave hopping relative to the case of no interactions ($\eta^{(0)}$). The ratio $\eta/\eta^{(0)}$ is shown as function of OD, and for parameters of our experiments as used in Fig. 3 of the main text.

$\Delta_{\rm s}$ and $\Delta_{\rm c}$ of Eqs.(H.29) and (H.30) are then obtained from

$$\Delta_\alpha(z) = \Delta E_\alpha(z) - \Delta_{\rm T} \tag{H.57}$$

for the $|100S_{1/2}\rangle$ ($\alpha = {\rm s}$) and the $|99P_{3/2}\rangle$ ($\alpha = {\rm c}$) Rydberg states.

The Monte Carlo simulations also permit the role of Rydberg-ground state dephasing to be separated from other loss mechanisms. To this end we have simulated the photon propagation with and without the random level shifts $\Delta_{\rm s}$ and $\Delta_{\rm c}$ and calculated the reduction η of the two-photon transmission. The ratio $\eta/\eta^{(0)}$ of this reduction with (η) and without ($\eta^{(0)}$) dipolar excitation exchange (see Fig. H.9), shows that the interaction significantly improves the performance of our protocol due to a motional averaging effect arising from the exchange-driven spin wave hopping. This effect improves the transmission by nearly a factor of two at the highest densities. Lastly, the simulations allow the effect of the mean shift (which follows the atomic cloud shape) to be separated from the fluctuating component of the shift which results from random atomic positions. At the highest densities used

in the experiment, the mean shift contributes approximately half of the total dephasing of the retrieval, with the rest coming from "atomic shot noise". While the mean shift does not change with the principal quantum number of the Rydberg level [357], the shot noise contribution decreases as n increases, since more ground state atoms participate and the fluctuations in their positions become less important.

H.6 Methods

H.6.1 Experimental procedure

The $^{87}\mathrm{Rb}$ atoms used for this experiment are cooled in a 3D magneto-optical trap (MOT) and loaded into a $1064\,\mathrm{nm}$ crossed optical dipole trap made with two horizontal beams crossed at a 32° angle [287, 257]. Each beam has a power of 8 W and a 50 $\mu\mathrm{m}$ waist, resulting in a cigar-shaped density profile with a 4:1 trap aspect ratio. After loading into the dipole trap, the gas is cooled to 20 $\mu\mathrm{K}$ using degenerate Raman sideband cooling in a near-detuned lattice. The peak atomic density at the highest optical depth is approximately $\rho = 1.9 \times 10^{12}$ cm^{-3}, which corresponds to a resonant absorption length of 1.8 μm for the probe field. Cooling and loading last for 300 ms, and then 1000 measurements are performed with a repetition period of 38 μs before preparing a new sample. The dipole trap is switched off during each measurement (for 7 μs) to avoid AC Stark shifts of the Rydberg levels. The gas is probed along the long axis of the cloud, as shown in Fig. 1.

The probe and control lasers are stabilized to a common cavity, and have a short-term linewidth of approximately $2\pi \times 100$ kHz. The 3.72 GHz microwave field driving $100S_{1/2}$ to $99P_{3/2}$ is delivered by an antenna outside the vacuum chamber. For measurements in-

volving other Rydberg states (Fig 3 insets), the microwave field drives a two-photon transition from $100S_{1/2}$ to $99S_{1/2}$ (at 3.67 GHz microwave frequency) or to $97S_{1/2}$ (at 11.4 GHz).

H.6.2 Phase-shift measurements

Phase-shift measurements are performed by interfering the transmitted probe field $\mathcal{E}$ with a weak local oscillator (LO) beam, which is detuned by -158 MHz from the probe. The LO is delivered to the experiment through the same fiber as the probe, and has a similar intensity. This detuning and power ensure that the LO does not interact with the Rydberg levels, so any phase shift in the probe-LO beatnote arises from phase shifts in the probe field. The LO has a square pulse shape and is switched on at the same time as the signal pulse. The probe-LO beat signal is delivered to single-photon counting modules, and the beat amplitude and phase are extracted from the timing of photon detection events. A slight non-uniformity of the phase across the pulse (visible in the light points in Fig. 2D) appears to result from rate-dependent timing delays in the detectors. Zero phase in Fig. 2D is defined by a control experiment without interactions, achieved by setting $n_g^{in} = 0$. This phase is slightly different from the phase measured without any atoms present, and results from the effects of atomic dispersion on the far-detuned LO, as well as small phase shifts on the probe arising from a minority of atoms not prepared in $|F = 2, m_F = 2\rangle$. Lastly, because of the negative detuning of the LO, the positive phase shift of the beatnote that is shown in Fig. 2D/3B actually corresponds to a phase *lag* of the probe, in agreement with the negative phase shift predicted by the solution to Eq. (1) for $C_3 > 0$.

	$\tilde{\eta}_s$	$\tilde{\eta}_g$	$\tilde{\eta}_2$	η_I	η_2
current	0.56	0.06	*0.034*	0.8	**0.027**
improved	0.99	0.93	*0.92*	0.95	**0.88**

Table H.1: Summary of efficiency measurements. The single-photon transmission probabilities for the signal and gate fields, in the absence of interactions, are $\tilde{\eta}_s$ and $\tilde{\eta}_g$, respectively. The probability that two incident photons would both be transmitted in absence of interactions is $\tilde{\eta}_2 = \tilde{\eta}_s\tilde{\eta}_g$. Interactions result in an additional loss captured by η_I, such that the probability for two photons to be transmitted with a phase shift is $\eta_2 = \tilde{\eta}_s\tilde{\eta}_g\eta_I$. η_I was measured using the signal (gate) field to be 0.77 (0.82); here, we take the average value 0.80.

H.6.3 Photon loss

The losses in the experiment are largely technical in origin and can be reduced through several straightforward improvements. The losses are summarized in Table H.1, and the possible improvements are discussed below.

The linear (non-interacting) signal transmission $\tilde{\eta}_s = 0.56$ is limited primarily by laser linewidth and imperfect optical pumping of atoms to the $|2, 2\rangle$ state (atoms in other states will not experience EIT resonance at the same laser frequency). It should be possible to improve $\tilde{\eta}_s$ to nearly 1 by reducing the laser linewidth further and improving the optical pumping or applying a larger magnetic field to shift the absorption profiles of other ground states away from the probe laser frequency. Other dephasing effects, such as Doppler broadening and collisions between ground state atoms and Rydberg atoms (section H.5) are slowly varying and produce a transmission decay that is Gaussian as a function of the time the photon spends in the cloud. For the signal photon, which is not stored, we estimate the impact of these effects on $\tilde{\eta}_s$ be less than 0.01 during the 180 ns transit time of the signal photon.

The linear (non-interacting) storage and retrieval efficiency is currently $\tilde{\eta}_g = 0.06$.

Separate measurements show that the storage and retrieval efficiency with only 100 ns storage time is 0.4, which then decreases to 0.06 at the 1.5 μs storage time needed to complete the interaction sequence. The storage and retrieval efficiency at short times is limited by the same effects as the signal transmission, as well as the finite optical depth: in Ref. [358] it is shown that the achievable storage and retrieval efficiency scales as $1 - 5.8/OD$ using optimized pulses and backwards retrieval. Therefore, this number could be improved to 0.84 with our current OD, and to 0.95 with OD doubled to 100.

The impact of the long storage time is more significant. The decrease in retrieval efficiency comes from dephasing of the stored spin wave, with contributions from Doppler broadening and collisions between ground state atoms and Rydberg atoms, as discussed in section H.5. Doppler broadening can be significantly reduced by going to lower temperatures. The collisional dephasing contains two contributions: random atomic positions (atomic shot noise) within the Rydberg orbit, as well as non-uniform density envelope across the cloud. The latter can be improved using a flat-bottom optical potential (as discussed in [260]), while the atomic shot noise can be improved by moving to higher principal quantum number, which has the effect of increasing the number of ground state atoms involved but decreasing the contribution from each individual atom [357], reducing the shot noise as n^{-3}, where n is the principal quantum number. To make the (Gaussian) Doppler and collisional dephasing decays less than 2% each during the storage time of 1.5 us, we need to improve the temperature by a factor of 5, and the impact of the collisional dephasing by a factor of 10. I the latter case, a factor of two can be obtained from the flat-bottom potential, with the remaining factor of 5 coming from an increase in the principal quantum number to $n = 170$. Even with these changes, we will remain far from the regime where

inelastic collisions with ground state atoms will play a role on the relevant timescales [359]. Together, these improvements can yield a storage and retrieval efficiency of about 0.93.

The additional losses resulting from the interaction process are shown in Eq. H.19 to scale as $\eta_I = 1 - 3\sqrt{2\pi}OD_b^{-3/2}$, depending only on OD_b. To reach $\eta_I = 0.95$, we will require $OD_b = 30$. OD_b increases with $n^{4/3}$, so increasing the quantum number to 170 together with increasing the atomic density by a factor of 2.5 (through additional cooling or larger total atom number) will achieve the desired result. Reducing the control Rabi frequency Ω_c during the signal pulse will allow OD_b to be further increased, at the expense of increasing the required storage time—there is an optimum value.

Taken together, it seems realistic to achieve combined linear transmission for the signal and gate photon of 0.99 and 0.93, and nonlinear losses of 0.95. This would result in a total transmission probability for two interacting photons of 0.88. Given that the dominant error in the interaction process is photon loss and not error in the phase shift, and that photon loss can be heralded by the absence of transmitted photons, we expect that higher-fidelity operations can be probabilistically achieved.

H.6.4 Two-mode measurements

For the measurements in Fig. 4 with two optical modes, two independently-aligned beams (modes A, B) are nearly overlapped on a beamsplitter before entering the chamber. Their separation (5.4 μm) is measured using a CCD camera that images the focal plane in the center of the atomic cloud. The output light is directed to two single-mode fibers by a beamsplitter. One of the fibers is aligned to each mode, allowing them to be separately detected by independent photodetectors. There is a small amount of crosstalk resulting

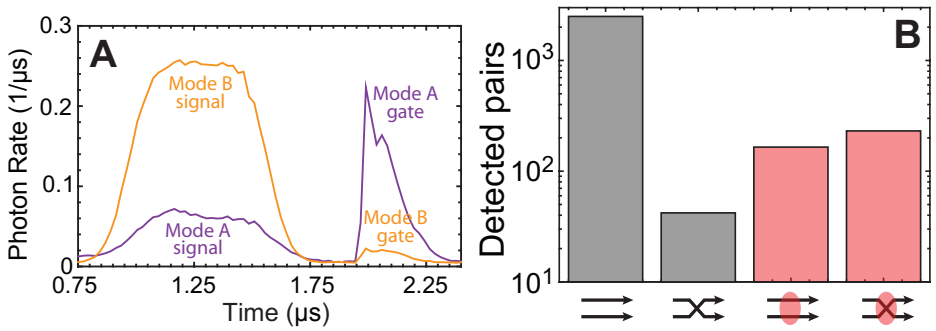

Figure H.10: A) Pulse shapes measured by the detectors shown in Fig. 4A of the main text. The full data record is averaged to produce these curves. B) Photon pair detection events. The parallel (crossed) arrows denote the number of signal and gate pairs detected in their incident (swapped) modes. The left two bars show the result of the alternate pulse sequence without interactions, while the right two bars show the result of the pulse sequence in panel A, where interactions are expected to be present. From left to right, the y-axis values are 2499, 42, 165, and 231.

from imperfect fiber alignment and finite separation between the modes (about 10% of the light detected in the mode A photon counter is actually from mode B, and vice-versa).

H.6.5 Pair detection events in separated optical mode measurements

Here, we describe additional measurements used to estimate the probability of photons hopping between spatially separated modes as described in Fig. 4 of the main text. This measurement involves alternating between the pulse sequence shown in Fig H.10A and another sequence where the signal pulse is sent after the gate pulse is retrieved. In the latter sequence, the signal and gate fields experience the same loss, but do not interact with each other as they are never present in the cloud at the same time. The difference between these measurements allows the influence of interactions to be isolated.

Fig H.10A shows the measured pulse shapes at each detector (Fig. 4A). As in the main text, the gate (signal) pulse is incident in mode A (B). The majority of the light in the

"wrong" detector (e.g., signal light in detector A) results from a slight mixing of the modes at the detectors (approximately 10%), since the modes are not perfectly orthogonal. To see the role of interactions above this background, we look at photon pair events as shown in Fig. H.10B. Without interactions, approximately 1.7(3)% of all transmitted pairs are in "swapped" modes. With interactions, 58(2)% of pairs exit in swapped modes, although the overall transmission is much lower. In analogy with T_c defined in Fig. 3 of the main text, we isolate the role of interactions over single-particle loss by computing the ratio of the number of pairs exiting in swapped modes (with interactions) to the total number of transmitted pairs in the absence of interactions. This yields 8.3(5)%, which we take as an estimate of the probability for a photon pair to switch modes as a result of the interaction.

This value is significantly lower than $T_c = 0.77$ reported in Fig. 3 for photons in the same mode. We attribute this to increased separation between the photons, as well as losses resulting from multiple signal and gate photons being present during the same pulse, since this measurement was performed with $\langle n_g^{in} \rangle \approx \langle n_s^{in} \rangle \approx 1$.

H.6.6 Influence and strength of the second pole

In the following, we estimate the relevance of the second pole in Eq. 10.28 in the main text, characterized by α_{B} and $\bar{\omega}_{\mathrm{B}}$, which gives rise to the resonant scattering into a different outgoing channel. First, we concentrate on the low momentum and energy regime. The analytical expressions for α and $\bar{\omega}$ describing the first pole are given by Eq. 10.23 in the main text. In turn, the parameters for the second pole derived by the diagrammatic method

take the form

$$\alpha_{\mathrm{B}} = -\frac{(\omega - cK)^2\Omega^6}{4\Delta^2(g^2+\Omega^2)^3}, \tag{H.58}$$

$$\bar{\omega}_{\mathrm{B}} = \frac{4\Omega^2 g^4}{(g^2+\Omega^2)^3}\frac{\Delta^2}{\omega - cK}. \tag{H.59}$$

Note that the weight α_{B} of the pole vanishes quadratically in the low energy $|\omega| \ll \omega_c$ and momentum $|K| \ll q_c$ limit, and can therefore be safely dropped.

Next, we analyse the influence of the second pole in the regime of far-detuned Rydberg polaritons with $|\omega|, \Omega \ll |\Delta|, g$. The diagrammatic approach provides the analytic expressions

$$\begin{aligned} \alpha_{\mathrm{B}} &= -\frac{\Omega^6(1+\frac{cK}{2\Delta})(\omega - cK)^2}{4\Delta^2(g^2+\Omega^2)^3\left(1-\frac{cK\Delta}{2g^2}\right)^2}, \\ \bar{\omega}_{\mathrm{B}} &= -\left(1+\frac{cK}{2\Delta}\right)^2\left(1-\frac{cK\Delta}{2g^2}\right)\frac{4\Omega^2 g^4}{(g^2+\Omega^2)^3}\frac{\Delta^2}{cK-\omega}. \end{aligned} \tag{H.60}$$

We find that, in the regime $cK\delta/2g^2 < 1$, the dimensionless parameters $\zeta(K,\omega)$ is strongly suppressed by the factor $(\Omega/\Delta)^6$. However, it is important to stress that the strength of the second pole diverges in a narrow parameter regime around $cK\delta/2g^2 \approx 1$.

H.6.7 Adiabatic elimination

In the following, we compare our diagrammatic approach with the previously successfully-applied study of the two-particle equation for the wave function in the regime $\omega = 0$, where the p-level has sometimes been adiabatically eliminated [285, 287, 257]. Furthermore, we present the natural extension of adiabatic elimination for finite frequencies. Then, the two-particle wave function contains four components: ψ_{ee} describes the amplitude for two photons, ψ_{ss} the amplitude for two Rydberg atoms, and $\psi_{es\pm}$ the amplitude for one photon and

one Rydberg atom with even (odd) symmetry. The Schrödinger equation reduces to (see Refs. [285, 287, 257] for more details)

$$\omega\psi_{ee} = -ic\partial_R\psi_{ee} - \frac{2g^2}{\Delta}\psi_{ee} - \frac{2g\Omega}{\Delta}\psi_{es+}, \tag{H.61}$$

$$\omega\psi_{es+} = -\frac{ic}{2}\partial_R\psi_{es+} - ic\partial_r\psi_{es-} - \frac{g^2+\Omega^2}{\Delta}\psi_{es+} - \frac{g\Omega}{\Delta}\left(\psi_{ee}+\psi_{ss}\right), \tag{H.62}$$

$$\omega\psi_{es-} = -\frac{ic}{2}\partial_R\psi_{es-} - ic\partial_r\psi_{es+} - \frac{g^2+\Omega^2}{\Delta}\psi_{es-}, \tag{H.63}$$

$$\omega\psi_{ss} = -\frac{2\Omega^2}{\Delta}\psi_{ss} - \frac{2g\Omega}{\Delta}\psi_{es+} + \frac{V(r)}{\hbar}\psi_{ss}, \tag{H.64}$$

where r denotes the relative coordinate and R the center-of-mass coordinate. For the translational invariant system, the latter coordinate is expressed in Fourier space with K the total momentum. We can solve the first, third and fourth equations for ψ_{ee}, ψ_{es-}, and ψ_{ss}, respectively, Inserting these expressions into Eq. (H.62), we obtain a single differential equation involving only the wave function ψ_{es+},

$$\hbar\bar{\omega}\psi_{es+} = -\frac{\hbar^2}{m}\partial_r^2\psi_{es+} + \alpha V_{\text{eff}}(r)\psi_{es+}. \tag{H.65}$$

This equation takes exactly the form of Eq. (10.21) in the main text with the identification $\psi_{es+} \sim \psi$. The expressions for α and $\bar{\omega}$ within the adiabatic elimination reduce to

$$\frac{\alpha m}{\hbar^2} = \frac{g^2\Omega^2}{c^2\hbar\Delta^2}\frac{2(\omega+\frac{g^2+\Omega^2}{\Delta}) - cK}{\left(\omega+2\frac{\Omega^2}{\Delta}\right)^2}, \tag{H.66}$$

$$\bar{\chi} = \frac{1}{\hbar}\frac{1}{\omega+2\Omega^2/\Delta},$$

$$\frac{\bar{\omega}m}{\hbar} = \left[cK - 2(\omega+\frac{\Omega^2+g^2}{\Delta})\right]^2 \times\frac{2\omega\frac{\Omega^2+g^2}{\Delta} + \omega(\omega-cK) - \frac{2\Omega^2}{\Delta}cK}{4c^2\left(\omega+\frac{2\Omega^2}{\Delta}\right)\left(\omega-cK+\frac{2g^2}{\Delta}\right)}. \tag{H.67}$$

These expressions fully agree with the result derived within the diagrammatic approach in the limit of large detuning $\Omega \ll |\Delta|$ and energies $|\omega| \ll |\Delta|$. In the physically interesting situation of Rydberg polaritons with $g \gtrsim |\Delta|$, we finally obtain the expressions (10.25) and (10.26) in the main text.

Appendix I

Supporting Material of Chapter 11

I.1 2D cluster state representation

In this section we prove that $|\psi_{\mathcal{C}_{2D}}\rangle$ in Eq. (3) of the main text represents the 2D cluster state. To this end we start first with the representation of a the 1D cluster state on $K+1$ qubits:

$$|\psi_{\mathcal{C}_{1D}}\rangle = \prod_{k=1}^{K} Z_{k,k+1} \, |+\rangle^{\otimes K+1} \, . \tag{I.1}$$

Using the swap operator $S_{i,j}$ that exchanges the quantum states of qubits i and j we can rewrite the 1D cluster state as

$$|\psi_{\mathcal{C}_{1D}}\rangle = \left(\prod_{k=1}^{K} S_{\mathcal{Q},k} Z_{\mathcal{Q},k} \right) |+\rangle_{\mathcal{Q}} \bigotimes_{k=1}^{K} |+\rangle_k \tag{I.2}$$

where we used the relation $Z_{b,c} = S_{a,b} Z_{a,c} S_{a,b}$, and identified the $K+1$th qubit with the ancilla $\mathcal{Q}$. Note that throughout this paper we use a convention where the ordering in the product is defined via $\prod_{j=1}^{k} M_j = M_k M_{k-1} \ldots M_1$. We now use the relation

$$S_{\mathcal{Q},v} Z_{\mathcal{Q},v} \, |\psi\rangle_{\mathcal{Q}} \otimes |+\rangle_v = H_{\mathcal{Q}} X_{\mathcal{Q},v} H_v \, |\psi\rangle_{\mathcal{Q}} \otimes |+\rangle_v \, , \tag{I.3}$$

where H_x is the Hadamard gate acting on qubit x. We note that this equality is not an operator identity but a property of states of the form $|\psi\rangle_{\mathcal{Q}} \otimes |+\rangle_v$, where the qubit v must be in the state $|+\rangle_v$ while the ancillary system $|\psi\rangle_{\mathcal{Q}}$ may be in an arbitrary state, potentially entangled to other systems. Using these relations, our state can be written as

$$|\psi_{\mathcal{C}_{1D}}\rangle = \left(\prod_{k=1}^{K} H_{\mathcal{Q}} X_{\mathcal{Q},k}\right) |+\rangle_{\mathcal{Q}} \bigotimes_{k=1}^{K} |0\rangle_k \,. \tag{I.4}$$

We note that this representation of the 1D cluster state has been also used in Ref. [328].

We now proceed to the construction of the 2D cluster state. From its definition, the 2D cluster state can be obtained from the 1D cluster state above by introducing additional entanglement (via phase gates) between qubits k and $k+N$ [334]. This gives a 2D cluster state on a square lattice with shifted periodic boundary conditions, where the extend of the (shifted) periodic direction is set by N.

$$\begin{aligned} |\psi_{\mathcal{C}_{2D}}\rangle &= \left(\prod_{k=N+1}^{K} Z_{k,k-N}\right)\left(\prod_{k=1}^{K} H_{\mathcal{Q}} X_{\mathcal{Q},k}\right) |+\rangle_{\mathcal{Q}} \bigotimes_{k} |0\rangle_k \\ &= \left(\prod_{k=1}^{K} H_{\mathcal{Q}} Z_{k,k-N} X_{\mathcal{Q},k}\right) |+\rangle_{\mathcal{Q}} \bigotimes_{k} |0\rangle_k \,. \end{aligned} \tag{I.5}$$

In the second line we used the fact the $[Z_{j,j+N}, X_{\mathcal{Q},k}] = 0$ for $j > k$, and $Z_{k,j}|0\rangle_j = \mathbb{1}_k \otimes \mathbb{1}_j |0\rangle_j$. Now we make use of the identity

$$Z_{n,m} X_{\mathcal{Q},n} |\psi\rangle_{\mathcal{Q},m} |0\rangle_n = X_{\mathcal{Q},n} Z_{\mathcal{Q},m} |\psi\rangle_{\mathcal{Q},m} |0\rangle_n \,, \tag{I.6}$$

where $|\psi\rangle_{\mathcal{Q},m}$ is an arbitrary state of $\mathcal{Q}$ and every qubit including $m \neq n$ but not n. Again, this relation is not an operator identity, but a property of a state where qubit n is in the separable state $|0\rangle_n$. Using this identity we arrive at

$$|\psi_{\mathcal{C}_{2D}}\rangle = \left(\prod_{k=1}^{K} H_{\mathcal{Q}} X_{\mathcal{Q},k} Z_{\mathcal{Q},k-N}\right) |+\rangle_{\mathcal{Q}} \bigotimes_{k} |0\rangle_k \tag{I.7}$$

which is (up to a shift of the index and a rotation of $\mathcal{Q}$) exactly our protocol given in eq. (3) of the main text.

I.2 General entanglement structure

In this section, we provide the explicit connection between the class of achievable states from using a single emitter with delayed quantum feedback and 2D tensor network states (PEPS). To this end, we use induction to show that the repeated application of $\hat{U}[k]$ in eq. (11.4) results in a 2D tensor network that 'grows' by an additional tensor in each time step [Fig. 11.4(b)]. This can be seen by induction: we assume that the quantum state of the system after $k-1$ steps can be written as

$$|\Psi(k-1)\rangle \otimes |0\rangle = \sum_{i_{\mathcal{Q}},\{i_j\}} \mathcal{C}[k-1]^{i_{\mathcal{Q}},\{i_j\}} \, |i_{\mathcal{Q}},\{i_j\}\rangle \otimes |0\rangle \,, \tag{I.8}$$

where $|0\rangle$ is the input state of the $k+N$-th qubit [Fig. 11.1(b)] and $\mathcal{C}[k-1]^{i_{\mathcal{Q}},\{i_j\}}$ denotes the contraction of the 2D tensor network formed by $U[\ell]$ ($\ell \in \{1,\cdots,k-1\}$) in Fig. 11.4(b) with open indices $i_{\mathcal{Q}},\{i_j\}$. The basis state $|i_{\mathcal{Q}},\{i_j\}\rangle$ enumerates configurations of $\mathcal{Q}$ and the array of $k-1$ output qubits ($j \in \{1,\cdots,k-1\}$) and N memory qubits in the delay line ($j \in \{k,\cdots,k+N-1\}$). The application of $\hat{U}[k]$ in the k-th step modifies the quantum state of k-th and $k+N$-th qubits and $\mathcal{Q}$. From Eq. (11.3) and (11.4), new quantum

amplitude $A_{i_{\mathcal{Q}},\{i_j\}}$ for a configuration $|i_{\mathcal{Q}},\{i_j\}\rangle$ can be written as

$$\begin{aligned} A_{i_{\mathcal{Q}},\{i_j\}} &= \sum_{i'_{\mathcal{Q}},\{i'_j\}} U[k]^{i_k}_{i_{k+N},i_{\mathcal{Q}},i'_k,i'_{\mathcal{Q}}} \prod_{j\notin\mathcal{Q},k} \delta_{i_j,i'_j} \mathcal{C}[k-1]^{i'_{\mathcal{Q}},\{i'_j\}} \\ &= \mathcal{C}[k]^{i_{\mathcal{Q}},\{i_j\}}, \end{aligned} \tag{I.9}$$

where the second line is achieved by identifying $U[k]^{i_k}_{i_{k+N},i_{\mathcal{Q}},i'_k,i'_{\mathcal{Q}}}$ as a rank-5 tensor in Fig. 11.4(a) and by realizing that the summations over i'_k and $i'_{\mathcal{Q}}$ are equivalent to the contraction of vertical and horizontal bonds of newly introduced tensor $U[k]$, respectively [see Fig. 11.4(b)]. We note that the generated network in Fig. 11.4(b) is contracted with shifted periodic boundary conditions.

This inductive construction also shows that arbitrary 2D tensor network satisfying Eq. (11.5) can be generated from our method via appropriate choice of unitary $\hat{U}[k]$. Interestingly, this class of states includes exotic states with topological order such as string-net states [338] or the ground state of Kitaev's Hamiltonian [339]. For example the latter state can be represented by a 2D network of translationally invariant tensors

$$U^{i_1,i_2,i_3,i_4}_{a,b,c,d} = \delta_{a+b,i_1}\delta_{d+a,i_2}\delta_{c+d,i_3}\delta_{b+c,i_4}/4, \tag{I.10}$$

where $i_1,\ldots,i_4$ denote the states of four physical qubits in a unit cell and $\{a,b,c,d\}$ run over the bond dimension 2. This tensor explicitly satisfies (11.5) and can immediately be translated into a protocol similar to the one for generating the 2D cluster state, i.e. using only controlled single photon generation and atom-photon phase gates between that atom an feedback photons.

I.3 Imperfections

Phase gate fidelity – Without shaping the wave packets of the emitted photons, each photon produced in a single step has a Lorentzian spectral profile, whose temporal profile is

$$f(t) = \sqrt{\gamma_L} e^{-\gamma_L t/2} \Theta(t) = i \int d\omega \, \frac{2\pi}{\sqrt{\gamma_L}} \frac{1}{\omega + i\gamma_L/2} e^{-i\omega t} \tag{I.11}$$

where we chose a normalization $\int dt |f(t)|^2 = 1$. The scattering phase shift for the chiral forward scattering (if the atom is in state $|g_2\rangle$) is determined by the transmission:

$$t(\omega) = \frac{\omega - i\gamma_R/2}{\omega + i\gamma_R/2} \tag{I.12}$$

such that the wave packet $f(t)$ transforms into

$$\tilde{f}(t) = i \int d\omega \, \frac{2\pi}{\sqrt{\gamma_L}} \frac{\omega - i\gamma_R/2}{\omega + i\gamma_R/2} \frac{1}{\omega + i\gamma_L/2} e^{-i\omega t} \tag{I.13}$$

$$= -\sqrt{\gamma_L} \left(\frac{\gamma_R + \gamma_L}{\gamma_R - \gamma_L} e^{-\gamma_L t/2} - 2 \frac{\gamma_R}{\gamma_R - \gamma_L} e^{-\gamma_R t/2} \right) \Theta(t) \tag{I.14}$$

It is straightforward to calculate the overlap

$$\int dt f^*(t) \tilde{f}(t) = -\frac{1 - \gamma_L/\gamma_R}{1 + \gamma_L/\gamma_R} \tag{I.15}$$

With this we obtain the fidelity of the controlled phase gate:

$$\mathcal{F}_Z = \frac{2\frac{\gamma_L}{\gamma_R}(\frac{\gamma_L}{\gamma_R} + 3) + 5}{5(\frac{\gamma_L}{\gamma_R} + 1)^2} = 1 - \frac{4}{5}\frac{\gamma_L}{\gamma_R} + \mathcal{O}\left(\frac{\gamma_L^2}{\gamma_R^2}\right). \tag{I.16}$$

If we shape the coupling via $\gamma_L(t) = \frac{4\Omega^2(t)}{\gamma}$ then $f(t) = \sqrt{\gamma_L(t)} \exp\left(-\int_0^t ds \gamma_L(s)/2\right)$. Pulse shaping allows to create photon wave packets that are symmetric in time. Straightforward calculation shows that, for example, the gaussian wave packet

$$f(t) = \sqrt{\mathcal{B}/\sqrt{\pi}} e^{-\mathcal{B}^2(t-t_0)^2/2} \tag{I.17}$$

can be obtained by

$$\gamma_L(t) = \frac{2\mathcal{B}e^{-\mathcal{B}^2(t-t_0)^2}}{\sqrt{\pi}(1-\mathrm{erf}(\mathcal{B}(t-t_0)))}. \tag{I.18}$$

The corresponding fidelity of the phase gate can be calculated from

$$\begin{aligned}\int dt f^*(t)\tilde{f}(t) &= 1 - \frac{\sqrt{\pi}e^{\frac{1}{4x^2}}\left(1-\mathrm{erf}\left(\frac{1}{2x}\right)\right)}{x} \\ &= -1 + 4x^2 + \mathcal{O}(x^4)\end{aligned} \tag{I.19}$$

with $x = \mathcal{B}/\gamma_R$, and the gaussian error function $\mathrm{erf}(z) = \frac{2}{\sqrt{\pi}}\int_0^z dt e^{-t^2}$. This gives the fidelity $\mathcal{F}_Z = 1-\frac{8}{5}x^2+\mathcal{O}(x^4)$. We note that the linear order in x vanishes in this expression unlike in the previous a case without the shaping of wave packet. This is a consequence of temporally symmetric wave packet, which can significantly improve the fidelity.

Fidelity of the controlled not gate – In the proposed implementation to create the 2D cluster state, the gate $\hat{X}_{\mathcal{Q},k+N}$ is realized by emission of a photon associated with the transition $|e_L\rangle \rightarrow |g_2\rangle$ during the second half of each timestep with period T. In order for the gate $\hat{X}_{\mathcal{Q},k+N}$ to work, we thus require $T/2$ to be much larger than the temporal extend of the emitted photon; otherwise, the next step in our protocol would proceed even before the gate $\hat{X}_{\mathcal{Q},k_N}$ is completed, leading to an error.

This gate fidelity can computed from the quantity

$$\epsilon = \int_{t_0}^{t_0+T/2} dt\gamma_L(t)\exp\left(-\int_0^t ds\gamma_L(s)\right) \tag{I.20}$$

via $\mathcal{F}_X = 1-\frac{2}{3}\epsilon+\frac{1}{6}\epsilon^2$. Without shaping the photon wave packet, i.e., with $\gamma_L(t) = \gamma_L$ as in eq. (I.11) one gets $\epsilon = e^{-\gamma_L T/2}$, while for the pulse shaped photon (I.18) (with $t_0 = -T/4$) we find $\epsilon = 1-\sqrt{2}\frac{\mathrm{erf}(\mathcal{B}T/4)}{\sqrt{1+\mathrm{erf}(\mathcal{B}T/4)}}$. For large $x = \mathcal{B}T/4 \gg 1$ we have $\epsilon \rightarrow e^{-x^2}/(\sqrt{\pi}x)$. In both cases the gate fidelity approaches 1 exponentially, but in the case of a shaped photon wave packet this approach is again faster.

Bibliography

[1] R. Shankar. *Principles of quantum mechanics*. Springer Science & Business Media, 2012.

[2] M. Hilbert and P. López. The world's technological capacity to store, communicate, and compute information. *Science*, 332(6025):60–65, 2011.

[3] R. P. Feynman. Simulating physics with computers. *International journal of theoretical physics*, 21(6-7):467–488, 1982.

[4] M. Kardar. *Statistical physics of particles*. Cambridge University Press, 2007.

[5] P. W. Anderson. Absence of Diffusion in Certain Random Lattices. *Physical Review*, 109(5):1492–1505, March 1958.

[6] R. Weaver. Anderson localization of ultrasound. *Wave motion*, 12(2):129–142, 1990.

[7] D. S. Wiersma, P. Bartolini, A. Lagendijk, and R. Righini. Localization of light in a disordered medium. *Nature*, 390(6661):671–673, 1997.

[8] T. Schwartz, G. Bartal, S. Fishman, and M. Segev. Transport and Anderson localization in disordered two-dimensional photonic lattices. *Nature*, 446(7131):52–55, 2007.

[9] G. Roati, C. D'Errico, L. Fallani, M. Fattori, C. Fort, M. Zaccanti, G. Modugno, M. Modugno, and M. Inguscio. Anderson localization of a non-interacting bose–einstein condensate. *Nature*, 453(7197):895–898, 2008.

[10] J. Billy, V. Josse, Z. Zuo, A. Bernard, B. Hambrecht, P. Lugan, D. Clément, L. Sanchez-Palencia, P. Bouyer, and A. Aspect. Direct observation of anderson localization of matter waves in a controlled disorder. *Nature*, 453(7197):891–894, 2008.

[11] D. M. Basko, I. L. Aleiner, and B. L. Altshuler. Metal–insulator transition in a weakly interacting many-electron system with localized single-particle states. *Annals of Physics*, 321(5):1126–1205, 2006.

[12] V. Oganesyan and D. A. Huse. Localization of interacting fermions at high temperature. *Physical review b*, 75(15):155111, 2007.

[13] A. Pal and D. A. Huse. Many-body localization phase transition. *Physical Review B*, 82(17):174411, November 2010.

[14] M. Schreiber, S. S. Hodgman, P. Bordia, H. P. Lüschen, M. H. Fischer, R. Vosk, E. Altman, U. Schneider, and I. Bloch. Observation of many-body localization of interacting fermions in a quasirandom optical lattice. *Science*, 349(6250):842–845, August 2015.

[15] J.-y. Choi, S. Hild, J. Zeiher, P. Schauß, A. Rubio-Abadal, T. Yefsah, V. Khemani, D. A. Huse, I. Bloch, and C. Gross. Exploring the many-body localization transition in two dimensions. *arXiv preprint arXiv:1604.04178*, 2016.

[16] A. C. Potter, T. Morimoto, and A. Vishwanath. Classification of interacting topological floquet phases in one dimension. *Phys. Rev. X*, 6:041001, Oct 2016.

[17] J. Zhang, P. W. Hess, A. Kyprianidis, P. Becker, A. Lee, J. Smith, G. Pagano, I.-D. Potirniche, A. C. Potter, A. Vishwanath, N. Y. Yao, and C. Monroe. Observation of a discrete time crystal. *Nature*, 543(7644):217–220, Mar 2017.

[18] S. Choi, J. Choi, R. Landig, G. Kucsko, H. Zhou, J. Isoya, F. Jelezko, S. Onoda, H. Sumiya, V. Khemani, C. von Keyserlingk, N. Y. Yao, E. Demler, and M. D. Lukin. Observation of discrete time-crystalline order in a disordered dipolar many-body system. *Nature*, 543(7644):221–225, Mar 2017.

[19] A. L. Burin. Energy delocalization in strongly disordered systems induced by the long-range many-body interaction. *arXiv.org*, November 2006.

[20] N. Y. Yao, C. R. Laumann, S. Gopalakrishnan, M. Knap, M. Mueller, E. A. Demler, and M. D. Lukin. Many-body localization in dipolar systems. *Physical Review Letters*, 113(24):243002, 2014.

[21] C. P. Slichter. *Principles of magnetic resonance*, volume 1. Springer Science & Business Media, 2013.

[22] A. J. Vega. Relaxation in spin-echo and spin-lock experiments. *Journal of Magnetic Resonance (1969)*, 65(2):252–267, 1985.

[23] P. Robyr, B. Meier, and R. Ernst. Radio-frequency-driven nuclear spin diffusion in solids. *Chemical Physics Letters*, 162(6):417–423, 1989.

[24] X. Wu and S. Zhang. Selective polarization inversion and depolarization of 13c in cross relaxation in nmr. *Chemical physics letters*, 156(1):79–81, 1989.

[25] S. Zhang, B. H. Meier, and R. R. Ernst. Polarization echoes in nmr. *Physical review letters*, 69(14):2149, 1992.

[26] G. Balasubramanian, P. Neumann, D. Twitchen, M. Markham, R. Kolesov, N. Mizuochi, J. Isoya, J. Achard, J. Beck, J. Tissler, et al. Ultralong spin coherence time in isotopically engineered diamond. *Nature Materials*, 8(5):383–387, 2009.

[27] J. Choi, S. Choi, G. Kucsko, P. C. Maurer, B. J. Shields, H. Sumiya, S. Onoda, J. Isoya, E. Demler, F. Jelezko, N. Y. Yao, and M. D. Lukin. Depolarization Dynamics in a Strongly Interacting Solid-State Spin Ensemble. *Physical Review Letters*, 118(9):093601, March 2017.

[28] S. R. Hartmann and E. L. Hahn. Nuclear double resonance in the rotating frame. *Physical Review*, 128(5):2042, 1962.

[29] C. Belthangady, N. Bar-Gill, L. M. Pham, K. Arai, D. Le Sage, P. Cappellaro, and R. L. Walsworth. Dressed-state resonant coupling between bright and dark spins in diamond. *Physical review letters*, 110(15):157601, 2013.

[30] A. D. Mirlin, Y. V. Fyodorov, F.-M. Dittes, J. Quezada, and T. H. Seligman. Transition from localized to extended eigenstates in the ensemble of power-law random banded matrices. *Physical Review E*, 54(4):3221, 1996.

[31] V. Kravtsov, O. Yevtushenko, P. Snajberk, and E. Cuevas. Lévy flights and multifractality in quantum critical diffusion and in classical random walks on fractals. *Physical Review E*, 86(2):021136, 2012.

[32] J. Smith, A. Lee, P. Richerme, B. Neyenhuis, P. W. Hess, P. Hauke, M. Heyl, D. A. Huse, and C. Monroe. Many-body localization in a quantum simulator with programmable random disorder. *Nature Physics*, 12(10):907–911, June 2016.

[33] P. Maurer, J. Maze, P. Stanwix, L. Jiang, A. V. Gorshkov, A. A. Zibrov, B. Harke, J. Hodges, A. S. Zibrov, A. Yacoby, et al. Far-field optical imaging and manipulation of individual spins with nanoscale resolution. *Nature Physics*, 6(11):912–918, 2010.

[34] P. Hauke, M. Heyl, L. Tagliacozzo, and P. Zoller. Measuring multipartite entanglement through dynamic susceptibilities. *Nature Physics*, advance online publication SP - EP -:–, March 2016.

[35] S. Choi, N. Y. Yao, and M. D. Lukin. Dynamical Engineering of Interactions in Qudit Ensembles. *Physical Review Letters*, 119(18):183603, November 2017.

[36] M. J. Burek, N. P. de Leon, B. J. Shields, B. J. Hausmann, Y. Chu, Q. Quan, A. S. Zibrov, H. Park, M. D. Lukin, and M. Lončar. Free-standing mechanical and photonic nanostructures in single-crystal diamond. *Nano Letters*, 12(12):6084–6089, 2012.

[37] L. S. Levitov. Delocalization of vibrational modes caused by electric dipole interaction. *Physical Review Letters*, 64(5):547, 1990.

[38] T. Langen, S. Erne, R. Geiger, B. Rauer, T. Schweigler, M. Kuhnert, W. Rohringer, I. E. Mazets, T. Gasenzer, and J. Schmiedmayer. Experimental observation of a generalized Gibbs ensemble. *Science*, 348(6231):207–211, 2015.

[39] E. Kaminishi, T. Mori, T. N. Ikeda, and M. Ueda. Entanglement pre-thermalization in a one-dimensional bose gas. *Nature Physics*, 11(12):1050–1056, 2015.

[40] S. Choi, N. Y. Yao, S. Gopalakrishnan, and M. D. Lukin. Quantum Control of Many-body Localized States. *arXiv.org*, August 2015.

[41] N. Y. Yao, C. R. Laumann, and A. Vishwanath. Many-body localization protected quantum state transfer. *arXiv.org*, August 2015.

[42] R. Adler. A study of locking phenomena in oscillators. *Proceedings of the IRE*, 34(6):351–357, 1946.

[43] M. C. Cross and P. C. Hohenberg. Pattern formation outside of equilibrium. *Rev. Mod. Phys.*, 65:851–1112, Jul 1993.

[44] A. M. Kaufman, M. E. Tai, A. Lukin, M. Rispoli, R. Schittko, P. M. Preiss, and M. Greiner. Quantum thermalization through entanglement in an isolated many-body system. *Science*, 353(6301):794–800, 2016.

[45] F. Wilczek. Quantum time crystals. *Physical review letters*, 109(16):160401, 2012.

[46] V. Khemani, A. Lazarides, R. Moessner, and S. L. Sondhi. Phase Structure of Driven Quantum Systems. *Physical Review Letters*, 116(25):250401, 2016.

[47] D. V. Else, B. Bauer, and C. Nayak. Floquet Time Crystals. *Physical Review Letters*, 117(9):090402, August 2016.

[48] C. W. von Keyserlingk, V. Khemani, and S. L. Sondhi. Absolute stability and spatiotemporal long-range order in floquet systems. *Phys. Rev. B*, 94:085112, Aug 2016.

[49] N. Y. Yao, A. C. Potter, I.-D. Potirniche, and A. Vishwanath. Discrete time crystals: rigidity, criticality, and realizations. *Physical Review Letters*, 118(3):030401, January 2017.

[50] L. Childress, M. V. Gurudev Dutt, J. M. Taylor, A. S. Zibrov, F. Jelezko, J. Wrachtrup, P. R. Hemmer, and M. D. Lukin. Coherent dynamics of coupled electron and nuclear spin qubits in diamond. *Science*, 314(5797):281–285, 2006.

[51] G. de Lange, Z. H. Wang, D. Ristè, V. V. Dobrovitski, and R. Hanson. Universal dynamical decoupling of a single solid-state spin from a spin bath. *Science*, 330(6000):60–63, 2010.

[52] M. W. Doherty, N. B. Manson, P. Delaney, F. Jelezko, J. Wrachtrup, and L. C. Hollenberg. The nitrogen-vacancy colour centre in diamond. *Physics Reports*, 528(1):1 – 45, 2013.

[53] G. Kucsko, S. Choi, J. Choi, P. C. Maurer, H. Sumiya, S. Onoda, J. Isoya, F. Jelezko, E. Demler, N. Y. Yao, and M. D. Lukin. Critical thermalization of a disordered dipolar spin system in diamond. *ArXiv e-prints*, September 2016.

[54] C. Deutsch, F. Ramirez-Martinez, C. Lacroûte, F. Reinhard, T. Schneider, J.-N. Fuchs, F. Piéchon, F. Laloë, J. Reichel, and P. Rosenbusch. Spin self-rephasing and very long coherence times in a trapped atomic ensemble. *Physical review letters*, 105(2):020401, 2010.

[55] A. M. Rey, L. Jiang, M. Fleischhauer, E. Demler, and M. D. Lukin. Many-body protected entanglement generation in interacting spin systems. *Phys. Rev. A*, 77:052305, May 2008.

[56] P. Cappellaro and M. D. Lukin. Quantum correlation in disordered spin systems: Applications to magnetic sensing. *Physical Review A*, 80(3):032311, 2009.

[57] J. S. Waugh, L. M. Huber, and U. Haeberlen. Approach to High-Resolution nmr in Solids. *Physical Review Letters*, 20(5):180–182, January 1968.

[58] R. Nandkishore and D. A. Huse. Many-body localization and thermalization in quantum statistical mechanics. *Annual Review of Condensed Matter Physics*, 6(1):15–38, 2015.

[59] D. A. Abanin, W. De Roeck, and F. Huveneers. Exponentially slow heating in periodically driven many-body systems. *Physical Review Letters*, 115(25):256803, July 2015.

[60] P. Bruno. Impossibility of spontaneously rotating time crystals: a no-go theorem. *Physical review letters*, 111(7):070402, 2013.

[61] H. Watanabe and M. Oshikawa. Absence of quantum time crystals. *Phys. Rev. Lett.*, 114:251603, Jun 2015.

[62] D. V. Else, B. Bauer, and C. Nayak. Prethermal Phases of Matter Protected by Time-Translation Symmetry. *Physical Review X*, 7(1):011026–011021, March 2017.

[63] C. W. von Keyserlingk and S. L. Sondhi. Phase structure of one-dimensional interacting Floquet systems. II. Symmetry-broken phases. *Phys. Rev. B*, 93:245146, Jun 2016.

[64] T.-Y. Li and J. A. Yorke. Period three implies chaos. *The American Mathematical Monthly*, 82(10):985–992, 1975.

[65] D. A. Abanin, W. D. Roeck, and F. Huveneers. Theory of many-body localization in periodically driven systems. *Annals of Physics*, 372:1 – 11, 2016.

[66] D. Abanin, W. De Roeck, W. W. Ho, and F. Huveneers. A Rigorous Theory of Many-Body Prethermalization for Periodically Driven and Closed Quantum Systems. *Communications in Mathematical Physics*, 354(3):809–827, June 2017.

[67] D. A. Abanin, W. De Roeck, W. W. Ho, and F. Huveneers. Effective hamiltonians, prethermalization, and slow energy absorption in periodically driven many-body systems. *Phys. Rev. B*, 95:014112, Jan 2017.

[68] D. B. Gutman, I. V. Protopopov, A. L. Burin, I. V. Gornyi, R. A. Santos, and A. D. Mirlin. Energy transport in the anderson insulator. *Phys. Rev. B*, 93:245427, Jun 2016.

[69] C. L. Degen, F. Reinhard, and P. Cappellaro. Quantum sensing. *Rev. Mod. Phys.*, 89(3):035002, July 2017.

[70] S. A. Diddams, T. Udem, J. C. Bergquist, E. A. Curtis, R. E. Drullinger, L. Hollberg, W. M. Itano, W. D. Lee, C. W. Oates, K. R. Vogel, and D. J. Wineland. An Optical Clock Based on a Single Trapped 199Hg+ Ion. *Science*, 293(5531):825–828, August 2001.

[71] J. M. Taylor, P. Cappellaro, L. Childress, L. Jiang, D. Budker, P. R. Hemmer, A. Yacoby, R. Walsworth, and M. D. Lukin. High-sensitivity diamond magnetometer with nanoscale resolution. *Nature Physics*, 4(10):810–816, September 2008.

[72] J. R. Maze, P. L. Stanwix, J. S. Hodges, S. Hong, J. M. Taylor, P. Cappellaro, L. Jiang, M. V. G. Dutt, E. Togan, A. S. Zibrov, A. Yacoby, R. L. Walsworth, and M. D. Lukin. Nanoscale magnetic sensing with an individual electronic spin in diamond. *Nature*, 455(7213):644–647, October 2008.

[73] L. M. Pham, D. Le Sage, P. L. Stanwix, T. K. Yeung, D. Glenn, A. Trifonov, P. Cappellaro, P. R. Hemmer, M. D. Lukin, H. Park, A. Yacoby, and R. L. Walsworth. Magnetic field imaging with nitrogen-vacancy ensembles. *New Journal of Physics*, 13(4):045021, April 2011.

[74] B. Bloom, T. Nicholson, J. Williams, S. Campbell, M. Bishof, X. Zhang, W. Zhang, S. Bromley, and J. Ye. An optical lattice clock with accuracy and stability at the 10-18 level. *Nature*, 506(7486):71–75, February 2014.

[75] D. Budker, P. W. Graham, M. Ledbetter, S. Rajendran, and A. O. Sushkov. Proposal for a Cosmic Axion Spin Precession Experiment (CASPEr). *Physical Review X*, 4(2):021030, May 2014.

[76] J. F. Barry, M. J. Turner, J. M. Schloss, D. R. Glenn, Y. Song, M. D. Lukin, H. Park, and R. L. Walsworth. Optical magnetic detection of single-neuron action potentials using quantum defects in diamond. *Proceedings of the National Academy of Sciences of the United States of America*, 113(49):14133–14138, December 2016.

[77] D. R. Glenn, R. R. Fu, P. Kehayias, D. Le Sage, E. A. Lima, B. P. Weiss, and R. L. Walsworth. Micrometer-scale magnetic imaging of geological samples using a quantum diamond microscope. *Geochemistry, Geophysics, Geosystems*, 18(8):3254–3267, August 2017.

[78] Basko, D M, Aleiner, I L, and Altshuler, B L. Metal–insulator transition in a weakly interacting many-electron system with localized single-particle states. *Annals of Physics*, 321(5):1126–1205, May 2006.

[79] A. Lazarides, A. Das, and R. Moessner. Fate of Many-Body Localization Under Periodic Driving. *Physical Review Letters*, 115(3):030402, July 2015.

[80] P. Ponte, Z. Papić, F. Huveneers, and D. A. Abanin. Many-Body Localization in Periodically Driven Systems. *Physical Review Letters*, 114(14):140401, April 2015.

[81] T. Mori, T. Kuwahara, and K. Saito. Rigorous Bound on Energy Absorption and Generic Relaxation in Periodically Driven Quantum Systems. *Physical Review Letters*, 116(12):120401, March 2016.

[82] W. W. Ho, S. Choi, M. D. Lukin, and D. A. Abanin. Critical Time Crystals in Dipolar Systems. *Physical Review Letters*, 119(1):010602, July 2017.

[83] J. C. Allred, R. N. Lyman, T. W. Kornack, and M. V. Romalis. High-Sensitivity Atomic Magnetometer Unaffected by Spin-Exchange Relaxation. *Physical Review Letters*, 89(13):130801, September 2002.

[84] C. Deutsch, F. Ramirez-Martinez, C. Lacroûte, F. Reinhard, T. Schneider, J. N. Fuchs, F. Piéchon, F. Laloë, J. Reichel, and P. Rosenbusch. Spin Self-Rephasing and Very Long Coherence Times in a Trapped Atomic Ensemble. *Physical Review Letters*, 105(2):020401, July 2010.

[85] P. Zanardi, M. G. A. Paris, and L. C. Venuti. Quantum criticality as a resource for quantum estimation. *Physical Review A*, 78(4):042105, October 2008.

[86] K. Macieszczak, M. Guţă, I. Lesanovsky, and J. P. Garrahan. Dynamical phase transitions as a resource for quantum enhanced metrology. *Physical Review A*, 93(2):022103, February 2016.

[87] M. Skotiniotis, P. Sekatski, and W. Dür. Quantum metrology for the Ising Hamiltonian with transverse magnetic field. *New Journal of Physics*, 17(7):073032, July 2015.

[88] I. Frérot and T. Roscilde. Quantum critical metrology. *arXiv preprint arXiv:1707.08804*, July 2017.

[89] H. Strobel, W. Muessel, D. Linnemann, T. Zibold, D. B. Hume, L. Pezzè, A. Smerzi, and M. K. Oberthaler. Fisher information and entanglement of non-Gaussian spin states. *Science*, 345(6195):424–427, July 2014.

[90] O. Hosten, N. J. Engelsen, R. Krishnakumar, and M. A. Kasevich. Measurement noise 100 times lower than the quantum-projection limit using entangled atoms. *Nature*, 529(7587):505–508, January 2016.

[91] J. G. Bohnet, B. C. Sawyer, J. W. Britton, M. L. Wall, A. M. Rey, M. Foss-Feig, and J. J. Bollinger. Quantum spin dynamics and entanglement generation with hundreds of trapped ions. *Science*, 352(6291):1297–1301, 2016.

[92] J. Aasi, J. Abadie, B. Abbott, R. Abbott, T. Abbott, M. Abernathy, C. Adams, T. Adams, P. Addesso, R. Adhikari, et al. Enhanced sensitivity of the LIGO gravitational wave detector by using squeezed states of light. *Nature Photonics*, 7(8):613–619, July 2013.

[93] E. L. Hahn. Spin Echoes. *Physical Review*, 80(4):580–594, November 1950.

[94] G. de Lange, Z. H. Wang, D. Ristè, V. V. Dobrovitski, and R. Hanson. Universal dynamical decoupling of a single solid-state spin from a spin bath. *Science*, 330(6000):60–63, September 2010.

[95] W.-J. Kuo and D. A. Lidar. Quadratic dynamical decoupling: Universality proof and error analysis. *Physical Review A*, 84(4):042329, October 2011.

[96] L. Jiang and A. Imambekov. Universal dynamical decoupling of multiqubit states from environment. *Physical Review A*, 84(6):060302, December 2011.

[97] P. C. Maurer, G. Kucsko, C. Latta, L. Jiang, N. Y. Yao, S. D. Bennett, F. Pastawski, D. Hunger, N. Chisholm, M. Markham, D. J. Twitchen, J. I. Cirac, and M. D. Lukin. Room-temperature quantum bit memory exceeding one second. *Science*, 336(6086):1283–1286, 2012.

[98] I. Lovchinsky, A. O. Sushkov, E. Urbach, N. P. de Leon, S. Choi, K. De Greve, R. Evans, R. Gertner, E. Bersin, C. Müller, L. McGuinness, F. Jelezko, R. L. Walsworth, H. Park, and M. D. Lukin. Nuclear magnetic resonance detection and spectroscopy of single proteins using quantum logic. *Science*, 351(6275):836–841, February 2016.

[99] I. Lovchinsky, J. D. Sanchez-Yamagishi, E. K. Urbach, S. Choi, S. Fang, T. I. Andersen, K. Watanabe, T. Taniguchi, A. Bylinskii, E. Kaxiras, P. Kim, H. Park, and M. D. Lukin. Magnetic resonance spectroscopy of an atomically thin material using a single-spin qubit. *Science*, 355(6324):503–507, February 2017.

[100] T. Kuwahara, T. Mori, and K. Saito. Floquet–Magnus theory and generic transient dynamics in periodically driven many-body quantum systems. *Annals of Physics*, 367:96–124, April 2016.

[101] W. H. Zurek, U. Dorner, and P. Zoller. Dynamics of a Quantum Phase Transition. *Physical Review Letters*, 95(10):105701, September 2005.

[102] M. E. Fisher, S.-k. Ma, and B. G. Nickel. Critical Exponents for Long-Range Interactions. *Physical Review Letters*, 29(14):917–920, October 1972.

[103] A. Dutta and J. K. Bhattacharjee. Phase transitions in the quantum Ising and rotor models with a long-range interaction. *Physical Review B*, 64(18):184106, October 2001.

[104] M. Knap, A. Kantian, T. Giamarchi, I. Bloch, M. D. Lukin, and E. Demler. Probing Real-Space and Time-Resolved Correlation Functions with Many-Body Ramsey Interferometry. *Physical Review Letters*, 111(14):147205, October 2013.

[105] S. Fey and K. P. Schmidt. Critical behavior of quantum magnets with long-range interactions in the thermodynamic limit. *Physical Review B*, 94(7):075156, August 2016.

[106] M. F. Maghrebi, Z.-X. Gong, M. Foss-Feig, and A. V. Gorshkov. Causality and quantum criticality in long-range lattice models. *Physical Review B*, 93(12):125128, March 2016.

[107] R. J. Elliott and C. Wood. The Ising model with a transverse field. I. High temperature expansion. *Journal of Physics C: Solid State Physics*, 4(15):2359–2369, October 1971.

[108] P. Pfeuty and R. J. Elliott. The Ising model with a transverse field. II. Ground state properties. *Journal of Physics C: Solid State Physics*, 4(15):2370–2385, October 1971.

[109] Z. Friedman. Ising model with a transverse field in two dimensions: Phase diagram and critical properties from a real-space renormalization group. *Physical Review B*, 17(3):1429–1432, February 1978.

[110] S. Sachdev. *Quantum phase transitions*. Cambridge University Press, Cambridge New York, 2011.

[111] A. I. Bugrii. Correlation Function of the Two-Dimensional Ising Model on a Finite Lattice: I. *Theoretical and Mathematical Physics*, 127(1):528–548, 2001.

[112] P. Fonseca and A. Zamolodchikov. Ising Field Theory in a Magnetic Field: Analytic Properties of the Free Energy. *Journal of Statistical Physics*, 110(3-6):527–590, 2003.

[113] F. H. L. Essler and R. M. Konik. Finite-temperature dynamical correlations in massive integrable quantum field theories. *Journal of Statistical Mechanics: Theory and Experiment*, 2009(09):P09018, September 2009.

[114] S. Kolkowitz, I. Pikovski, N. Langellier, M. D. Lukin, R. L. Walsworth, and J. Ye. Gravitational wave detection with optical lattice atomic clocks. *Physical Review D*, 94(12):124043, December 2016.

[115] G. S. Uhrig. Keeping a quantum bit alive by optimized π-pulse sequences. *Physical Review Letters*, 98(10):100504, 2007.

[116] J. Bylander, S. Gustavsson, F. Yan, F. Yoshihara, K. Harrabi, G. Fitch, D. G. Cory, Y. Nakamura, J.-S. Tsai, and W. D. Oliver. Noise spectroscopy through dynamical decoupling with a superconducting flux qubit. *Nature Physics*, 7(7):565–570, July 2011.

[117] G. A. Paz-Silva and D. A. Lidar. Optimally combining dynamical decoupling and quantum error correction. *Scientific reports*, 2013.

[118] E. M. Kessler, P. Komar, M. Bishof, L. Jiang, and A. S. Sørensen. Heisenberg-limited atom clocks based on entangled qubits. *Physical Review*, 112(19):190403, 2014.

[119] D. G. Lucarelli. Quantum optimal control via gradient ascent in function space and the time-bandwidth quantum speed limit. *arXiv.org*, 2016.

[120] V. M. Frey, S. Mavadia, L. M. Norris, and W. de Ferranti. Application of optimal band-limited control protocols to quantum noise sensing. *arXiv.org*, 2017.

[121] N. H. Lindner, G. Refael, and V. Galitski. Floquet topological insulator in semiconductor quantum wells. *Nature*, 7(6):490–495, March 2011.

[122] L. Jiang, T. Kitagawa, J. Alicea, A. R. Akhmerov, D. Pekker, G. Refael, J. I. Cirac, E. Demler, M. D. Lukin, and P. Zoller. Majorana Fermions in Equilibrium and in Driven Cold-Atom Quantum Wires. *Physical Review Letters*, 106(22):220402, June 2011.

[123] T. Iadecola, L. H. Santos, and C. Chamon. Stroboscopic symmetry-protected topological phases. *Physical Review B*, 92(12):125107, September 2015.

[124] U. Haeberlen and J. S. Waugh. Coherent Averaging Effects in Magnetic Resonance. *Phys. Rev.*, 175(2):453–467, 1968.

[125] B. Yan, S. A. Moses, B. Gadway, J. P. Covey, K. R. A. Hazzard, A. M. Rey, D. S. Jin, and J. Ye. Observation of dipolar spin-exchange interactions with lattice-confined polar molecules. *Nature*, 501(7468):521–525, September 2013.

[126] G. A. Álvarez, D. Suter, and R. Kaiser. Localization-delocalization transition in the dynamics of dipolar-coupled nuclear spins. *Science*, 349(6250):846–848, 2015.

[127] M. Gärttner, J. G. Bohnet, A. Safavi-Naini, M. L. Wall, J. J. Bollinger, and A. M. Rey. Measuring out-of-time-order correlations and multiple quantum spectra in a trapped-ion quantum magnet. *Nature Physics*, 2017.

[128] K. X. Wei, C. Ramanathan, and P. Cappellaro. Exploring Localization in Nuclear Spin Chains. *arXiv.org*, December 2016.

[129] A. Brinkmann and M. Edén. Second order average Hamiltonian theory of symmetry-based pulse schemes in the nuclear magnetic resonance of rotating solids: Application to triple-quantum dipolar recoupling. *The Journal of chemical physics*, 120(24):11726–11745, June 2004.

[130] A. Ajoy and P. Cappellaro. Quantum Simulation via Filtered Hamiltonian Engineering: Application to Perfect Quantum Transport in Spin Networks. *Physical Review Letters*, 110(22):220503, May 2013.

[131] H. Frydrych, G. Alber, and P. Bažant. Constructing Pauli pulse schemes for decoupling and quantum simulation. *Physical Review A*, 89(2):022320, February 2014.

[132] D. Hayes, S. T. Flammia, and M. J. Biercuk. Programmable quantum simulation by dynamic hamiltonian engineering. *New Journal of Physics*, 16(8):083027, 2014.

[133] C. Senko, P. Richerme, J. Smith, A. Lee, I. Cohen, A. Retzker, and C. Monroe. Realization of a Quantum Integer-Spin Chain with Controllable Interactions. *Physical Review X*, 5(2):021026, June 2015.

[134] R. B. Potts and C. Domb. Some generalized order-disorder transformations. *Mathematical Proceedings of the Cambridge Philosophical Society*, 48(01):106–4, October 2008.

[135] D. A. Huse. Simple three-state model with infinitely many phases. *Physical Review B*, 24(9):5180–5194, November 1981.

[136] F. D. M. Haldane. Nonlinear field theory of large spin Heisenberg antiferromagnets. Semiclassically quantized solitons of the one-dimensional easy Axis Neel state. *Physical Review Letters*, 50(15):1153–1156, 1983.

[137] P. Fendley. Parafermionic edge zero modes in Zn-invariant spin chains. *Journal of Statistical Mechanics: Theory and Experiment*, 2012(11):P11020, November 2012.

[138] H. Labuhn, D. Barredo, S. Ravets, S. de Léséleuc, T. Macrì, T. Lahaye, and A. Browaeys. Tunable two-dimensional arrays of single Rydberg atoms for realizing quantum Ising models. *Nature*, 534(7609):667–670, June 2016.

[139] J. Zeiher, J.-y. Choi, A. Rubio-Abadal, T. Pohl, R. van Bijnen, I. Bloch, and C. Gross. Coherent many-body spin dynamics in a long-range interacting Ising chain. *ArXiv e-prints*, May 2017.

[140] H. Bernien, S. Schwartz, A. Keesling, H. Levine, A. Omran, H. Pichler, S. Choi, A. S. Zibrov, M. Endres, M. Greiner, V. Vuletić, and M. D. Lukin. Probing many-body dynamics on a 51-atom quantum simulator. *Nature*, 551(7682):579, 2017.

[141] M. Rotteler and P. Wocjan. Equivalence of Decoupling Schemes and Orthogonal Arrays. *IEEE transactions on information theory*, 52(9):4171–4181, September 2006.

[142] M. Stollsteimer and G. Mahler. Suppression of arbitrary internal coupling in a quantum register. *Physical Review A*, 64(5):052301, October 2001.

[143] M. A. Nielsen, M. J. Bremner, J. L. Dodd, A. M. Childs, and C. M. Dawson. Universal simulation of Hamiltonian dynamics for quantum systems with finite-dimensional state spaces. *Physical Review A*, 66(2):022317, August 2002.

[144] D. A. Abanin, W. De Roeck, W. W. Ho, and F. Huveneers. Effective Hamiltonians, prethermalization and slow energy absorption in periodically driven many-body systems. *Physical Review B*, 95(1):014112, January 2017.

[145] W. Dür, J. I. Cirac, M. Lewenstein, and D. Bruß. Distillability and partial transposition in bipartite systems. *Physical Review A*, 61(6):062313, May 2000.

[146] D. Bertsimas, J. N. Tsitsiklis, and J. Tsitsiklis. *Introduction to Linear Optimization (Athena Scientific Series in Optimization and Neural Computation, 6)*. Athena Scientific, 1997.

[147] A. Prakash, C. G. West, and T.-C. Wei. Detection of gapped phases of a one-dimensional spin chain with on-site and spatial symmetries. *Physical Review B*, 94(4):045136, March 2016.

[148] I. Affleck, T. Kennedy, E. H. Lieb, and H. Tasaki. Rigorous results on valence-bond ground states in antiferromagnets. *Physical Review Letters*, 59(7):799–802, August 1987.

[149] L. D'Alessio and M. Rigol. Long-time Behavior of Isolated Periodically Driven Interacting Lattice Systems. *Physical Review X*, 4(4):041048, December 2014.

[150] A. Lazarides, A. Das, and R. Moessner. Equilibrium states of generic quantum systems subject to periodic driving. *Physical Review E*, 90(1):012110, July 2014.

[151] P. Ponte, A. Chandran, Z. Papić, and D. A. Abanin. Periodically driven ergodic and many-body localized quantum systems. *Annals of Physics*, 353:196–204, February 2015.

[152] S. Choi, D. A. Abanin, and M. D. Lukin. Dynamically induced many-body localization. *Phys. Rev. B*, 97:100301, March 2018.

[153] T. D. Ladd, F. Jelezko, R. Laflamme, Y. Nakamura, C. Monroe, and J. L. O'Brien. Quantum computers. *Nature*, 464(7285):45–53, April 2010.

[154] M. A. Nielsen and I. L. Chuang. *Quantum Computation and Quantum Information: 10th Anniversary Edition - Michael A. Nielsen, Isaac L. Chuang - Google Books*. Cambridge university press, 2010.

[155] J. L. O'Brien. Optical quantum computing. *Science*, 318(5856):1567–1570, 2007.

[156] H. Häffner, C. Roos, and R. Blatt. Quantum computing with trapped ions. *Physics Reports*, 469(4):155 – 203, 2008.

[157] J. A. Jones. Quantum computing with {NMR}. *Progress in Nuclear Magnetic Resonance Spectroscopy*, 59(2):91 – 120, 2011.

[158] D. Loss and D. DiVincenzo. Quantum computation with quantum dots. *Phys. Rev. A*, 57:120–126, Jan 1998.

[159] N. Y. Yao, L. Jiang, A. V. Gorshkov, P. C. Maurer, G. Giedke, J. I. Cirac, and M. D. Lukin. scalable architecture for a room temperature solid-state quantum information processor. *Nature Communications*, 3:800–8, 1.

[160] M. Žnidarič, T. c. v. Prosen, and P. Prelovšek. Many-body localization in the heisenberg xxz magnet in a random field. *Phys. Rev. B*, 77:064426, Feb 2008.

[161] C. Monthus and T. Garel. Many-body localization transition in a lattice model of interacting fermions: Statistics of renormalized hoppings in configuration space. *Phys. Rev. B*, 81:134202, Apr 2010.

[162] J. H. Bardarson, F. Pollmann, and J. E. Moore. Unbounded Growth of Entanglement in Models of Many-Body Localization. *Physical Review Letters*, 109(1):017202, July 2012.

[163] M. Serbyn, Z. Papić, and D. A. Abanin. Local conservation laws and the structure of the many-body localized states. *Phys. Rev. Lett.*, 111:127201, Sep 2013.

[164] M. Serbyn, Z. Papić, and D. A. Abanin. Universal slow growth of entanglement in interacting strongly disordered systems. *Phys. Rev. Lett.*, 110:260601, Jun 2013.

[165] S. Iyer, V. Oganesyan, G. Refael, and D. Huse. Many-body localization in a quasiperiodic system. *Phys. Rev. B*, 87:134202, Apr 2013.

[166] Y. Bahri, R. Vosk, E. Altman, and A. Vishwanath. Localization and topology protected quantum coherence at the edge of 'hot' matter. *arXiv.org*, July 2013.

[167] B. Bauer and C. Nayak. Area laws in a many-body localized state and its implications for topological order. *Journal of Statistical Mechanics: Theory and Experiment*, 2013(09):P09005, 2013.

[168] D. A. Huse, R. Nandkishore, and V. Oganesyan. Phenomenology of fully many-body-localized systems. *Physical Review B*, 90(17):174202, November 2014.

[169] R. Nandkishore, S. Gopalakrishnan, and D. A. Huse. Spectral features of a many-body-localized system weakly coupled to a bath. *Phys. Rev. B*, 90:064203, Aug 2014.

[170] M. Serbyn, Z. Papić, and D. A. Abanin. Quantum quenches in the many-body localized phase. *Phys. Rev. B*, 90:174302, Nov 2014.

[171] N. Yao, C. Laumann, J. I. Cirac, M. Lukin, and J. Moore. Quasi many-body localization in translation invariant systems. *arXiv preprint arXiv:1410.7407*, 2014.

[172] A. Chandran, I. H. Kim, G. Vidal, and D. A. Abanin. Constructing local integrals of motion in the many-body localized phase. *arXiv.org*, July 2014.

[173] R. Nandkishore and D. A. Huse. Many body localization and thermalization in quantum statistical mechanics. *arXiv.org*, April 2014.

[174] M. Pino. Entanglement growth in many-body localized systems with long-range interactions. *arXiv.org*, March 2014.

[175] V. Khemani, R. Nandkishore, and S. L. Sondhi. Non-local Adiabatic Response of a Localized System to Local Manipulations. *arXiv.org*, November 2014.

[176] B. Bauer and C. Nayak. Analyzing many-body localization with a quantum computer. *Phys. Rev. X*, 4:041021, Nov 2014.

[177] A. L. Burin. Many-body delocalization in a strongly disordered system with long-range interactions: Finite-size scaling. *Physical Review B*, 91(9):094202, 2015.

[178] R. Vasseur, A. C. Potter, and S. A. Parameswaran. Quantum criticality of hot random spin chains. *Phys. Rev. Lett.*, 114:217201, May 2015.

[179] A. C. Potter, R. Vasseur, and S. A. Parameswaran. Universal properties of many-body delocalization transitions. *Phys. Rev. X*, 5:031033, Sep 2015.

[180] M. Serbyn, M. Knap, S. Gopalakrishnan, Z. Papić, N. Y. Yao, C. R. Laumann, D. A. Abanin, M. D. Lukin, and E. A. Demler. Interferometric probes of many-body localization. *Phys. Rev. Lett.*, 113:147204, Oct 2014.

[181] M. Saffman, T. G. Walker, and K. Molmer. Quantum information with Rydberg atoms. *Reviews Of Modern Physics*, 82(3):2313–2363, 2010.

[182] G. Giedke, J. M. Taylor, D. D'Alessandro, M. D. Lukin, and A. Imamoğlu. Quantum measurement of a mesoscopic spin ensemble. *Phys. Rev. A*, 74:032316, Sep 2006.

[183] A. Goban, C. L. Hung, S. P. Yu, J. D. Hood, J. A. Muniz, J. H. Lee, M. J. Martin, A. C. McClung, K. S. Choi, D. E. Chang, O. Painter, and H. J. Kimble. Atom–light interactions in photonic crystals. *Nature Communications*, 5, May 2014.

[184] S. John and J. Wang. Quantum optics of localized light in a photonic band gap. *Phys. Rev. B*, 43:12772–12789, Jun 1991.

[185] S. John and J. Wang. Quantum electrodynamics near a photonic band gap: Photon bound states and dressed atoms. *Phys. Rev. Lett.*, 64:2418–2421, May 1990.

[186] D. Basko, I. Aleiner, and B. Altshuler. Possible experimental manifestations of the many-body localization. *Phys. Rev. B*, 76:052203, Aug 2007.

[187] K. K. Ni, S. Ospelkaus, M. H. G. de Miranda, A. Pe'er, B. Neyenhuis, J. J. Zirbel, S. Kotochigova, P. S. Julienne, D. S. Jin, and J. Ye. A High Phase-Space-Density Gas of Polar Molecules. *Science*, 322(5899):231–235, October 2008.

[188] N. Strohmaier, D. Greif, R. Jördens, L. Tarruell, H. Moritz, T. Esslinger, R. Sensarma, D. Pekker, E. Altman, and E. Demler. Observation of elastic doublon decay in the fermi-hubbard model. *Phys. Rev. Lett.*, 104:080401, Feb 2010.

[189] S. Trotzky, P. Cheinet, S. Foelling, M. Feld, U. Schnorrberger, A. M. Rey, A. Polkovnikov, E. A. Demler, M. D. Lukin, and I. Bloch. Time-resolved observation and control of superexchange interactions with ultracold atoms in optical lattices. *Science*, 319(5861):295–299, 2008.

[190] T. Fukuhara. Quantum dynamics of a mobile spin impurity. *Nature Physics*, 9(4):235–241, February 2013.

[191] M. W. Johnson, M. H. S. Amin, S. Gildert, T. Lanting, F. Hamze, N. Dickson, R. Harris, A. J. Berkley, J. Johansson, P. Bunyk, E. M. Chapple, C. Enderud, J. P. Hilton, K. Karimi, E. Ladizinsky, N. Ladizinsky, T. Oh, I. Perminov, C. Rich, M. C. Thom, E. Tolkacheva, C. J. S. Truncik, S. Uchaikin, J. Wang, B. Wilson, and G. Rose. Quantum annealing with manufactured spins. *Nature*, 473(7346):194–198, May 2011.

[192] T. Lanting, A. J. Przybysz, A. Y. Smirnov, F. M. Spedalieri, M. H. Amin, A. J. Berkley, R. Harris, F. Altomare, S. Boixo, P. Bunyk, N. Dickson, C. Enderud, J. P. Hilton, E. Hoskinson, M. W. Johnson, E. Ladizinsky, N. Ladizinsky, R. Neufeld, T. Oh, I. Perminov, C. Rich, M. C. Thom, E. Tolkacheva, S. Uchaikin, A. B. Wilson, and G. Rose. Entanglement in a quantum annealing processor. *Phys. Rev. X*, 4:021041, May 2014.

[193] M. Stern, G. Catelani, Y. Kubo, C. Grezes, A. Bienfait, D. Vion, D. Esteve, and P. Bertet. Flux qubits with long coherence times for hybrid quantum circuits. *Phys. Rev. Lett.*, 113, Sep 2014.

[194] K. R. Brown, A. W. Harrow, and I. L. Chuang. Arbitrarily accurate composite pulse sequences. *Physical Review A*, 70(5):052318, November 2004.

[195] T. Kitagawa, E. Berg, M. Rudner, and E. Demler. Topological Characterization of Periodically-Driven Quantum Systems. *Physical Review B*, 82(23):235114, 2010.

[196] J. Li, R. Fan, H. Wang, B. Ye, B. Zeng, H. Zhai, X. Peng, and J. Du. Measuring out-of-time-order correlators on a nuclear magnetic resonance quantum simulator. *arXiv.org*, September 2016.

[197] H. Lignier, C. Sias, D. Ciampini, Y. Singh, A. Zenesini, O. Morsch, and E. Arimondo. Dynamical Control of Matter-Wave Tunneling in Periodic Potentials. *Physical Review Letters*, 99(22):220403, November 2007.

[198] A. Verdeny, A. Mielke, and F. Mintert. Accurate Effective Hamiltonians via Unitary Flow in Floquet Space. *Physical Review Letters*, 111(17):175301, October 2013.

[199] A. Roy and A. Das. Fate of dynamical many-body localization in the presence of disorder. *Physical Review B*, 91(12):121106, March 2015.

[200] A. Haldar and A. Das. Dynamical many-body localization and delocalization in periodically driven closed quantum systems. *Annalen der Physik*, 107(7):1600333, March 2017.

[201] D. J. Luitz, N. Laflorencie, and F. Alet. Many-body localization edge in the random-field Heisenberg chain. *Physical Review B*, 91(8):081103, February 2015.

[202] A. L. Burin. Analytical theory of many-body localization in the presence of periodic drive. *arXiv.org*, February 2017.

[203] T. E. Lee. Floquet engineering from long-range to short-range interactions. *Physical Review A*, 94(4):040701, August 2016.

[204] M. V. Berry. Regular and irregular semiclassical wavefunctions. *Journal of Physics A: Mathematical and General*, 10(12):2083, 1977.

[205] S. W. McDonald and A. N. Kaufman. Spectrum and eigenfunctions for a hamiltonian with stochastic trajectories. *Phys. Rev. Lett.*, 42:1189–1191, Apr 1979.

[206] E. J. Heller. Bound-state eigenfunctions of classically chaotic hamiltonian systems: Scars of periodic orbits. *Phys. Rev. Lett.*, 53:1515–1518, Oct 1984.

[207] S. Sridhar. Experimental observation of scarred eigenfunctions of chaotic microwave cavities. *Phys. Rev. Lett.*, 67:785–788, Aug 1991.

[208] L. Huang, Y.-C. Lai, D. K. Ferry, S. M. Goodnick, and R. Akis. Relativistic quantum scars. *Phys. Rev. Lett.*, 103:054101, Jul 2009.

[209] P. J. J. Luukko, B. Drury, A. Klales, L. Kaplan, E. J. Heller, and E. Räsänen. Strong quantum scarring by local impurities. *Scientific Reports*, 6:37656 EP –, Nov 2016. Article.

[210] J. Keski-Rahkonen, P. J. J. Luukko, L. Kaplan, E. J. Heller, and E. Räsänen. Controllable quantum scars in semiconductor quantum dots. *Phys. Rev. B*, 96:094204, Sep 2017.

[211] C. J. Turner, A. A. Michailidis, D. A. Abanin, M. Serbyn, and Z. Papic. Quantum many-body scars. *ArXiv e-prints*, November 2017.

[212] M. V. Berry. Quantum scars of classical closed orbits in phase space. *Proceedings of the Royal Society of London. Series A, Mathematical and Physical Sciences*, 423(1864):219–231, 1989.

[213] E. Bogomolny. Smoothed wave functions of chaotic quantum systems. *Physica D: Nonlinear Phenomena*, 31(2):169 – 189, 1988.

[214] D. Perez-Garcia, F. Verstraete, M. M. Wolf, and J. I. Cirac. Matrix product state representations. *Quantum Inf. Comput.*, 7(5):401–430, July 2007.

[215] N. Schuch, D. Pérez-García, and I. Cirac. Classifying quantum phases using matrix product states and projected entangled pair states. *Phys. Rev. B*, 84:165139, Oct 2011.

[216] I. Cohen, P. Richerme, Z.-X. Gong, C. Monroe, and A. Retzker. Simulating the haldane phase in trapped-ion spins using optical fields. *Phys. Rev. A*, 92:012334, Jul 2015.

[217] R. M. W. van Bijnen and T. Pohl. Quantum magnetism and topological ordering via rydberg dressing near förster resonances. *Phys. Rev. Lett.*, 114:243002, Jun 2015.

[218] A. Mazurenko, C. S. Chiu, G. Ji, M. F. Parsons, M. Kanász-Nagy, R. Schmidt, F. Grusdt, E. Demler, D. Greif, and M. Greiner. A cold-atom fermi–hubbard antiferromagnet. *Nature (London)*, 545:462–466, 2017.

[219] J. Cai, A. Retzker, F. Jelezko, and M. B. Plenio. A large-scale quantum simulator on a diamond surface at room temperature. *Nat. Phys.*, 9:168–173, 2013.

[220] R. Barends, A. Shabani, L. Lamata, J. Kelly, A. Mezzacapo, U. L. Heras, R. Babbush, A. G. Fowler, B. Campbell, Y. Chen, and *et al.* Digitized adiabatic quantum computing with a superconducting circuit. *Nature (London)*, 534(7606):222–226, Jun 2016.

[221] B. Kraus, H. P. Büchler, S. Diehl, A. Kantian, A. Micheli, and P. Zoller. Preparation of entangled states by quantum markov processes. *Phys. Rev. A*, 78:042307, Oct 2008.

[222] F. Verstraete, M. M. Wolf, and J. I. Cirac. Quantum computation and quantum-state engineering driven by dissipation. *Nat. Phys.*, 5:633–636, 2009.

[223] F. Ticozzi and L. Viola. Stabilizing entangled states with quasi-local quantum dynamical semigroups. *Phil. Trans. R. Soc. A*, 370(1979):5259–5269, 2012.

[224] J. Cho, S. Bose, and M. S. Kim. Optical pumping into many-body entanglement. *Phys. Rev. Lett.*, 106:020504, Jan 2011.

[225] V. V. Albert and L. Jiang. Symmetries and conserved quantities in lindblad master equations. *Phys. Rev. A*, 89:022118, Feb 2014.

[226] F. Iemini, D. Rossini, R. Fazio, S. Diehl, and L. Mazza. Dissipative topological superconductors in number-conserving systems. *Phys. Rev. B*, 93:115113, Mar 2016.

[227] J. T. Barreiro, M. Müller, P. Schindler, D. Nigg, T. Monz, M. Chwalla, M. Hennrich, C. F. Roos, P. Zoller, and R. Blatt. An open-system quantum simulator with trapped ions. *Nature (London)*, 470:486–491, 2010.

[228] F. Reiter, L. Tornberg, G. Johansson, and A. S. Sørensen. Steady-state entanglement of two superconducting qubits engineered by dissipation. *Phys. Rev. A*, 88:032317, Sep 2013.

[229] D. D. B. Rao and K. Mølmer. Deterministic entanglement of rydberg ensembles by engineered dissipation. *Phys. Rev. A*, 90:062319, Dec 2014.

[230] M. Roghani and H. Weimer. Dissipative preparation of entangled many-body states with rydberg atoms. *Quantum Science and Technology*, 2018.

[231] M. J. Kastoryano, F. Reiter, and A. S. Sørensen. Dissipative preparation of entanglement in optical cavities. *Phys. Rev. Lett.*, 106:090502, Feb 2011.

[232] F. Haldane. Continuum dynamics of the 1-d heisenberg antiferromagnet: Identification with the o(3) nonlinear sigma model. *Phys. Lett. A*, 93(9):464 – 468, 1983.

[233] F. Pollmann, A. M. Turner, E. Berg, and M. Oshikawa. Entanglement spectrum of a topological phase in one dimension. *Phys. Rev. B*, 81:064439, Feb 2010.

[234] M. den Nijs and K. Rommelse. Preroughening transitions in crystal surfaces and valence-bond phases in quantum spin chains. *Phys. Rev. B*, 40:4709–4734, Sep 1989.

[235] D. Pérez-García, M. M. Wolf, M. Sanz, F. Verstraete, and J. I. Cirac. String order and symmetries in quantum spin lattices. *Phys. Rev. Lett.*, 100:167202, Apr 2008.

[236] M. Endres, H. Bernien, A. Keesling, H. Levine, E. R. Anschuetz, A. Krajenbrink, C. Senko, V. Vuletic, M. Greiner, and M. D. Lukin. Atom-by-atom assembly of defect-free one-dimensional cold atom arrays. *Science*, 354(6315):1024–1027, 2016.

[237] D. Barredo, S. de Léséleuc, V. Lienhard, T. Lahaye, and A. Browaeys. An atom-by-atom assembler of defect-free arbitrary two-dimensional atomic arrays. *Science*, 354(6315):1021–1023, 2016.

[238] B. J. Lester, N. Luick, A. M. Kaufman, C. M. Reynolds, and C. A. Regal. Rapid production of uniformly filled arrays of neutral atoms. *Phys. Rev. Lett.*, 115:073003, Aug 2015.

[239] D. Petrosyan, J. Otterbach, and M. Fleischhauer. Electromagnetically Induced Transparency with Rydberg Atoms. *Physical Review Letters*, 107(21):213601, November 2011.

[240] C. Gardiner and P. Zoller. *Quantum Noise: A Handbook of Markovian and Non-Markovian Quantum Stochastic Methods with Applications to Quantum Optics*, volume 56. Springer Science & Business Media, 2004.

[241] G. Vidal. Efficient classical simulation of slightly entangled quantum computations. *Phys. Rev. Lett.*, 91:147902, Oct 2003.

[242] H.-J. Briegel, W. Dür, J. I. Cirac, and P. Zoller. Quantum repeaters: The role of imperfect local operations in quantum communication. *Phys. Rev. Lett.*, 81:5932–5935, Dec 1998.

[243] M. Lukin, M. Fleischhauer, R. Cote, L. Duan, D. Jaksch, J. I. Cirac, and Z. P. Dipole blockade and quantum information processing in mesoscopic atomic ensembles. *Physical Review Letters*, 87:037901, 2001.

[244] F. Reiter and A. S. Sørensen. Effective operator formalism for open quantum systems. *Phys. Rev. A*, 85:032111, Mar 2012.

[245] J. M. Deutsch. Quantum statistical mechanics in a closed system. *Phys. Rev. A*, 43:2046–2049, Feb 1991.

[246] J. Eisert, M. Friesdorf, and C. Gogolin. Quantum many-body systems out of equilibrium. *Nat Phys*, 11(2):124–130, Feb 2015.

[247] M. Sanz, M. M. Wolf, D. Pérez-García, and J. I. Cirac. Matrix product states: Symmetries and two-body hamiltonians. *Phys. Rev. A*, 79:042308, Apr 2009.

[248] D. Perez-Garcia, F. Verstraete, M. M. Wolf, and J. I. Cirac. Peps as unique ground states of local hamiltonians. *Quantum Inf. Comput.*, 8(6):650–663, July 2008.

[249] N. Schuch, M. M. Wolf, F. Verstraete, and J. I. Cirac. Computational complexity of projected entangled pair states. *Phys. Rev. Lett.*, 98:140506, Apr 2007.

[250] K. Birnbaum, A. Boca, R. Miller, A. Boozer, T. Northup, and H. J. Kimble. Photon blockade in an optical cavity with one trapped atom. *Nature*, 436(7047):87–90, 2005.

[251] I. Schuster, A. Kubanek, A. Fuhrmanek, T. Puppe, P. W. H. Pinkse, K. Murr, and G. Rempe. Nonlinear spectroscopy of photons bound to one atom. *Nature Physics*, 4(5):382–385, April 2008.

[252] I. Friedler, D. Petrosyan, M. Fleischhauer, and G. Kurizki. Long-range interactions and entanglement of slow single-photon pulses. *Physical Review A*, 72(4):043803, October 2005.

[253] A. V. Gorshkov, J. Otterbach, M. Fleischhauer, T. Pohl, and M. D. Lukin. Photon-photon interactions via Rydberg blockade. *Physical Review Letters*, 107(13):133602, 2011.

[254] J. D. Pritchard, D. Maxwell, A. Gauguet, K. J. Weatherill, M. P. A. Jones, and C. S. Adams. Cooperative Atom-Light Interaction in a Blockaded Rydberg Ensemble. *Physical Review Letters*, 105(19):193603, November 2010.

[255] Y. O. Dudin and A. Kuzmich. Strongly Interacting Rydberg Excitations of a Cold Atomic Gas. *Science*, 336(6083):887–889, May 2012.

[256] T. Peyronel, O. Firstenberg, Q.-Y. Liang, S. Hofferberth, A. V. Gorshkov, T. Pohl, M. D. Lukin, and V. Vuletic. Quantum nonlinear optics with single photons enabled by strongly interacting atoms. *Nature*, 488(7409):57–60, July 2012.

[257] O. Firstenberg, T. Peyronel, Q.-Y. Liang, A. V. Gorshkov, M. D. Lukin, and V. Vuletić. Attractive photons in a quantum nonlinear medium. *Nature*, 502(7469):71–5, October 2013.

[258] H. Gorniaczyk, C. Tresp, J. Schmidt, H. Fedder, and S. Hofferberth. Single Photon Transistor Mediated by Rydberg Interaction. *Physical Review Letters*, 113:053601, August 2014.

[259] D. Tiarks, S. Baur, K. Schneider, S. Durr, and G. Rempe. Single-Photon Transistor Using a Förster Resonance. *Physical Review Letters*, 113:053602, August 2014.

[260] D. Tiarks, S. Schmidt, G. Rempe, and S. Dürr. Optical π phase shift created with a single-photon pulse. *Science Advances*, 2(4):e1600036–e1600036, April 2016.

[261] B. Hacker, S. Welte, G. Rempe, and S. Ritter. A photon–photon quantum gate based on a single atom in an optical resonator. *Nature*, 536(7615):193–196, July 2016.

[262] K. M. Beck, M. Hosseini, Y. Duan, and V. Vuletić. Large conditional single-photon cross-phase modulation. *Proceedings of the National Academy of Sciences*, 113(35):9740–9744, 2016.

[263] A. Stern and N. H. Lindner. Topological quantum computation—from basic concepts to first experiments. *Science*, 339(6124):1179–1184, 2013.

[264] C. Monroe and J. Kim. Scaling the Ion Trap Quantum Processor. *Science*, 339(6124):1164–1169, March 2013.

[265] L. Lu, J. D. Joannopoulos, and M. Soljačić. Topological photonics. *Nature Photonics*, 8(11):821–829, October 2014.

[266] D. E. Chang, V. Vuletic, and M. D. Lukin. Quantum nonlinear optics — photon by photon. *Nature Photonics*, 8(9):685–694, August 2014.

[267] D. Maxwell, D. J. Szwer, D. Paredes-Barato, H. Busche, J. D. Pritchard, A. Gauguet, K. J. Weatherill, M. Jones, and C. S. Adams. Storage and control of optical photons using Rydberg polaritons. *Physical Review Letters*, 110(10):103001, 2013.

[268] S. Ravets, H. Labuhn, D. Barredo, L. Béguin, T. Lahaye, and A. Browaeys. Coherent dipole-dipole coupling between two single Rydberg atoms at an electrically-tuned Forster resonance. *Nature Physics*, 10(12):914–917, December 2014.

[269] H. Gorniaczyk, C. Tresp, P. Bienias, A. Paris-Mandoki, W. Li, I. Mirgorodskiy, H. P. Büchler, I. Lesanovsky, and S. Hofferberth. Enhancement of single-photon transistor by Stark-tuned Förster resonances. *arXiv.org*, November 2015.

[270] C. R. Murray, A. V. Gorshkov, and T. Pohl. Many-body decoherence dynamics and optimised operation of a single-photon switch. *arXiv.org*, July 2016.

[271] A. P. Schnyder, S. Ryu, A. Furusaki, and A. W. W. Ludwig. Classification of topological insulators and superconductors in three spatial dimensions. *Physical Review B*, 78(19):195125, November 2008.

[272] C. W. J. Beenakker. Random-matrix theory of Majorana fermions and topological superconductors. *Reviews Of Modern Physics*, 87(3):1037–1066, September 2015.

[273] A. Y. Kitaev. Unpaired Majorana fermions in quantum wires. *Phys. Usp.*, 44(10S):131–136, 2001.

[274] V. Mourik, K. Zuo, S. M. Frolov, S. R. Plissard, E. P. A. M. Bakkers, and L. P. Kouwenhoven. Signatures of Majorana Fermions in Hybrid Superconductor-Semiconductor Nanowire Devices. *Science*, 336(6084):1003–1007, May 2012.

[275] M. F. Maghrebi, N. Y. Yao, M. Hafezi, T. Pohl, O. Firstenberg, and A. V. Gorshkov. Fractional quantum Hall states of Rydberg polaritons. *Physical Review A*, 91(3):033838, March 2015.

[276] A. Sommer, H. P. Büchler, and J. Simon. Quantum Crystals and Laughlin Droplets of Cavity Rydberg Polaritons. *arXiv.org*, June 2015.

[277] P. Bienias, S. Choi, O. Firstenberg, M. F. Maghrebi, M. Gullans, M. D. Lukin, A. V. Gorshkov, and H. P. Büchler. Scattering resonances and bound states for strongly interacting Rydberg polaritons. *Physical Review A*, 90(5):053804, February 2014.

[278] M. Fleischhauer and M. Lukin. Dark-state polaritons in electromagnetically induced transparency. *Phys. Rev. Lett.*, 84(22):5094–7, May 2000.

[279] I. Carusotto and C. Ciuti. Quantum fluids of light. *Rev. Mod. Phys.*, 85:299, 2013.

[280] D. E. Chang, V. Gritsev, G. Morigi, V. Vuletic, M. D. Lukin, and E. A. Demler. Crystallization of strongly interacting photons in a nonlinear optical fibre. *Nature Phys.*, 4:884, 2008.

[281] J. Otterbach, M. Moos, D. Muth, and M. Fleischhauer. Wigner Crystallization of Single Photons in Cold Rydberg Ensembles. *Phys. Rev. Lett.*, 111(11):113001, September 2013.

[282] I. Fushman, D. Englund, A. Faraon, N. Stoltz, P. Petroff, and J. Vuckovic. Controlled phase shifts with a single quantum dot. *Science*, 320(5877):769–72, May 2008.

[283] A. Rauschenbeutel, G. Nogues, S. Osnaghi, P. Bertet, M. Brune, J. Raimond, and S. Haroche. Coherent Operation of a Tunable Quantum Phase Gate in Cavity QED. *Phys. Rev. Lett.*, 83(24):5166–5169, December 1999.

[284] G. Kirchmair, B. Vlastakis, Z. Leghtas, S. E. Nigg, H. Paik, E. Ginossar, M. Mirrahimi, L. Frunzio, S. M. Girvin, and R. J. Schoelkopf. Observation of quantum state collapse and revival due to the single-photon Kerr effect. *Nature*, 495(7440):205–9, March 2013.

[285] A. A. Gorshkov, J. Otterbach, M. Fleischhauer, T. Pohl, and M. Lukin. Photon-Photon Interactions via Rydberg Blockade. *Phys. Rev. Lett.*, 107:133602, September 2011.

[286] V. Parigi, E. Bimbard, J. Stanojevic, A. J. Hilliard, F. Nogrette, R. Tualle-Brouri, A. Ourjoumtsev, and P. Grangier. Observation and measurement of interaction-induced dispersive optical nonlinearities in an ensemble of cold rydberg atoms. *Phys. Rev. Lett.*, 109:233602, 2012.

[287] T. Peyronel, O. Firstenberg, Q.-Y. Liang, S. Hofferberth, A. V. Gorshkov, T. Pohl, M. D. Lukin, and V. Vuletić. Quantum nonlinear optics with single photons enabled by strongly interacting atoms. *Nature*, 488(7409):57–60, August 2012.

[288] M. Fleischhauer, A. Imamoglu, and J. P. Marangos. Electromagnetically induced transparency: Optics in coherent media. *Rev. Mod. Phys.*, 77(April):633–673, 2005.

[289] C. Liu, Z. Dutton, C. H. Behroozi, and L. V. Hau. Observation of coherent optical information storage in an atomic medium using halted light pulses. *Nature*, 409(6819):490–3, January 2001.

[290] D. F. Phillips, A. Fleischhauer, A. Mair, R. L. Walsworth, and M. D. Lukin. Storage of light in atomic vapor. *Phys. Rev. Lett.*, 86:783–786, Jan 2001.

[291] B. Julsgaard, J. Sherson, J. I. Cirac, J. Fiurasek, and E. S. Polzik. Experimental demonstration of quantum memory for light. *Nature*, 432(7016):482–486, 11 2004.

[292] A. Gaëtan, Y. Miroshnychenko, T. Wilk, A. Chotia, M. Viteau, D. Comparat, P. Pillet, A. Browaeys, and P. Grangier. Observation of collective excitation of two individual atoms in the Rydberg blockade regime. *Nat. Phys.*, 5(2):115–118, January 2009.

[293] E. Urban, T. a. Johnson, T. Henage, L. Isenhower, D. D. Yavuz, T. G. Walker, and M. Saffman. Observation of Rydberg blockade between two atoms. *Nat. Phys.*, 5(2):110–114, January 2009.

[294] H. Schempp, G. Günter, M. Robert-de Saint-Vincent, C. S. Hofmann, D. Breyel, A. Komnik, D. W. Schönleber, M. Gärttner, J. Evers, S. Whitlock, and M. Weidemüller. Full counting statistics of laser excited rydberg aggregates in a one-dimensional geometry. *Phys. Rev. Lett.*, 112:013002, Jan 2014.

[295] D. Maxwell, D. J. Szwer, D. Paredes-Barato, H. Busche, J. D. Pritchard, A. Gauguet, K. J. Weatherill, M. P. A. Jones, and C. S. Adams. Storage and control of optical photons using rydberg polaritons. *Phys. Rev. Lett.*, 110:103001, Mar 2013.

[296] P. Schausz, M. Cheneau, M. Endres, T. Fukuhara, S. Hild, A. Omran, T. Pohl, C. Gross, S. Kuhr, and I. Bloch. Observation of spatially ordered structures in a two-dimensional rydberg gas. *Nature*, 491(7422):87–91, 11 2012.

[297] R. Heidemann, U. Raitzsch, V. Bendkowsky, B. Butscher, R. Löw, L. Santos, and T. Pfau. Evidence for coherent collective rydberg excitation in the strong blockade regime. *Phys. Rev. Lett.*, 99:163601, Oct 2007.

[298] S. Baur, D. Tiarks, G. Rempe, and S. Dürr. Single-photon switch based on rydberg blockade. *arXiv:1307.3509*, 2013.

[299] L. Li, Y. O. Dudin, and A. Kuzmich. Entanglement between light and an optical atomic excitation. *Nature*, 498:466–469, 2013.

[300] C. Chin, R. Grimm, P. Julienne, and E. Tiesinga. Feshbach resonances in ultracold gases. *Rev. Mod. Phys.*, 82:1225–1286, Apr 2010.

[301] B. He, A. V. Sharypov, J. Sheng, C. Simon, and M. Xiao. Two-photon dynamics in coherent rydberg atomic ensemble. *arXiv:1401.1540*, 2014.

[302] A. Abrikosov, L. Gorkov, and I. Dzyaloshinski. *Methods of quantum fiedld theory in statistical physics*. Dover Publications, New York, 1963.

[303] M. Olshanii. Atomic scattering in the presence of an external confinement and a gas of impenetrable bosons. *Phys. Rev. Lett.*, 81:938–941, Aug 1998.

[304] G. E. Astrakharchik, J. Boronat, J. Casulleras, and S. Giorgini. Beyond the tonks-girardeau gas: Strongly correlated regime in quasi-one-dimensional bose gases. *Phys. Rev. Lett.*, 95:190407, Nov 2005.

[305] S. Chen, L. Guan, X. Yin, Y. Hao, and X.-W. Guan. Transition from a tonks-girardeau gas to a super-tonks-girardeau gas as an exact many-body dynamics problem. *Phys. Rev. A*, 81:031609, Mar 2010.

[306] M. D. Girardeau and G. E. Astrakharchik. Wave functions of the super-tonks-girardeau gas and the trapped one-dimensional hard-sphere bose gas. *Phys. Rev. A*, 81:061601, Jun 2010.

[307] E. Haller, M. Gustavsson, M. J. Mark, J. G. Danzl, R. Hart, G. Pupillo, and H.-C. Nägerl. Realization of an excited, strongly correlated quantum gas phase. *Science*, 325(5945):1224–1227, 2009.

[308] S. Sala, P.-I. Schneider, and A. Saenz. Inelastic confinement-induced resonances in low-dimensional quantum systems. *Phys. Rev. Lett.*, 109:073201, Aug 2012.

[309] P. Kok, W. J. Munro, K. Nemoto, T. C. Ralph, J. P. Dowling, and G. J. Milburn. Linear optical quantum computing with photonic qubits. *Reviews of Modern Physics*, 79(1):135–174, January 2007.

[310] J.-W. Pan, Z.-B. Chen, C.-Y. Lu, H. Weinfurter, A. Zeilinger, and M. Żukowski. Multiphoton entanglement and interferometry. *Reviews of Modern Physics*, 84(2):777–838, May 2012.

[311] E. Knill, R. Laflamme, and G. J. Milburn. A scheme for efficient quantum computation with linear optics : Abstract : Nature. *Nature*, 409(6816):46–52, January 2001.

[312] P. Walther, K. J. Resch, T. Rudolph, E. Schenck, H. Weinfurter, V. Vedral, M. Aspelmeyer, and A. Zeilinger. Experimental one-way quantum computing. *Nature*, 434(7030):169–176, March 2005.

[313] X. Ding, Y. He, Z. C. Duan, N. Gregersen, M. C. Chen, S. Unsleber, S. Maier, C. Schneider, M. Kamp, S. Höfling, C.-Y. Lu, and J.-W. Pan. On-Demand Single Photons with High Extraction Efficiency and Near-Unity Indistinguishability from a Resonantly Driven Quantum Dot in a Micropillar. *Physical Review Letters*, 116(2):020401, January 2016.

[314] I. Aharonovich, D. Englund, and M. Toth. Solid-state single-photon emitters. *Nature Photonics*, 10(10):631–641, September 2016.

[315] H. M. Wiseman and G. J. Milburn. *Quantum Measurement and Control*. Cambridge University Press, 2010.

[316] A. L. Grimsmo. Time-Delayed Quantum Feedback Control. *Physical Review Letters*, 115(6):060402, August 2015.

[317] H. Pichler and P. Zoller. Photonic Circuits with Time Delays and Quantum Feedback. *Physical Review Letters*, 116(9):093601–093606, March 2016.

[318] A. Sipahigil, R. E. Evans, D. D. Sukachev, M. J. Burek, J. Borregaard, M. K. Bhaskar, C. T. Nguyen, J. L. Pacheco, H. A. Atikian, C. Meuwly, R. M. Camacho, F. Jelezko, E. Bielejec, H. Park, M. Loncar, and M. Lukin. An integrated diamond nanophotonics platform for quantum-optical networks. *Science*, 354(6314):847–850, November 2016.

[319] J. Volz, M. Scheucher, C. Junge, and A. Rauschenbeutel. Nonlinear π phase shift for single fibre-guided photons interacting with a single resonator-enhanced atom. *Nature Photonics*, 8(12):965–970, November 2014.

[320] A. Reiserer, N. Kalb, G. Rempe, and S. Ritter. A quantum gate between a flying optical photon and a single trapped atom. *Nature*, 508(7495):237–240, April 2014.

[321] T. G. Tiecke, J. D. Thompson, N. P. de Leon, L. R. Liu, V. Vuletic, and M. Lukin. Nanophotonic quantum phase switch with a single atom. *Nature*, 508(7495):241–244, April 2014.

[322] I. Söllner, S. Mahmoodian, S. L. Hansen, L. Midolo, A. Javadi, G. Kiršanskė, T. Pregnolato, H. El-Ella, E. H. Lee, J. D. Song, S. Stobbe, and P. Lodahl. Deterministic photon–emitter coupling in chiral photonic circuits. *Nature Nanotechnology*, 10(9):775–778, July 2015.

[323] I. C. Hoi, A. F. Kockum, L. Tornberg, A. Pourkabirian, G. Johansson, P. Delsing, and C. M. Wilson. Probing the quantum vacuum with an artificial atom in front of a mirror. *Nature Physics*, 11(12):1045–1049, September 2015.

[324] A. Stute, B. Casabone, B. Brandstätter, K. Friebe, N. E, and R. Blatt. Quantum-state transfer from an ion to a photon. *Nature Photonics*, 7(3):219–222, 2013.

[325] C. Eichler, J. Mlynek, J. Butscher, P. Kurpiers, K. Hammerer, T. J. Osborne, and A. Wallraff. Exploring Interacting Quantum Many-Body Systems by Experimentally Creating Continuous Matrix Product States in Superconducting Circuits. *Physical Review X*, 5(4):041044, December 2015.

[326] P. Lodahl, S. Mahmoodian, and S. Stobbe. Interfacing single photons and single quantum dots with photonic nanostructures. *Reviews of Modern Physics*, 87(2):347–400, May 2015.

[327] H. J. Briegel, D. E. Browne, W. Dür, R. Raussendorf, and M. Van den Nest. Measurement-based quantum computation. *Nature Physics*, 5(1):19–26, January 2009.

[328] N. H. Lindner and T. Rudolph. Proposal for Pulsed On-Demand Sources of Photonic Cluster State Strings. *Physical Review Letters*, 103(11):113602, September 2009.

[329] S. E. Economou, N. Lindner, and T. Rudolph. Optically Generated 2-Dimensional Photonic Cluster State from Coupled Quantum Dots. *Physical Review Letters*, 105(9):093601, August 2010.

[330] I. Schwartz, D. Cogan, E. R. Schmidgall, Y. Don, L. Gantz, O. Kenneth, N. H. Lindner, and D. Gershoni. Deterministic generation of a cluster state of entangled photons. *Science*, 354(6311):434–437, October 2016.

[331] C. Schön, E. Solano, F. Verstraete, I. Cirac, and M. M. Wolf. Sequential Generation of Entangled Multiqubit States. *Physical Review Letters*, 95(11):110503–4, September 2005.

[332] F. Verstraete and J. I. Cirac. Renormalization algorithms for quantum-many body systems in two and higher dimensions. *arXiv.org*, page 0407066 (2004), 2004.

[333] P. Lodahl, S. Mahmoodian, S. Stobbe, A. Rauschenbeutel, P. Schneeweiss, J. Volz, H. Pichler, and P. Zoller. Chiral quantum optics. *Nature*, 541(7638):473–480, January 2017.

[334] R. Raussendorf and H. J. Briegel. A One-Way Quantum Computer. *Physical Review Letters*, 86(22):5188–5191, May 2001.

[335] J. I. Cirac, P. Zoller, H. J. Kimble, and H. Mabuchi. Quantum State Transfer and Entanglement Distribution among Distant Nodes in a Quantum Network. *Physical Review Letters*, 78(16):3221–3224, April 1997.

[336] M. Pechal, L. Huthmacher, C. Eichler, S. Zeytinoğlu, A. A. Abdumalikov, S. Berger, A. Wallraff, and S. Filipp. Microwave-Controlled Generation of Shaped Single Photons in Circuit Quantum Electrodynamics. *Physical Review X*, 4(4):041010, October 2014.

[337] T. Baba. Slow light in photonic crystals. *Nature Photonics*, 2(8):465–473, August 2008.

[338] O. Buerschaper, M. Aguado, and G. Vidal. Explicit tensor network representation for the ground states of string-net models. *Physical Review B*, 79(8):085119, February 2009.

[339] A. Y. Kitaev. Fault-tolerant quantum computation by anyons. *Annals of Physics*, 303(1):2–30, January 2003.

[340] M. Varnava, D. E. Browne, and T. Rudolph. Loss Tolerance in One-Way Quantum Computation via Counterfactual Error Correction. *Physical Review Letters*, 97(12):120501, September 2006.

[341] M. V. Gustafsson, T. Aref, A. F. Kockum, M. K. Ekstrom, G. Johansson, and P. Delsing. Propagating phonons coupled to an artificial atom. *Science*, 346(6206):207–211, October 2014.

[342] E. Van Oort and M. Glasbeek. Electric-field-induced modulation of spin echoes of nv centers in diamond. *Chemical Physics Letters*, 168(6):529–532, 1990.

[343] E. Betzig. Nobel lecture: Single molecules, cells, and super-resolution optics. *Rev. Mod. Phys.*, 87:1153–1168, Oct 2015.

[344] N. Bar-Gill, L. M. Pham, A. Jarmola, D. Budker, and R. L. Walsworth. Solid-state electronic spin coherence time approaching one second. *Nature Communications*, 4:ncomms2771, April 2013.

[345] X. Chen, Z. C. Gu, and X. G. Wen. Classification of gapped symmetric phases in one-dimensional spin systems. *Physical Review B*, 83:035107, 2011.

[346] X. Chen, Z.-C. Gu, and X.-G. Wen. Complete classification of one-dimensional gapped quantum phases in interacting spin systems. *Physical Review B*, 84(23):235128, December 2011.

[347] F. Pollmann and A. M. Turner. Detection of symmetry-protected topological phases in one dimension. *Physical Review B*, 86(12):125441, September 2012.

[348] G. Vidal. Classical Simulation of Infinite-Size Quantum Lattice Systems in One Spatial Dimension. *Physical Review Letters*, 98(7):070201, February 2007.

[349] B. Efron. Nonparametric estimates of standard error: The jackknife, the bootstrap and other methods. *Biometrika*, 68(3):589–599, 1981.

[350] A. Gilchrist, N. K. Langford, and M. A. Nielsen. Distance measures to compare real and ideal quantum processes. *Phys. Rev. A*, 71:062310, Jun 2005.

[351] R. H. Hadfield. Single-photon detectors for optical quantum information applications. *Nature Photonics*, 3:696–705, 2009.

[352] D. P. Arovas, A. Auerbach, and F. D. M. Haldane. Extended heisenberg models of antiferromagnetism: Analogies to the fractional quantum hall effect. *Phys. Rev. Lett.*, 60:531–534, Feb 1988.

[353] M. Artin. *Algebra*, chapter 10, pages 290–322. Pearson, 2 edition, 8 2010.

[354] E. Fermi. Sopra lo spostamento per pressione delle righe elevate delle serie spettrali. *Il Nuovo Cimento (1924-1942)*, 11(3):157, Sep 2008.

[355] C. H. Greene, A. S. Dickinson, and H. R. Sadeghpour. Creation of polar and nonpolar ultra-long-range rydberg molecules. *Phys. Rev. Lett.*, 85:2458–2461, Sep 2000.

[356] E. L. Hamilton, C. H. Greene, and H. R. Sadeghpour. Shape-resonance-induced long-range molecular rydberg states. *Journal of Physics B: Atomic, Molecular and Optical Physics*, 35(10):L199, 2002.

[357] A. Gaj, A. T. Krupp, J. B. Balewski, R. Löw, S. Hofferberth, and T. Pfau. From molecular spectra to a density shift in dense rydberg gases. *Nature communications*, 5:4546, 2014.

[358] A. Gorshkov, A. André, M. D. Lukin, and A. Sørensen. Photon storage in Λ-type optically dense atomic media. II. Free-space model. *Physical Review A*, 76(3):033805, September 2007.

[359] M. Schlagmüller, T. C. Liebisch, F. Engel, K. S. Kleinbach, F. Böttcher, U. Hermann, K. M. Westphal, A. Gaj, R. Löw, S. Hofferberth, T. Pfau, J. Pérez-Ríos, and C. H. Greene. Ultracold chemical reactions of a single rydberg atom in a dense gas. *Phys. Rev. X*, 6:031020, Aug 2016.